Dissertation

submitted to the
Combined Faculties for the Natural Sciences and for Mathematics
of the Ruperto Carola University of Heidelberg, Germany
for the degree of
Doctor of Natural Sciences

Put forward by

Dipl.-Phys.: Julian Weichsel

born in: Schweinfurt

Oral examination: 08.12.2010

Modeling and quantitative analysis of actin cytoskeleton networks

Referees: Prof. Dr. Ulrich S. Schwarz

Prof. Dr. Heinz Horner

Zusammenfassung

In eukaryotischen Zellen bildet das Strukturprotein Aktin Polymernetzwerke aus, die sehr dynamisch und für viele zelluläre Prozesse lebenswichtig sind. In dieser Arbeit werden theoretische Konzepte vorgestellt, um die Eigenschaften komplexer Aktin-Netzwerkstrukturen zu verstehen und mit Messungen mittels Fluoreszenz- und Elektronenmikroskopie zu vergleichen.

Ein Großteil der Arbeit behandelt dabei flache vernetzte Aktinstrukturen, die durch gerichtete Polymerisation gegen eine äußere Kraft anwachsen. Dieser Netzwerktyp ist ein wichtiger Bestandteil von sich bewegenden Zellen, wird aber auch von intrazellulären Pathogenen zur Fortbewegung missbraucht. Eine zentrale, experimentell messbare Eigenschaft solcher Netzwerke ist ihre Kraft-Geschwindigkeits-Relation. Verschiedene aktuelle Messungen ergaben hierfür widersprüchlich erscheinende Ergebnisse. In einem relativ einfachen physikalischen Modell wird gezeigt, dass in wachsenden Aktin-Netzwerken zwei stationäre Filament-Orientierungsverteilungen miteinander konkurrieren. Strukturelle Übergänge zwischen den beiden Architekturen werden durch Änderung der Wachstumsgeschwindigkeit des Netzwerks initiiert. Mit zusätzlichen Annahmen zur mechanischen Stabilität einzelner Filamente werden die experimentell gefundenen Eigenarten der Kraft-Geschwindigkeits-Relation (eine Abfolge von konvexen und konkaven Verläufen sowie Hysterese) theoretisch begründet. Das Modell wird zusätzlich auf Aktinwachstum gegen gekrümmte Hindernisse wie intrazelluläre Pathogene erweitert.

Um in der Zukunft spezifische Vorhersagen des Modells experimentell zu überprüfen, wurde eine Methode zur automatischen Analyse von Elektronenmikroskopiebildern von Aktin-Netzwerken entwickelt. Erste Ergebnisse lassen eine gute Übereinstimmung erwarten. Des Weiteren wurde eine Methode entwickelt, um Änderungen in der Aktin-Struktur von adhärenten Zellen in einem Hochdurchsatzverfahren mit Fluoreszenzmikroskopie zu bewerten.

Abstract

Inside eukaryotic cells, the structural protein actin forms polymer networks which are both very dynamic and vital for many cellular processes. In this work, we develop theoretical approaches to model the structure of complex actin networks and to compare specific predictions to fluorescence and electron microscopy data.

For the main part of this work, we focus on flat polarized networks of crosslinked actin filaments, which are able to push against an external force by directed polymerization. Such networks are an essential part of migrating cells, in which the constituent filaments protrude the cell membrane at the front. Moreover they are also exploited by pathogens for transport in the cell. An important characteristic of this network growth is the force-velocity relation, for which recent experiments gave conflicting results. Using a generic model for actin network growth, we show that two fundamentally different network architectures compete in growing actin gels. Changing network growth velocity induces transitions between them. With additional assumptions on the mechanical stability of single filaments, we arrive at a unifying framework to explain the puzzling characteristics of the force-velocity relation (both convex and concave parts occur as well as a hysteresis loop). We also extend the model to describe actin network growth against curved obstacles like intracellular pathogens.

To test specific predictions of our model in the future, we develop an automatic analysis method for electron microscopy images of actin networks. A first proof-of-principle experiment is performed, which yields results in agreement with the model predictions. Additionally, we introduce another method to quantify changes in actin structures of adherent cells from high-throughput fluorescence microscopy.

Contents

List of Symbols

δ_{fil} Unit length increment in actin polymerization, page 29

$\hat{k}_{\mathrm{b}}$ Branching rate per filament per unit time, Eq. (3.2), page 31

$\hat{n}$ Unit vector defining the local orientation in an image, page 90

$\hat{n}'$ Eigenvector of the structure tensor, Eq. (7.5), page 91

$\kappa(\theta)$ Spring constant of a single filament, Eq. (5.5), page 72

κ_0 Orientation independent spring constant of a single filament, Eq. (5.5), page 72

λ_i Eigenvalues of the Jacobi-Matrix, Eq. (3.14)-(3.18), page 36

$\langle X_{\mathrm{fib}} \rangle$ Mean of a Gaussian parameter distribution, page 115

$\mathcal{D}_p$ Optimized Sobel derivative filter, Eq. (7.11), page 93

$\mathcal{G}$ Filter which has the shape of a Gaussian window function, Eq. (7.11), page 93

$\mathcal{O}$ Order parameter of the network pattern, Eq. (3.29), page 40

$\mathcal{W}$ Branching angle dependent weighting factor distribution, Eq. (3.1), page 30

ϕ Angle of local orientation in an image, Eq. (7.7), page 91

σ Standard deviation of a Gaussian distribution

$\sigma_{\mathcal{G}}$ Standard deviation of the Gaussian window function in pixel, page 93

$\mathbf{J}$ Structure tensor, Eq. (7.3), page 91

Θ Tangent orientation angle of a bent filament, Eq. (5.6), page 76

θ Direction of a growing filament with respect to the vertical line of reference, page 30

θ_{c} Critical orientation angle for outgrowth, Eq. (3.4), page 31

$\theta_{\mathrm{fil}}^{\mathrm{fmax}}$ Maximum angle, up to which each filament carries the maximum force, page 73

θ_{max} Maximum orientation of filaments that contribute in pushing, Eq. (5.1), page 69

$\tilde{v}_{\mathrm{nw}}^{=}$ Lateral network velocity in the rotated obstacle frame, page 55

$\tilde{v}_{\mathrm{nw}}^{\perp}$ Orthogonal network velocity in the rotated obstacle frame, page 55

$\tilde{}$ Indicating variables in the rotated obstacle frame, page 54

φ Skew angle of a linear obstacle, page 53

$\vec{v}_i$ Eigenvectors of the Jacobi-Matrix, Eq. (3.26), page 38

$\vec{x}$ Pixel position in an image, page 91

$A_{\mathrm{fib,c}}$ Effective fiber area at the percolation threshold, page 17

A_{fib} Effective fiber area, Eq. (2.1), page 17

B Bending modulus of an actin filament, Eq. (5.6), page 76

c_{c} Image coherency, Eq. (7.10), page 93

$d_{\mathrm{br}}^{=}$ Lateral width of the non-periodic obstacle surface, page 46

$d_{\mathrm{br}}^{\perp}$ Vertical width of the branching region, page 29

d_{fib} Mean nearest neighbor fiber distance, Eq. (2.4), page 19

d_{gap} Width of the gap between bulk network and obstacle surface, page 70

F_{ext} External force acting against network growth, page 68

$f_{\mathrm{fil}}^{\mathrm{model}}$ Force carried by a single filament, Eq. (5.2), page 70

F_{stall} Stall force of the actin network, page 79

$g(\vec{x})$ Continuous image gray value scalar field, page 90

$h_{\mathcal{G}}$ Size of the Gaussian window function in pixel, page 93

$J_{p'p'}$ Eigenvalue of the structure tensor, Eq. (7.5), page 91

J_{pq} Structure tensor component, Eq. (7.4), page 91

$k_{\mathrm{B}}T$ Thermal energy scale, Eq. (5.3), page 71

k_{b} Branching rate per unit time, Eq. (3.2), page 31

k_{c} Capping rate per filament per unit time, Eq. (3.1), page 30

k_{gr} Total rate of outgrowth per filament per unit time, page 48

$k_{\mathrm{gr}}^{=}$ Rate of lateral outgrowth per filament per unit time, Eq. (4.1), page 48

$k_{\mathrm{gr}}^{\perp}$ Rate of orthogonal outgrowth per filament per unit time, Eq. (3.5), page 31

L Filament backbone length, page 77

$l_{\mathrm{fib,c}}$ Fiber length at percolation, page 18

l_{fib} Fiber length in the random fiber model, page 15

N Distribution of the number of filaments in the branching region, Eq. (3.1), page 30

$N_{\bar{\theta}}$ Integrated filament number around $\bar{\theta}$, Eq. (3.6), page 34

$N_{\bar{\theta}}^{\mathrm{ss35}}$ Steady state number of filaments in the ± 35 pattern, Eq. (3.12), page 35

N_{fib} Absolute filament number in the random fiber model, page 15

N_{front} Number of topmost filaments that are stalled by the obstacle load, page 29

p Connectivity probability between nearest neighbors, page 17

P_{cross} Crossing probability of two randomly oriented fibers, page 19

p_{c} Connectivity probability at the percolation threshold, page 17

r_{br} Length scale ratio, Eq. (4.12), page 50

s_{fib} Bundle strength in the adjusted random fiber model, page 110

u_{c} Generalized velocity parameter, Eq. (3.23), page 37

v_{fil} Single filament barbed end polymerization velocity, page 28

$v_{\mathrm{fil}}^{\perp}$ Projected polymerization velocity perpendicular to the leading edge, Eq. (3.3), page 31

v_{nw} Growth velocity of the leading edge, page 28

w Window function, defining a neighborhood in an image, Eq. (7.2), page 90

w_{fib} Bundle width in the adjusted random fiber model, page 110

x Indentation length of a single filament, Eq. (5.5), page 72

List of Abbreviations

ADF	Actin depolymerizing factors
AFM	Atomic force microscope
Arp	Actin related proteins
EM	Electron microscopy
HIV	Human immunodeficiency virus
ss35	± 35 steady state
ss70	$+70/0/-70$ steady state

List of Figures

Chapter 1

Introduction

The structural protein *actin* is strongly conserved in all eukaryotic cells. To fulfill its diverse functions under very different cellular conditions, it interacts with a large number of accessory proteins. These multiple interactions constrain the evolutionary variability of actin, because any enhancement in the interaction with one protein is likely to alter the cooperation with another protein to the worse. Due to this central role, evolutionary changes can be found more dominantly in the proteins interacting with actin rather than in actin itself.

As it has developed its current structure relatively early, actin not only fulfills a single cellular function, but rather it is involved in very different cellular tasks mostly regarding cell-mechanical aspects like stability and force generation. Depending on the surrounding conditions, actin cooperates with different groups of accessory proteins and self-organizes into variable network structures that are specialized for different tasks. For cellular motility for instance, a growing actin network generates the necessary work for protrusion, while contractile actin bundles and the cortex below the plasma membrane stabilize adherent cells.

Actin networks are also very relevant in the medical context as they are involved in many disease-related processes in the cell. In the host, different pathogens hijack actin and its accessory protein machinery to efficiently infect the system. Some causative agents like the bacterium *Listeria* are using a very specific actin related mechanism, similar to growing actin networks in migrating cells, to move through the cytoplasm of their host. For others, like the *HI-virus*, actin has been shown to be a crucial host factor for successful infection, but the underlying mechanistic details are still unknown.

In this work, we will discuss different theoretical approaches and quantitative experimental strategies, which we hope will help in the understanding of the self-organization of this fascinating biomaterial.

1.1 Acti(o)n on the single filament level

The building blocks of actin cytoskeleton networks are actin filaments in a combination with accessory proteins linking the structures. Each individual filament however is again a composition of elementary globular actin subunits [2, 47, 85]. These subunits do not bind in a strictly linear fashion. They are rather built from the association of two protofilaments. Protofilaments form as linear strings of actin monomers joined end-to-end and form a filament segment by lateral combination in a helical structure. This stabilizes larger filaments against thermal breakage. Weak noncovalent bonds hold together subunits in a combination of side-to-side and end-to-end protein contacts.

Globular actin monomers are asymmetric and assemble head-to-tail to generate filaments with inherent structural polarity (cf. Fig. 1.1). In this sense, an actin filament holds a *plus* and

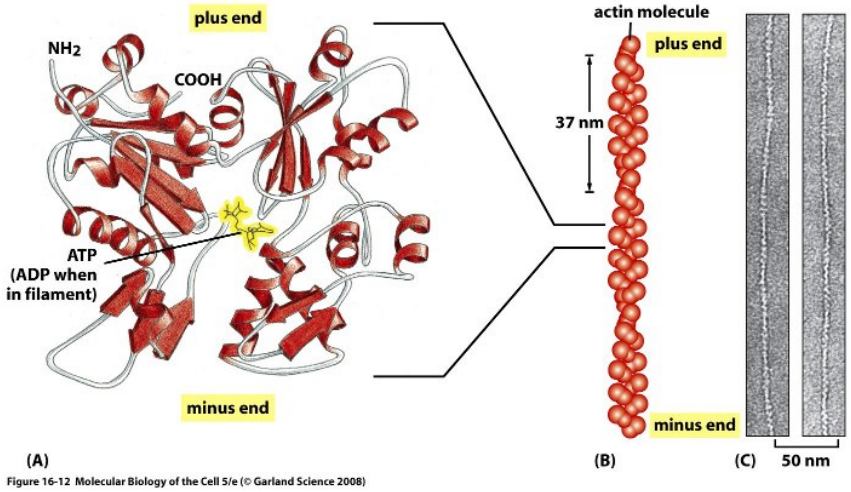

Figure 1.1: Structure of an actin filament. (a) Globular actin monomers are asymmetric and can hold a single nucleotide. The size of this protein is $5.4\ \mathrm{nm}$ in diameter. (b) An actin filament consists of two protofilaments, wrapped around each other in a helix with a periodicity of $37\ \mathrm{nm}$. Due to the lateral combination of two linear protofilaments, the addition of a single actin monomer extends the helical filament by $2.7\ \mathrm{nm}$. (c) Electron micrographs of actin filaments. Assembled filaments hold a diameter around $5 - 9\ \mathrm{nm}$. Image adapted from [2].

minus end, also denoted as *barbed* and *pointed* end, respectively. This structural polarity has a strong effect on filament polymerization rates at the two ends. The kinetic rate constants for association and dissociation of subunits are much greater at the barbed end compared to the pointed end. Therefore filaments will elongate primarily at this end, if an excess of globular actin monomers is available at either side. Under these conditions, when the available monomer reservoir is large enough to admit spontaneous net filament growth, the free energy change for addition of a subunit is less than zero. This free energy change is thus available in the cell to perform mechanical work, like pushing against a load. In this way for instance the growth of actin filaments protrudes the leading edge of motile cells, as will be discussed later in detail.

1.2 Actin cytoskeleton networks: the Swiss Army knife of cell mechanics

In living cells, actin filaments organize in two prototypical families of network structures [2]. On the one hand, bundles of parallel filaments are formed, while on the other hand gel-like fibrous networks organize (cf. Fig. 1.2). Depending on the required function, actin subunits and filaments interact with a selection out of hundreds of different accessory proteins to fulfill a special task. The resulting structures are dynamic and can be readily depolymerized and adapted to changing environmental conditions. In this sense actin is a multi purpose protein, conserved over a wide range of different species, carrying out various specific functions.

Vital cellular processes require different forms of actin networks to function properly. For instance, filaments form the dense *actin cortex*, a second layer below the plasma membrane of animal cells, that adds mechanical strength to the lipid bilayer. During proliferation, actin assembly in the *contractile ring* at the center of a dividing cell pinches the cell in two after the chromosomes have separated. Adherent cells build thick contractile actin bundles, the so called

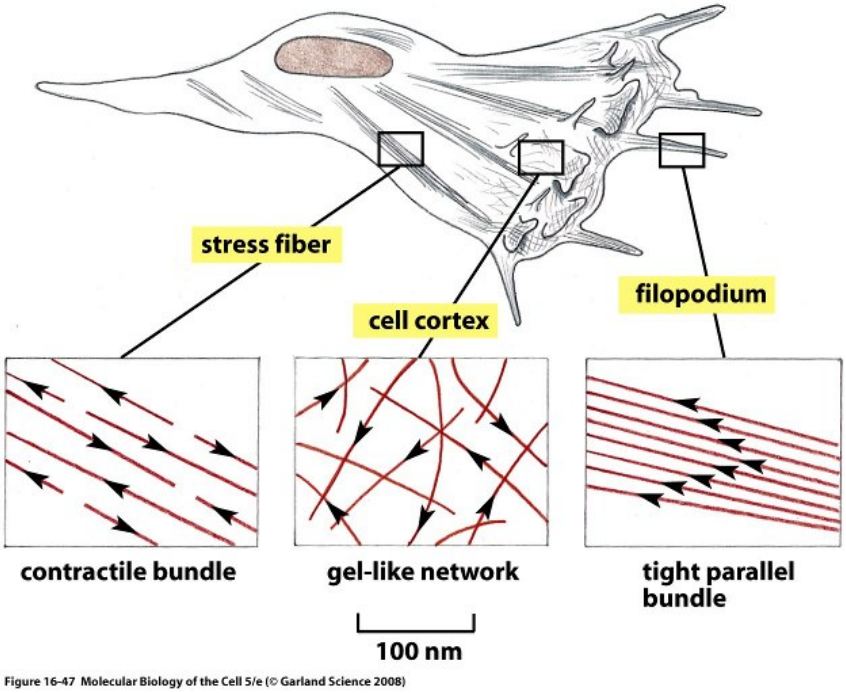

Figure 1.2: Different types of actin networks perform diverse tasks in the cell. Amongst others actin filaments are organized as contractile bundles in *stress fibers*, gel-networks in the *cortex* and tight parallel bundles in *filopodia* protrusions. Image taken from [2].

stress fibers, that are able to provide mechanical stability and probe the stiffness of their environment. *Stereocilia* in the inner ear contain actin bundles and oscillate in response to sound, an essential process in hearing. *Filopodia* also contain bundles of parallel actin filaments, that form cell surface protrusions that cells use to explore their neighboring environment. And *lamellipodium actin networks*, a polarized actin structure growing against a load and performing the necessary work for protrusion, are an essential constituent of migrating cells.

In the following, we will highlight two paradigms of this diverse set of different actin networks in more detail, as those will become important in the course of this work.

Actin networks in cell adhesion

Many cells that adhere to a substrate form prominent actin bundles and – on a cellular scale – again networks of these bundles (cf. Fig. 1.3). These stress fibers incorporate the bundling crosslinker α-actinin. As the crosslinking distance between single filaments bundled by α-actinin is rather large, the molecular motor myosin II is able to enter the loosely packed fibers and enables them to contract [90].

Actin network based motility

Animal cells almost exclusively move by crawling. During this complex process, three distinct activities are cycled [2]. First, in *protrusion* a polar actin network pushes out the membrane at the front of the cell. Second, in the *attachment* phase, the adhesion sites form which connect the actin cytoskeleton to the substratum. Third, the cell body is pulled forward by contracting elements in the *traction* phase. The precise chronology of these phases varies over different

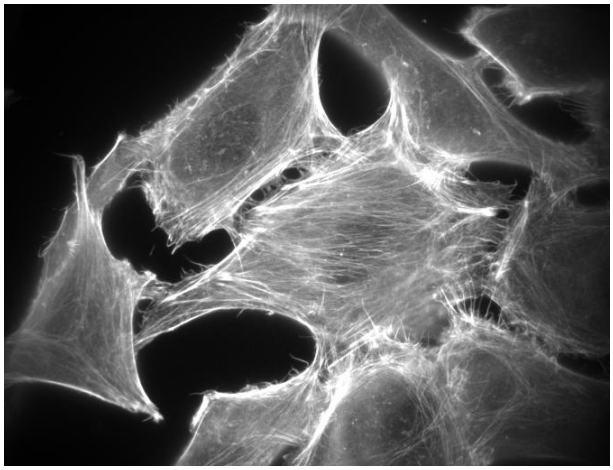

Figure 1.3: Fluorescence microscopy image of adherent cells on a flat substrate. Filamentous actin is labeled in the gray value image. Prominent stress fibers and the cortex are visible in these cells. This image has been taken by Nikolas Herold in the group of Hans-Georg Kräusslich.

cell lines. Fish epidermal *keratocyte* cells seem to move very continuously and maintain an almost constant shape during this process (cf. Fig. 1.4), while other cells like *fibroblasts* move in a more irregular way.

The lamellipodium actin networks are growing towards the cell membrane at the front in the protrusion phase of the migration cycle. Close to the membrane, individual actin filaments are able to form branches at their sides at which new filaments nucleate and grow subsequently. This branch formation is mediated by the Arp2/3 (actin related protein) complex. Further away from the membrane these polarized gel-like actin networks are also crosslinked by filamin proteins.

This process of work performance by growing polar actin networks can also be exploited by intracellular pathogens [37]. Amongst other parasites, the bacteria *Shigella*, *Listeria* and *Rickettsia* as well as *Vaccinia virus* activate actin growth locally on their surface and are subsequently pushed through the cytoplasm of the cell, in this way efficiently infecting their host [35]. In electron microscopic (EM) images, a tail of actin filaments is visible behind these pathogens (cf. Fig. 1.5). In recent years, it has also been possible to reconstitute this transport process in experiments for the propulsion of plastic beads [14] and lipid vesicles [32, 106].

1.3 Experimental techniques, results and observed anomalies

Actin networks have been the subject of many experimental approaches. Different meaningful observables can be measured using specialized techniques. Here, we will focus on two classes of experiments, as these appear most important in our context. On the one hand, the architecture of actin networks has been deduced by combining microscopy with image processing. On the other hand, the dependence of the actin network growth velocity on an external force has been measured. This is an important characteristic of the bulk network, because also subtle features, which are not directly accessible experimentally, are inherently incorporated in this ensemble property and alter the *force-velocity relation*.

Actin networks have been investigated by virtually every microscopic technique available today. Especially lamellipodium actin networks are of great importance in this context, as they combine a relatively limited system of molecular players with a very flat, quasi two dimensional

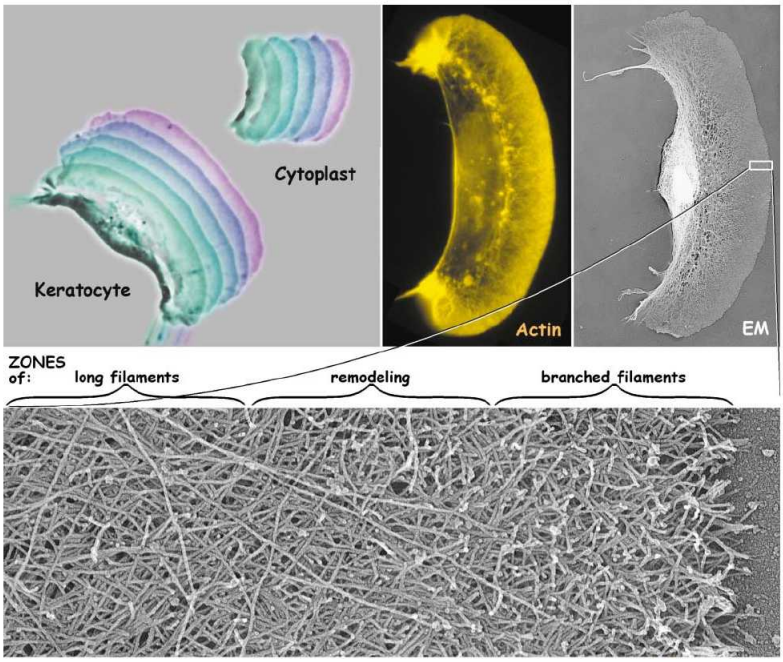

Figure 1.4: Motile fish epidermal keratocyte cell crawling continuously over a flat substrate. A thin layer of polar actin filaments pushes out the front, which is an essential step in the migration process. Adapted from review [89].

(2D) spatial domain, which is well suited for microscopy. According to a model based analysis, generic aspects of network organization have been extracted from fluorescence microscopy images labeled for actin [96]. As the resolution of these optical microscopes is not sufficiently high to resolve individual filaments, the resulting images show blurred structural patterns, that could only be classified in relation to simulated artificial images according to a simple network model for actin. Contrarily, modern electron microscopy facilities yield a resolution well below the diameter of actin filaments. Lamellipodium actin networks visualized in this technique appear to be branched networks with a characteristic relative branching angle of around 70° between filaments [76, 103]. Very recent data suggests that the apparently very large degree of Arp2/3 mediated branching could also be an artifact in some of the EM microscopy approaches [107]. Up to now, this new finding is controversially discussed and not yet finally resolved. Here we will explore the consequences of branching and will discuss possible implications in due course. The EM imaging technique also yielded results for the orientation distribution of actin filaments in the networks. Initially the results hint to a distribution with peaks at around $\pm 35^\circ$ with respect to a reference orientation, normal to the leading edge [66, 108]. This observation also coincided with a model for actin network organization [66, 97]. Still, more recent experiments correlating live-cell microscopy and EM yielded filament orientation distributions in the networks that changed with decreasing velocity of protrusion to broader distributed patterns [54]. Extending earlier theoretical studies, we will elaborate on this apparent controversy and show that changes in the growth velocity trigger transitions of the steady state network structure in a simple model for branched actin network growth. For EM tomography images of actin lamellipodium networks, we will also introduce and benchmark different data analysis methods that could be used in the future to test our model predictions.

The microscopic analyses mentioned above have all been performed on a relatively limited number of images. For instance, the preparation and image acquisition in EM is a very time consuming, delicate procedure. In case of optical fluorescence microscopy, fully automated

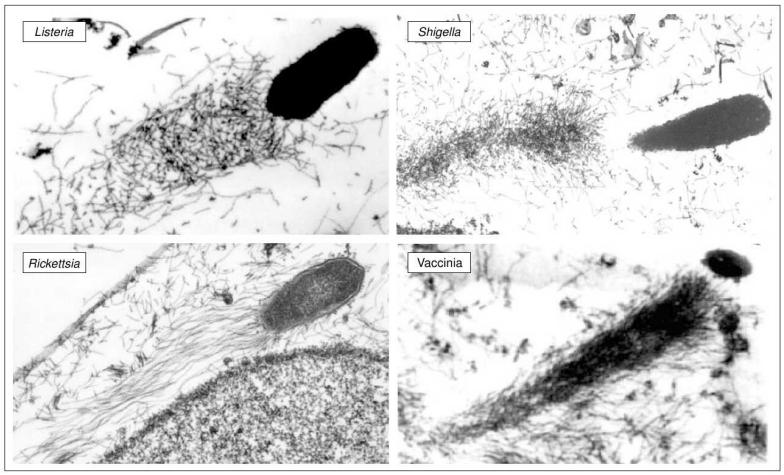

Figure 1.5: Specific intracellular pathogens are exploiting the actin machinery of the host, in order to move efficiently through the cytoplasm of an infected cell. In this way, the parasites are able to spread to other non-infected cells in their proximity rapidly. Images taken from review [37]. The original data comes from [36] for *Shigella*, *Listeria* and *Rickettsia* and from [29] for *Vaccinia*.

devices have been developed and introduced to the lab in recent years. These setups permit to acquire large image data sets very efficiently in cell-based high-throughput approaches [25, 81]. Here, a whole ensemble of cells is seeded on a substrate and subsequently a large number of images is taken at random positions. Subsequently the resulting data can be analyzed and classified by automated image processing and statistical routines. We have also adopted this technique in our work to classify network topology and detect changes in the actin cytoskeleton of adherent cells, which is accessible on the optical resolution of the light microscope.

The polymerization velocity of single cytoskeleton filaments at their leading edge depends on the force that is applied at the filament tip. For microtubule filaments this relation has been measured experimentally some time ago [23]. However, due to technical difficulties it has not been possible to perform a similar experiment for the force-velocity relation of individual actin filaments. Nevertheless, it has been accomplished successfully for ensembles of growing filaments in different setups. This bulk characteristic however is expected not only to be determined by the single filament work performance, but also by filament cooperativity and the subtle structural characteristics of the whole ensemble, i.e. the actin network organization. By letting actin networks grow against a deformable object like a micropipette [67] or the cantilever of an atomic force microscope (AFM) [82], it has been possible to measure force-velocity relations for the growing networks. However, results from different experiments are conflicting. On the one hand, a convex decline was measured [67, 69], while on the other hand, a load-independent phase [112] often followed by a concave velocity decrease near the stall force was observed [82, 91]. A particularly remarkable feature that was found in the context of one of the AFM experiments was that the network growth velocity at a given force is altered by the loading history of the system [82]. Due to its particular importance in our context, this experimental setup and results that feature hysteresis effects are shown in Fig. 1.6. Although in principle the discrepancies in conflicting experiments might be attributed to technical differences and a varying obstacle geometry [71, 72], in this work we will show theoretically that a simple generic mechanism exists which can explain most of the observed anomalies.

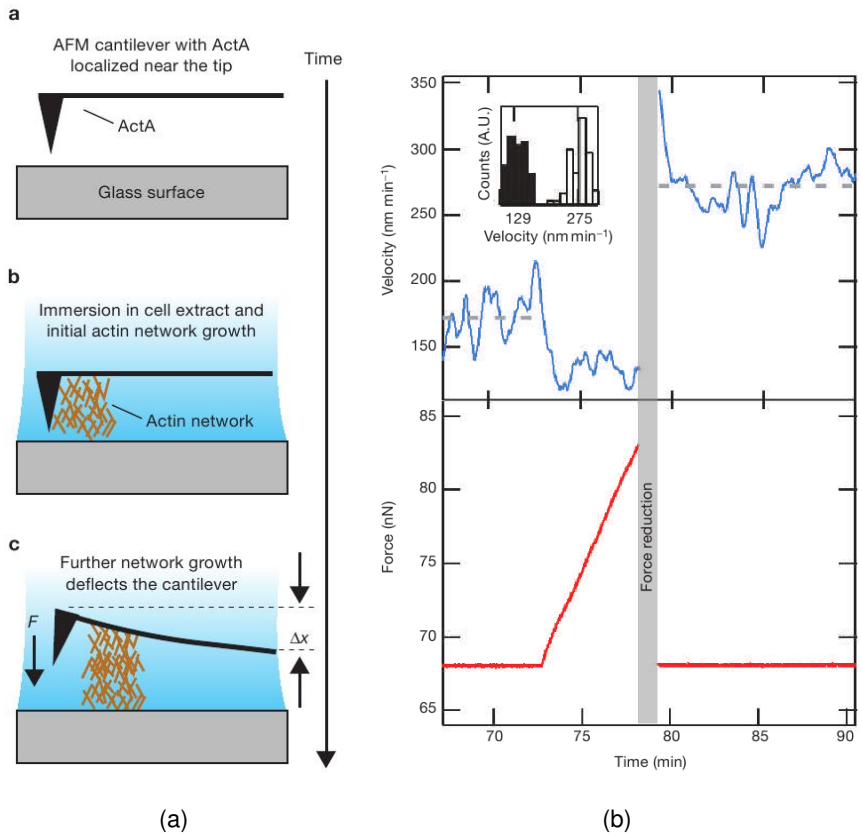

Figure 1.6: Setup and original results of atomic force microscopy measurements, indicating memory effects in growing actin networks [82]. (a) Actin network growth is activated by functionalizing the cantilever tip of an AFM. During growth it is technically feasible to either adjust the cantilever position in a way that constraints force to a constant level or to keep the position constant (yielding linearly increasing force on a network growing at a constant rate). (b) Measurement including loading history dependent growth velocities. For a constant load at around $68\ \mathrm{nN}$ the network grows in an apparent stationary regime with a fairly constant velocity at $170\ \mathrm{nm/min}$. Subsequently the load on the network is increased linearly and the velocity slightly drops, but stays more or less at a constant level. Then the applied force on the network is instantaneously lowered to its initial value. The velocity however does not approach its initial steady state again, but rather remains at significantly higher values around $270\ \mathrm{nm/min}$ where an apparent steady state is maintained. Images are taken from [82], where also the experiment is described in more detail.

1.4 Related theoretical work

Modeling the spatial organization of the actin cytoskeleton is a very active and increasingly sophisticated research field. To give an illustrative overview over previously published theoretical concepts, we will restrict ourselves to selected work, closely related to different aspects of this thesis. The most influential work and alternative concepts, will be discussed and compared to our methods in detail at a later stage, in the context of the relevant chapters.

A body of theoretical work focuses on different properties of generic network models based on individual filaments. Although such networks sometimes do not incorporate any specific protein-protein interactions for actin, often they are used to understand certain aspects of actin networks in the cell. For instance, the influence of architecture on the elastic properties of polymer networks has been analyzed extensively in [41, 42, 44, 45, 113]. There, the elastic response of different rather generic network models was compared with each other. In this context, also the *Mikado model*, a simple stochastic network model consisting of randomly oriented and positioned crosslinked sticks, was introduced to the biological context [113]. Later,

a variation of this model was also used to understand transport phenomena on actin networks by molecular motors [38]. We will also elaborate on different variants of the established random fiber or Mikado model in this thesis. Foremost we will use this model as an adjustable tool to benchmark different data analysis methods in the second part.

More specific models, that focus on lamellipodium actin networks or actin in the tail of small propelled particles, also have been suggested. These models, incorporate certain molecular aspects, which are specific for actin networks. In this way, the results from such approaches are less generic. However, as more details of the biological system are incorporated, they are in this sense more realistic and often focus on specific aspects that can be readily compared to experimental results. Amongst many other publications, dynamic network models were used in [15, 61, 98] to estimate the growth velocity of actin networks against an external force, the so-called *force-velocity relation*. In [48], an effective model for lamellipodium networks was incorporated to understand the separation of lamellipodium networks in two distinct substructures further away from the leading edge. A network model, which focused on the orientational order of growing lamellipodium actin networks was introduced in [97].

As an alternative to the network representations based on individual filaments, different continuum description of actin networks have been developed in recent years. A hydrodynamic theory for *active polar gels* was developed in [57, 58]. This theory complemented a generic fluid description with polar filaments and active forces due to molecular motors, which are incorporated in the network. Within this ansatz, the emergence of topological defects like asters, vortices and spirals in an active gel of polar filaments was predicted. More specifically for lamellipodium networks, the emergence of orientational patterns was predicted in [66], however the precise mechanism to obtain steady state filament growth was left open. This problem was solved by the autocatalytic description, in which it was elaborated that a unique steady state growth velocity exists for the networks [16]. In this context, also a force-velocity relation for actin was obtained, that is constant and thus not altered by the force on the network.

For some of these bulk models, a force-velocity relation for single filaments is needed. In the pioneering publications [74, 84], a Brownian ratchet mechanism was analyzed according to which polymerizing filaments can perform work on an external load. This model was refined later to incorporate new experimental knowledge of the biological system [75]. An alternative approach was introduced in [21, 22]. Here an abstract end-tracking motor is introduced that alters the filament polymerization at the end of the filament, where the force is acting.

Despite the existing comprehensive modeling background on actin filament networks, many open questions and puzzling experimental results have not been explained so far. None of these models was able to incorporate all different experimental observations for the force-velocity relation in a unified framework. Also structural transitions in actin networks, that have been observed experimentally have not been understood in a detailed description including a mechanism which yields the steady state. Hence, this is our starting point to model actin network growth in the lamellipodium of migrating cells and the emergent force-velocity relation in this system.

Recently, also network model based approaches have been introduced to interpret and analyze experimental microscopy images. In [27], simple network models were fit to data extracted from EM images of the lamellipodium to extract information about the actin network architecture. Microtubule and actin filament reconstruction on single fluorescence microscopy images has been performed in [64]. Also model based realizations of lamellipodium actin networks were blurred and subsequently these simulated artificial fluorescence images have been compared to experimental ones [96]. From this setup, also information about the emergent structures in fluorescence microscopy images of actin networks was deduced. These techniques were not only applied to actin networks. Microtubule characteristics have been estimated from fluores-

cence microscopy data by a model based approach [100] and the growth of keratin intermediate filament networks has been simulated and compared to electron microscopic images [6]. In this work we will also elaborate on a new way for a model based analysis of fluorescently labeled actin data from cell-based automated screens. This approach agrees well with the methodical spirit of the approaches mentioned here.

1.5 Overview and main results

Actin cytoskeleton networks play a fundamental role in very different vital and also disease related cellular processes. Therefore, the behavior of these networks has been in the focus of active scientific research for many years and a combination of experiment and theory has led to a deep understanding of many of the involved processes. Still, from time to time innovational experimental techniques reveal unexpected characteristics, that do not fit in the generally accepted present picture of actin network behavior. In this work, we will elaborate on the physics of different actin network models, which are well suited to describe certain intracellular conditions, in order to contribute to the comprehension of puzzling experimental results.

Actin network growth in the lamellipodium of migrating cells is an established model system, frequently used both in experimental and theoretical approaches. As it combines a relatively simple and reasonably well understood molecular machinery with a flat quasi two dimensional network geometry, it is very well suited for theory and microscopic imaging. Due to its paradigmatic status, a large number of different mathematical models have been created so far to describe and understand certain aspects of this system. However, to this point none of these approaches has been able to suggest a possible mechanistic explanation for anomalous experimental results in the behavior of these networks, that have been observed in recent years. Here, we have been able to extend previous theoretical considerations with new aspects to arrive at a comprehensive and plausible theoretical framework, that is able to explain many of these puzzling features. We suggest a possible mechanism that explains structural transitions in the steady state of growing networks as well as different shapes and also memory effects in the force-velocity relation of this system. Additionally, together with our experimental collaborators, we have combined experiments and data analysis to a workflow, that would be well suited to test specific predictions of our model in the future.

The thesis is divided in two parts. **Part I** (**chapters 2–6**) is concerned about mathematical modeling of actin cytoskeleton networks, while in the subsequent **part II** (**chapters 7–9**), methods for the analysis of quantitative data from biological experiments are introduced and tested. **Chapters 6** and **9** briefly summarize the findings of the two individual parts.

In **chapter 2**, we introduce the *random fiber model* or *Mikado model* as a generic static 2D model for actin cytoskeleton networks on various spatial scales. In this context, we approximate the *percolation transition* of this model, within two independent approaches using numerical simulations as well as heuristic arguments. This transition is an important prerequisite, to allow a mechanical response as well as continuous transport on the network that has been analyzed before. The random fiber model can be easily adjusted and extended to emulate specific actin networks arising in the context of different cellular conditions. Hence, we will also use variants of this model to benchmark the data analysis procedures in part II.

In **chapter 3**, we analyze the dynamics of actin networks under conditions, which are active in the lamellipodium of migrating cell. Using two different dynamic approaches – a continuum model as well as a discretized stochastic network simulation – we show, that transitions in the orientational patterns in growing actin networks exist [111]. The most important parameter that triggers transitions between two competing patterns is the growth velocity of the bulk network.

In **chapter 4**, we extend our theory for lamellipodium networks to the situation in which actin networks are growing on the surface of small curved particles such as intracellular pathogens. Most importantly, this new aspect changes the boundaries of the network. By approximating a curved particle surface piecewise-linearly, we are able to adapt the continuum description to this situation and compare to stochastic simulations, which incorporate the full geometry of the problem. Here, similar structural patterns as observed for lamellipodium networks emerge within a rotated coordinate frame that is adjusted to the local obstacle surface skew.

In **chapter 5**, we add a new hierarchical level to the model of lamellipodium network growth by coupling network structure and velocity to an external force that is applied against growth. We compare the two extreme cases in which the single filament velocity against an external load is either limited by the thermodynamics of polymerization or the mechanical stability of the filament. In the latter case complex characteristics emerge in the force-velocity relation of actin networks as a direct consequence of the coupling of two competing structural patterns with the single filament work performance. These results are able to explain different experimental observations that appeared mutually exclusive before within a unified simple theoretical framework. Most importantly, also hysteresis in the force-velocity relation is predicted. Using these findings, we are able to theoretically reconstitute experiments on growing actin networks that have found loading history dependencies of the steady state velocity of an actin network under force [111].

In **chapter 7**, we have joined forces with our experimental collaborators, **Edit Urban** and coworkers in the group of **John Victor Small** at the *Institute of Molecular Biotechnology* in Vienna. Here, we combine an experimental setup with a compatible data analysis workflow to test specific model predictions of chapter 3. From the correlation of live-cell microscopy with high resolution EM, it is possible to extract lamellipodium network patterns from fish keratocyte cells. The initial live-microscopy adds information of the dynamical state of the system at the time of fixation for EM. We incorporate two independent analysis methods using digital image processing of the EM data. In these mostly automated approaches, the structural orientation pattern of the actin network is readily extracted from the images. We benchmark the procedure using a variant of the random fiber model introduced in chapter 2 and perform and analyze a single proof-of-principle experiment with keratocyte cells, which yields results in agreement to the model predictions.

In **chapter 8**, we elaborate on an automated approach to classify actin bundle networks in large ensembles of adherent cells from automated fluorescence microscopy [110]. Here, the experiments have been conducted by **Nikolas Herold** and **Maik Lehmann** in the group of **Hans-Georg Kräusslich** from the *Department of Infectious Diseases, Virology* of the *University Hospital of Heidelberg*. We introduce a new parameter called *image coherency* to the biological context, to parameterize actin networks in ensembles of cells. For another variant of the random fiber model as well as for cell populations treated with actin toxins, this analysis is tested successfully. As a first application, we compared the measure for cells that have been treated with HIV-1 to their wildtype analogues, but could not find detectable changes to the actin cytoskeleton on the resolution of the optical microscope. Nevertheless, in the future the new image parameter could be especially useful when incorporated in the multi parametric analysis of cell based screens, where different ensembles of cells that have been perturbed in one or the other way need to be classified and compared to a wildtype control population.

Part I

Mathematical modeling

Modeling actin networks on different length scales

Cytoskeleton actin networks are shaped by many different regulating processes and organize on different length and time scales in biological systems. Specific conditions of the environment determine the emerging architecture of the filamentous networks. Therefore a hypothetical unified model for the actin cytoskeleton had to incorporate all possible mechanisms that influence network formation on different scales. Such a model would subsequently converge to predictions for the structure of the network in the relevant limits as shown in Fig. 1.7. The formulation of such a unified framework is however not realistic up to date, because many individual processes determining actin network organization are not yet well understood or even unknown. Additionally, the most important mechanisms with respect to the network characteristics of interest would be buried under less important or even irrelevant processes, which had to be regarded nevertheless. As an alternative, it seems appealing to keep modeling efforts rather generic. Results achieved from such considerations are applicable to actin networks on different scales or even to other (bio-)polymer networks in general. However, this simple *theory for everything* will lack sufficient mechanistic detail to predict and explain more specific characteristics of actin networks, that only occur under certain conditions.

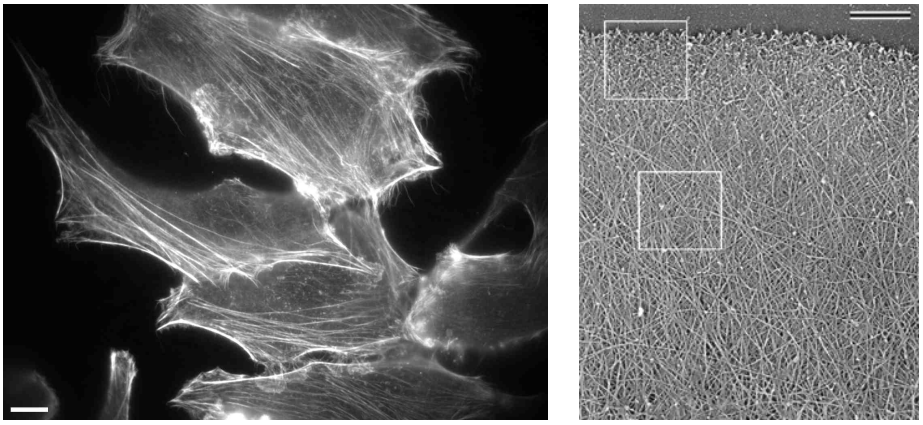

(a) (b)

Figure 1.7: Cytoskeleton actin fiber networks on different length scales emerge according to the environmental conditions in eukaryotic cells. Image (a) shows the architecture of thick actin bundles in adherent JC-53 cells. The scale bar determines $10\ \mu m$ here. This fluorescence microscopy image has been taken by our experimental collaborator, Nikolas Herold in the group of Hans-Georg Kräusslich. (b) Dendritic actin networks in a motile keratocyte cell. Single actin fibers are the elementary constituents of this network. The scale bar here shows $1\ \mu m$, which is one order of magnitude smaller compared to (a). Image modified from [104].

To cope with these two competing goals, in the modeling part of this thesis we will follow a dual strategy. On the one hand, we will study a simple and generic fiber network model in Ch. 2. The results that will be obtained from this model are sufficiently general that they apply to various fibrous networks on different length scales within and outside the biological context. On the other hand, in Ch. 3 we will incorporate the molecular basis of actin network growth in the lamellipodium of migrating cells in a dynamic network model and continuum theory. Although, this molecular framework might seem to be restricted to rather specific conditions, on our level of abstraction it is actually still valid for a large range of interesting situations. In Ch. 4 we will therefore adjust the model geometry to another biological situation of interest as well. Here, actin networks that grow against the surface of small obstacles are considered. For instance, certain intracellular pathogens exploit this mechanism in order to be transported through the

cytoplasm of their host cell, but also the surface of artificial plastic beads can be functionalized for actin growth in experiment, which induces propulsion of these particles. In Ch. 5, simple thermodynamic and mechanical arguments will complement our dynamic lamellipodium model to predict the force-velocity relation of actin networks growing against an external load. This is a very important characteristic as it also incorporates the microscopic rules of network creation and it has also been measured in different experimental setups.

Chapter 2

Static model for actin network structure

To model the spatial organization of the actin cytoskeleton, we begin with one of the simplest static fiber models, the *random fiber* or *Mikado model* (cf. Fig. 2.1). Despite its simplicity, it incorporates an abstract form of stochasticity in the network architecture that is fundamental for cytoskeleton network assembly. In the following modeling chapters, we will also deal with more detailed dynamic models for actin network growth, that implement specific reaction processes for actin filament nucleation and polymerization on the single filament level. This precise mechanistic understanding is disregarded in the random fiber model at this point and the model therefore does not yield the precise actin architecture under specific situations of interest. This generic unspecific randomness however can also be an advantage of the model, as it is indeed applicable under various, mechanistically very different conditions. For instance,

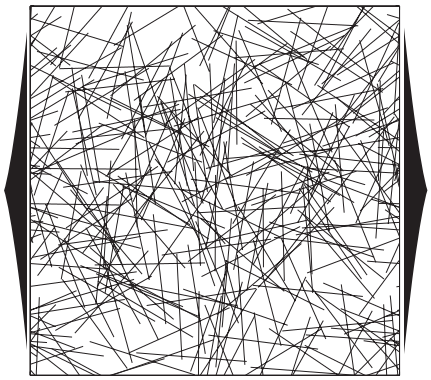

Figure 2.1: Exemplary realization of a random fiber network for $N_{\mathrm{fib}} = 300$ filaments with length $l_{\mathrm{fib}} = 0.3$ and periodic boundary conditions in the horizontal direction.

in the biological context it has been used before to analyze the elastic properties of filamentous polymer networks [44, 45, 113] as well as the transport by molecular motors on complex tracks defined by the network [38]. We will be concerned with the percolation of these networks in the following, which is a necessary condition for an elastic response, as well as for continuous transport on the network. In the second part of this thesis, we will come back to stochastic realizations of networks from this model to benchmark our image processing algorithms and network parameters that will be used to quantify microscopy images of actin networks on different length scales. Therefore this simple model combines the required structural randomness without the restrictions of specific mechanistic details of network creation in a generic picture

applicable for very different situations and purposes.

2.1 Model definition and parameters

Geometry

The random fiber model is defined for two spatial dimensions (cf. Fig. 2.1). Within this 2D network model a single length scale exists. We will use the edge length of the quadratic simulation box of unit area to scale the single filament length. Filaments are given as linear line segments with length l_{fib}. Their individual position and orientation is chosen uniformly randomly in 2D. At the horizontal (left and right) boundaries of the simulation box we have incorporated periodic conditions, while the vertical edges are not continued periodically. This aspect reflects, that we want to test the structural connectivity of the bottom and the top of the box by the network in the following section with methods from percolation theory. In this context two fibers are assumed to be connected, if they intersect.

Parameters and network creation

The set of parameters that is necessary for the creation of a random fiber network are the filament length l_{fib} and the filament number density that corresponds to the absolute filament number within our unit area box, N_{fib}. Subsequently the network is created fiber by fiber via choosing a random position for its center inside the box and a random orientation angle between 0° and 180° relative to a constant axis of reference until the given number of fibers N_{fib} exists. Fig. 2.2 displays exemplary network realizations for different sets of the two model parameters for illustration.

Although we will stick to these two model parameters in the remainder of this section, later on we will extend the available parameter space for specific purposes. To test image processing algorithms that extract the fiber orientation distribution from dendritic filament networks in Ch. 7, we will switch from a uniformly randomly distributed fiber orientation to more specific non-uniform distributions that will turn out to be important in the context of growing actin networks in the following modeling sections. In Ch. 8, we will benchmark a new parameter that can be extracted to characterize network images. As this parameter will be applied to fluorescence microscopy images of actin bundle networks that consist mostly of stress fibers and the cortex at the cell membrane, the model networks used to benchmark this approach need to reflect the different characteristics. On the one hand, we will therefore introduce additional parameters for the fiber bundle width and fluorescence strength. On the other hand, we will also generalize the parameters N_{fib} and f_{fib} to parameter distributions and evaluate a whole ensemble of networks. However, we will highlight the applied changes in the model in the relevant sections of this thesis.

2.2 Percolation in random fiber networks

For a meaningful analysis of the continuous transport on a random network and its elastic response, the percolation of the network is a necessary prerequisite. Classical problems in percolation theory deal with the properties of clusters on regular lattices [11, 101]. Consider for instance a quadratic lattice of nodes in 2D. Every node on this lattice holds four nearest neighbors. Each pair of two individual nearest neighbors on this lattice gets connected with constant

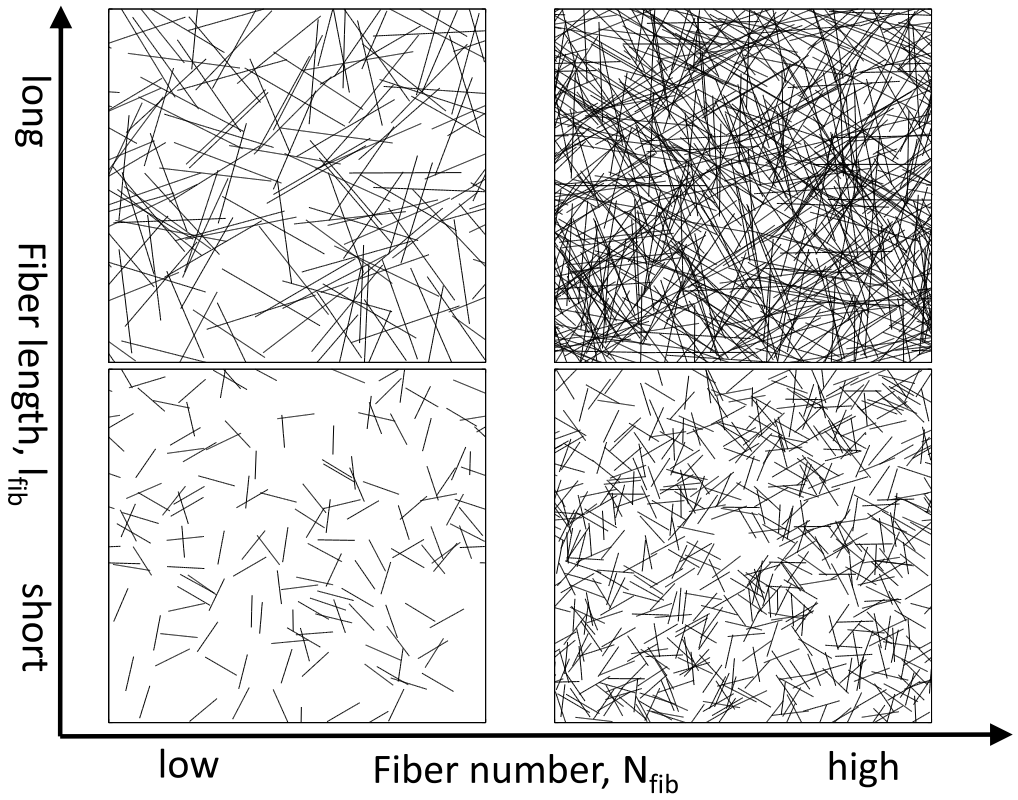

Figure 2.2: Dependence of the appearance of the fiber network on the two model parameters for all four combinations of $N_{\mathrm{fib}} = \{150, 600\}$ and $l_{\mathrm{fib}} = \{0.1, 0.3\}$.

probability p. In this way, clusters of connected nodes form in the network and the characteristics of these clusters, for instance their size distribution, are functions of the connectivity probability. The percolation threshold is defined at the probability, for which an interconnected cluster is observed on an infinite network for the first time. At this threshold a transition occurs and subsequently most nodes in the lattice are connected to the largest cluster. In the mentioned example of bond percolation on a square lattice, this transition point has been calculated analytically to be exactly at the connectivity probability $p_{\mathrm{c}} = 0.5$ [53, 94, 105]. However, analytical progress is often hard in this field and so stochastic simulations of random networks are a valuable substitute. In these simulations, large numbers of (finite size) networks are created in the computer for increasing connectivity parameter and an interconnected cluster is defined to percolate the network if it spans over opposite boundaries of the lattice. For sufficiently large system size, this transition is relatively sharp, while for smaller networks finite size effects become apparent.

It is possible to generalize the definitions above to random fiber networks. Nodes are defined at irregular positions off lattice, at the center-point of each individual fiber. Two nodes are connected, if their respective fibers intersect and the network percolates if the same cluster spans over the bottom and the top boundary of the simulation box. In this picture, we will show that our two model parameters fiber number and length can be coupled to yield the effective parameter fiber area (density),

$$A_{\mathrm{fib}} = N_{\mathrm{fib}} l_{\mathrm{fib}}^2 \,, \tag{2.1}$$

that triggers percolation at the critical point $A_{\mathrm{fib,c}}$. In Fig. 2.3 three exemplary random fiber networks are plotted with color labeled clusters. An efficient way to determine connected clusters

as described in [46, 101] for regular networks was generalized to this off lattice model. From left to right the fiber area is increased stepwise from values smaller than the transition point to a value around $A_{\mathrm{fib,c}}$ and beyond. In the first network on the left hand side, many small separated clusters can be found. In the middle, a percolating cluster forms. However it holds relatively weak spots, where the removal of only a few single fibers would already disrupt the connectivity. On the right hand side, all fibers but very few are connected to the largest percolating cluster. The connectivity of this largest cluster is rather redundant such that many fibers had to be removed to separate it into parts.

$A_{\mathrm{fib}} < A_{\mathrm{fib,c}}$ $A_{\mathrm{fib}} \simeq A_{\mathrm{fib,c}}$ $A_{\mathrm{fib}} > A_{\mathrm{fib,c}}$

Figure 2.3: Random realizations of fiber networks well below (left), around (middle) and well above (right) the percolation threshold $A_{\mathrm{fib,c}}$. The active parameters are $l_{\mathrm{fib}} = 0.15$ and $N_{\mathrm{fib}} = \{150, 250, 350\}$ for the left, middle and right network respectively. For the network drawn in the middle at parameters around the percolation threshold, a fragile but percolating cluster can be observed in many realizations.

In the following, we will follow two different approaches to evaluate reasonable approximations for the percolation threshold of random fiber networks. First, in Sec. 2.2.1 we will evaluate stochastic simulations to measure the effective parameter fiber area $A_{\mathrm{fib,c}}$ at the transition point. Second, in Sec. 2.2.2 we will exploit an apparent analogy of random fiber networks and the bond percolation on a square lattice to arrive at an heuristic approximation for the percolation threshold. These two results will subsequently be compared to simulation results for this problem that have been published before in [86].

2.2.1 Numerical approach

We have conducted stochastic simulations to evaluate the parameter $A_{\mathrm{fib,c}}$ at the percolation transition. For a given constant number of fibers N_{fib} in the network, the fiber length was increased in 100 steps around the expected threshold and in each step the percolation of 1000 network realizations was analyzed. This procedure was repeated for various fiber numbers. A given network realization percolates in these simulations, if at least one interconnected cluster reaches the bottom and the top boundary of the simulation box.

The results that are obtained from the calculations are shown in Fig. 2.5(a). For relatively large fiber number (i.e. number of nodes) the observed percolation transition is rather sharp, while for smaller networks finite size effects appear. The fiber length at percolation $l_{\mathrm{fib,c}}$ is approximated from each of these simulations by interpolating the curves linearly to the point where the relative number of percolations is 0.5. These results are also plotted in a phase diagram in Fig. 2.5(b) indicating model parameter regimes for percolating and non-percolating networks. A fit of these different transition points from network simulations according to the

equation,

$$N_{\mathrm{fib}} = A_{\mathrm{fib,c}} l_{\mathrm{fib,c}}^{-2} \,, \tag{2.2}$$

yields the critical fiber area at the percolation threshold to be,

$$A_{\mathrm{fib,c}}^{\mathrm{num}} = 5.470 \,. \tag{2.3}$$

2.2.2 Heuristic approach

As an alternative to the numerical analysis of the percolation transition in random fiber networks done in the previous section, we will now derive an analytical approximation of the parameters N_{fib} and l_{fib} at the transition point from simple heuristic arguments. Starting with a fiber network consisting of uniformly randomly distributed rods in a box of unit area, we can define a mean nearest neighbor fiber distance as the inverse square root of the fiber density (i.e. number),

$$d_{\mathrm{fib}} := \sqrt{\frac{1}{N_{\mathrm{fib}}}} \,. \tag{2.4}$$

This definition is motivated by the nearest neighbor distance given on a regular quadratic lattice, which is the simplest 2D lattice for which the bond percolation threshold is known exactly [53, 94]. For the random fiber network each fiber center is defined as a node on a (irregularly spaced) lattice. In this sense, an analogy between the random fiber network and the bond percolation problem on a square lattice emerges. Although we do not have regularly spaced lattice nodes in our setting, we have already defined an average lattice constant in Eq. (2.4). As mentioned before, analytical arguments identify the bond percolation threshold on a square lattice at a connection probability between neighboring nodes of exactly $p_{\mathrm{c}} = 0.5$ [53, 94]. Hence, if we take our analogy between these different setups seriously, we expect the random fiber network to percolate around a fiber length at which the crossing probability of two *nearest neighbor* fibers at a mean distance d_{fib} reaches 0.5.

To calculate the crossing probability P_{cross} of two uniformly randomly oriented fibers as a function of their center point distance d_{fib} and individual length l_{fib}, we consider only the case where $l_{\mathrm{fib}}/2 \geqslant d_{\mathrm{fib}}$. This partial solution of the problem will be sufficient to evaluate the model parameters at $P_{\mathrm{cross}} = 0.5$. We start to calculate the crossing probability of the two fibers by first considering the situation sketched in Fig. 2.4(a). Here, the angles of both fibers relative to their horizontal dashed connecting line are so small that they reach or cross the normal drawn through the middle point of their connecting line. The angle α at which one fiber end lies exactly on the normal line in the middle of the two nodes is defined as,

$$\cos\alpha = \frac{d_{\mathrm{fib}}}{l_{\mathrm{fib}}} \,. \tag{2.5}$$

The subsequent probability for each fiber to hold an angle smaller or equal to α is,

$$P_\alpha = \frac{\alpha}{2\pi} = \frac{\arccos\frac{d_{\mathrm{fib}}}{l_{\mathrm{fib}}}}{2\pi} \,. \tag{2.6}$$

In order to form a crosslink in situation (a) both fibers must hold an angle smaller or equal to α with respect to their connecting line and both fibers must point in the same vertical direction, i.e. up or down. Therefore the crossing probability in this situation is given by,

$$P_{\mathrm{cross,a}}(d_{\mathrm{fib}}, l_{\mathrm{fib}}) = 4 \cdot 2 \cdot \left(\frac{\arccos\frac{d_{\mathrm{fib}}}{l_{\mathrm{fib}}}}{2\pi} \right)^2 \,. \tag{2.7}$$

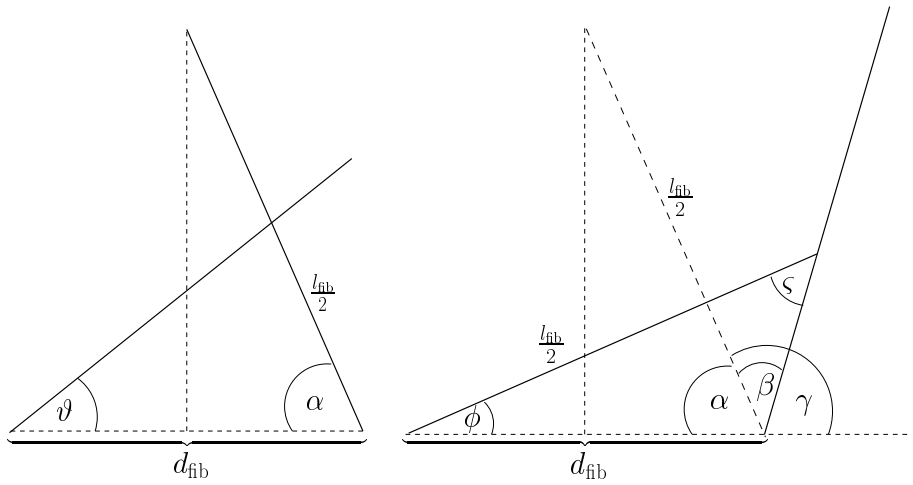

(a) (b)

Figure 2.4: Sketch of the two situations of neighboring fibers at distance $d_{\rm fib}$ that are considered one by one. Only one side of each fiber from its center point is drawn in the sketch, while another side reaches out to the opposite side and is neglected in the drawing. The total length of each fiber is $l_{\rm fib}$ and therefore each side of the fiber from its center point spans a distance $l_{\rm fib}/2$. The two centers of the fibers are connected by the horizontal dashed line. The condition $l_{\rm fib}/2 \geqslant d_{\rm fib}$ is always satisfied.

The additional factor of 2 arises because of the left-right symmetry and the factor of 4 reflects the two different sides of each fiber.

To obtain the total crosslink probability of the two fibers, we also have to regard a second situation shown in Fig. 2.4(b). Here the angle of one of the fibers relative to the connection line exceeds α by an angle β. The angle ϕ is subsequently defined by the second fiber oriented in a way that it just touches the first fiber at its end at an angle ς. This angle ϕ is given by,

$$\phi = \pi - (\alpha + \beta) - \varsigma \,, \tag{2.8}$$

with

$$\varsigma = \arcsin\left[\frac{2d_{\rm fib}\sin(\alpha+\beta)}{l_{\rm fib}}\right] \,, \tag{2.9}$$

and α as defined in Eq. (2.5). The probability for the two fibers to cross in this situation (b) subsequently writes,

$$P_{\rm cross,b}(d_{\rm fib}, l_{\rm fib}) = 4\frac{1}{\pi^2}\int_0^\gamma \phi(\beta)\,{\rm d}\beta = 4\frac{1}{\pi^2}\int_0^\gamma \pi - (\alpha+\beta) - \arcsin\left[\frac{2d_{\rm fib}\sin(\alpha+\beta)}{l_{\rm fib}}\right]{\rm d}\beta \,, \tag{2.10}$$

where the factor of 4 arises again due to the different sides of each fiber.

The total crossing probability of the two fibers as a function of their length and center point distance is subsequently given by the sum of Eq. (2.7) and Eq. (2.10),

$$P_{\rm cross}(d_{\rm fib}, l_{\rm fib}) = P_{\rm cross,a}(d_{\rm fib}, l_{\rm fib}) + P_{\rm cross,b}(d_{\rm fib}, l_{\rm fib}) \,. \tag{2.11}$$

From this result we conclude that the ratio of fiber distance over fiber length $d_{\rm fib}/l_{\rm fib} = A_{\rm fib}^{-1/2}$ is the only effective parameter in the problem that determines the crossing probability of the two fibers and therefore percolation.

Using Eq. (2.11) together with Eq. (2.4), we can calculate the active fiber number N_{fib} and length l_{fib} at $P_{\mathrm{cross}} = 0.5$. Reconsidering our heuristic argument above, this set of model parameters should approximate the percolation threshold accordingly. We plot the heuristic approximate for the percolation transition in Fig. 2.5(b) together with the numerical results for comparison. We can calculate a fiber area at the transition from our result, which is given by,

$$A_{\mathrm{fib,c}}^{\mathrm{heur}} = 5.247\,. \tag{2.12}$$

This percolation threshold is only a little bit smaller than our initial result from numerical stochastic simulations. This is satisfactory considering our simple argument. The fact that the heuristic derivation systematically underestimates the fiber area necessary for percolation, can be understood from our simple assumptions. Compared to the setup of bond percolation on a square lattice, where every node holds connections to its four neighbors with equal, independent probabilities, here the situation is different. Any connection between neighboring fibers that is formed, has an effect on the probability for another connection on a different side of the fiber. The individual connections of a single node are formed according to *conditional* probabilities in this case and are not limited to four. As we did not regard this dependency in our derivation, the results deviate from the previous simulations, which are more accurate from this point of view.

2.2.3 Percolation phase diagram

As no exact analytical result is known for the percolation threshold of random fiber networks, we will compare our findings with previously published numerical results for this problem. Already in 1974 Pike and Seager published an extensive computer study on the percolation threshold of diverse random networks [86, 99]. Compared to our numerical approach in Sec. 2.2.1, the difficult challenge back then was to get along with the strongly limited computer power. For random fiber networks they found,

$$A_{\mathrm{fib,c}}^{\mathrm{Pike}} = 5.712\,. \tag{2.13}$$

This number compares reasonably well to our previous results, although the relative difference to our numerical solution is still around 4%. A more recent publication of the same numerical issue only recently published, reports the area density of the fibers at the percolation threshold to be $A_{\mathrm{fib,c}} = 5.637$ [63]. For better accessibility all results are shown and compared again in Tab. 2.1. For visual comparison, Pike and Seager's result has also been included in our percolation phase diagram in Fig. 2.5(b). Although the three different results for the percolation threshold deviate, they are already relatively hard to distinguish on the scale of this plot.

source / method	$A_{\mathrm{fib,c}} = N_{\mathrm{fib}} l_{\mathrm{fib,c}}^2$	**rel. diff.**
numerical	5.470	0
heuristic	5.247	4.1%
Pike et al. [86]	5.712	4.4%
Li et al. [63]	5.637	3.1%

Table 2.1: Different values for the percolation threshold of random fiber networks from different sources and methods. The values have been obtained in numerical stochastic simulations (Sec. 2.2.1) and according to an heuristic argument (Sec. 2.2.2). For comparison, also previously published results are included at the end of the table. In the last column the relative difference of all values from our numerical results is given.

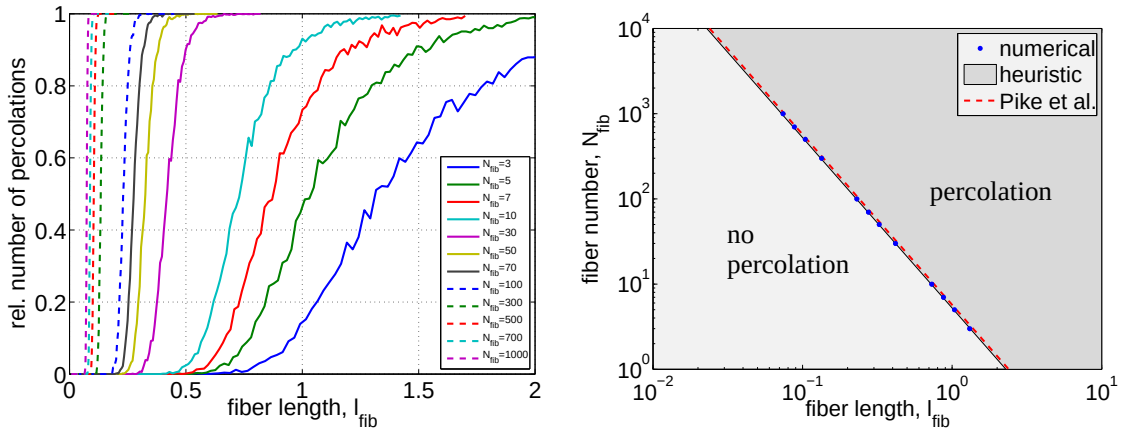

(a) (b)

Figure 2.5: Percolation transition in random fiber networks. (a) Results from different stochastic simulations. For various constant fiber number the fiber length is increased stepwise in 100 iterations and for each length 1000 network realizations are analyzed for percolation. For networks containing a relatively large number of fibers (i.e. nodes) a rather sharp transition is observed. In smaller networks, finite size effects become apparent. The fiber length at the percolation transition was approximated by the linear interpolation of each curve to the relative number of percolations 0.5. (b) Phase diagram indicating the percolating and non-percolating phases of random fiber networks in the parameter space spanned by N_{fib} and l_{fib}. Blue points mark the results from the numeric simulations shown in (a). The gray background indicates the outcome of our heuristic argument derived in Sec. 2.2.2 and the red dashed line represents previously published numerical results [86].

2.3 Summary and discussion

In this chapter we have introduced a simple generic structural model for actin cytoskeleton networks on different length scales. Although it is independent of the specific rules that determine how actin networks in different biological conditions are generated, this model reflects the structural randomness characteristic for cytoskeleton networks. Therefore it has been used before as a valuable tool to determine generic physical properties of biological actin networks.

Here, we elaborated on the percolation transition of this network model, which is a necessary prerequisite for many different physical processes, like the elastic response of the network or continuous transport on randomly connected tracks by molecular motors. Our main goal in this chapter was to gain a basic understanding of the impact of the model parameters, fiber density N_{fib} and length l_{fib}, on the percolation threshold, but not to numerically evaluate this threshold to exceedingly high precision. The most important result in this context was built on an heuristic argument, where we exploited the analogy between random fiber networks and the bond percolation problem on a square lattice. From this argument a simple yet convincing and reasonably accurate approximation for the percolation threshold of random fiber networks was deduced. Additionally, we have been numerically calculating the percolation threshold in the network model as well. Compared to the first numerical results that have been published on this model system, we found a relative difference around 4%. To clarify this issue we have found a second numerical work only recently published, where the critical area density of the fibers is evaluated to be in between the two numerical results. However, in our simulations we applied periodic boundaries at the lateral sides of the model networks and therefore the comparability of the different approaches is limited. Additionally, due to our different focus, we did not use sophisticated finite size scaling techniques in our numerical approach, which probably would have increased the numerical precision to a higher degree.

In the following chapters, we will not deal with the random fiber model but rather introduce a growth model for actin networks, which reflects the molecular rules of network creation in a much more specific way. In this sense the dynamic model will be more accurate when describing specific situations in the cell, however at the expense of applicability under more general conditions. Therefore, in the chapters of the second part of this thesis, which are mainly concerned with extracting quantitative information from different microscopy images of actin networks, we will come back to the random fiber model. In this context, artificial images generated by different variants of this model, that are adjusted to our specific needs at that stage, are a valuable tool to benchmark our image processing algorithms and network parameters.

Chapter 3

Actin network dynamics in the lamellipodium of motile cells

The process of continuous cell motility can be divided in a sequence of different phases [72]. In the protruding step the leading edge plasma membrane is pushed out, while afterwards the cell retracts by pulling the cell body forward (cf. Fig. 3.1). Here we are interested in the first step of the migration cycle, which takes place in the rather flat and spread out leading front of the cell, the so called lamellipodium. The necessary work for protrusion is performed by a network of polymerizing actin filaments. Most of these filaments are growing towards the leading edge of the cell, given by the restricting plasma membrane at the front, and are pushing against the membrane tension [71]. The details of this mechanism are governed by the delicate interplay of work performance by the filament network (which will be the focus of Ch. 5) and, as we will emphasize in this section, the architecture of the complex actin network growing within the lamellipodium.

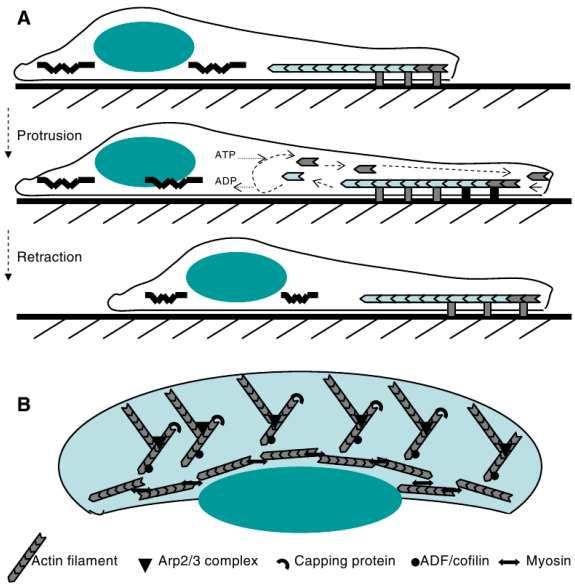

Figure 3.1: Sketch of the different phases of the motility cycle for a keratocyte cell. (a) side view, (b) top view; In the front part of the cell the spread out lamellipodium actin network is pushing out the membrane to the right. Afterwards the cell retracts by pulling the cell body forward. Image adopted from [72].

3.1 Model definition and key assumptions

From a modeling perspective, actin networks growing in the lamellipodium of migrating cells are very well suited for theoretical analysis. Several characteristics of this paradigm allow to simplify the theoretical model to finally end up at a minimum framework only reflecting the most important features of this complex system.

Geometry

First, we will simplify the geometry of the system. If we consider typical spatial dimensions for a bulk lamellipodium network, the height of the network ($\sim 0.1\ \mu m$) is at least one order of magnitude smaller compared to its dimension parallel to the surface ($\sim 1 - 50\ \mu m$). Filaments are growing in the surface plane in this quasi two dimensional domain, which is constraint by the plasma membrane to either side. Therefore we will restrict our model to the two dimensional dynamics of actin filaments. As we will emphasize below, we are interested in actin dynamics within some ten nanometers from the leading edge only. Then the lateral dimension of the region of interest is also much larger compared to the vertical, and can therefore be assumed as isotropic and treated by a small sample section with periodic lateral boundary conditions. As the curvature of the membrane at the front will be rather small on the scale of this sample section, it can also be neglected in this framework. Note however, that in Ch. 4 the structure of actin networks growing and pushing against small spherical particles will be analyzed and there the exact shape of the obstacle surface at the front will have a dominant effect on actin network architecture. For now, we end up with a rectangular simulation box, that is constraint by a flat cell membrane at the front, by our maximum distance of interest at the back and holds periodic conditions in the lateral direction. An illustration of such a simulation box with growing filaments inside is shown in Fig. 3.4 on page 30 together with a simplified sketch of the geometry. As the model is restricted to two dimensions, we neglect steric interactions between different filaments.

Molecular processes

Next, we need to analyze what are the most important chemical processes taking place in the lamellipodium region of interest. Fig. 3.2 features the *dendritic nucleation model* indicating the molecular processes involved in actin network growth [76, 87]. It has been implemented before as a complex system of reaction kinetic equations [73]. We will use this molecular model as a starting point to isolate the most important processes determining network architecture.

Polar actin filaments are polymerizing actin subunits primarily on one side, at their so called barbed end. A capping protein is able to also bind to filament barbed ends, which inhibits further growth and terminates elongation. When some unspecified external stimulus triggers a signaling cascade in the cell, the Arp2/3 complex is activated. This protein is able to initiate new filament branches on preexisting filaments with a characteristic relative angle difference of around 70° between both [76, 103]. Although the exact mechanism and chronology of the activation process is not yet very well established and subject of current research [7], it turns out that Arp2/3 is most active in close proximity to the leading edge membrane. The reason for this might be membrane bound proteins which could be essential for the activation process. Arp2/3 is the most important growth factor in this model and constrained to a region close to the leading front. We are interested in actin network architecture and its impact on work performance against the membrane and thus we will focus on the actin dynamics within the first few ten nanometers from the front boundary. Within this small distance from the leading edge, depolymerization of actin filaments can be neglected and is treated only effectively in our

model. As filaments are growing out of the lower boundary of the simulation box they vanish and their protein building blocks are assumed to be recycled to the monomer pool which is available in the cytoplasm of the cell. According to these considerations we end up with a simplified molecular framework featuring the most important reactions of actin network dynamics (cf. Fig. 3.3).

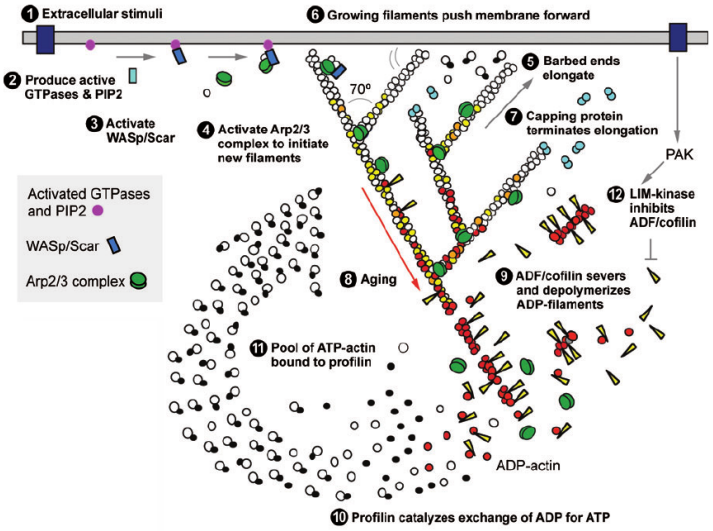

Figure 3.2: The *dendritic nucleation model*, featuring the most important chemical processes within the lamellipodium of motile cells. An external stimulus activates the Arp2/3 complex, which initiates new filament branches on preexisting filaments close to the leading edge membrane with a characteristic angle difference of 70° between mother and daughter filament. Filaments are polymerizing at their barbed end and pushing against the cell membrane. Capping proteins are able to bind to the barbed ends of filaments and prevent further growth. Filaments that have been outgrown by the network to regions further away from the membrane are depolymerized and the resulting monomers enter a reservoir pool which diffuses in the cytoplasm and can be used again to fuel the reaction at the front. Image taken from [87].

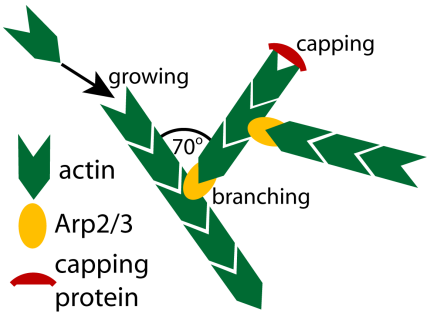

Figure 3.3: Simplified version of the *dendritic nucleation model* (cf. Fig. 3.2) used in our context. For network architecture, the most important processes close to the leading edge are actin filament growth, Arp2/3 mediated filament branching and filament barbed end capping.

Zero-order branching model

As a prerequisite for continuous and stable actin network growth, the system has to evolve into a stationary state for a given set of parameters. Apart from small variations, due to the stochastic nature of the relevant processes, a steady state will be characterized by a constant filament

density for a network growing with constant bulk velocity. In experimental setups, the external parameter that defines the growth state of actin networks is often some external force or load pushing against the direction of growth. Actin networks protruding against such an external load will be the subject of Ch. 5. In this and the next chapter however, we are not interested in the details of work performance by the network, but rather in the evolving network architecture during steady state growth. Therefore we will not explicitly consider how an external force determines the network growth velocity, but rather treat the growth velocity of the bulk network v_{nw} itself as the external model parameter that can be set to tune the state of the system. In our context this velocity is defined by the motion of the leading edge membrane or some obstacle surface that is propelled by the growing network.

We can identify the requirements necessary for steady state network growth in our simplified microscopic picture (Fig. 3.3). As a start, we classify which reactions raise and lower the total number of filaments in the system. Arp2/3 mediated branching nucleates a new filament on a preexisting filament, which increases their total number. Contrarily, capping proteins bind to the barbed end of filaments and prevent further filament polymerization. This reaction reduces the filament number in the system, as capped filaments will eventually be outgrown by the bulk network and leave the simulation box at the bottom. We do not model their further fate, which in practice might be remodeling into a lamellum or direct depolymerization by ADF/cofilin proteins. However, there exists a second process for filament annihilation, which emerges implicitly from the directed network growth. While the network bulk grows towards the leading edge of the cell and pushes out the front with a constant velocity v_{nw}, there exist also filaments with their barbed end pointing away from the front. Although polymerizing at a constant rate v_{fil} like all other actin fibers, these filaments are not directed towards the front and might not be able to keep up with the remaining network. Subsequently, they are outgrown by the bulk and leave the region of interest. While the first two mentioned processes, branching and capping, do not depend on the external parameter v_{nw}, the outgrowth rate of filaments is a function of network velocity.

In order to evolve a constant filament number in the steady state, the three mentioned processes - namely branching, capping and outgrowth - must exactly balance. Following earlier work we assume that there exists a sufficiently large reservoir of capping proteins in the cytoplasm of the cell such that these proteins will be available in excess at all times during growth and do not limit the capping reaction [16, 66]. Subsequently, the reaction rate for capping will be proportional to the number of existing (uncapped) filaments (i.e. first-order). For branching the situation is very different. Biochemical evidence suggests the availability of activated branching agents Arp2/3 rather than the availability of actin filaments is the rate-limiting factor for branching [88]. This implies that branching should be modeled effectively as a zero-order rather than as a first-order process in the number of actin filaments. This assumption has been used before in analytical treatments [16] and network simulations [96], but its consequences have not yet been fully explored. Our assumptions lead to a steady state filament number with regard to capping and branching reactions. However, there also exists the additional outgrowth process mentioned before. This process is determined by the network velocity, which can be varied as an external parameter to tune the system. In the following, we will show that this leads to fascinating transitions in the structure of growing actin networks, which in essence could explain a variety of puzzling experimentally observed anomalies [111]. A first-order branching rate, together with first-order capping rate has been analyzed in [16]. We will emphasize the differences in the two models in the discussion at the end of this chapter.

3.1.1 Stochastic network simulations

To analyze the emerging network architecture in our model for lamellipodium actin network growth, we have implemented a two dimensional stochastic network simulation. A snapshot of a stochastically growing network from such a simulation is shown in Fig. 3.4(b). To speed up simulations, filament growth is treated deterministically, i.e. each filament barbed end grows with constant tangential velocity v_{fil}. That means each barbed end elongates by one unit length increment δ_{fil} per unit time. Stochastic capping and branching events are simulated within a branching region of constant vertical width $d_{\mathrm{br}}^{\perp} = 2\delta_{\mathrm{fil}}$ close to the leading edge of the network, using a Gillespie-like procedure [33]. Here, we assume the width of the branching region from the position of the plasma membrane to be comparable to the actin monomer diameter, because membrane bound proteins are involved in the activation of the branching agent Arp2/3. The precise impact of this width on our results will be discussed below. The deterministic treatment of actin polymerization in contrast to stochastic branching and capping reactions is justified due to the relatively high actin monomer concentration in the cytoplasm compared to the other two reaction proteins. New filaments are able to branch from barbed ends of existing filaments. Adopting measured values, the branching angle relative to the mother filament is chosen randomly from a Gaussian distribution with mean 70° and a standard deviation of 5°. The side of the mother filament from which the new filament grows is selected uniformly randomly. The branching reaction is assumed to be of zero-order and therefore the branching probability per unit time remains constant during the simulations. Contrarily capping is assumed to be a first-order reaction in the number of filaments and the capping probability per unit time is adjusted by the new filament number in the branching region after each reaction. As we disregard uncapping reactions, capped filaments will eventually be outgrown by the bulk network and thus leave the simulation box.

For the simulation box we are using periodic boundary conditions in the lateral (x-)direction. Although we thus do not have a lateral length scale in the model by now, we will deal with non-periodic conditions in Ch. 4 for which also a lateral spatial scale needs to be introduced. In Fig. 3.4 the top of the yellow region defines the flat plasma membrane, which exerts a load on the filaments that are crossing this boundary. As a consequence these fastest topmost filaments are stalled by the load of the membrane and do not grow anymore. Our external parameter, the network velocity v_{nw}, can thus be adjusted in two ways: On the one hand, we can define a constant number N_{front} of topmost filaments that is required to carry the load of the membrane and which is stalled at the obstacle. As the remainder of the network keeps on growing, the identification of N_{front} is updated after each simulation step and a steady state network velocity v_{nw} evolves. Here the steady state network velocity is a monotonically decreasing function of N_{front}. On the other hand, the velocity of the leading edge can be set to a constant value v_{nw} directly. All filaments that are faster than the leading edge will get stalled at the top until the membrane moves on. In this picture a steady state value for N_{front} emerges. Apart from small stochastic variations, these two techniques yield analogous results for the steady state. As we will be interested in the stationary situation, in the following it is irrelevant which of the two parameters is adjusted in simulations. Most often we will therefore only state the relevant network velocity v_{nw} when describing a steady state condition, as this parameter seems more accessible and meaningful than N_{front} when comparing to experiments (cf. Ch. 7). The steady state of the system is completely defined by either of the two. However, steady state network growth evolves only within the velocity range, $0 < v_{\mathrm{nw}} < v_{\mathrm{fil}}$.

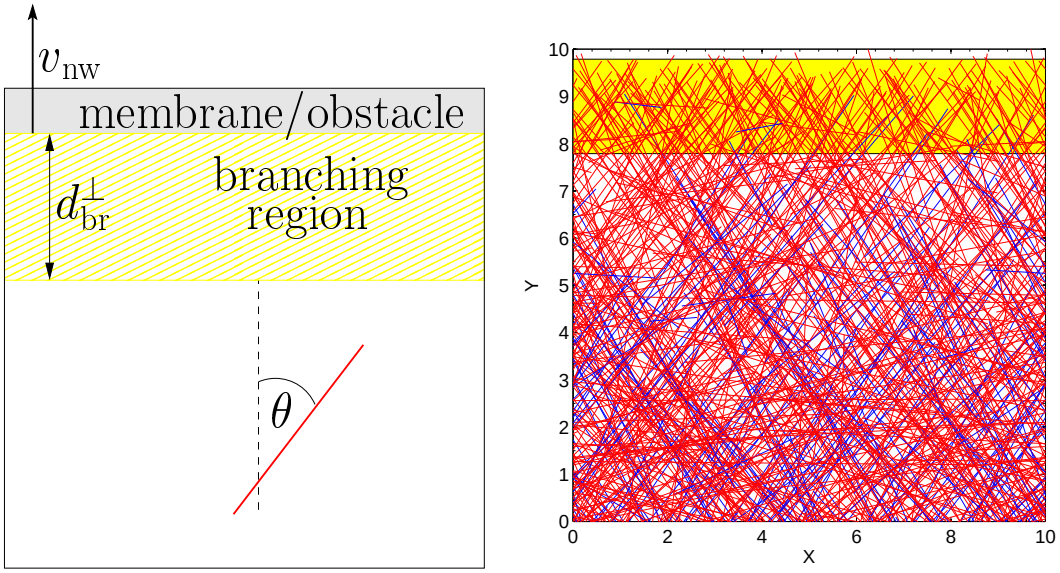

Figure 3.4: Model of the growing lamellipodium network. The network is growing in two dimensions with periodic boundary conditions in x-direction. Capping and branching reactions are assumed to be only active within the yellow *branching region* of constant width $d_{\mathrm{br}}^{\perp}$ at the top of the network very close to the plasma membrane or leading edge. Red filaments are actively growing at their barbed end, while blue filaments have been capped and will eventually be outgrown by the network and leave the box at the bottom. The growth of the first few topmost filaments is stalled by the load of the membrane or an external force. This process adjusts the steady state network velocity v_{nw} of the network. (a) Sketch of the setup. (b) Snapshot of a stochastic network simulation.

3.1.2 Continuum model

As a powerful alternative approach to the stochastic framework introduced above, we also develop on a deterministic rate equation for dendritic network growth. Following earlier approaches of this kind [16, 66], we introduce a distribution function $N(\theta, t)$ for the number of uncapped barbed ends in the branching region pointing in direction[1] θ at time t. This means in detail that the number of filaments per unit leading edge area with angles between θ and $\theta + d\theta$ is given by $N(\theta, t)d\theta$ at time t. In this region, the filaments are able to branch and get capped. In addition, they might leave the branching region if outgrown by the bulk network. The rate equation incorporating these processes therefore reads,

$$\frac{\partial N(\theta,t)}{\partial t} = \underbrace{\hat{k}_{\mathrm{b}} \int_{-180^\circ}^{+180^\circ} \mathcal{W}(\theta,\theta') N(\theta',t)\, \mathrm{d}\theta'}_{\text{branching}} - \underbrace{k_{\mathrm{c}} N(\theta,t)}_{\text{capping}} - \underbrace{k_{\mathrm{gr}}^{\perp}(\theta, v_{\mathrm{nw}}) N(\theta,t)}_{\text{outgrowth}} . \tag{3.1}$$

The three terms on the right hand side represent branching, capping and outgrowth. As in the stochastic framework, capping is assumed to be a first-order reaction with a constant rate k_{c}. In the branching term, $\mathcal{W}(\theta, \theta')$ is a branching angle dependent weighting factor distribution,

[1] Note, that we will often use the term *orientation* rather than the more precise *direction* in the following. This reflects that in previously published literature these two parameters are not well discriminated and both are most often denoted as *orientation*. However, in a rigorous way the orientation would be defined modulo 180°, while the direction has a range modulo 360°.

which we assume to be a Gaussian around an absolute angle difference of 70° with standard deviation $\sigma = 5^\circ$ between the branching mother and daughter filament barbed ends at θ' and θ, respectively. Because here we assume branching to be a zero-order reaction, the branching rate $\hat{k}_\mathrm{b}$ is normalized with regard to the total number of new filament ends,

$$\hat{k}_\mathrm{b} = \frac{k_\mathrm{b}}{\mathcal{W}_\mathrm{tot}} \,,\; \mathcal{W}_\mathrm{tot} = \int_{-\pi}^{+\pi}\int_{-\pi}^{+\pi} \mathcal{W}(\theta,\theta')N(\theta',t)\,\mathrm{d}\theta'\,\mathrm{d}\theta \,. \tag{3.2}$$

Here k_b is a constant rate parameter indicating the total number of branches per unit time in the whole branching region. Like in the network simulations, we again assume that network growth velocity is the external parameter that can be tuned to an arbitrary value between 0 and v_fil. Filaments are growing with constant velocity v_fil in their respective tangential barbed end direction. The important filament growth velocity component in our model is however their growth speed perpendicular to the leading edge. This projected polymerization speed depends on the filament orientation and is defined as,

$$v_\mathrm{fil}^\perp(\theta) := v_\mathrm{fil}\cos\theta \,. \tag{3.3}$$

Due to the competition between single filament growth and network growth, a critical orientation angle,

$$\theta_\mathrm{c} = \arccos(v_\mathrm{nw}/v_\mathrm{fil}) \,, \tag{3.4}$$

exists above which the single filament cannot follow the network anymore and therefore is outgrown by the bulk. Hence, for a given filament orientation θ, we write the rate of orthogonal outgrowth as a function of the network growth velocity,

$$k_\mathrm{gr}^\perp(\theta, v_\mathrm{nw}) = \begin{cases} 0 & \text{if } |\theta| \le \theta_\mathrm{c} \\ \frac{v_\mathrm{nw} - v_\mathrm{fil}\cos\theta}{(d_\mathrm{br}^\perp/2)} & \text{if } |\theta| > \theta_\mathrm{c} \end{cases} \,. \tag{3.5}$$

The factor of 2 arises because we assume that new filaments are generated on average in the middle of the growing region. Because we are using $d_\mathrm{br}^\perp = 2\delta_\mathrm{fil}$, new filaments are assumed to appear at a distance δ_fil from the leading edge. Taken together, Eq. (3.5) states that the rate of outgrowth is zero up to the critical angle θ_c and then increases up to a maximal value at $|\theta| = 180^\circ$ (cf. Fig. 3.5).

3.2 Stationary states and phase diagram

In the following we will analyze results from stochastic network simulations. We will focus on networks growing in the stationary state which is defined by a growth at constant network velocity v_nw, i.e. the velocity of the leading edge. As mentioned earlier, in this section we omit an external force on the network and treat the growth velocity v_nw as the external parameter that can be adjusted from the outside to tune the system and analyze how its steady state structure changes. It will turn out that an important characteristic of the network is the filament orientation distribution, which will be measured from these simulations.

Later on, we will test the new insights gained in the stochastic framework using the deterministic continuum approach. Here, it will not only be possible to reproduce the previous results, but also to generalize the predictions to a much larger parameter space.

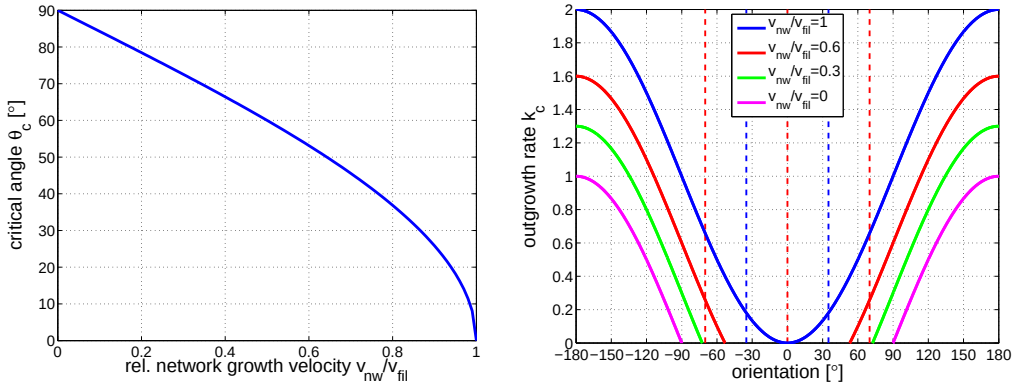

(a) (b)

Figure 3.5: Plot of critical angle (a) and filament outgrowth rate (b) for varying network growth velocity v_{nw}. Hence, these plots illustrate Eq. (3.4) and Eq. (3.5) respectively. The dashed lines in (b) indicate characteristic angles at $+70/0/-70$ and ± 35 degrees that will become important later on.

3.2.1 Stochastic network simulations

We start the analysis by simply comparing random snapshots in time of networks growing steadily at different constant velocity v_{nw}. Fig. 3.6 shows such networks sampled from a simulation in which the velocity was reduced in two steps from $v_{\mathrm{nw}}/v_{\mathrm{fil}} = 0.95$ (a) to $v_{\mathrm{nw}}/v_{\mathrm{fil}} = 0.76$ (b) and finally to $v_{\mathrm{nw}}/v_{\mathrm{fil}} = 0.3$ (c). Before the snapshots were taken, the system always had enough time to adjust to the new situation. After this adjustment time the history of the network is forgotten, i.e. the previous steady state does not influence the results anymore. To have a clear separation of filaments in the images, their total number in the simulation box was held approximately constant by adjusting the branching probability for each of the three steady states. We will show in the following two sections that this change in branching probability has no influence on the characteristics of our results. The capping probability remained constant in the simulation at $k_{\mathrm{c}} = 0.05$ per filament per unit time.

From a visual inspection of the network images it is already evident that the network structure changes with changing velocity v_{nw}. Most notably, the orientation of filaments seems to broaden when going from fast to slow growing states. This is due to the fact, that although all filaments are growing with the same velocity v_{fil} in their individual direction, the important filament property is the projected velocity $v_{\mathrm{fil}} \cos(\theta)$ orthogonal to the leading edge. If this orientation dependent velocity is smaller then the velocity of the leading edge, then the filaments are growing out of the simulation box eventually. When this process is fast, the filaments vanish from the picture before they can contribute a significant amount of new branches to the network.

To quantify this effect, we have measured the orientation distribution of filaments with their barbed end inside the branching region of the network and averaged over time. Measuring the orientation distribution of all filaments in the whole box yields similar phenomena. However, as capping is not active outside the yellow region, artifacts from filaments that are growing just outside below the branching region with approximately the same speed would emerge. This effect could be compensated by introducing capping processes in the whole simulation box, but here we rather restrict our analysis to the branching region. As shown in Fig. 3.6(d)–(f), our simulations revealed that the filament orientation distribution indeed changes dramatically as a function of network growth velocity. For fast and slow growing networks, a dominant $+70/0/–70$ degree distribution was found, whereas for a network of intermediate velocity, a ± 35 degree pattern emerges. Similar symmetric patterns emerge for different Arp2/3 branching

angles within a reasonable regime. However, the absolute orientations of the patterns are determined by the branching angle. Fig. 3.7 features schematic representations of the two different orientation patterns observed. A sample movie of the stochastic network simulation shown in Fig. 3.6 is available online, under this link[2].

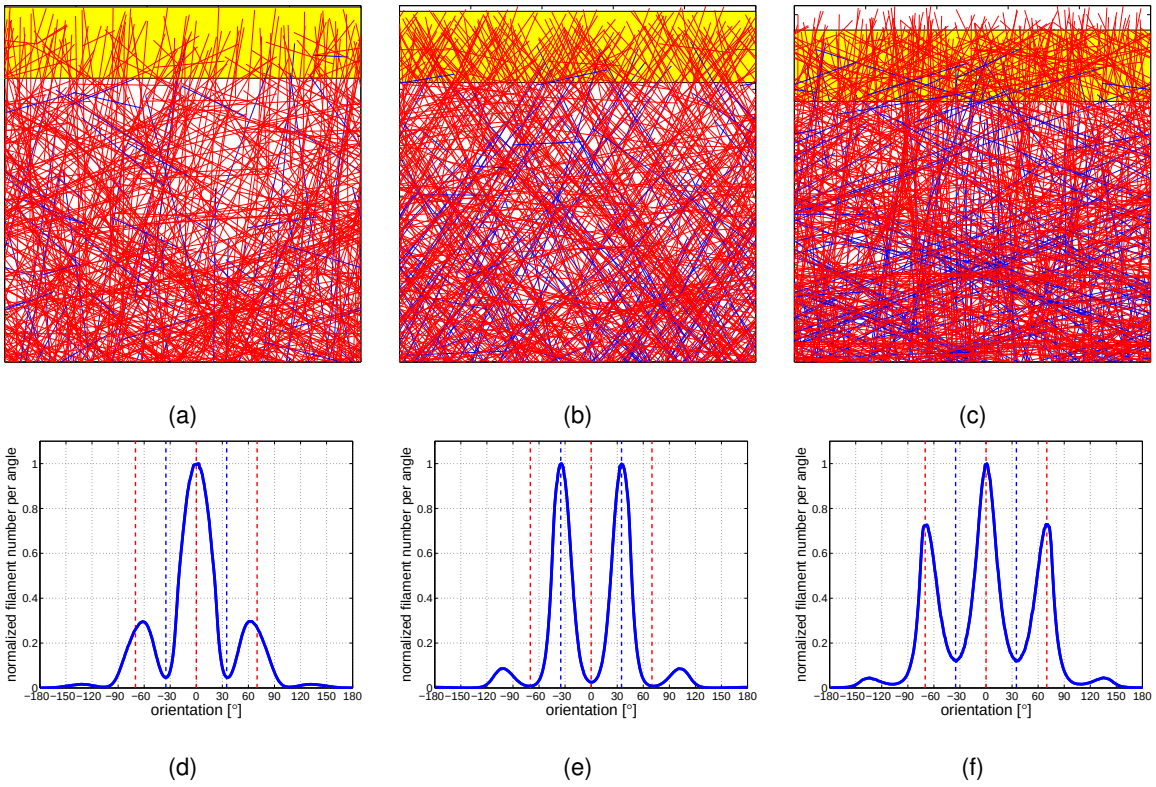

Figure 3.6: Stochastic network simulations. (a),(b),(c) Snapshots of the steady state network organization according to decreasing network growth velocities. Growing and capped filaments are shown in red and blue, respectively. The yellow region at the top corresponds to the branching-region, where capping and branching reactions occur. The network velocity v_{nw} is adjusted in these simulations by assuming that a constant number of filaments at the top N_{front} is obstructed by the membrane and not able to grow. The larger N_{front}, the lower the yellow region and the smaller v_{nw}. In these simulations the capping probability was chosen constant at $k_{\mathrm{c}} = 0.05$ per filament per unit time, while the integral branching rate k_{b} was adjusted for an approximately constant filament density within the simulation box. All uncapped barbed ends deterministically grow with velocity v_{fil}. (d),(e),(f) Filament orientation distributions of all filaments within the yellow growing region at the top averaged over time for the steady state above each figure. The vertical red and blue dotted lines mark the prominent angles $+70/0/-70$ and ± 35 degrees respectively. (a) and (d) $k_{\mathrm{b}} = 30$, $N_{\mathrm{front}} = 2$, $v_{\mathrm{nw}}/v_{\mathrm{fil}} \simeq 0.95$. (b) and (e) $k_{\mathrm{b}} = 22$, $N_{\mathrm{front}} = 20$, $v_{\mathrm{nw}}/v_{\mathrm{fil}} \simeq 0.76$. (c) and (f) $k_{\mathrm{b}} = 9$, $N_{\mathrm{front}} = 140$, $v_{\mathrm{nw}}/v_{\mathrm{fil}} \simeq 0.30$.

In the following we will show that the observed transitions in filament orientation patterns are generic. They can also be observed in the deterministic continuum model defined before in Sec. 3.1.2. In order to compare the stochastic network simulations to the continuum model, we will follow two promising directions from here. First, in the following section we will simplify the continuum model equation (3.1) and find the steady states of the simplified system analytically. We will be able to determine the stability of the found fixed points in linear approximation and derive the dependence of the transitions between steady states on the different model parameters as analytical expressions. Second, in Sec. 3.2.3 the full nonlinear model equation will be solved numerically with high precision. These calculations are computationally much less ex-

[2]http://www.pnas.org/content/vol0/issue2010/images/data/0913730107/DCSupplemental/SM1.avi

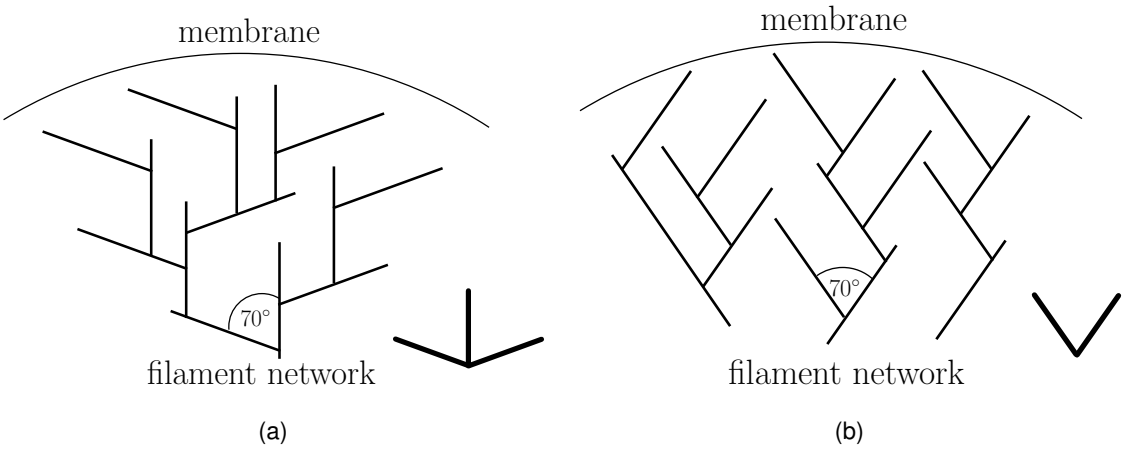

Figure 3.7: Schematic representation of the two different dominant orientation patterns. (a) A $+70/0/-70$ dominated network is observed for fast and slow network velocity like those observed in Fig. 3.6(a) and (c). (b) The competing distribution with peaks at ± 35 degrees emerges at intermediate growth velocity as illustrated in Fig. 3.6(b).

pensive than the stochastic network simulations and can thus be carried out to sample a large parameter range.

3.2.2 Analytical treatment of a simplified continuum description

In the rate equation approach Eq. (3.1), the number of filament ends in the branching region with angles between θ and $\theta + d\theta$ is given by $N(\theta, t)d\theta$. By integrating this equation stepwise over finite-sized angle bins, we obtain a finite number of coupled ordinary differential equations describing the temporal behavior of the filament number in every angle bin,

$$N_{\bar{\theta}} = \int_{\bar{\theta}-\Delta\theta/2}^{\bar{\theta}+\Delta\theta/2} N(\theta', t)\, \mathrm{d}\theta' \,, \tag{3.6}$$

with mean angle $\bar{\theta}$ and full width $\Delta\theta$. To find the solution of Eq. (3.1) we will choose 360 angle bins in Sec. 3.2.3 and approach the problem numerically. For analytical progress, here we reduce the number of equations by choosing a large bin size of $\Delta\theta = 35°$, that is half of the assumed Arp2/3 branching angle. In addition we assume that branching is restricted to pairs of angle bins with a relative angle difference of $70°$, that the rate according to which filaments grow out of the branching region is given by the rate for the mean angle of the corresponding bin $k_{\mathrm{gr}}^{\perp}(\bar{\theta})$, and that the branching of filaments with orientations $|\theta| > 87.5°$ can be neglected as they grow out of the branching region sufficiently quickly. We then arrive at a system of five

coupled nonlinear ordinary differential equations,

$$\begin{aligned}
\frac{\partial N_{-70^\circ}}{\partial t} &= \frac{1}{2}\hat{k}_\mathrm{b} N_{0^\circ} - \left(k_\mathrm{c} + k_\mathrm{gr}^\perp(70^\circ)\right) N_{-70^\circ} && (3.7)\\
\frac{\partial N_{-35^\circ}}{\partial t} &= \frac{1}{2}\hat{k}_\mathrm{b} N_{+35^\circ} - \left(k_\mathrm{c} + k_\mathrm{gr}^\perp(35^\circ)\right) N_{-35^\circ} && (3.8)\\
\frac{\partial N_{0^\circ}}{\partial t} &= \frac{1}{2}\hat{k}_\mathrm{b} \left(N_{-70^\circ} + N_{+70^\circ}\right) - k_\mathrm{c} N_{0^\circ} && (3.9)\\
\frac{\partial N_{+35^\circ}}{\partial t} &= \frac{1}{2}\hat{k}_\mathrm{b} N_{-35^\circ} - \left(k_\mathrm{c} + k_\mathrm{gr}^\perp(35^\circ)\right) N_{+35^\circ} && (3.10)\\
\frac{\partial N_{+70^\circ}}{\partial t} &= \frac{1}{2}\hat{k}_\mathrm{b} N_{0^\circ} - \left(k_\mathrm{c} + k_\mathrm{gr}^\perp(70^\circ)\right) N_{+70^\circ}\,, && (3.11)
\end{aligned}$$

with

$$\hat{k}_\mathrm{b} = \frac{k_\mathrm{b}}{\mathcal{W}_\mathrm{tot}} = \frac{k_\mathrm{b}}{N_{-70^\circ} + N_{-35^\circ} + N_{0^\circ} + N_{+35^\circ} + N_{+70^\circ}}\,.$$

Due to the symmetry around 0°, only three of these equations are independent. The equations are nonlinear due to our assumption that the branching reaction is independent of the total number of preexisting filaments.

To identify and analyze the stationary states of equations (3.7)–(3.11), we are solving $\partial N_{\bar{\theta}}/\partial t = 0$ for all $\bar{\theta}$. If we take into account only the physically meaningful subspace of non-negative filament numbers, two steady state solutions emerge. The first solution,

$$\begin{aligned}
N_{-70^\circ}^{\mathrm{ss35}} &= 0\\
N_{-35^\circ}^{\mathrm{ss35}} &= k_\mathrm{b} \tfrac{1}{4(k_\mathrm{c} + k_\mathrm{gr}^\perp(35^\circ))}\\
N_{0^\circ}^{\mathrm{ss35}} &= 0\\
N_{+35^\circ}^{\mathrm{ss35}} &= k_\mathrm{b} \tfrac{1}{4(k_\mathrm{c} + k_\mathrm{gr}^\perp(35^\circ))}\\
N_{+70^\circ}^{\mathrm{ss35}} &= 0\,,
\end{aligned} \qquad (3.12)$$

represents a dominant ± 35 degree orientation distribution in the steady state (ss35) while the second solution,

$$\begin{aligned}
N_{-70^\circ}^{\mathrm{ss70}} &= k_\mathrm{b} \tfrac{k_\mathrm{c} + k_\mathrm{gr}^\perp(70^\circ) - \sqrt{2k_\mathrm{c}\left(k_\mathrm{c} + k_\mathrm{gr}^\perp(70^\circ)\right)}}{2\left({k_\mathrm{gr}^\perp}^2(70^\circ) - k_\mathrm{c}^2\right)}\\
N_{-35^\circ}^{\mathrm{ss70}} &= 0\\
N_{0^\circ}^{\mathrm{ss70}} &= k_\mathrm{b} \tfrac{1 - \sqrt{\frac{k_\mathrm{c} + k_\mathrm{gr}^\perp(70^\circ)}{2k_\mathrm{c}}}}{k_\mathrm{c} - k_\mathrm{gr}^\perp(70^\circ)}\\
N_{+35^\circ}^{\mathrm{ss70}} &= 0\\
N_{+70^\circ}^{\mathrm{ss70}} &= k_\mathrm{b} \tfrac{k_\mathrm{c} + k_\mathrm{gr}^\perp(70^\circ) - \sqrt{2k_\mathrm{c}\left(k_\mathrm{c} + k_\mathrm{gr}^\perp(70^\circ)\right)}}{2\left({k_\mathrm{gr}^\perp}^2(70^\circ) - k_\mathrm{c}^2\right)}\,,
\end{aligned} \qquad (3.13)$$

corresponds to the competing $+70/0/{-}70$ pattern (ss70).

In order to investigate how the stability of these fixed points depends on model parameters, we are using linear stability analysis [102]. For this purpose the eigenvalues λ_i of the Jacobi-Matrix of the nonlinear system (equations (3.7)–(3.11)) at the positions of the fixed points N^{ss35} (solution (3.12)) and N^{ss70} (solution (3.13)) have to be calculated. Starting with ss35, the

eigenvalues of the Jacobi-Matrix read,

$$\lambda_1^{\mathrm{ss35}} = -\left(k_\mathrm{c} + k_\mathrm{gr}^\perp(35^\circ)\right) \tag{3.14}$$

$$\lambda_2^{\mathrm{ss35}} = -2\left(k_\mathrm{c} + k_\mathrm{gr}^\perp(35^\circ)\right) \tag{3.15}$$

$$\lambda_3^{\mathrm{ss35}} = -\left(k_\mathrm{c} + k_\mathrm{gr}^\perp(70^\circ)\right) \tag{3.16}$$

$$\lambda_4^{\mathrm{ss35}} = -\frac{1}{2}\left(2k_\mathrm{c} + k_\mathrm{gr}^\perp(70^\circ) + \sqrt{8\left(k_\mathrm{c} + k_\mathrm{gr}^\perp(35^\circ)\right)^2 + {k_\mathrm{gr}^\perp}^2(70^\circ)}\right) \tag{3.17}$$

$$\lambda_5^{\mathrm{ss35}} = -\frac{1}{2}\left(2k_\mathrm{c} + k_\mathrm{gr}^\perp(70^\circ) - \sqrt{8\left(k_\mathrm{c} + k_\mathrm{gr}^\perp(35^\circ)\right)^2 + {k_\mathrm{gr}^\perp}^2(70^\circ)}\right) . \tag{3.18}$$

Now, we have to determine for which sets of parameters k_c, $k_\mathrm{gr}^\perp(35^\circ)$ and $k_\mathrm{gr}^\perp(70^\circ)$ all eigenvalues are strictly negative, as for these sets the fixed point N^{ss35} is asymptotically stable. However, the two parameters $k_\mathrm{gr}^\perp(35^\circ)$ and $k_\mathrm{gr}^\perp(70^\circ)$ are not independent but rather both of them are determined by the bulk velocity of the network v_nw as given in Eq. (3.5). If we omit the ill-defined cases $k_\mathrm{c} = k_\mathrm{gr}^\perp(35^\circ) = 0$ and $k_\mathrm{c} = k_\mathrm{gr}^\perp(70^\circ) = 0$, in which the filament number diverges, the first four eigenvalues $\lambda_1^{\mathrm{ss35}}$-$\lambda_4^{\mathrm{ss35}}$ are strictly negative for all possible (non-negative) values for the parameters. The last eigenvalue λ_5^{ss35} however changes its sign when the relation,

$$k_\mathrm{gr}^\perp(70^\circ) = \frac{k_\mathrm{c}^2 + 4k_\mathrm{c}k_\mathrm{gr}^\perp(35^\circ) + 2{k_\mathrm{gr}^\perp}^2(35^\circ)}{k_\mathrm{c}} , \tag{3.19}$$

is satisfied.

Although the expressions for some of the eigenvalues of the ss70 solution are rather complicated, it can be shown that in this case also only one eigenvalue,

$$\lambda_5^{\mathrm{ss70}} = -k_\mathrm{c} - k_\mathrm{gr}^\perp(35^\circ) + \sqrt{\frac{k_\mathrm{c}\left(k_\mathrm{c}+k_\mathrm{gr}^\perp(70^\circ)\right)}{2}} , \tag{3.20}$$

changes its sign, while all the others are strictly negative in the parameter range mentioned before. Note that the branching rate k_b does not appear in the eigenvalues and therefore has no influence on the stability of the steady state. This justifies a posteriori our choice to adjust the branching probability to keep the filament density constant in Fig. 3.6. $\lambda_5^{\mathrm{ss70}}$ changes its sign under the same condition as we have found before for $\lambda_5^{\mathrm{ss35}}$ (Eq. (3.19)). However, both eigenvalues $\lambda_5^{\mathrm{ss35}}$ and $\lambda_5^{\mathrm{ss70}}$ hold opposite signs whenever they do not vanish. Therefore we can conclude that for the whole parameter range (apart from the subset where Eq. (3.19) is exactly satisfied) either the ss35 steady state is asymptotically stable and the ss70 solution is a saddle or vice versa. Eq. (3.19) marks the transition between these two steady state solutions.

Next we analyze for which bulk network velocities v_nw Eq. (3.19) is fulfilled. If we start at small v_nw such that the critical angle is $\theta_\mathrm{c} \geq 70^\circ$ and only filaments with a larger orientation angle than θ_c are growing out of the branching region, we get from Eq. (3.5), $k_\mathrm{gr}^\perp(70^\circ) = k_\mathrm{gr}^\perp(35^\circ) = 0$ and Eq. (3.19) is never fulfilled (for $k_\mathrm{c} > 0$). For increasing network speed, $35^\circ \leq \theta_\mathrm{c} < 70^\circ$ (i.e. $k_\mathrm{gr}^\perp(70^\circ) > 0 \wedge k_\mathrm{gr}^\perp(35^\circ) = 0$), we obtain a single solution for v_nw that satisfies Eq. (3.19),

$$v_\mathrm{nw} = \frac{1}{2}k_\mathrm{c}d_\mathrm{br}^\perp + v_\mathrm{fil}\cos(70^\circ) \text{ , for } 35^\circ \leq \theta_\mathrm{c} < 70^\circ . \tag{3.21}$$

Once the network velocity has reached the value where the critical angle $\theta_\mathrm{c} < 35^\circ$ (i.e. $k_\mathrm{gr}^\perp(70^\circ) >$

$k_{\mathrm{gr}}^{\perp}(35^\circ) > 0$), two solutions emerge,

$$\begin{aligned} v_{\mathrm{nw}\,1,2} &= \tfrac{1}{8}\left(-3k_{\mathrm{c}}d_{\mathrm{br}}^{\perp} + 8v_{\mathrm{fil}}\cos(35^\circ)\right) \\ &\quad \pm\tfrac{1}{8}\sqrt{k_{\mathrm{c}}d_{\mathrm{br}}^{\perp}\left(k_{\mathrm{c}}d_{\mathrm{br}}^{\perp} + 16v_{\mathrm{fil}}\cos(35^\circ) - 16v_{\mathrm{fil}}\cos(70^\circ)\right)}\,, \\ &\quad \text{for } \theta_{\mathrm{c}} < 35^\circ\,. \end{aligned} \tag{3.22}$$

Due to the restrictions on the critical angle, solution (3.21) is valid for network bulk velocities $v_{\mathrm{fil}}\cos(35^\circ) \geq v_{\mathrm{nw}} > v_{\mathrm{fil}}\cos(70^\circ)$, while solution (3.22) holds in the domain $v_{\mathrm{nw}} > v_{\mathrm{fil}}\cos(35^\circ)$. This restriction is never fulfilled by the negative square-root in Eq. (3.22) and so we can neglect this solution in the following.

By inspection of Eq. (3.21) and Eq. (3.22), we can identify the model parameters that influence the stability of the fixed point. On the one hand, the branching rate has no impact on the normalized orientation distribution as mentioned before, but rather scales the steady state filament number per angle bin linearly (cf. equations (3.12) and (3.13)). This is important for the physical force the network can carry, but not for its architecture. On the other hand, two velocities determine the stability. In Sec. 5.5, we will use the single filament velocity v_{fil} together with the length scale δ_{fil} to obtain the system time and subsequently determine physical units. Therefore without loss of generality, we can assume v_{fil} to be some given constant at this point. The remaining parameter that defines the stability criterion is given by a generalized velocity u_{c} that is defined as the product of the capping rate k_{c} and the size of the branching region $d_{\mathrm{br}}^{\perp}$,

$$u_{\mathrm{c}} := k_{\mathrm{c}}d_{\mathrm{br}}^{\perp}\,. \tag{3.23}$$

Substituting this definition in equations (3.21) and (3.22), we obtain

$$v_{\mathrm{nw}} = \frac{1}{2}u_{\mathrm{c}} + v_{\mathrm{fil}}\cos(70^\circ)\,, \tag{3.24}$$

and

$$\begin{aligned} v_{\mathrm{nw}\,1,2} &= \tfrac{1}{8}\left(-3u_{\mathrm{c}} + 8v_{\mathrm{fil}}\cos(35^\circ)\right) \\ &\quad \pm\tfrac{1}{8}\sqrt{u_{\mathrm{c}}\left(u_{\mathrm{c}} + 16v_{\mathrm{fil}}\cos(35^\circ) - 16v_{\mathrm{fil}}\cos(70^\circ)\right)}\,, \end{aligned} \tag{3.25}$$

respectively.

The generalized velocity u_{c} basically defines a measure for the probability for a filament to get capped before it grows out of the branching region. Filaments growing inside the branching zone with a relative velocity u_{c} away from the leading edge are able to grow for a mean free path length $d_{\mathrm{br}}^{\perp}$ until they get capped. Although, the stability of the steady states could be given as a function of the abstract parameter u_{c}, we will in general stick to a constant size of the branching region $d_{\mathrm{br}}^{\perp}$ and vary only k_{c} for simplicity in the following. This capping rate appears to be the essential and more accessible parameter in the biological context. However, of course it is also always possible to derive the impact of changing branching region size from these results by simply considering Eq. (3.23). In other words, we have to expect similar effects when increasing $d_{\mathrm{br}}^{\perp}$ by some factor as we will find for the increase in k_{c} by the same factor.

A phase diagram showing the separate regions in which either ss35 is asymptotically stable and ss70 is a saddle or vice versa is given in Fig. 3.11(a) on page 42. There the constants were chosen such that filament barbed ends grow with a velocity v_{fil} of one actin monomer increment δ_{fil} per unit time step and the width of the branching region $d_{\mathrm{br}}^{\perp}$ equals $2\delta_{\mathrm{fil}}$. The transitions between the two fixed points are given by Eq. (3.24) and Eq. (3.25) and marked as black lines. The corresponding regions of stability in between are labeled accordingly.

So far we have understood that the system, starting in close proximity of the stable fixed point, will eventually end up in this state. We now have to also analyze the attraction of trajectories by the saddle point. Although this point is repelling in a single dimension (given by the eigenvector of the positive eigenvalue), there is also a four-dimensional subspace (the remaining four eigenvectors) of initial conditions attracted to this state in its neighborhood. In the following it will be specified which initial conditions exactly are still converging to the saddle.

Let us assume we are in the parameter range in which the ss35 is a node while the ss70 solution is a saddle point. If we evaluate the subspace spanned by the four eigenvectors $\vec{v}_i^{\,\mathrm{ss70}}$ with negative eigenvalues at the saddle, they have the form

$$\vec{v}_1^{\,\mathrm{ss70}} = \begin{bmatrix} 1 \\ 0 \\ 0 \\ 0 \\ -1 \end{bmatrix}, \; \vec{v}_2^{\,\mathrm{ss70}} = \begin{bmatrix} 0 \\ 1 \\ 0 \\ -1 \\ 0 \end{bmatrix}, \; \vec{v}_3^{\,\mathrm{ss70}} = \begin{bmatrix} 1 \\ 0 \\ a \\ 0 \\ 1 \end{bmatrix}, \; \vec{v}_4^{\,\mathrm{ss70}} = \begin{bmatrix} 1 \\ 0 \\ b \\ 0 \\ 1 \end{bmatrix}, \tag{3.26}$$

where a and b are constants depending on the parameters. Here we can see that the eigenvectors $\vec{v}_1^{\,\mathrm{ss70}}$, $\vec{v}_3^{\,\mathrm{ss70}}$ and $\vec{v}_4^{\,\mathrm{ss70}}$ span the three dimensional subspace where the $N_{\pm 35^\circ}$ fiber population vanishes. As the two different orientation distributions are not coupled via branching in this model, this is a trivial case. From initial conditions where there are no fibers in the $N_{\pm 35^\circ}$ orientation bins, this steady state can never be reached. The remaining eigenvector $\vec{v}_2^{\,\mathrm{ss70}}$ however spans a subspace only featuring non-physical (negative) fiber numbers in exactly one bin. Therefore we can conclude that initial conditions of positive fiber numbers in all bins will in general not approach this saddle point in the system.

A similar reasoning applies for parameters for which the ss35 fixed point is unstable. Again we can write down the eigenvectors of the negative eigenvalues, i.e. the subspace that is attracted to the saddle in its vicinity

$$\vec{v}_1^{\,\mathrm{ss35}} = \begin{bmatrix} 0 \\ 1 \\ 0 \\ 1 \\ 0 \end{bmatrix}, \; \vec{v}_2^{\,\mathrm{ss35}} = \begin{bmatrix} 0 \\ -1 \\ 0 \\ 1 \\ 0 \end{bmatrix}, \; \vec{v}_3^{\,\mathrm{ss35}} = \begin{bmatrix} -1 \\ 0 \\ 0 \\ 0 \\ 1 \end{bmatrix}, \; \vec{v}_4^{\,\mathrm{ss35}} = \begin{bmatrix} 1 \\ a \\ b \\ a \\ 1 \end{bmatrix}, \tag{3.27}$$

where a is again some constant depending on the parameters and b is given by,

$$b = \frac{k_{\mathrm{gr}}^{\perp}(70^\circ) - \sqrt{8(k_{\mathrm{c}} + k_{\mathrm{gr}}^{\perp}(35^\circ))^2 + k_{\mathrm{gr}}^{\perp}(70^\circ)^2}}{2(k_{\mathrm{c}} + k_{\mathrm{gr}}^{\perp}(35^\circ))}. \tag{3.28}$$

As $b < 0$ for all relevant sets of parameters, we can conclude again that the vectors $\vec{v}_1^{\,\mathrm{ss35}}$ and $\vec{v}_2^{\,\mathrm{ss35}}$ span the trivial subspace where no fibers are in the $N_{\pm 70^\circ}$ and N_{0° orientation bins and the remaining vectors $\vec{v}_3^{\,\mathrm{ss35}}$ and $\vec{v}_4^{\,\mathrm{ss35}}$ span a subspace in which at least one fiber number is negative. Therefore here again all physically meaningful conditions in the vicinity of the saddle point will be repelled.

3.2.3 Numerical solution of the continuum model

In order to solve Eq. (3.1) numerically without the simplifying assumptions of Sec. 3.2.2, we divided the continuum of possible filament orientations in 360 angle bins. In this way, we obtain 360 coupled nonlinear ordinary differential equations that can be iterated in time numerically using the Euler method until a steady state is found. We also checked for artifacts due to the finite size of the angle bins. Here, a width of one degree seemed sufficiently small such that a further increase in the number of bins did not alter the results significantly anymore.

To compare the two versions of the continuum model in more detail, in Fig. 3.8 we show the steady state filament orientation distribution for the simplified and the full rate equation approach. Here the steady state of the full model evolved from the numerical iteration of Eq. (3.1) for a given set of parameters, while the solution of the simplified continuum model was calculated according to either Eq. (3.12) or Eq. (3.13) in their respective phase of stability. This yields similar results compared to iterating equations (3.7)–(3.11) in time. The capping rate was chosen as in the stochastic simulations at $k_\mathrm{c} = 0.05$ per filament per unit time. The branching rate was held constant at $k_\mathrm{b} = 20$ per unit time in these calculation. However as mentioned before, this choice only influences the total number of filaments but not their relative orientation distribution. From (a) to (c) the network bulk velocity is reduced and the stationary distribution switches from the $+70/0/–70$ state in the *fast growth phase* (a) to the ±35 pattern in the *medium growth phase* (b) and then back to another $+70/0/–70$ distribution in the *slow growth phase* (c). The agreement between the two approaches is good. For each case shown, the orientation range in which growth is possible (that is up to the critical angle θ_c) is indicated by a horizontal black line. For very fast network growth, the critical angle θ_c is close to zero and filaments with larger orientations are suppressed. So the dominant orientation will be close to zero with branching angles around $\pm70°$ relative to the leading edge normal. Once the network growth velocity reduces to a point where the critical angle is sufficiently large to prevent filaments at $\pm35°$ from growing out of the network, the ±35 solution dominates and the system changes to the *medium growth phase*. As the growth velocity is reduced further, the critical angle increases above $70°$ and the $+70/0/–70$ pattern dominates again.

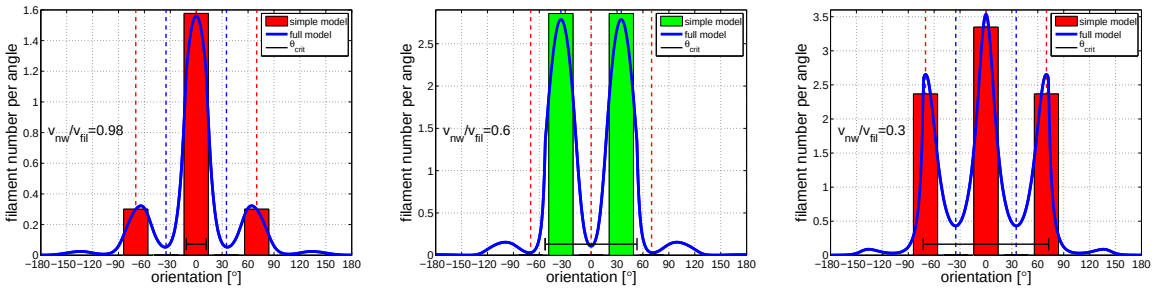

Figure 3.8: Comparison of the steady states of the analytically solved reduced model (bars) and the numerically solved full model (curves) for $k_\mathrm{b} = 20$ and $k_\mathrm{c} = 0.05$. Network bulk velocity v_nw is decreasing from (a) to (c): (a) $v_\mathrm{nw}/v_\mathrm{fil} = 0.98$, (b) $v_\mathrm{nw}/v_\mathrm{fil} = 0.6$ and (c) $v_\mathrm{nw}/v_\mathrm{fil} = 0.3$. The vertical red and blue dotted lines mark the prominent angles $+70/0/–70$ and ±35, respectively. The horizontal solid black line marks the orientation range $|\theta| \leq \theta_\mathrm{c}$ in which single filaments are not outgrown by the bulk network, i.e. $k_\mathrm{gr}^{\perp}(|\theta| \leq \theta_\mathrm{c}) = 0$.

A similar comparison of steady states from the iteration of the full continuum model and the stochastic network simulations can be found in Fig. 3.9. Here, we adjusted the continuum steady states to the parameters already used for the network simulations shown in Fig. 3.6 of Sec. 3.2.1 (page 33). Again the two approaches give similar results.

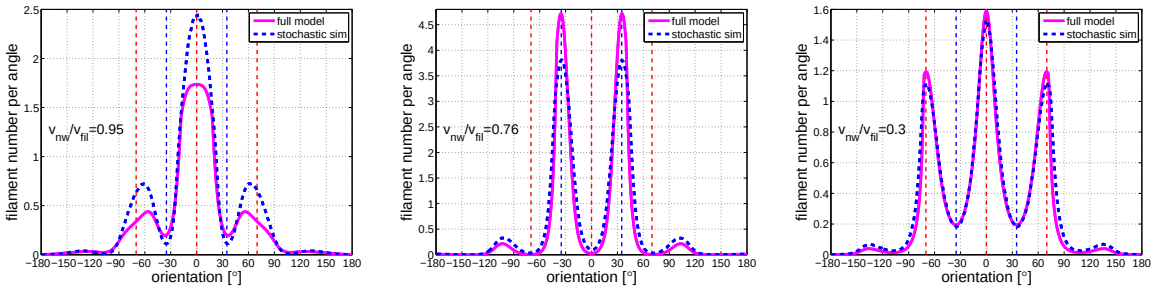

(a) (b) (c)

Figure 3.9: Comparison of the steady states from the full continuum model (magenta) and stochastic network simulations (dashed blue). The steady states of the stochastic simulations correspond to the ones already shown in Fig. 3.6(d)–(f) of Sec. 3.2.1. The numerical continuum model has been adjusted to these parameters, i.e. (a) $k_\mathrm{b} = 30$, $v_\mathrm{nw}/v_\mathrm{fil} \simeq 0.95$, (b) $k_\mathrm{b} = 22$, $v_\mathrm{nw}/v_\mathrm{fil} \simeq 0.76$ and (c) $k_\mathrm{b} = 9$, $v_\mathrm{nw}/v_\mathrm{fil} \simeq 0.30$. The capping rate was held constant at $k_\mathrm{c} = 0.05$.

In order to simplify the identification of the two different orientation patterns in the following, we define as an appropriate order parameter the relative difference of filaments in the angle bin around 0° to the one around 35°,

$$\mathcal{O} = \frac{N_{0^\circ} - N_{35^\circ}}{N_{0^\circ} + N_{35^\circ}} = [-1, +1] \ . \tag{3.29}$$

For a perfect $+70/0/-70$ distribution this parameter will approach $+1$, while for the competing ± 35 pattern, it will approach -1. Fig. 3.10(a) shows the evolution of the order parameter as a function of the bulk network velocity. The order parameter is shown both for stepwise decreasing and stepwise increasing velocities, indicating that the network can adapt sufficiently fast to attain the steady state values. In this sense we understand all changes in the external parameter – which is the network velocity v_nw at this point – as quasistatic in the following if not explicitly stated differently. This effectively means, that we assume the timescale of system equilibration to be much faster than the one for changing external clues in the biological system. Apart from a single but very important exception in Ch. 5, we therefore will not treat non-equilibrium effects in this thesis. Fig. 3.10(b) shows the evolution of the order parameter $\mathcal{O}$ for different values of the branching and capping rates and for quasistationary changes in network velocity v_nw. The three curves for constant capping rate $k_\mathrm{c} = 0.05$ but different values for the branching rate k_b collapse, indicating that the order parameter is independent of the branching rate. Considering the findings of the previous section, this result is not surprising as the order parameter only incorporates relative filament numbers but not their absolute value, which would indeed be altered by k_b. Contrarily, when the capping rate k_c is increased over three orders of magnitude, the clear distinction between the two different phases vanishes. In Fig. 3.10(c), the two maximum values of the order parameter for the *fast* and *slow growth phases* as well as the minimum value for the *medium growth phase* are given for increasing capping rate. The absolute magnitude of these peak values is rapidly decreasing until the different orientation patterns can not be discriminated well anymore. In this limit the orientation distribution in steady state features a bulk continuum rather than clear discriminated peaks. This also justifies a posteriori our choice of a small capping rate $k_\mathrm{c} = 0.05$ per unit time in the steady state results presented before in the figures 3.8 and 3.9. Our model predicts that, if this value was significantly larger, one could not observe the characteristic orientation distributions found in electron micrographs of the leading edge of mobile cells in e.g. [66, 96, 108].

Using the definition of the order parameter (Eq. (3.29)) again, we can now deduce the actual

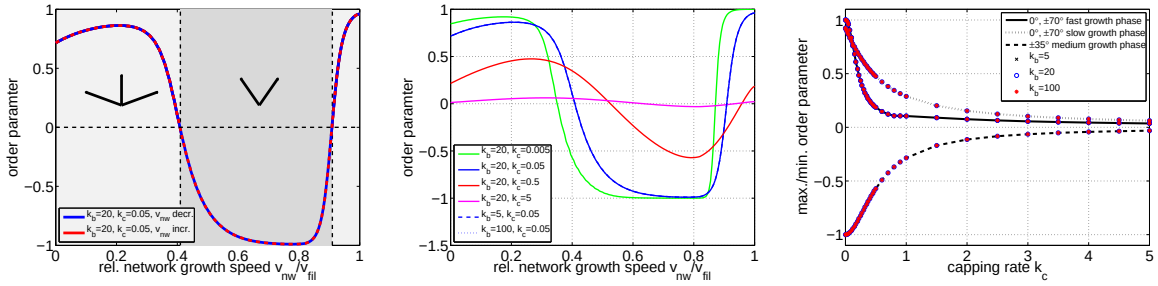

(a) (b) (c)

Figure 3.10: Evolution of the order parameter $\mathcal{O}$ (Eq. (3.29)) in steady state with changing network velocity v_{nw}. (a) For the parameter values used earlier in Fig. 3.8, i.e. $k_{\mathrm{b}} = 20$ and $k_{\mathrm{c}} = 0.05$. (b) For different parameter values for capping and branching rate, the evolution of the order parameter with network velocity varies. The three curves for $k_{\mathrm{c}} = 0.05$ (dashed, dotted and solid blue) collapse, indicating that k_{b} does not influence the relative filament numbers. (c) Only plotting the locally maximum order parameters in the *fast* and *slow growth phase* (i.e. $+70/0/-70$), and the minimum order parameter in the *medium growth phase* (i.e. ± 35) versus increasing capping rate. This yields a decreasing discrimination of the different phases, as the separation of different peaks in the orientation distribution becomes less prominent. Again these results show no dependence on the branching rate as the order parameter does not depend on absolute filament numbers, which would be altered by changing the branching rate k_{b}.

phase from steady state orientation distributions. For positive order parameter, the system is in the $+70/0/-70$ state, i.e. either the *fast* or *slow growth phase*. For negative order parameter, the steady state distribution is given by the ± 35 state in the *medium growth phase*. In this sense, we can thus define a structural phase transition at exactly the point, where $\mathcal{O}$ vanishes. According to this definition of the transition point, it is now possible to numerically solve the full continuum model Eq. (3.1) for quasi-static changes in the external parameter v_{nw} and for different capping rates and classify each observed stationary state as one of the two phases. These results are given as a phase diagram in Fig. 3.11(b). Again the results were also obtained for different branching rates k_{b}, which has no significant influence as expected. The phase diagram again nicely demonstrates the expected behavior of the system, which was already observed earlier. For fast and slowly moving networks a $+70/0/-70$ state is obtained, while for networks in the intermediate velocity range the ± 35 pattern emerges. In the solution of the full continuum model also the capping rate has only a very limited influence on this band-like appearance of the phase diagram. Contrarily, in the phase diagram shown in Fig. 3.11(a) resulting from the analytical arguments in Sec. 3.2.2, the ± 35 pattern vanishes at large capping rate. This artifact of the reduced rate equation model follows from the assumption that filaments with an orientation larger than $87.5°$ do not branch. As the capping rate increases, the angle-dependent outgrowth term favoring persistence of filaments with small angles becomes less important and the $+70/0/-70$ pattern is favored because it involves more angle bins in this model. As the full rate equation model does not share this assumption, it does not predict the elimination of the ± 35 pattern for large capping rate.

Finally we also conducted simulations to support our previous prediction from Sec. 3.2.2, that a change in capping rate k_{c} should have a similar effect on the filament orientation distribution compared to a change in the orthogonal width of the branching region $d_{\mathrm{br}}^{\perp}$ given that the generalized velocity parameter $u_{\mathrm{c}} = k_{\mathrm{c}} d_{\mathrm{br}}^{\perp}$ (Eq. (3.23)) stays constant in both variations. To test this, we have measured the network velocity at the transition from *fast* to *medium* and *slow growth phase* for varying k_{c} and $d_{\mathrm{br}}^{\perp}$ while keeping the generalized velocity constant at two different values, $u_{\mathrm{c}} = 0.1 = \mathrm{const.}$ and $u_{\mathrm{c}} = 1 = \mathrm{const.}$ Fig. 3.12 shows that indeed the transition velocities do not change in both cases. The effective parameter that therefore determines the

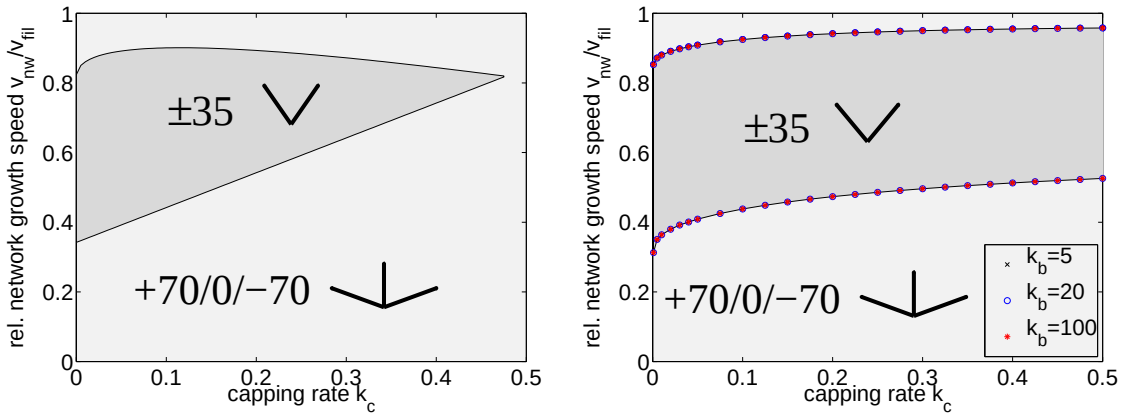

Figure 3.11: Phase diagrams resulting from the rate equation approach. The dark and bright gray regions correspond to stability of the ± 35 and $+70/0/-70$ orientation patterns, respectively. (a) Analytical results from a linear stability analysis of the reduced model (cf. Sec. 3.2.2). The black line at the transition corresponds to Eq. (3.24) and Eq. (3.25) in their corresponding region of validity. (b) Numerical solution of the model equation (3.1) according to three different branching rates $k_\mathrm{b} = \{5,\ 20,\ 100\}$.

stability of the steady states of the system is indeed the generalized velocity u_c, rather than k_c and $d_\mathrm{br}^\perp$ separately.

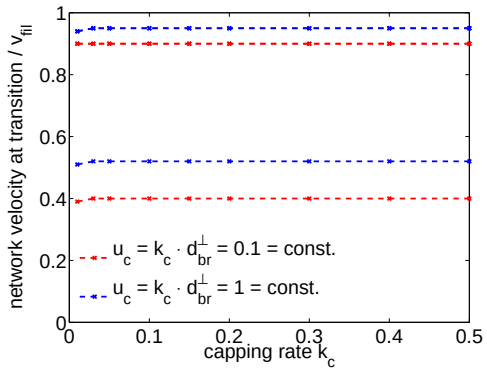

Figure 3.12: Plot of the network velocities at the two orientation transitions for changing capping rate k_c. Here the branching region width $d_\mathrm{br}^\perp$ has been adjusted to keep the generalized velocity parameter $u_\mathrm{c} = k_\mathrm{c} d_\mathrm{br}^\perp$ constant. Therefore no significant change is observed in the transition velocities of the numerical solution of the full continuum model Eq. (3.1), as predicted by analytical arguments in Sec. 3.2.2.

3.3 Summary and discussion

In our theoretical analysis of this chapter, we focused on the network growth velocity as the external parameter which we assumed could be varied in a (Gedanken-)experimental setup to tune the state of the system. This led to transitions in the orientation distribution of filaments growing in a stationary state. We have shown, that for large and small network growth velocities, the stable steady state is a $+70/0/-70$ pattern, while for intermediate network growth velocity, the stable steady state is a ± 35 pattern. This conclusion was drawn both from stochastic network simulations and a deterministic rate equation approach (which was treated both by a

full numeric analysis and a linear stability analysis of a reduced version), thus our predictions are very robust with regard to the theoretical approach employed. The value of the branching rate k_b was found to be irrelevant regarding the orientation pattern, while the capping rate k_c and the orthogonal width of the branching region $d_{\mathrm{br}}^{\perp}$ had identical but only weak effect. This leaves the network growth velocity v_{nw} as the main factor determining which orientation pattern dominates.

The model suggests that in growing actin networks a competition between two self-organizing filament orientation patterns exists. Our central assumption differing from earlier work is that branching is assumed to be a zero-order reaction in the number of filaments. This means that only a certain number of branching points can be established within a given region at the leading edge per unit time, independent of the number of existing actin filaments. If Arp2/3 is activated before filament binding, this would imply that its activation time is larger than all other time scales involved in actin filament branching [88]. Recent evidence suggests that Arp2/3 might be activated after filament binding [7]. In this case, successful branching might be limited by the availability of nucleation promoting factors localized at the leading edge. If this process takes longer than the nascent branching points take to grow away from the leading edge, then branching is effectively also a zero-order process.

As an instructive alternative to our zero-order branching rate assumption, a first-order branching rate, together with first-order capping has been analyzed before in [16]. For this model to be valid, the cytoplasm has to hold a sufficiently large reservoir of activated Arp2/3, capping protein and actin monomers, such that all of these proteins are always available in excess and not limiting the reactions. Then both, branching and capping can be modeled as first-order reactions which are both proportional to the number of existing filaments. For vanishing outgrowth rate, branching and capping must exactly balance each other to yield a steady state filament number. In case they do not exactly balance and there are more branching than capping events taking place per unit time, the outgrowth rate has to be adjusted accordingly to annihilate all filaments that are created in excess. As the outgrowth rate is a monotonically increasing function of the network bulk velocity v_{nw} (Eq. (3.5)), there exists only a single unique bulk velocity for a given set of branching and capping rates that yields a steady state [16]. This steady state has been shown to evolve in a dominant ± 35 pattern for a standard parameter set estimated from literature and simulations [97]. The transitions in filament orientations observed here are therefore not included in the first-order branching model, because the network velocity in steady state is not an accessible external parameter in this model anymore, but rather a fixed constant set by the intrinsic properties of the system. This first-order description is also called *autocatalytic model*, because an increase in force on a growing network in this model temporarily decreases the network velocity and the outgrowth rate. Therefore the filament number in the network increases subsequently until the denser network is able to accommodate the higher external load and the initial steady state value of the protrusion velocity is reestablished. Due to these processes an increase to arbitrarily high filament densities in the network is possible in this model. In reality of course this increase will be limited by some physical process. For very high filament densities excluded volume effects might be the limiting step and could limit efficient filament network growth [98]. However, an increase to arbitrary high filament numbers (or densities) is not part of our model, as the first-order capping rate will limit this process. Therefore for the moderate filament densities active here, our assumption of vanishing steric effects between crossing filaments seems quite reasonable as filaments are still able to cross each other within the limited height of the three dimensional lamellipodium in the migrating cell.

Previous experimental electron microscopy (EM) studies analyzing the orientation distribution of actin filaments in the lamellipodia of different cell lines revealed very distinct peaks at $\pm 35^{\circ}$ in the networks [66, 96, 108]. As shown in this work and also in earlier theoretical studies,

filament branching at an characteristic angle around $70°$ is a compelling explanation for this observed orientation pattern [66, 96, 97, 111]. Additionally to the ± 35 steady state our model predicts transitions to a second $+70/0/-70$ pattern for changing steady state protrusion speed of the network. By now, a clear impact of the network growth velocity on structure has also been observed in experiment using correlated data from live-cell microscopy and EM of the lamellipodium [54]. In course of this thesis we will use a similar experimental setup to test our model predictions more specifically in Ch. 7.

All of the mentioned structural actin network models rely on the dendritic nucleation assumption and especially on filament branching at a characteristic angle to explain experimentally observed network patterns. Very recent experimental results however, extracting actin filament networks from 3D EM tomographs of the lamellipodium, show puzzling characteristics that do not match with the generally applied molecular model of Arp2/3 mediated $70°$ branching. The thorough analysis of three dimensional tomographs suggests that apparent branchpoints in the 2D EM images could be artifacts in projected images after all and that branched filaments do not exist in the network [107]. The observation of unbranched networks is especially surprising as branch formation by Arp2/3 has also been shown in in-vitro studies before [76, 87]. In any case the new perspective of unbranched filament networks in the lamellipodium of migrating cells will fuel the discussion about the precise role of Arp2/3 in the future. Up to now it is a matter of debate why exactly filament branches can not be found in the modern EM images and if there might also be technical difficulties involved in this EM technique or the subsequent analysis of the images.

Apart from modeling network dynamics using Arp2/3 mediated $70°$ branching, also a Brownian ratchet model by Mogilner and Oster predicts an optimum filament orientation that roughly corresponds to the values observed in EM [74]. For a single actin filament protruding against an external force a non-trivial filament orientation at around $\pm 48°$ exists, which yields optimum efficiency in protrusion. This could be an alternative explanation for the experimentally observed network patterns, that is independent of the process of filament branching. However, this model also yields conflicting results compared to different measurements of the force-velocity relation of growing actin networks and is thus not unambiguous either from this point of view. Later in Ch. 5, we will not use the network velocity as the external model parameter anymore, but we will relate the network velocity to external force. As one possibility for the coupling of these two parameters, we will discuss the work by Mogilner and Oster in detail at that point.

Due to the nice agreement of our three different modeling strategies in this chapter (i.e. stochastic network simulations, full continuum model and simplified continuum model), we conclude that our results are realistic and generic for the defined model system according to the key assumptions made in Sec. 3.1. In the two following modeling chapters, we will therefore often focus on results from our continuum description as these calculations can be conducted for a wide range of parameters within a reasonable computation time. We will however support these results by exemplary comparison to stochastic network simulations, which have the advantage to incorporate stochasticity in the branching and capping reactions and also to discretize the individual filaments accordingly.

Chapter 4

Actin network growth in the tail behind small propelled particles

Intracellular actin networks pushing from the inside of the cell against its membrane are essential for cell motility as elaborated in the previous chapter. However, the mechanism for actin polymer growth against an external load is sufficiently generic, such that it is also functional in different contexts. Small intracellular pathogens, amongst others the bacterium *Listeria* [59] and *Vaccinia virus* [30] (cf. Fig. 1.5 on page 6) are exploiting this robustness when they activate actin network growth inside a host cell. The polymerizing actin networks are subsequently pushing and propelling the pathogen through its host, always accompanied by a *tail* of dendritic actin filaments. Ironically, the actin cytoskeleton, which evolved to support the animal cell in its structural functions, supports the effective infection of its own organism in this way [37]. A schematic of this dynamic process is drawn in Fig. 4.1.

In this chapter, we will extend our modeling approach to highlight similarities and differences in the structure of growing actin networks behind small propelled particles compared to actin network growth within the lamellipodium of migrating cells.

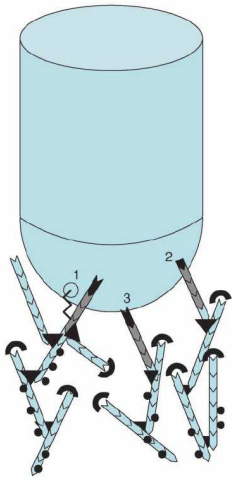

Figure 4.1: Sketch of growing actin filaments pushing against the back of a small propelled particle. Again, growth, branching and capping processes are active in the filament network. Image taken from [71].

4.1 Model definition and key assumptions

Molecular processes and zero-order branching

The molecular basis of actin network growth in cell migration is well preserved over a wide range of different animal cells [89]. Indeed these mechanisms are sufficiently universal that they are exploited by different pathogens in their respective host cells. Therefore, the molecular assumptions and foundations introduced before in Sec. 3.1 will remain unchanged in the following analysis as well. Additionally, we will hold on to our zero-order branching model assumption for the same arguments as before. Here again we assume the activated branching agent Arp2/3 at the leading edge of the network as a limiting factor in network growth. This is a necessary condition to achieve stability of structurally different stationary states for variable network growth velocity v_{nw}.

Geometry

Different from the molecular foundation, which is expected to be relatively well preserved over all biological model systems of interest, there will be a major change in the geometry of the problem already apparent when comparing the two situations in Fig. 3.1(b) and Fig. 4.1. Compared to actin networks growing in the flat and wide domain of the lamellipodium, here we approach a situation in which both lateral dimensions of the network (parallel to the leading edge) as well as the orthogonal length scale of the branching region (perpendicular to the leading edge) are comparable. This means that we had to deal with a fully three dimensional problem in a realistic treatment of this case.

However, in order to keep up the strong analogy to the lamellipodium networks discussed in the previous chapter, we will not treat the full 3D situation at this point. Rather we will highlight the impact of curved particle surfaces with finite lateral width at the leading edge of the network to network structure. This leads to an interesting model system with new effects in comparison to the previous lamellipodium situation. In this way, we also avoid additional assumptions for the azimuth angle distribution of the 3D branch, that had to be incorporated in a full 3D model, although quantitative measurements for this distribution are not available so far.

Although, we restrict ourselves to a two dimensional model system in the following, we still need to consider the 2D size and shape of the propelled particle. As some of the propelled pathogens have a lateral dimension that is comparable to the width of the branching region close to the particle surface (eg. the diameter of *Vaccinia Virus* is of the order of a hundred nanometers [24]), laterally periodic conditions of the simulation box do not seem appropriate at this point anymore. Filaments are now able to leave the region of interest not only in the orthogonal direction, but there is a new rate involved for outgrowth to the side of the network. Therefore, we will have to introduce a second length scale in our model, which incorporates the lateral dimension of the propelled particle.

As the particle surface can not be assumed flat anymore on the lateral length scale of the particle diameter, also the surface curvature can not be neglected anymore. We will study a parabolic particle surface as a generic shape at the end of this section. Although small particles in the biological context most often show a convex shape, we will also discuss concave surfaces, that resemble more the lamellipodium shape.

Summarizing these considerations, we end up with a simulation box according to a given lateral width (without periodic conditions), a constant orthogonal width of the branching region and a curved obstacle at the top. A snapshot of a network growing in such a geometry is shown in Fig. 4.2. Note that the width of the branching region $d_{\mathrm{br}}^{=}$ is given parallel to the upper and

lower boundaries of the rectangular simulation box and not with respect to the local obstacle tangent.

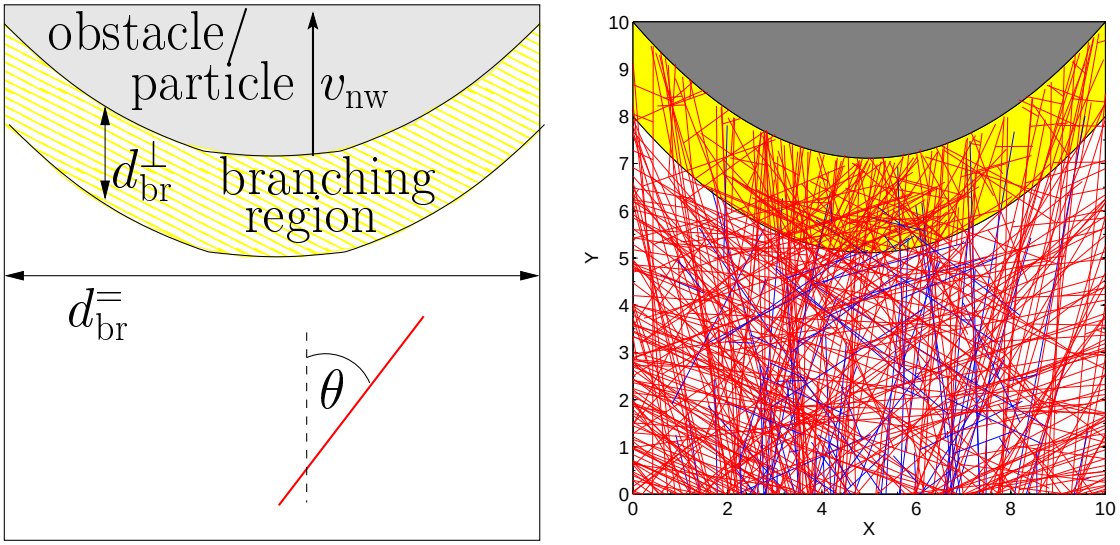

(a) (b)

Figure 4.2: Sketch (a) and simulation snapshot (b) of an actin network in the tail of a small propelled particle, with parabolic surface shape. The network is growing in two dimensions with a lateral length scale $d_{\mathrm{br}}^{=}$ giving the width of the box in x-direction and an orthogonal size of the yellow branching region, $d_{\mathrm{br}}^{\perp}$. Capping and branching reactions are assumed to be only active within this yellow region in very close proximity to the leading edge. Red filaments are actively growing at their barbed end, while blue filaments have been capped and will eventually be outgrown by the bulk network and leave the box at the bottom. The growth velocity v_{nw} of the network is set as the external parameter of the network and triggers how many filaments are stalled by the obstacle.

Modeling strategy

We chose a gradual strategy to approach the problem of a parabolic obstacle shape step by step. We will start with a setup that is comparable to the lamellipodium situation, which has been analyzed in detail before. From there, we will change the geometry of the setup step-by-step and analyze the impact on the network structure.

In this spirit, we will start with a flat obstacle shape in Sec. 4.2. However, in contrast to the previous section we will drop the periodic boundary conditions in the lateral direction. The stability of the different stationary states in this setup can still be analytically analyzed with the help of a modified continuum model analytically (similar to Sec. 3.2.2) and also by numerically solving the full modified continuum model. These results will be compared to the steady state conditions from representative stochastic network simulations.

In the subsequent Sec. 4.3, we will approximate a curved leading edge by a piecewise linear obstacle shape. For this approximation, we will numerically solve the full continuum model in the linearized geometry and compare to stochastic simulations for a parabolic (non-linear) particle surface.

4.2 Flat horizontal leading edge shape

In this section we will develop some insight into the impact of the lateral boundary conditions on the network structure. Compared to the lamellipodium networks discussed in Ch. 3, only these lateral boundaries at the left and right side of the simulation box will be changed from periodic to absorbing at this point. Here absorbing means that similar conditions apply at the side of the network as have already been active at the lower boundary before. Filaments that grow out of the network on either of these sides (i.e. left, right or bottom) are assumed to leave the region close to the particle surface and get depolymerized at some point.

4.2.1 Continuum model and phase diagram

To adopt the continuum theory introduced in Sec. 3.1.2 to the new boundary conditions, we have to explicitly include a second outgrowth rate in the lateral direction. Like for the lamellipodium analysis before, here we again assume a hypothetical experimental setup in which the network growth velocity is an external parameter, that can be manipulated and set to a specific value. Incorporating a second length scale $d_{\mathrm{br}}^{=}$ for the lateral diameter of the network (or propelled particle) in the model, we can formulate an expression for the lateral outgrowth rate of filaments to either of the two sides of the network,

$$k_{\mathrm{gr}}^{=}(\theta, v_{\mathrm{nw}}) = \begin{cases} \frac{v_{\mathrm{nw}} \tan\theta}{(d_{\mathrm{br}}^{=}/2)} & \text{if } |\theta| \leq \theta_{\mathrm{c}} \\ \frac{v_{\mathrm{fil}} \sin\theta}{(d_{\mathrm{br}}^{=}/2)} & \text{if } |\theta| > \theta_{\mathrm{c}} \end{cases} \text{, with } \theta_{\mathrm{c}} = \arccos(v_{\mathrm{nw}}/v_{\mathrm{fil}}) \,, \tag{4.1}$$

thus complementing the orthogonal outgrowth rate from Eq. (3.5). Here, the outgrowth rate again is given as the ratio of projected filament growth velocity in the lateral direction $v_{\mathrm{fil}} \sin\theta$ and the lateral length scale $d_{\mathrm{br}}^{=}$. As before, filaments are assumed to nucleate in the middle of the branching region, and therefore only half of this width is taken into account. The term $v_{\mathrm{nw}} \tan\theta$ emerges for filaments with orientations $|\theta| \leq \theta_{\mathrm{c}}$, that would grow faster than the obstacle in orthogonal direction. Such filaments are assumed to be blocked and stalled by the propelled particle and only grow with the velocity of the obstacle v_{nw} in the orthogonal direction. The polymerization velocity v_{fil} of those blocked filaments is thus given by $v_{\mathrm{nw}}/\cos\theta$. The sign of the rate $k_{\mathrm{gr}}^{=}$ determines, if filaments are growing out to the left or right side. At this point, we have a left-right symmetry in the system according to a flat leading edge and absorbing boundaries on either side. We can thus neglect the sign and just use the absolute value of the outgrowth rate in the equations. However, in the continuum model that will be discussed in Sec. 4.3 the left-right symmetry will be broken by a skewed obstacle surface and subsequently the sign of the rate will become important again.

Analytical phase diagram from linear stability analysis

For the same reasons as discussed in Sec. 3.2.2, it is possible to simplify the continuum model again and end up with five coupled differential equation, similar to equations (3.7)–(3.11) on page 35. The only difference that adjusts the change in boundary conditions here is that we now need to include also the lateral outgrowth rate explicitly. Therefore, an absolute outgrowth rate $k_{\mathrm{gr}}(\theta) = k_{\mathrm{gr}}^{\perp}(\theta) + k_{\mathrm{gr}}^{=}(\theta)$ replaces the exclusively orthogonal outgrowth $k_{\mathrm{gr}}^{\perp}(\theta)$ in the previous

equations,

$$\frac{\partial N_{-70^\circ}}{\partial t} = \frac{1}{2}\hat{k}_\mathrm{b} N_{0^\circ} - (k_\mathrm{c} + k_\mathrm{gr}(70^\circ))\, N_{-70^\circ} \tag{4.2}$$

$$\frac{\partial N_{-35^\circ}}{\partial t} = \frac{1}{2}\hat{k}_\mathrm{b} N_{+35^\circ} - (k_\mathrm{c} + k_\mathrm{gr}(35^\circ))\, N_{-35^\circ} \tag{4.3}$$

$$\frac{\partial N_{0^\circ}}{\partial t} = \frac{1}{2}\hat{k}_\mathrm{b}\,(N_{-70^\circ} + N_{+70^\circ}) - k_\mathrm{c} N_{0^\circ} \tag{4.4}$$

$$\frac{\partial N_{+35^\circ}}{\partial t} = \frac{1}{2}\hat{k}_\mathrm{b} N_{-35^\circ} - (k_\mathrm{c} + k_\mathrm{gr}(35^\circ))\, N_{+35^\circ} \tag{4.5}$$

$$\frac{\partial N_{+70^\circ}}{\partial t} = \frac{1}{2}\hat{k}_\mathrm{b} N_{0^\circ} - (k_\mathrm{c} + k_\mathrm{gr}(70^\circ))\, N_{+70^\circ}\,. \tag{4.6}$$

For filaments growing in the N_{0° angle bin both outgrowth rates vanish, because these filaments are growing at $v_\mathrm{fil} = 1 \geq v_\mathrm{nw}$ parallel to the lateral boundaries of the network.

Apart from the change in outgrowth rates, the structure of the equations stays the same. Therefore, also the two physically meaningful stationary states remain unchanged as given in Eq. (3.12) and Eq. (3.13) for the ± 35 and $+70/0/-70$ pattern respectively. Then, the same arguments as used before also apply for the stability analysis of the steady states. Hence, we can use Eq. (3.19) as a starting point and evaluate the stability of the two steady states according to the adjusted outgrowth rates.

For convenience, we write down the original equation (3.19) again,

$$k_\mathrm{c} k_\mathrm{gr}(70^\circ) = k_\mathrm{c}^2 + 4k_\mathrm{c} k_\mathrm{gr}(35^\circ) + 2k_\mathrm{gr}^2(35^\circ)\,. \tag{4.7}$$

The parameter values for which this equation is exactly fulfilled defines the transitions in the orientation distribution of the growing network. To determine the transitions, we will follow a very similar strategy as before in Sec. 3.2.2. Starting from small network velocities v_nw, we will treat the different possibilities for the outgrowth rates given in equations (3.5) and (4.1) in a case-by-case analysis.

For $\theta_\mathrm{c} \geq 70^\circ$, the orthogonal outgrowth rates vanish as all relevant filament orientations grow faster towards the top than the obstacle and then are slowed down to v_nw in this direction. The outgrowth rates for the different orientation bins therefore read,

$$k_\mathrm{gr}^\perp(\theta) = 0 \text{ and } k_\mathrm{gr}^=(\theta) = \frac{v_\mathrm{nw}\tan\theta}{(d_\mathrm{br}^=/2)} \text{ for } \theta = [35^\circ, 70^\circ]\,. \tag{4.8}$$

Inserting $k_\mathrm{gr} = k_\mathrm{gr}^\perp + k_\mathrm{gr}^=$ in Eq. (4.7) and omitting again the ill-defined cases of $k_\mathrm{b} = 0$, $k_\mathrm{c} = 0$ and $d_\mathrm{br}^= = 0$ here (and additionally $d_\mathrm{br}^\perp = 0$ in the following), it can be shown that the relation (4.7) is never exactly fulfilled.

Increasing the network velocity to the point where $35^\circ \leq \theta_\mathrm{c} < 70^\circ$ leads to the outgrowth rates,

$$k_\mathrm{gr}^\perp(35^\circ) = 0 \text{ and } k_\mathrm{gr}^\perp(70^\circ) = \frac{v_\mathrm{nw} - v_\mathrm{fil}\cos(70^\circ)}{(d_\mathrm{br}^\perp/2)}\,, \tag{4.9}$$

in orthogonal direction according to Eq. (3.5) and,

$$k_\mathrm{gr}^=(35^\circ) = \frac{v_\mathrm{nw}\tan(35^\circ)}{(d_\mathrm{br}^=/2)} \text{ and } k_\mathrm{gr}^=(70^\circ) = \frac{v_\mathrm{fil}\sin(70^\circ)}{(d_\mathrm{br}^=/2)}\,, \tag{4.10}$$

in the lateral direction according to Eq. (4.1). These rates yield a quadratic equation for the

network velocities v_{nw} that satisfy Eq. (4.7),

$$\begin{aligned} 0 &= v_{\mathrm{nw}}^2 \left[8 \tan^2(35^\circ) \tfrac{1}{{k_{\mathrm{c}}}^2 {d_{\mathrm{br}}^{=}}^2} \right] + v_{\mathrm{nw}} \left[8 \tan(35^\circ) \tfrac{1}{k_{\mathrm{c}} d_{\mathrm{br}}^{=}} - 2 \tfrac{1}{k_{\mathrm{c}} d_{\mathrm{br}}^{\perp}} \right] \\ &\quad + \left[1 - 2 v_{\mathrm{fil}} \sin(70^\circ) \tfrac{1}{k_{\mathrm{c}} d_{\mathrm{br}}^{=}} + 2 v_{\mathrm{fil}} \cos(70^\circ) \tfrac{1}{k_{\mathrm{c}} d_{\mathrm{br}}^{\perp}} \right] , \\ &\quad \text{for } 35^\circ \leq \theta_{\mathrm{c}} < 70^\circ . \end{aligned} \tag{4.11}$$

Reconsidering Sec. 3.2.2, we can again identify a reduced set of effective parameters at this point that determines stability. Here, the generalized velocity parameter $u_{\mathrm{c}} = k_{\mathrm{c}} d_{\mathrm{br}}^{\perp}$ as defined in Eq. (3.23) can be found again, together with a new parameter for the length scale ratio in lateral and orthogonal direction,

$$r_{\mathrm{br}} := \frac{d_{\mathrm{br}}^{=}}{d_{\mathrm{br}}^{\perp}} . \tag{4.12}$$

Reformulated in these effective parameters, Eq. (4.11) reads,

$$\begin{aligned} 0 &= v_{\mathrm{nw}}^2 \left[8 \tan^2(35^\circ) \tfrac{1}{{u_{\mathrm{c}}}^2 {r_{\mathrm{br}}}^2} \right] + v_{\mathrm{nw}} \left[8 \tan(35^\circ) \tfrac{1}{u_{\mathrm{c}} r_{\mathrm{br}}} - 2 \tfrac{1}{u_{\mathrm{c}}} \right] \\ &\quad + \left[1 - 2 v_{\mathrm{fil}} \sin(70^\circ) \tfrac{1}{u_{\mathrm{c}} r_{\mathrm{br}}} + 2 v_{\mathrm{fil}} \cos(70^\circ) \tfrac{1}{u_{\mathrm{c}}} \right] , \\ &\quad \text{for } 35^\circ \leq \theta_{\mathrm{c}} < 70^\circ . \end{aligned} \tag{4.13}$$

To complete the stability analysis, we will now treat the remaining possibility of a critical angle, $\theta_{\mathrm{c}} < 35^\circ$. In this case the adjusted outgrowth rates read,

$$k_{\mathrm{gr}}^{\perp}(\theta) = \frac{v_{\mathrm{nw}} - v_{\mathrm{fil}} \cos\theta}{(d_{\mathrm{br}}^{\perp}/2)} \text{ and } k_{\mathrm{gr}}^{=}(\theta) = \frac{v_{\mathrm{fil}} \sin\theta}{(d_{\mathrm{br}}^{=}/2)} \text{ for } \theta = [35^\circ, 70^\circ] . \tag{4.14}$$

These rates together with Eq. (4.7) and our effective parameters u_{c} and r_{br} can be simplified to a second quadratic equation for the network velocities at the transitions,

$$\begin{aligned} 0 &= v_{\mathrm{nw}}^2 \left[8 \tfrac{1}{u_{\mathrm{c}}^2} \right] + v_{\mathrm{nw}} \left[6 \tfrac{1}{u_{\mathrm{c}}} - 16 v_{\mathrm{fil}} \cos(35^\circ) \tfrac{1}{u_{\mathrm{c}}^2} + 16 v_{\mathrm{fil}} \sin(35^\circ) \tfrac{1}{u_{\mathrm{c}}^2 r_{\mathrm{br}}} \right] \\ &\quad + \Big[1 + 2 v_{\mathrm{fil}} \cos(70^\circ) \tfrac{1}{u_{\mathrm{c}}} - 2 v_{\mathrm{fil}} \sin(70^\circ) \tfrac{1}{u_{\mathrm{c}} r_{\mathrm{br}}} - 8 v_{\mathrm{fil}} \cos(35^\circ) \tfrac{1}{u_{\mathrm{c}}} + 8 v_{\mathrm{fil}} \sin(35^\circ) \tfrac{1}{u_{\mathrm{c}} r_{\mathrm{br}}} \\ &\qquad + 8 v_{\mathrm{fil}}^2 \cos^2(35^\circ) \tfrac{1}{u_{\mathrm{c}}^2} - 16 v_{\mathrm{fil}}^2 \cos(35^\circ) \sin(35^\circ) \tfrac{1}{u_{\mathrm{c}}^2 r_{\mathrm{br}}} + 8 v_{\mathrm{fil}}^2 \sin^2(35^\circ) \tfrac{1}{u_{\mathrm{c}}^2 r_{\mathrm{br}}^2} \Big] , \\ &\quad \text{for } \theta_{\mathrm{c}} < 35^\circ . \end{aligned} \tag{4.15}$$

According to Eq. (4.13) and Eq. (4.15) we can now again draw the regions of stability for the two different stationary orientation patterns in parameter space. Here, however we have introduced a new and independent parameter, which makes the full phase diagram three dimensional. To keep the following results as accessible as possible, we will again refer to the network velocity v_{nw} together with the capping rate k_{c} (rather than the generalized velocity u_{c}) as model parameters. We will incorporate the length scale ratio r_{br} (Eq. (4.12)) as the third dimension that influences stability. Network growth velocities v_{nw} that fulfill Eq. (4.13) together with the condition $v_{\mathrm{fil}} \cos(35^\circ) \geq v_{\mathrm{nw}} > v_{\mathrm{fil}} \cos(70^\circ)$ or Eq. (4.15) at $v_{\mathrm{nw}} > v_{\mathrm{fil}} \cos(35^\circ)$ are identified as transition points between the different orientation distributions in the three dimensional parameter space spanned by k_{c}, r_{br} and v_{nw} in Fig. 4.3(a). In the limit of large length scale ratios, $r_{\mathrm{br}} \gg 1$, the lateral outgrowth rate can be neglected and the phase diagram approaches the lamellipodium conditions similar to Fig. 3.11(a) on page 42. For relatively small $r_{\mathrm{br}} \lesssim 7$ the lateral outgrowth of intermediate filament orientations at around $\pm 35^\circ$ is so large, that this orientation pattern is not stable anymore independent of the growth velocity (cf. Fig. 4.3(b)).

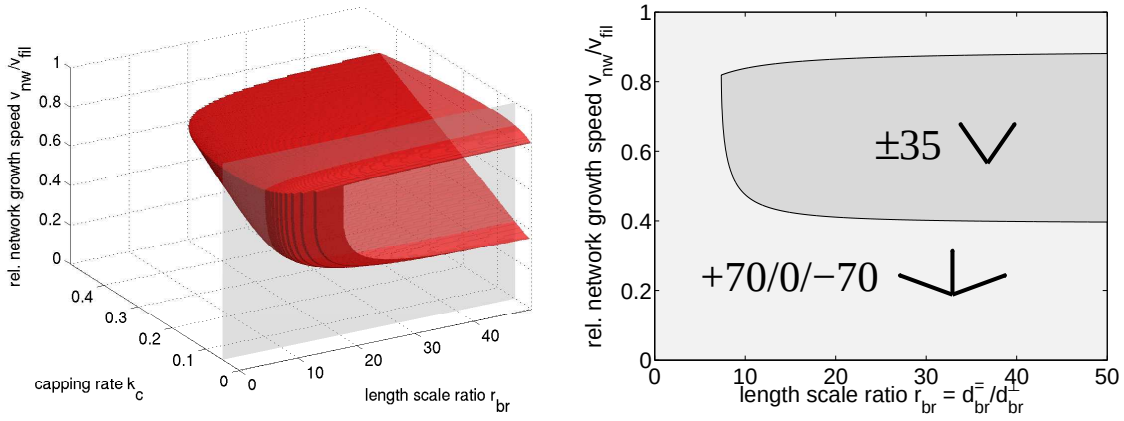

(a) (b)

Figure 4.3: Analytical phase diagrams from linear stability analysis. (a) Hypersurface of transitions (red) in the three dimensional parameter space spanned by the network velocity v_{nw}, the capping rate k_{c} and the length scale ratio r_{br}. (b) 2D slice through the 3D hypersurface along the transparent gray plane in (a) at $k_{\mathrm{c}} = 0.05$. A dominant ± 35 structure can be found at intermediate velocity and intermediate to large length scale ratio. In the limit of large $r_{\mathrm{br}} \gg 1$, the situation approaches actin networks growing in the lamellipodium, i.e. periodic lateral boundaries. For too small r_{br}, the lateral outgrowth of filaments oriented at $\pm 35^{\circ}$ dominates and the $+70/0/-70$ pattern is favored for all possible values of v_{nw}.

Numerical solution of the full continuum model

To compare and test the analytical results against the full continuum model, we have solved the full model equation (3.1) numerically in 360 coupled angle bins. For the correct treatment of filaments growing out towards the sides of the network, the outgrowth rate has been adjusted in these equations as already discussed above and explicitly shown in Eq. (4.1). The 3D parameter space is sampled by reducing the network velocity v_{nw} quasistatically from v_{fil} to 0 for various sets of parameters k_{c} and r_{br}. By calculating the order parameter $\mathcal{O}$ (as defined in Eq. (3.29)) for each steady state condition orientation transitions are identified at those points in parameter space where $\mathcal{O}$ changes its sign. Hence, in three dimensions the isosurface $\mathcal{O}(v_{\mathrm{nw}}, k_{\mathrm{c}}, r_{\mathrm{br}}) = 0$ is extracted from the three dimensional data.

Fig. 4.4 shows the resulting phase diagram obtained from this numerical procedure. The results from the numerical continuum approach coincide very well with our previous analytical findings for the simplified version (Fig. 4.3). As discussed in detail before in Sec. 3.2.3, a major difference in the two methods is observed for larger capping rate k_{c}, where the ± 35 steady state vanishes in the simplified framework. Apart from this discrepancy the similarity is satisfying. Again, in the limit of large length scale ratio $r_{\mathrm{br}} \gg 1$, similar results compared to the periodic boundary conditions before are obtained as we would expect (cf. Fig. 3.11(b)). The prediction from the analytical analysis, namely that for small values of r_{br} the ± 35 pattern is not dominant at intermediate velocities, is also confirmed in the numerical results.

4.2.2 Comparison to stochastic network simulations

Compared to the stochastic network simulations described in Sec. 3.1.1, the only change in the algorithm to adopt network growth to the new conditions at this point is a change in the lateral boundary conditions of the simulation box. The horizontal boundaries of the box can now be understood as absorbing rather than periodic, i.e. filaments growing out to the side of the box

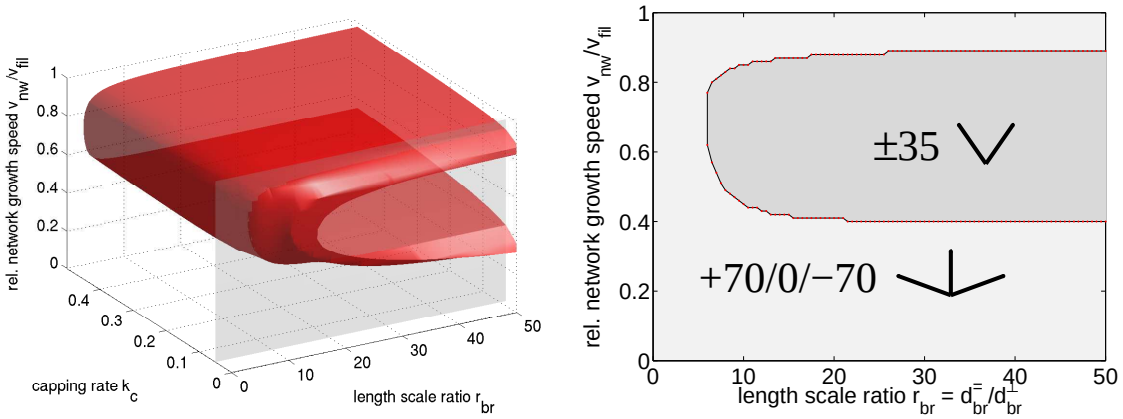

(a) (b)

Figure 4.4: Phase diagram from the numerical iteration of Eq. (3.1) in time for $k_\mathrm{b} = 20$. (a) Three dimensional parameter space representation. The red hypersurface corresponds to parameter conditions for which the order parameter $\mathcal{O}$ (Eq. (3.29)) changes its sign. The transparent plane marks again the slice of the 3D plot at $k_\mathrm{c} = 0.05$, which is shown in (b) in two dimensions. For the 2D plot also the discrete positions in parameter space at which transitions in the order parameter have been sampled are shown as red dots. The diagrams coincide very well with results obtained from the simplified continuum model in Fig. 4.3.

will not be regarded anymore afterwards, very similar to the ones that leave the simulation box at the bottom. In this way a new filament orientation dependent lateral outgrowth process is introduced in simulations and alters network structure in the stationary state.

Fig. 4.5 shows two exemplary results of filament orientation distributions found in steady state in stochastic network simulations, the full continuum model and the simplified continuum framework according to only five different angle bins between $-90°$ and $+90°$. The parameter sets of the two cases shown here in (a) and (b) do not differ in their network velocity v_nw, but rather in our new model parameter, the length scale ratio $r_\mathrm{br} = d_\mathrm{br}^{=}/d_\mathrm{br}^{\perp}$, which becomes important in the model as soon as the lateral length scale is comparable to the orthogonal dimension of the branching region. It is evident, that for small $r_\mathrm{br} = 3$ also at intermediate velocities the ± 35 pattern of the network is not stable anymore and rather the network organizes in the alternative $+70/0/-70$ structure (cf. Fig. 4.5(a)). This behavior has been predicted by our continuum theory and states the major difference so far when comparing actin networks in the tail behind small propelled particles to those growing in the lamellipodium of a moving cell. For larger ratio $r_\mathrm{br} = 20$, this discrepancy is diminished and the network organizes in the ± 35 degree dominated distribution as found in the previous section (cf. Fig. 4.5(b)). Comparing the results from our different approaches the similarity is very satisfying, despite the fact that the outgrowth rate of filaments is not incorporated explicitly in stochastic simulations, but is rather a result of the finite simulation box and their particular boundary conditions.

4.3 Curved leading edge shape

At this point we have understood what impact a finite lateral length scale of the branching region (i.e. the obstacle) has on the network architecture of growing actin networks. In this section we will approach the more important condition of curved leading edge shape. In stochastic network simulations with arbitrary obstacle shape, the lateral outgrowth of filaments emerges by the interplay of single filament growth and obstacle movement and geometry. However, in order to

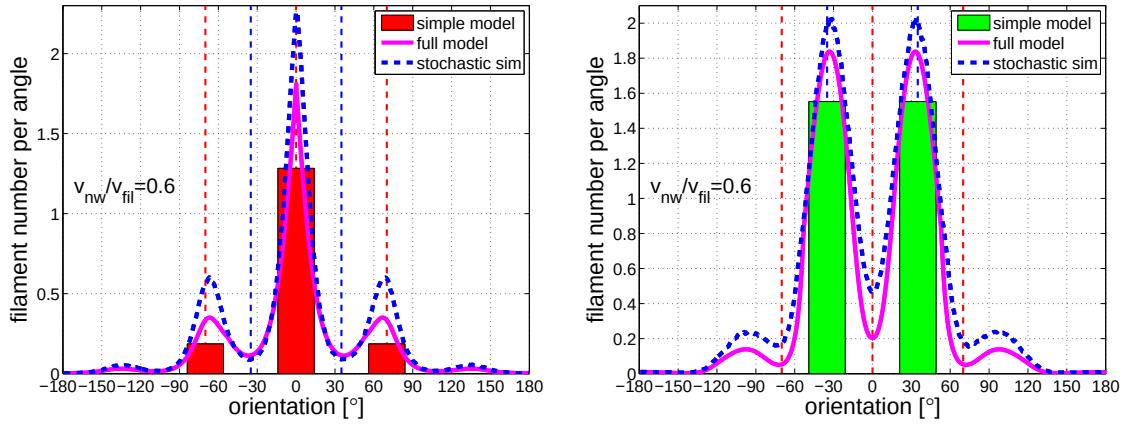

Figure 4.5: Comparison of the steady state distributions for networks growing in a domain with flat leading edge and laterally absorbing boundaries at $v_{\mathrm{nw}}/v_{\mathrm{fil}} = 0.6$, $k_{\mathrm{b}} = 20$, $k_{\mathrm{c}} = 0.05$, (a) $r_{\mathrm{br}} = 3$, (b) $r_{\mathrm{br}} = 20$; The results were obtained according to three different methods, the simplified continuum model (bars), the full continuum model (magenta line) and stochastic simulations (dashed blue).

map these simulations to the continuum description again, we have to find a way to express the outgrowth rates explicitly as mathematical expressions. Especially for the lateral rate this task is not trivial for curved obstacle surface. Therefore in the following we will first introduce a piecewise linear leading edge approximation to approach this problem. It will turn out that within this approximate framework, it is indeed possible to treat a wide spectrum of particle surface shapes in a modified continuum framework and compare the results to stochastic network simulations for specific examples.

4.3.1 Piecewise-linear leading edge approximation

Finding explicit expressions for the lateral outgrowth rate of filaments is in general very hard for curved obstacle shape. However, we can always try to approximate the obstacle shape by a continuous piecewise-linear leading edge. The construction of this approximation is sketched in Fig. 4.6 for a parabola-like obstacle surface.

In the first step the branching region is separated in n lateral sections of size $d^{=}_{\mathrm{br},i}$ ($i = 1,\ldots,n$). Subsequently the nonlinear curvature shape in each section is approximated by a linear shape connecting the obstacle positions at the left and right boundary of the individual lateral section. In this way we end up with a combination of lateral sections with linear but skewed (i.e. non-flat) obstacle shape according to a skew angle φ_i and lateral dimension $d^{=}_{\mathrm{br},i}$. The orthogonal width of the branching region $d^{\perp}_{\mathrm{br}}$ remains unchanged. The individual sections are coupled to their direct neighbors via the lateral outgrowth rates $k^{=}_{\mathrm{gr},i}$ to the left and the right. For $i = 1$ and $i = n$ the outgrowth rate to the left and the right respectively is not coupled to any other lateral neighbor but rather annihilates filaments in the system.

What is left is to formulate a continuum model, that is able to cope with linear skewed leading edge shape and formulate exact expressions for the left and right lateral outgrowth rates in this model. Subsequently, we can approximate arbitrary surface shape as a coupled combination of such continuum descriptions. For ever smaller $d^{=}_{\mathrm{br},i}$, i.e. ever more fine-grained lateral obstacle slices, this method will lead to more and more accurate results compared to stochastic network simulations for the real (curved) surface shape. However, as we will demonstrate at the end of

this section, already a very coarse-grained description is able to predict the stochastic network results quite accurately with comparatively low computational effort.

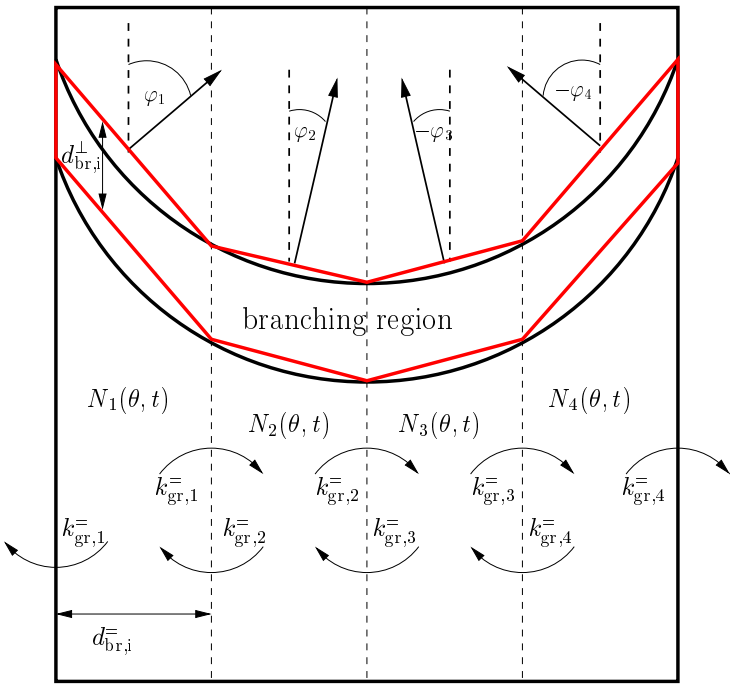

Figure 4.6: Sketch of the piecewise-linear leading edge approximation for arbitrary curvature. Curved particle surfaces (black) can be approximated by individual filament populations in adjacent domains with constant skew angle φ_i of the obstacle (red). In this way the curved shape of the branching zone is approximated by a combination of parallelograms. The different domains are coupled via the lateral outgrowth of filaments. In this way, almost arbitrary surface shapes can be translated into the continuum model framework. If the propelled particle surface holds an additional left-right symmetry (like a parabola does), it is sufficient to solve only for one side of the coupled systems with appropriate lateral boundary conditions in the middle of the simulation box.

Skewed linear leading edge

The problem of finding an explicit expression for the lateral outgrowth rate out of the branching region close to a single and isolated linear obstacle with arbitrary but constant skew angle $\varphi =]-90°, 90°[$, finds a rather easy solution in a particular coordinate frame that is adjusted to the obstacle skew. Fig. 4.7(a) shows a sketch of the model system we are interested in at this point. The branching region in the simulation box is given by a parallelogram, with rotated (or skewed) upper and lower side. The orthogonal width of the branching region $d^{\perp}_{\mathrm{br}}$ is given parallel to the lateral sides of the simulation box, while the lateral space scale $d^{=}_{\mathrm{br}}$ is defined as the horizontal width of the box. Our external parameter, the network velocity v_{nw} is defined as before in vertical direction. In this coordinate frame it is not trivial to find an explicit expression for the rates of lateral filament outgrowth to the left and right side of the simulation box. However, a simple rotation of coordinate frame to the point where the skew angle φ of the branching region vanishes, simplifies the situation effectively (Fig. 4.7(b)). In this frame the obstacle geometry appears flat horizontal, very similar to the setup analyzed in Sec. 4.2. The main difference here is that we have to deal with a new non-vanishing lateral network growth velocity $\tilde{v}^{=}_{\mathrm{nw}}$ in the model. (Where applicable, we will denote variables in the rotated coordinate frame by $\tilde{}$.) This velocity component incorporates the effect of a finite obstacle skew angle φ

in this frame and can be deduced from a separation of the initial network velocity vector v_{nw} in its orthogonal $\tilde{v}_{\mathrm{nw}}^{\perp}$ and lateral $\tilde{v}_{\mathrm{nw}}^{=}$ component, perpendicular and tangential to the obstacle surface respectively. In the following we will refer to the original coordinate system Fig. 4.7(a) as the (simulation) box frame and to the rotated picture Fig. 4.7(b) as the obstacle frame.

Using the definition of our obstacle frame for a given skew angle φ, we can now deduce the relevant parameters in this frame. First of all the filament orientation angles $\tilde{\theta}$ are given relative to the obstacle here, i.e. $\tilde{\theta} = 0^{\circ}$ describes filaments growing perpendicular to the upper or lower boundaries of the obstacle. The separation of the network growth velocity is given by,

$$\tilde{v}_{\mathrm{nw}}^{\perp} = v_{\mathrm{nw}} \cos\varphi \text{ and } \tilde{v}_{\mathrm{nw}}^{=} = v_{\mathrm{nw}} \sin\varphi \,. \tag{4.16}$$

The spatial dimensions, scaling the two independent outgrowth rates, have to be adjusted as,

$$\tilde{d}_{\mathrm{br}}^{\perp} = d_{\mathrm{br}}^{\perp} \cos\varphi \text{ and } \tilde{d}_{\mathrm{br}}^{=} = \frac{d_{\mathrm{br}}^{=}}{\cos\varphi} \,, \tag{4.17}$$

in the box frame. According to these definitions, we can now reformulate the continuum description in the box frame. The central equation (3.1) for the temporal evolution of orientation dependent filament number remains unchanged according to the new orientation angles $\tilde{\theta}$ in this coordinate system,

$$\frac{\partial N(\tilde{\theta},t)}{\partial t} = \hat{k}_{\mathrm{b}} \int_{-180^{\circ}}^{+180^{\circ}} \mathcal{W}(\tilde{\theta},\theta') N(\theta',t)\, \mathrm{d}\theta' - k_{\mathrm{c}} N(\tilde{\theta},t) - \tilde{k}_{\mathrm{gr}}^{\perp}(\tilde{\theta},\tilde{v}_{\mathrm{nw}}^{\perp}) N(\tilde{\theta},t) - |\tilde{k}_{\mathrm{gr}}^{=}(\tilde{\theta},\tilde{v}_{\mathrm{nw}}^{=})| N(\tilde{\theta},t) \,, \tag{4.18}$$

with orthogonal outgrowth rate,

$$\tilde{k}_{\mathrm{gr}}^{\perp}(\tilde{\theta},\tilde{v}_{\mathrm{nw}}^{\perp}) = \begin{cases} 0 & \text{if } |\tilde{\theta}| \le \tilde{\theta}_{\mathrm{c}} \\ \frac{\tilde{v}_{\mathrm{nw}}^{\perp} - v_{\mathrm{fil}} \cos\tilde{\theta}}{(\tilde{d}_{\mathrm{br}}^{\perp}/2)} & \text{if } |\tilde{\theta}| > \tilde{\theta}_{\mathrm{c}} \end{cases} , \tag{4.19}$$

and lateral outgrowth rate,

$$\tilde{k}_{\mathrm{gr}}^{=}(\tilde{\theta},\tilde{v}_{\mathrm{nw}}^{=}) = \begin{cases} \frac{\tilde{v}_{\mathrm{nw}}^{=} + \tilde{v}_{\mathrm{nw}}^{\perp} \tan\tilde{\theta}}{(\tilde{d}_{\mathrm{br}}^{=}/2)} & \text{if } |\tilde{\theta}| \le \tilde{\theta}_{\mathrm{c}} \\ \frac{\tilde{v}_{\mathrm{nw}}^{=} + v_{\mathrm{fil}} \sin\tilde{\theta}}{(\tilde{d}_{\mathrm{br}}^{=}/2)} & \text{if } |\tilde{\theta}| > \tilde{\theta}_{\mathrm{c}} \end{cases} . \tag{4.20}$$

Here the lateral outgrowth rate compared to Eq. (4.1) is biased by the finite lateral velocity of the growing region in the obstacle frame $\tilde{v}_{\mathrm{nw}}^{=}$. This feature also breaks the left-right symmetry in the resulting filament orientation distribution. The sign of the outgrowth rate determines, whether filaments are growing out to the left ($\tilde{k}_{\mathrm{gr}}^{=} < 0$) or the right ($\tilde{k}_{\mathrm{gr}}^{=} > 0$) of the branching region, which becomes important when combining this approach with the piecewise-linear approximation that was introduced before. Capping and branching rates as well as the filament polymerization velocity v_{fil} remain unchanged by this coordinate change.

It can be seen from Fig. 4.7(b), that the deduced outgrowth rates are not exact but rather only approximations. For the derivation of the rates, we had to assume a rectangular shape of the branching region in the obstacle frame. This however is not the case due to our definition of the branching region as illustrated in the sketch. Therefore, the continuum outgrowth rates will deviate from the rates observed in stochastic network simulations. However for reasonably small skew angle φ and orthogonal branching region width $d_{\mathrm{br}}^{\perp}$, our approximation seems justified. Indeed the introduced error will not alter the results significantly as shown below.

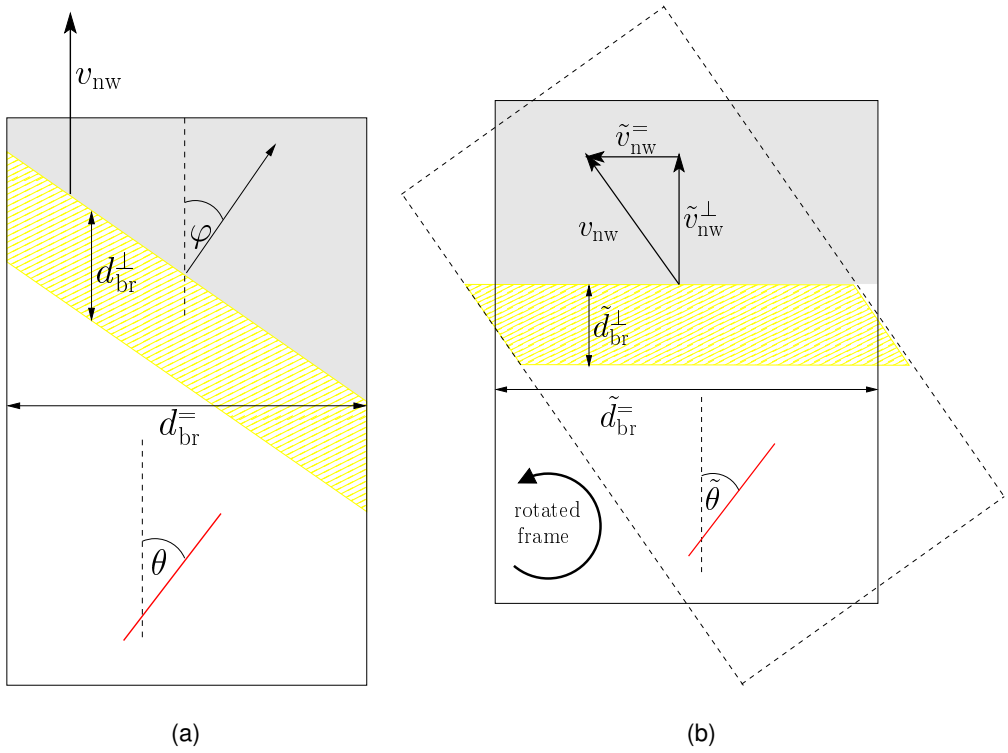

Figure 4.7: Within an adjusted (rotated) frame, a modified continuum model is still applicable to solve the skewed leading edge problem. (a) *Box or lab frame*: A generic skewed linear obstacle with skew angle $|\varphi| < 90^\circ$ within the simulation box in which the actin network can grow. The obstacle's velocity in the vertical direction is given by v_{nw} in this coordinate frame. The orthogonal and lateral dimensions of the branching region are given by $d_{\mathrm{br}}^{\perp}$ and $d_{\mathrm{br}}^{=}$ respectively. (b) *Obstacle frame*: The whole simulation box is rotated by an angle φ counter-clockwise. This simplifies the system for applying the continuum model, because in this framework a flat obstacle moves by an orthogonal velocity $\tilde{v}_{\mathrm{nw}}^{\perp}$ in the vertical direction. The initial skew of the system is now implicitly expressed as an additional finite lateral motion of the leading edge with a velocity $\tilde{v}_{\mathrm{nw}}^{=}$. This velocity biases the lateral outgrowth rates in the continuum model discussed above and breaks the left-right symmetry with respect to filament orientation. This change in coordinate frame will also be very illustrative, when interpreting steady state orientation distributions obtained from stochastic network simulations according to skewed or curved obstacle shape.

We applied the new modified version of our continuum model to obstacle surfaces with two different skew angles $\varphi = 30^\circ$ and $\varphi = 60^\circ$ using the full numerical rate equation approach with 360 angle bins. As we are only concerned with a single linear skewed obstacle with filament annihilating boundaries at both lateral sides of the branching region, the resulting filament distributions for φ and $-\varphi$ are symmetric but flipped (i.e. $\theta \leftrightarrow -\theta$) and we will only regard positive skew angles. Fig. 4.8 and Fig. 4.9 show three dimensional subspaces of the four dimensional phase diagram (now including also the skew angle φ) according to the same parameter sets as used before, but for $\varphi = 30^\circ$ and $\varphi = 60^\circ$ rather than $\varphi = 0^\circ$. Here, the order parameter $\mathcal{O}$ is determined as defined before in Eq. (3.29), but now within the obstacle frame rather than the box system. Additionally, we take the mean of the two bins $\tilde{\theta} = +35^\circ$ and $\tilde{\theta} = -35^\circ$ in this formula as a value for N_{35°, because the left-right symmetry of the orientation distribution does not exist in this case. The network growth velocity that is altered in these simulations is the orthogonal network velocity in the obstacle coordinate system $\tilde{v}_{\mathrm{nw}}^{\perp}$, which is equal to v_{nw} in the case of $\varphi = 0^\circ$, i.e. a non-skewed linear obstacle surface. Again, on the right hand side of each figure in (b) a 2D slice through the 3D hypersurface of orientation pattern transitions is shown for $k_{\mathrm{c}} = 0.05$.

We find that for $\varphi = 30°$ the situation changes completely compared to the $\varphi = 0°$ case. Here, the ± 35 pattern dominates the network for small length scale ratio $r_{\mathrm{br}} = d_{\mathrm{br}}^{=}/d_{\mathrm{br}}^{\perp}$ and all possible orthogonal network growth velocities $\tilde{v}_{\mathrm{nw}}^{\perp}$. This behavior reflects the important impact of the obstacle skew angle to the lateral outgrowth rate and subsequently the orientation distribution in steady state. For $\varphi = 60°$ the situation slightly changes again and we find the typical three different growth regimes for fast, intermediate and slow orthogonal growth velocity.

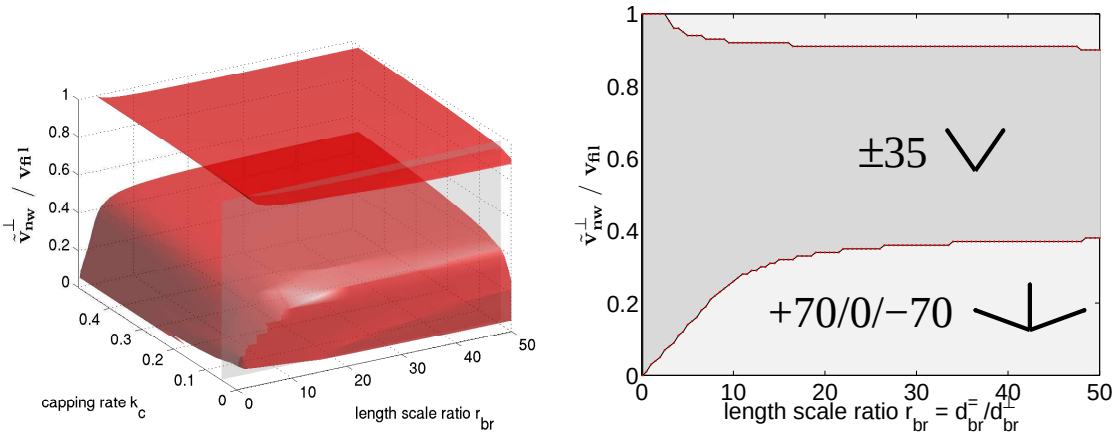

Figure 4.8: Results from the numerical model with 360 angle bins. Subspaces of the four dimensional phase diagram in the parameter space spanned by the capping rate k_{c}, the length scale ratio in the box system $r_{br} = d_{\mathrm{br}}^{=}/d_{\mathrm{br}}^{\perp}$, the orthogonal network growth velocity defined in the obstacle frame $\tilde{v}_{\mathrm{nw}}^{\perp}$ and the newly introduced obstacle skew angle φ. Orientation distributions and the respective order parameter $\mathcal{O}$ were measured in the obstacle frame. Here, $\varphi = 30°$ has been chosen for the obstacle skew angle. (a) Three dimensional hypersurface of the transition velocities of the two different orientation patterns in the box frame. (b) Slice through the hypersurface as indicated by the transparent gray plane in (a) at $k_{\mathrm{c}} = 0.05$. The different orientation patterns are indicated between the lines of transitions. The branching rate was held constant at $k_{\mathrm{b}} = 20$ per unit time, but has again no influence on these results.

Fig. 4.10 features two dimensional slices through the four dimensional phase diagrams. Now the two axes denote orthogonal obstacle velocity $\tilde{v}_{\mathrm{nw}}^{\perp}$ and obstacle skew angle φ at $k_{\mathrm{c}} = 0.05$, $r_{\mathrm{br}} = 5$ (a) and $r_{\mathrm{br}} = 40$ (b). We find that for relatively small length scale ratio $r_{\mathrm{br}} = 5$, i.e. in regimes where the lateral outgrowth rate becomes more and more important compared to the orthogonal outgrowth, an obstacle skew angle of around $\varphi \simeq 35°$ strengthens the stability of the ± 35 pattern. This is the case because at these obstacle skewness filaments with the orientation $\tilde{\theta} \simeq \varphi$ have a small or even vanishing lateral outgrowth rate. Their lateral polymerization velocity diminishes the effect of the lateral obstacle motion in the obstacle frame (cf. Eq. (4.20)).

Triangular shaped leading edge

Now that we have gained some insight about the impact of a skewed linear and autonomous obstacle surface on the steady state structure of the actin networks, we will slowly approach the situation of a parabola shaped, i.e. curved leading edge. Reconsidering the piecewise-linear leading edge approximation (i.e. Fig. 4.6 on page 54), we can approximate the parabola by substituting separate regions of the obstacle by skewed linear obstacles, which are coupled via their lateral outgrowth.

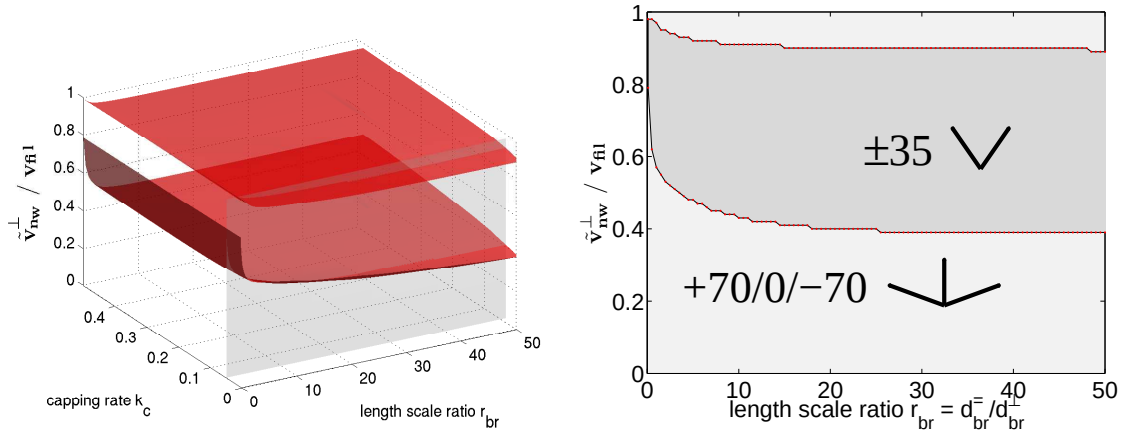

(a) (b)

Figure 4.9: Same as Fig. 4.8, with obstacle skew angle $\varphi = 60°$.

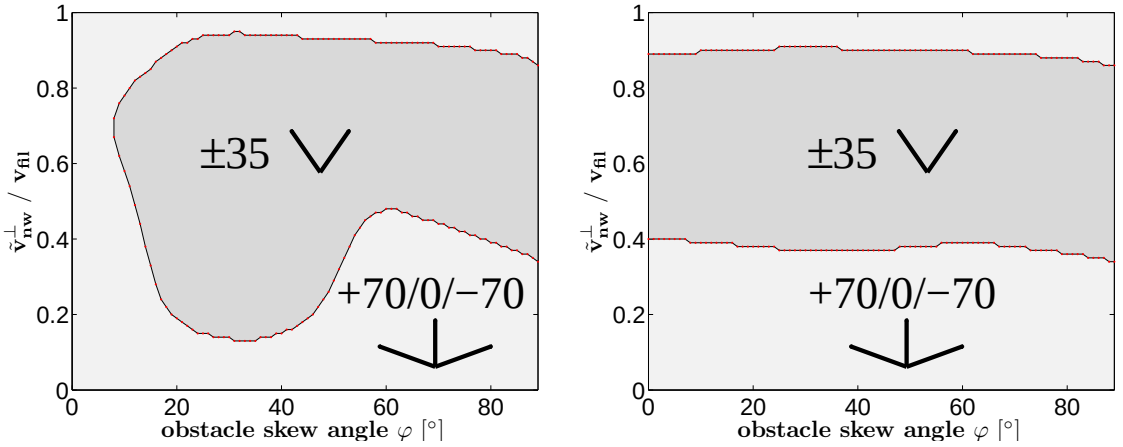

(a) (b)

Figure 4.10: Two dimensional slices through the four dimensional phase diagram for $k_\mathrm{c} = 0.05$ and $r_\mathrm{br} = 5$ (a) and $r_\mathrm{br} = 40$ (b). The orientation patterns are measured with respect to the obstacle frame. The branching rate was again fixed at $k_\mathrm{b} = 20$.

The roughest approximation of a parabola with $n = 1$ separate domains would be just a linear horizontal ($\varphi = 0°$) obstacle surface with filament absorbing lateral edges, which has been analyzed in detail in Sec. 4.2 already. Hence, the next logical step in fine-graining the problem is $n = 2$. This corresponds to a symmetric triangular shaped obstacle made out of two separate regions in the left and right half of the network with skew angles $\pm\varphi$, that are determined by the exact shape of the parabola. It is clear that the network in one of the two equivalent domains will hold all relevant information. The steady state orientation distribution in the second domain can be easily accessed by a simple transformation $\theta \to -\theta$ of the distribution in the first domain. Therefore, we do not need to simulate the situation on both sides exactly, but rather only adjust one domain to the new situation. For this we are starting with a single linear skewed obstacle surface in the domain $i = 1$. For $n = 2$ one side of this network domain holds filament absorbing conditions at lateral outgrowth, while the other side would be coupled to the second domain $i = 2$. As the situation is symmetric, a deterministic model will always have a symmetric

lateral outgrowth from domain 1 to 2 and vice versa. We therefore need to adjust the boundary conditions on one side of the first domain accordingly to reflect the coupled situation. Filaments growing out at this side of the simulation box will be reinjected after the suitable $\theta \rightarrow -\theta$ transformation. This simply means in the box system, that all filaments in the orientation bin around θ that are growing out of this side of the domain during some unit time step, are instantaneously reinjected at the same side but now in the orientation bin around $-\theta$. In this way it is possible to treat the full triangular situation with comparable rather than twice the computational effort of an individual linear skewed obstacle. The only difference that adjust the calculations is the change in boundary conditions on one lateral side of the simulation box.

Comparison to exemplary steady states from stochastic network simulations

In the following, we will compare representative steady states for individual linear skewed obstacles from stochastic network simulations and the numerically solved continuum model. In order to get a feeling for the impact of the lateral boundary conditions on the results, we have also calculated the same situation for the left hand side of a triangular shaped leading edge, i.e. with adjusted filament reinjecting lateral boundary conditions on the right side of the branching region. The orientation distributions are given in the box frame, i.e. in the (lab) frame of reference that would also be appropriate in an usual experimental setup. For illustration, we additionally add the shifted filament orientation distribution of the skewed autonomous obstacle from the continuum model that would be observed within the obstacle frame.

Representative network snapshots from the skewed obstacle stochastic network simulations can be found in Fig. 4.11 for four different parameter sets and constant obstacle skew angle $\varphi = 30°$. The time averaged orientation distributions from these stochastic simulations together with the steady states from the two different continuum models, i.e. for one individual skewed leading edge and the right side of a triangular obstacle surface, are plotted in Fig. 4.12. Analyzing these results, we find that the change in lateral boundary conditions due to the triangular shape approximation has not a big influence on the filament orientations in the stationary states shown here. For some parameter sets it is even not possible to discriminate the red and magenta lines corresponding to the two versions of the continuum model. Another important aspect that becomes apparent is that the obstacle frame is necessary to interpret our findings.

In the box (or lab) frame, the resulting filament orientations at this obstacle skew angle $\varphi = 30°$, which is rather close to half of the characteristic branching angle $70°/2$, can easily be misinterpreted. Within a hypothetical experimental setup the observer in the lab would measure a dominant $+70/0/–70$ pattern for the distributions in Fig. 4.12(a)–(c) and an apparent ± 35 pattern for the parameters in (d). However, reconsidering the continuum model derivation in Sec. 4.3.1, we now have the background to reinterpret these findings again. As we have shown before the appropriate coordinate frame for filaments growing below a skewed linear leading edge is the rotated obstacle frame (cf. Fig. 4.7(b)). In this frame similar orientation patterns as found before for a flat leading edge were obtained in the analysis. Therefore, the steady state filament orientation distributions have to be classified also in this rotated frame either (black line for the continuum model in Fig. 4.12). Here, it becomes evident that the actual pattern which is observed for the parameter sets in Fig. 4.12(a)–(c) is the ± 35 distribution and in (d) the $+70/0/-70$, which is the exact opposite result as would have been found in the box frame.

In Fig. 4.13 steady state distributions for another four different parameters sets are plotted. The skew angle of the linear obstacle has been increased to $\varphi = 60°$ in these calculations. For the same argument as before the network patterns have to be characterized in the obstacle frame.

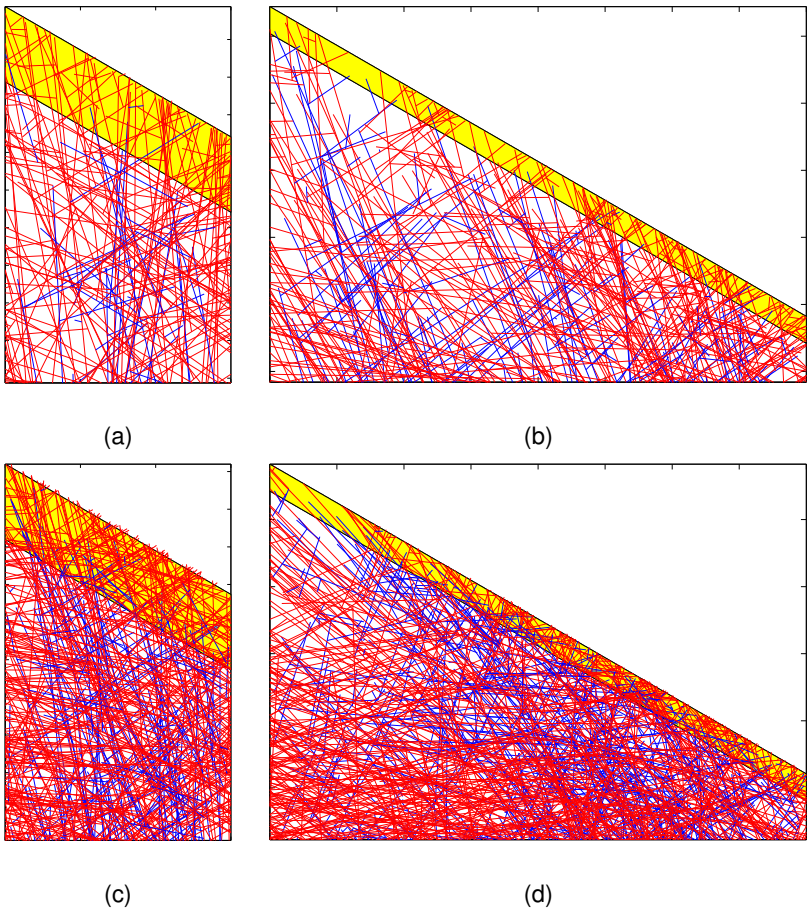

Figure 4.11: Exemplary snapshots of the steady state network structure from stochastic network simulations according to a skewed obstacle or branching region. As before blue filaments have been capped, while red filaments are growing. The active parameter sets in the simulations are $\varphi = 30°$, $k_\mathrm{b} = 20$, $d_\mathrm{br}^\perp = 2\delta_\mathrm{fil}$ and (a) $\tilde{v}_\mathrm{nw}^\perp / v_\mathrm{fil} = 0.6$, $r_\mathrm{br} = 3$, (b) $\tilde{v}_\mathrm{nw}^\perp / v_\mathrm{fil} = 0.6$, $r_\mathrm{br} = 20$, (c) $\tilde{v}_\mathrm{nw}^\perp / v_\mathrm{fil} = 0.2$, $r_\mathrm{br} = 3$, (d) $\tilde{v}_\mathrm{nw}^\perp / v_\mathrm{fil} = 0.2$, $r_\mathrm{br} = 20$. The size of the images is scaled to fit. The orthogonal width of the branching region is kept constant in the simulation and can be used as a reference length scale in the images.

The characteristics of the steady state filament orientations obtained from stochastic network simulations are well resembled by the adjusted continuum description. However, in a quantitative comparison of the results differences become apparent. Especially for high network velocity $\tilde{v}_\mathrm{nw}^\perp$ in combination with a large length scale ratio r_br, the results from both methods can differ. This is due to spatial effects in the stochastic framework, where the position of each individual filament is resolved. For finite obstacle skew angle and fast growth velocity, filaments tend to accumulate at the lower end of the skewed branching region (cf. Fig. 4.11(b)). This effect also gets stronger with increasing skew angle of the obstacle. In this situation in combination with a rather large lateral box dimension $d_\mathrm{br}^=$, our derivation of the lateral outgrowth rate is not valid anymore, because we assumed new filaments to be created in the middle of the branching region both laterally and orthogonally.

4.3.2 Parabola shaped leading edge

Finally, as a last step in this chapter, we will approach our initial goal and predict the actin network structure in the tail of a parabola shaped curved particle. This exact situation can only

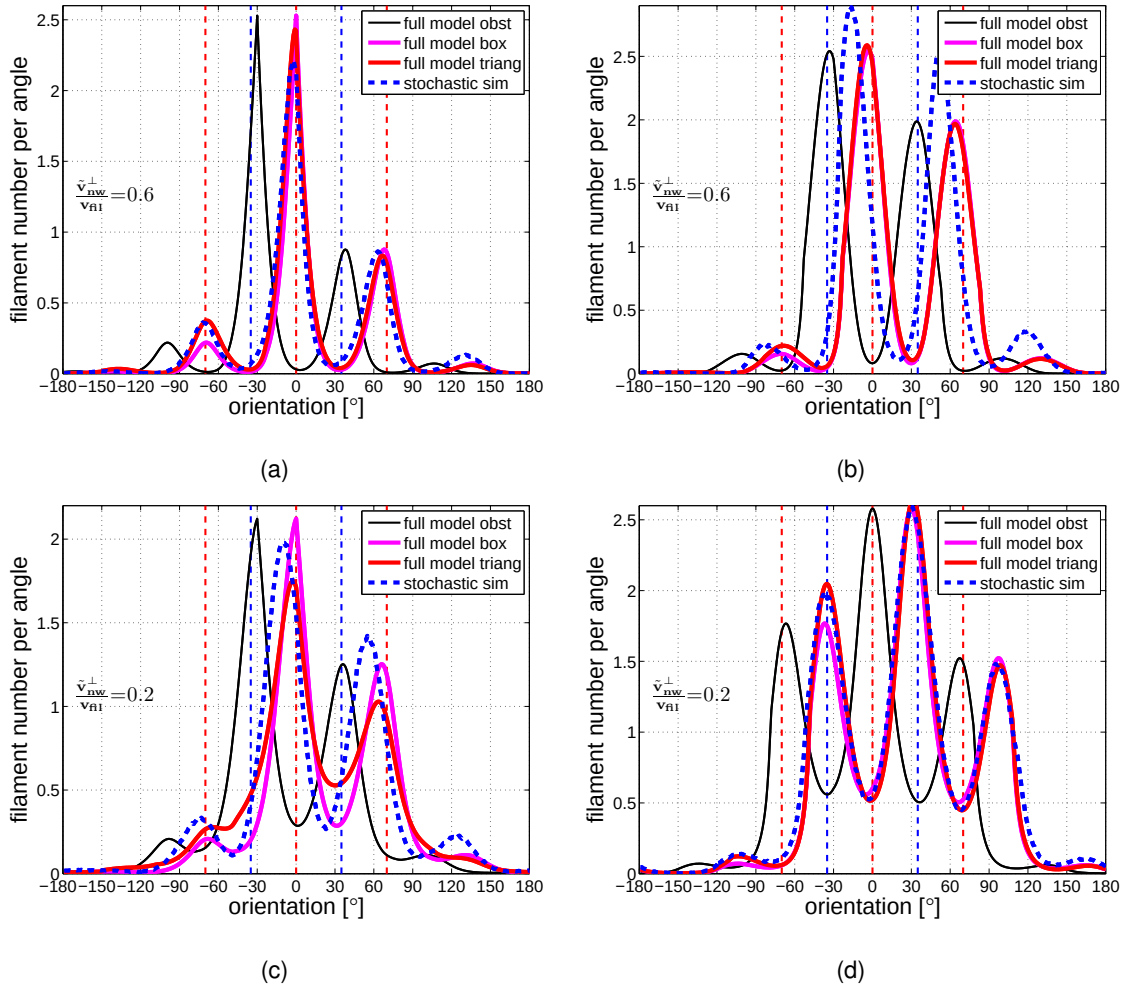

Figure 4.12: Steady state results for the filament orientation distributions from the full continuum model for an autonomous linear skewed obstacle in the rotated obstacle frame (black) and the box frame (magenta), left hand side of a triangular continuum model (red), i.e. a linear skewed obstacle with reinjecting boundaries at one lateral side of the growing region and the stochastic network simulations as shown in Fig. 4.11 (dashed blue). The active parameters are $\varphi = 30°$, $k_b = 20$, $d^{\perp}_{br} = 2\delta_{fil}$ and (a) $\tilde{v}^{\perp}_{nw}/v_{fil} = 0.6$, $r_{br} = 3$, (b) $\tilde{v}^{\perp}_{nw}/v_{fil} = 0.6$, $r_{br} = 20$, (c) $\tilde{v}^{\perp}_{nw}/v_{fil} = 0.2$, $r_{br} = 3$, (d) $\tilde{v}^{\perp}_{nw}/v_{fil} = 0.2$, $r_{br} = 20$;

be approached in the stochastic network simulations. However, combining our developments of the previous sections, we approximate the situation by a triangular leading edge shape in the piecewise linear approximation (with $n = 2$) of the continuum model.

Snapshots of the resulting networks from stochastic simulations for four different parameter sets can be found in Fig. 4.14. The parabola shape is defined by the skew angle $\varphi = 30°$ of the linear approximation in the left hand side of the simulation box in combination with the lateral length scale $d^{=}_{br}$ in the simulations.

The steady state filament orientation distributions in the left hand side of the simulation box are shown in Fig. 4.15. From our previous considerations, we know that the details of network organization depend on the local skew of the obstacle. Therefore, we only analyze one side of the simulation box and compare to the same side of a triangular shaped leading edge approximation. Again there is a left right symmetry in the situation and we would find similar filament orientation distributions in the opposite side of the box but with flipped angles ($\theta \leftrightarrow -\theta$). Here, the resulting filament orientation patterns have to be evaluated in the respective obstacle

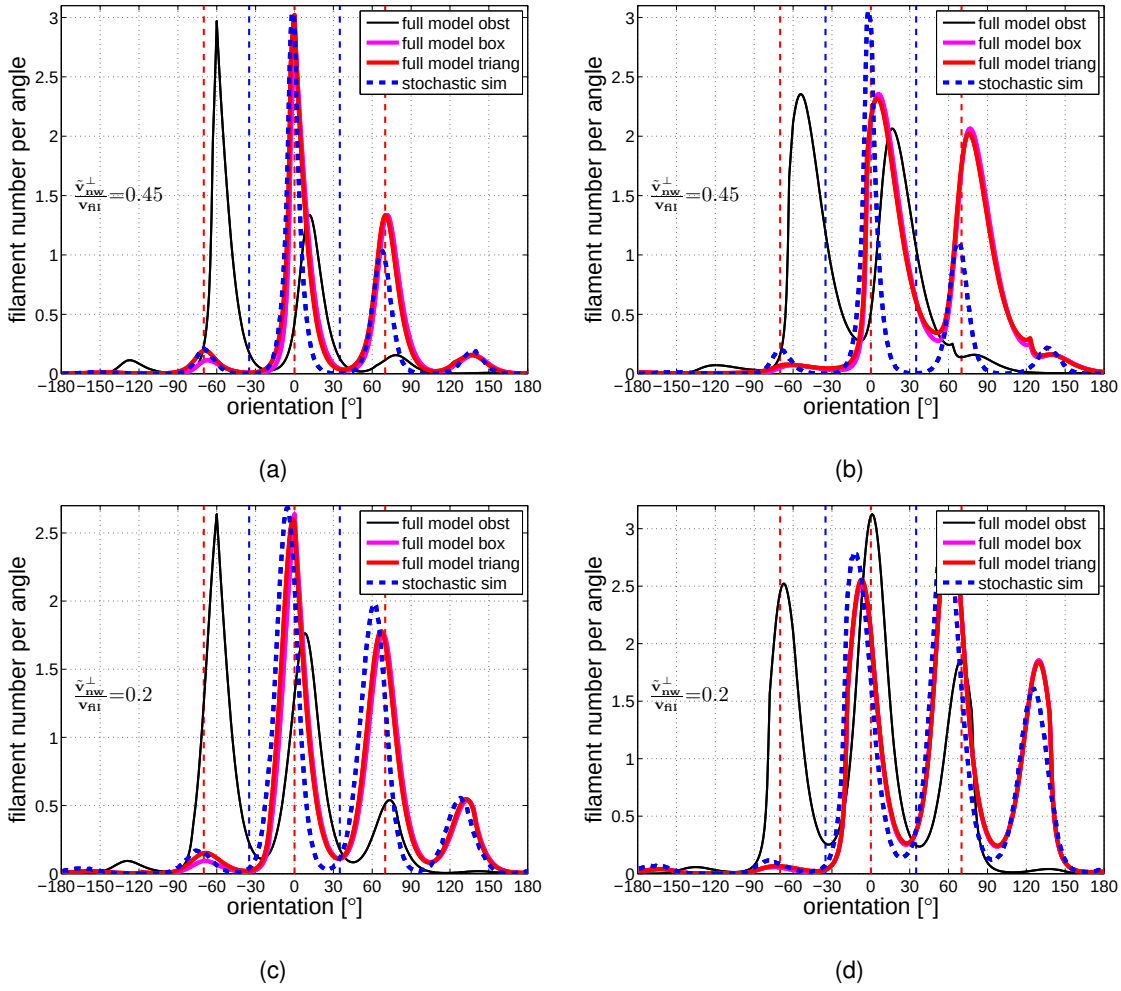

Figure 4.13: Similar to Fig. 4.12, but with $\varphi = 60°$.

frame for the same reason as discussed in the previous section. Therefore, we again plot the results of the continuum model in this rotated obstacle frame for illustration. Considering the linear approximation of the curved obstacle in the continuum model, the characteristics of the orientation patterns from stochastic simulations are reproduced well by the model. However, the absolute height of the individual orientation peaks in the distributions are not always accurate. Still, we believe that the continuum model is very helpful in understanding and interpreting our findings. It is a computationally cheap alternative to the stochastic simulations, that can quickly give reasonable estimates for the steady state network structure under different parameter conditions. As we have already shown in the Fig. 4.12 and Fig. 4.13, the impact of the lateral boundary conditions in the triangular approximation is only minor. Therefore, the results for a concave leading edge shape similar to a (strongly curved) lamellipodium of motile cells would not differ significantly from those shown here in Fig. 4.14, however with flipped angles ($\theta \leftrightarrow -\theta$) again.

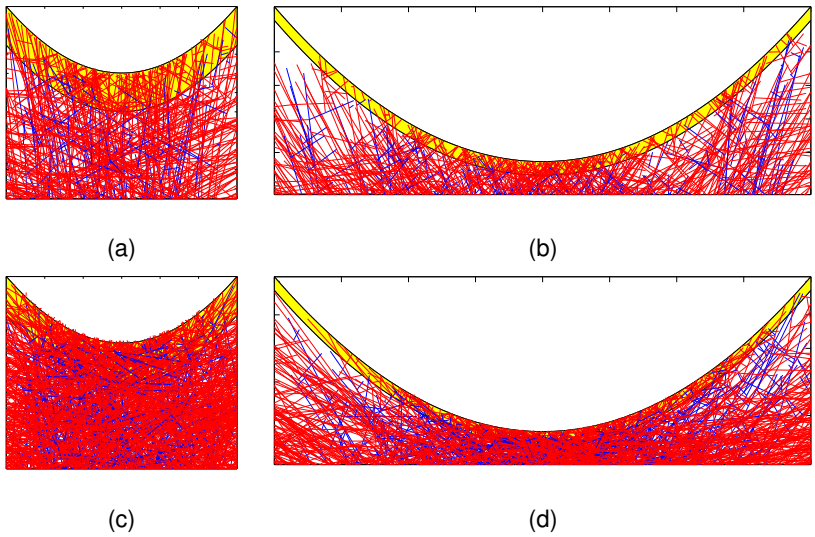

Figure 4.14: Representative snapshots of the steady state network structure from stochastic network simulations according to a parabola shaped obstacle or branching region. The active parameter sets for the left and the right half of the simulation box in this setup are $\varphi = 30°$, $k_\mathrm{b} = 20$, $d_\mathrm{br}^\perp = 2\delta_\mathrm{fil}$ and (a) $\tilde{v}_\mathrm{nw}^\perp/v_\mathrm{fil} = 0.6$, $r_\mathrm{br} = 3$, (b) $\tilde{v}_\mathrm{nw}^\perp/v_\mathrm{fil} = 0.6$, $r_\mathrm{br} = 20$, (c) $\tilde{v}_\mathrm{nw}^\perp/v_\mathrm{fil} = 0.2$, $r_\mathrm{br} = 3$, (d) $\tilde{v}_\mathrm{nw}^\perp/v_\mathrm{fil} = 0.2$, $r_\mathrm{br} = 20$; The parabola shape is defined by the approximated obstacle skew angle at one side of the simulation box, together with the given length scale ratio in this side. The images are scaled to fit in the figure. The orthogonal width of the branching region is kept constant in the simulation and can be used as a reference length scale.

4.4 Summary and discussion

In this chapter, we have extended our network model to predict actin cytoskeleton network structure in the tail behind small propelled particles. Small in our context means, that the lateral and orthogonal width of the growing region, defined at the obstacle surface, are comparable. Starting with a flat horizontal obstacle shape, we extended our continuum model to also include linearly skewed obstacles and eventually an approximation applicable for generic obstacle shapes. These results have been compared to stochastic network simulations that incorporate the full obstacle geometry in two dimensions. As a suitable example, steady state network orientation distributions for a parabola shaped obstacle have been calculated for different parameter sets. In essence, it turned out that the obstacle geometry has a strong impact on the organization of the network.

For laterally small particles the previously observed sequence of three different growth phases with decreasing network growth velocity are not obtained anymore. This characteristic difference to lamellipodium networks results from an increasing lateral outgrowth rate with decreasing horizontal width of the propelled particle. Filament orientation distributions for skewed rotated linear obstacle surface are easily misclassified. The proper frame for this characterization is a rotated frame defined by the obstacle skew angle. In this *obstacle frame*, the particle surface lies horizontally but the initial skew manifests in a finite lateral motion of the obstacle. In this frame similar network structures as found before can be observed, however without left-right symmetry.

As a microscopic basis for these results, we have used the zero-order branching rate assumption together with the same molecular reactions as introduced before in Ch. 3. Therefore, very similar limitations to these key assumptions apply here compared to the ones discussed before (cf. Sec. 3.3). The puzzling experimental results that could not identify a significant number of branching points in EM tomographs have been conducted exclusively for lamellipodium

actin networks so far [107]. Therefore it is not yet clear, if this observation also applies for actin networks in the tail behind small propelled particles. However, the proteins built in these networks are widely preserved and so the precise role of Arp2/3 as a branching agent in our model had to be questioned and adjusted, if unbranched networks could be verified in different experimental setups in the future.

A strong limitation of our model is the restriction to effectively two spatial dimensions. Although this assumption is very well fulfilled in lamellipodium networks, actin networks behind small particles are growing in three spatial dimensions. At this point however, we derived a simplified model system by extending the lamellipodium network model accordingly in 2D. From this approach, we obtained interesting new physics in the simplified 2D networks that could be readily compared to the situation of lamellipodium network growth. Still, in the future it will be worthwhile to extend the model to three spatial dimensions. An additional simple model for the azimuth angle characteristic of Arp2/3 branching will have to be implemented then. Three dimensional models according to an exclusively autocatalytic branching model exist and to our knowledge are all using uniformly randomly distributed azimuth branching angles together with a 70° inclination angle for Arp2/3 in e.g. [15, 17, 98].

As in the previous chapter, we denoted the network growth velocity as the external parameter again, that could be used to trigger structural changes in hypothetical experiments. However, as mentioned before the different models for network growth dynamics can easily be coupled with models for single filament growth under force to yield force-velocity relations for the growing networks. This characteristic has already been measured by experimentalists in diverse setups. For lamellipodium actin networks the coupling of network velocity to external force will be combined to our structural model in the following chapter.

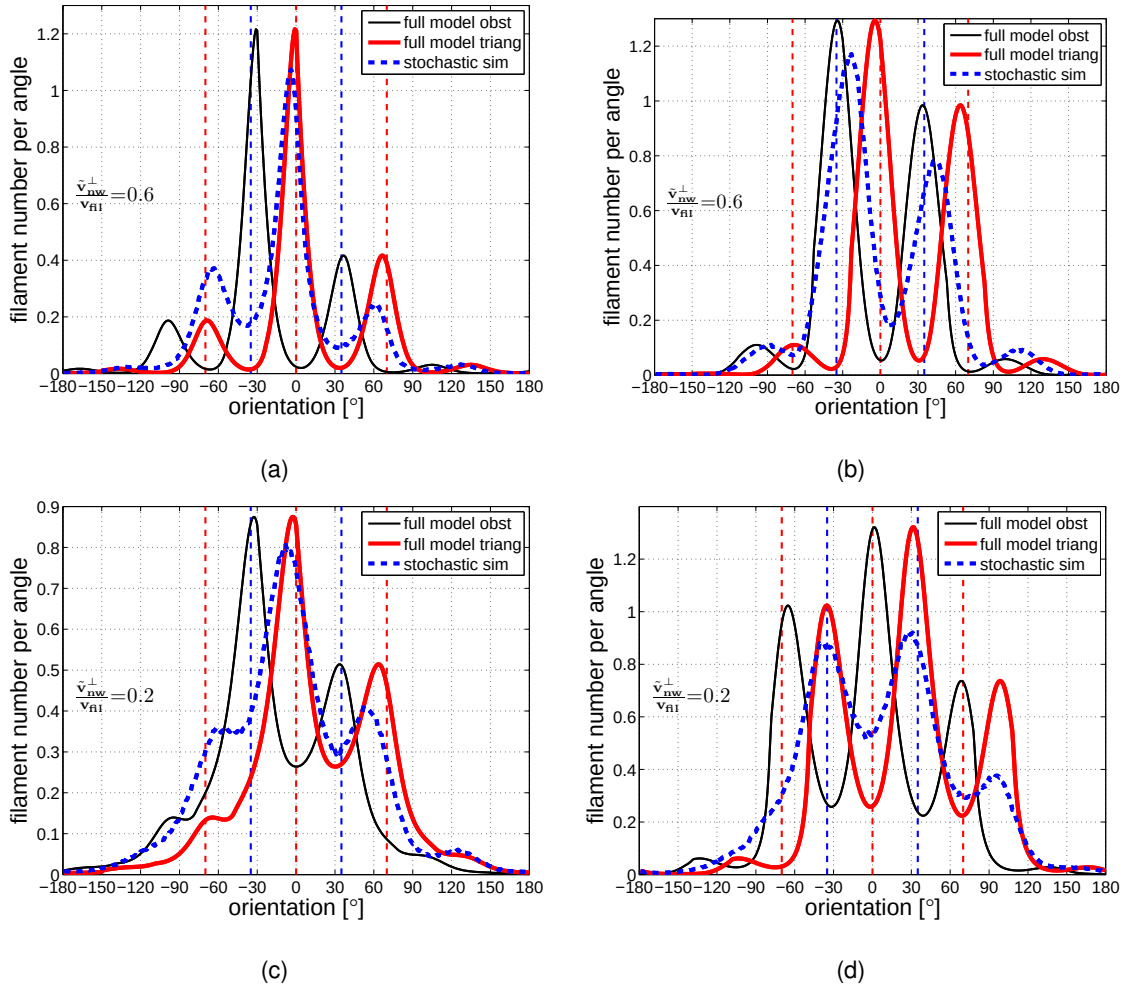

Figure 4.15: Filament orientation distributions at steady state. The blue dashed line indicates the results obtained by averaging filament orientations over time. Only filaments positioned in the left hand side of the branching region, which is separated in the middle are considered. The parabola shape is defined by the mean skew angle of the piecewise linear approximation with $n = 2$ separate linearly skewed obstacle domains and $\varphi_{1,2} = \pm 30^{\circ}$ together with the length scale ratio r_{br}, which is constant in both domains. The results are compared to the steady state solution of the continuum model for the left hand side of a triangular shape (red line). For these results only the lateral boundary conditions at the right side for a single skewed linear obstacle at $\varphi = 30^{\circ}$ are adjusted as described in the main text. In order to interpret the resulting filament orientation distribution it is again illustrative to switch to the obstacle frame via a suitable coordinate rotation and plot the continuum model results in that way (black line). Parameter sets valid for the left and right half space of the parabola/triangle separately are $\varphi = 30^{\circ}$, $k_{\mathrm{b}} = 20$, (a) $\tilde{v}^{\perp}_{\mathrm{nw}}/v_{\mathrm{fil}} = 0.6$, $r_{\mathrm{br}} = 3$, (b) $\tilde{v}^{\perp}_{\mathrm{nw}}/v_{\mathrm{fil}} = 0.6$, $r_{\mathrm{br}} = 20$, (c) $\tilde{v}^{\perp}_{\mathrm{nw}}/v_{\mathrm{fil}} = 0.2$, $r_{\mathrm{br}} = 3$, (d) $\tilde{v}^{\perp}_{\mathrm{nw}}/v_{\mathrm{fil}} = 0.2$, $r_{\mathrm{br}} = 20$;

Chapter 5

Network growth against an external force

In Ch. 3 and Ch. 4, we have been concerned with structural aspects, namely the architecture emerging in growing actin networks with respect to different geometries of the leading edge obstacle (i.e. either a flat membrane or curved particles) that is propelled by the growing network. We tried to illustrate our findings in the context of hypothetical biological Gedanken-experiments in which the networks could be manipulated directly by the observer. There, the network growth velocity v_{nw} turned out to be a convenient external parameter that could be used to influence the network structure and to trigger orientation transitions in the growing actin networks. The growth velocity has successfully been measured in different published setups (cf. Sec. 1.3 and Ch. 7) and in one case the results have also been correlated to the observed filament orientation distributions [54]. For an experimentalist it is practically impossible though to directly control the network growth velocity from the outside.

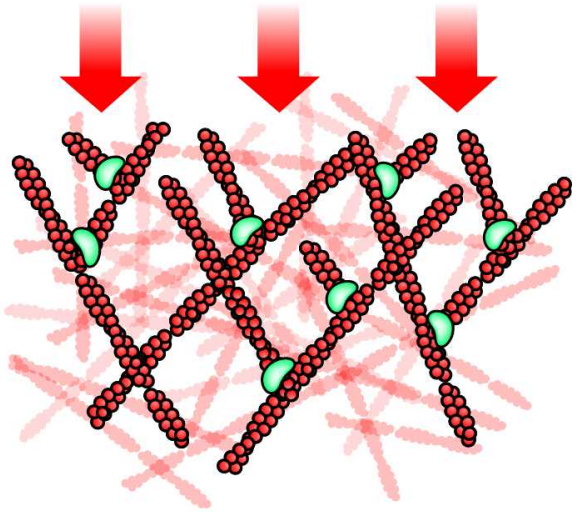

Figure 5.1: Sketch of an actin network growing against an externally applied force (red arrows). Image adapted from [28].

An indirect manipulation of v_{nw} can be achieved by *chemically* perturbing the molecular machinery regulating actin growth. Due to the high complexity of the involved signaling networks however, it is hard to rule out side-effects from this procedure that could bias the measurement. As an alternative it is possible to *mechanically* perturb the system by applying a force against

the growing network, using for instance the cantilever of an atomic force microscope [12, 82, 91] or other micromanipulation techniques [67, 69, 112]. In this way, the velocity of the growing network is not altered directly, but rather by the subtle interplay of the network architecture and the work performance on the single filament level (cf. Fig. 5.1).

Another challenge in such an experimental setup is to access and analyze the emerging network structure before and after the external manipulation directly. The nanometer scale of single actin filaments requires sophisticated measurement techniques like EM [3, 5, 104] or super-resolution light microscopy [8, 43, 95], which are often not applicable in this experimental design. Therefore, a typical measurement coming from such a setup is the important force-velocity relation characterizing the efficiency of protrusion for the growing networks under force. In this observable, the network architecture is incorporated implicitly, too. It can be expected to have a strong influence on network growth velocity under a given external force.

To approach these experimentally more realistic conditions within our theoretical framework, we need to add another stage of hierarchical complexity to the model. We will incorporate different scenarios that couple the network growth velocity to the new experimental parameter, the external force or load acting on the network against the direction of growth. Subsequently, we can test our predictions for the force-velocity relation resulting from the different scenarios by comparing their characteristics to published experimental data. We will find that the interplay of network structure and single filament work performance leads to fascinating effects in the growth-velocity relation, that hold the potential to explain some of the puzzling experimental anomalies that have been observed for this system (cf. Sec. 1.3 and Sec. 5.6).

5.1 Model definition and key assumptions

To model the impact of an external force F_{ext} on the growth velocity of the actin network v_{nw}, we need to take into account the coupling of network architecture and single filament load sharing. This means that we have to add a new relation between external force and resulting network growth velocity to our framework, that in general also depends on the active network structure. We thus end up with two models that can be defined individually, but are coupled as illustrated in Fig. 5.2. Both parts of the combined model will be described in detail below.

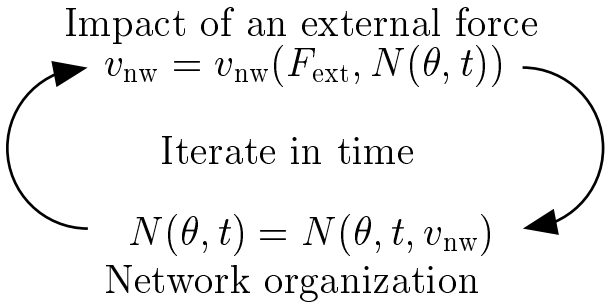

Figure 5.2: A complete model that is able to cover the impact of an external force on the network growth needs to consider also the active network structure. Hence, our strategy is to cycle two coupled parts of the model relating the velocity of a given network structure to the external force and the network organization to the growth velocity until a consistent steady state evolves.

A specific model for the evolving network organization in combination with another specific model for the impact of a constant external force on the network growth state can be iterated in time as shown in Fig. 5.2 until a consistent stationary growth state evolves. In the later simulations in which the external force is altered stepwise to yield the force-velocity relation

for the networks, we are (apart from one very specific exception in Sec. 5.3.3) always iterating until a steady state emerges after each small change in external force. In this sense, we are implicitly assuming a quasistatic experimental procedure, in which the internal equilibration time scale of the microscopic system is much faster than that of the changing external parameter $F_{\mathrm{ext}}(t)$.

Network organization

The lower part of the scheme in Fig. 5.2 represents the network organization of the growing filaments. This has been the main concern of the previous two chapters and so we can rely on the foundation that was built there. At this point we want to develop a generic picture for network growth under the effect of an external force and do not want to bury the essential characteristics of this process under additional details. Therefore, in the following we will not consider the more complex obstacle geometries of Ch. 4 and rely on a 1D flat (infinitely stiff) obstacle shape with periodic lateral boundaries. This means that the model reflects the conditions of lamellipodium growth as introduced in Ch. 3. The essential assumptions for the molecular details of the system and most importantly the zero-order branching model as defined in Sec. 3.1 will be adopted as well. Due to the very good agreement of the continuum model with the stochastic simulations that was demonstrated under these conditions, we will rely on Eq. (3.1) on page 30 for describing the temporal evolution of the network orientation distribution $N(\theta, t)$. This equation represents the full continuum model for a network growing with periodic lateral boundary conditions and will be solved numerically for 360 coupled angle bins as described before.

Impact of an external force

To formulate the upper part of the scheme in Fig. 5.2, we first need to specify which filaments in the network are sharing the external force. Using the continuum framework for modeling the network structure, we will not regard the elastic response of the whole network to the external load. In our picture the network consists of a dense elastic bulk at the lower end in which the topmost leading edge filaments that are the subject of Eq. (3.1) are anchored by crosslinkers. Fig. 5.3 shows a sketch of this setup. During steady state growth the response of the elastic bulk does not influence the growth dynamics as all vertical layers of the network are growing at the same rate v_{nw}. Our model implicitly averages over the different polymer lengths.

In order to model how the external force F_{ext} is shared amongst the protruding filament orientations $N(\theta, t)$ in the network, we need an additional steady state condition. As an essential requirement for stationary network growth with constant velocity v_{nw} under a constant external force F_{ext}, all filaments that do not contribute in pushing against the load have to grow with a slower perpendicular velocity $v_{\mathrm{fil}}^{\perp}(\theta) = v_{\mathrm{fil}} \cos\theta$ than the network does in the direction orthogonal to the obstacle surface. Additionally, all filaments that are pushing continuously against the load have to protrude with the same perpendicular velocity as the leading edge. Combining these two aspects, we can write as a necessary condition for stationary network growth,

$$v_{\mathrm{nw}} = v_{\mathrm{fil}}^{\perp}(\theta) = v_{\mathrm{fil}}^{\perp}(\theta_{\max}) = v_{\mathrm{fil}} \cos\theta_{\max}, \text{ for all } |\theta| \leq \theta_{\max}\,. \tag{5.1}$$

Here, filaments with the orientation $\theta_{\max}$ are the fastest filaments that do not contribute in pushing anymore. $\theta_{\max}$ must correspond to the critical angle θ_{c} (Eq. (3.4)) of the growing network, which in turn defines the steady state growth velocity. If this condition was not the case in steady state, some filaments that are not working were growing faster than the leading edge and they would catch up to the obstacle eventually and contribute in pushing after all. This

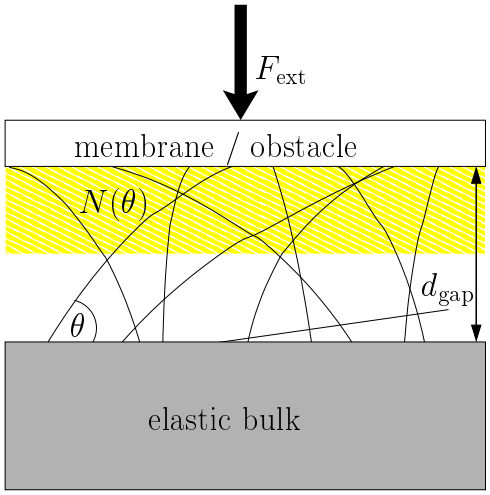

Figure 5.3: When considering the impact of an external force in the following, we neglect the elastic response of the lower bulk network. This part of the network can be understood as an isotropic elastic material under constant compression in steady state. It does not alter the dynamics of the topmost working filaments close to the leading edge $N(\theta)$. These filaments are anchored by crosslinks at their initial orientation θ on top of the bulk and protrude against the load F_{ext} that is acting on the obstacle or membrane. Depending on the specific model, these filaments are bent by the force of the obstacle or their polymerization rate decreases as their barbed end is obstructed by the obstacle surface. During continuous growth all vertical layers shown here are assumed to grow with equal velocity v_{nw} such that their individual positions relative to the obstacle stay constant. Although in steady state there is a constant turnover of working filaments that get capped, absorbed by the bulk and replaced by newly branched filaments, the average filament distributions $N(\theta)$ and the width of the gap d_{gap} between the bulk and the obstacle surface stays the same.

would have an impact on the growth state of the network and therefore a steady state would not have been observed in the first place.

Once we have a specific model that specifies how the external force is distributed amongst the different filament orientations, we can calculate the resulting network velocity by integrating over the contribution from the individual filament orientations that are sharing the load,

$$F_{\mathrm{ext}}(t) = \int_{-\theta_{\max}}^{+\theta_{\max}} f_{\mathrm{fil}}^{\mathrm{model}}(\theta) N(\theta, t)\, \mathrm{d}\theta\,. \tag{5.2}$$

In this expression, $f_{\mathrm{fil}}^{\mathrm{model}}(\theta)$ indicates the amount of force that can be carried by a single filament with orientation θ in steady state. Different models that yield detailed definitions for this function under certain assumptions will be discussed below. For a given external force F_{ext} acting on the network, we can evaluate the growth velocity v_{nw} from this expression. For a given network structure $N(\theta, t)$ the angle $\theta_{\max}$ indicates up to which orientation load is carried by the filaments. Inserting $\theta_{\max}$ in Eq. (5.1) subsequently yields the growth velocity v_{nw} of the network.

On the level of an individual filament, at least two mechanisms limits growth. On the one hand the thermodynamics of actin polymerization are altered if a force is applied on its barbed end. As a consequence the filament polymerization velocity v_{fil} will slow down until the filament is stalled at high enough forces. Sec. 5.2 will analyze the consequences for network protrusion, when this effect is assumed to dominate. As an alternative model, we will analyze the case where filaments are working without any impact on their polymerization velocity v_{fil}, until the mechanical strength of the filament can not accommodate the external force anymore and limits efficient protrusion (Sec. 5.3). In the following we will introduce explicit expressions for

$f_{\mathrm{fil}}^{\mathrm{model}}(\theta)$ for these two cases and elaborate on their impact on the force-velocity relation of the growing actin network.

5.2 Protrusion limited by thermodynamics: the Brownian ratchet

In order to model the thermodynamics of actin polymerization as the limiting factor for effective protrusion of a single filament under force, we are using the simplest variant of a Brownian ratchet. This model was introduced in [84]. Later on it was extended in [74] and [75] to accommodate new experimental findings.

The basic idea we want to adopt for our purposes here is that some obstacle like the membrane is applying a force on the barbed end of an actin filament. Due to steric effects the obstacle subsequently obstructs the filament end and new subunits can not be added. However, due to the finite temperature of its surroundings the obstacle as well as the filament tip itself are fluctuating and so by chance the obstacle moves away a sufficient amount from the filament from time to time such that a new subunit can bind. This process can be approximated for our conditions by,

$$v_{\mathrm{fil}}^{\perp}(\theta) = v_{\mathrm{fil}} \cos\theta \exp\left(-\frac{f_{\mathrm{fil}}^{\mathrm{br}}(\theta)\delta_{\mathrm{fil}}\cos\theta}{k_{\mathrm{B}}T}\right), \tag{5.3}$$

where $v_{\mathrm{fil}}^{\perp}(\theta)$ is the projected velocity perpendicular to the obstacle surface for a filament in orientation θ, $f_{\mathrm{fil}}^{\mathrm{br}}(\theta)$ is the force applied on the filament tip by the obstacle and $k_{\mathrm{B}}T$ is the thermal energy scale [74, 75]. This equation can be understood, as a large enough gap of width $\delta_{\mathrm{fil}}\cos\theta$ against the force $f_{\mathrm{fil}}^{\mathrm{br}}$ has to form between the obstacle and the filament tip to embed a new subunit with a rate $v_{\mathrm{fil}}/\delta_{\mathrm{fil}}$. The probability for the emergence of such a gap is given by a Boltzmann factor, that alters the original filament polymerization rate and therefore also the tangential growth velocity v_{fil} of the filament. As we are interested in filament growth perpendicular to the obstacle surface another term $\cos\theta$ emerges in the equation to yield this velocity component $v_{\mathrm{fil}}^{\perp}(\theta)$.

Combining Eq. (5.3) for the Brownian ratchet and Eq. (5.1) for the steady state growth velocity condition, we can calculate how the external force will be distributed over different filament orientations in steady state,

$$f_{\mathrm{fil}}^{\mathrm{br}}(\theta) = \frac{k_{\mathrm{B}}T}{\delta_{\mathrm{fil}}\cos\theta} \ln\left(\frac{\cos\theta}{\cos\theta_{\max}}\right). \tag{5.4}$$

When the external force on the network is increased, so will $\theta_{\max}$ such that the force is redistributed and the network will continue to grow at a slower pace. In the following, we are only interested on relative characteristics of the force-velocity relation and not on the absolute magnitude of the external force. Therefore, we will set the thermal energy $k_{\mathrm{B}}T = 1$, because it only scales the individual force per filament by some constant factor.

By iterating Eq. (5.4) in combination with Eq. (5.2) and Eq. (3.1) for the temporal evolution of the network, the corresponding force-velocity relation Fig. 5.4 is obtained. In this simulation the force was changed quasi-stationary as mentioned before. That means, that after every small change in force the system had enough time to evolve a stationary state. For numerical stability, the stall force of the network was assumed to be located at the point at which all filaments in the network with an orientation $\theta \leq \theta_{\max} = 89°$ were not able to carry the external load anymore. The force-velocity relation shows a convex decrease over the whole force range, that is in essence due to the exponentially decreasing single filament polymerization rate with applied force. In this scenario, no anomalous effects are observed at the structural transitions

of the actin network, which are indicated by a change in the background intensity of the figure. Thus the network goes through the two transitions with a continuous change in velocity.

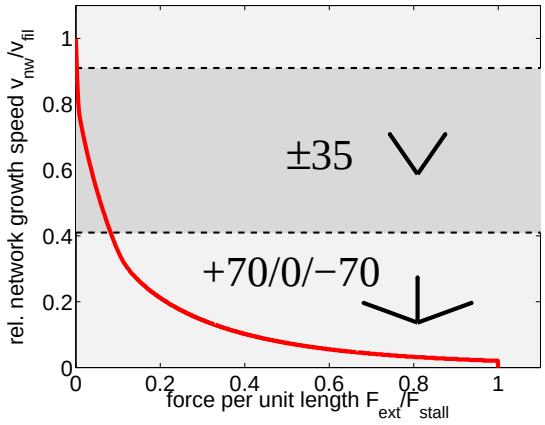

Figure 5.4: Force-velocity relation incorporating the Brownian ratchet mechanism Eq. (5.4) for a network with reaction rates $k_\mathrm{b} = 20$, $k_\mathrm{c} = 0.05$. The force on the network is normalized by the stall force. A convex decay in the protrusion velocity is observed, without significant hysteresis effects at the filament orientation transitions.

5.3 Protrusion limited by filament stability: the force spring model

As an alternative model, we treat another scenario limiting effective growth of the network against an applied force. Focusing on mechanical aspects rather than the thermodynamics of actin filament polymerization, here we assume that each single filament behaves like a Hookean spring. Following a calculation based on linear elasticity theory of thin rods [74], we assume the force carried by a single filament is given by,

$$f_\mathrm{fil}^\mathrm{fs}(\theta) = \kappa(\theta)x = \kappa_0 \sin^{-2}(\theta)x\,, \tag{5.5}$$

with an indentation length x orthogonal to the leading edge which is assumed to be the same for all filaments (cf. Fig. 5.5). In the future, this treatment has to be replaced by more detailed

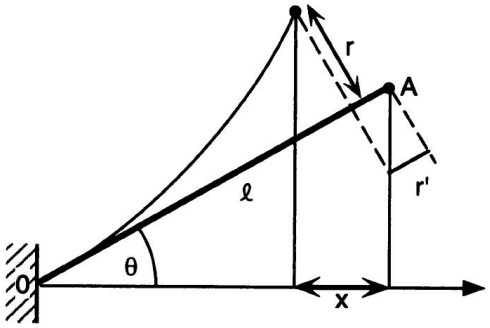

Figure 5.5: Sketch of the force spring approximation for the mechanical stability of individual filaments. For reasonably large orientation angle, filaments behave like Hookean springs with an orientation dependent spring constant $\kappa(\theta)$. Image taken from [74].

mechanical models for specific situations of interest and also for obstacles with curvature. As an example for such a more detailed model, we will treat filaments as bending rods in Sec. 5.3.4 and compare the results. The orientation-dependent effective spring constant $\kappa(\theta)$ used here

approximates bending of an elastic beam for sufficiently large orientation angles θ. Due to the fast decay with increasing orientation angle, it leads to a strong difference in the ability of the two competing network architectures – the ± 35 and the $+70/0/\text{–}70$ patterns – to grow forward while carrying a certain amount of load. At small angles the expression in Eq. (5.5) is not valid and compression is expected to dominate, thus we assume filaments with an orientation angle smaller than $\theta_{\mathrm{fil}}^{\max} = 10^\circ$ to carry a constant maximal force $f_{\mathrm{fil}}^{\max} = 1$ (related to the Euler buckling force). This then determines the value of $\kappa_0 x$. Because κ_0 and x are assumed to be the same for all filaments, only their product matters.

5.3.1 Hysteresis in the force-velocity relation

For a given external force, we now can again solve the coupled equations (3.1) and (5.2) together with Eq. (5.5) numerically by iterating the orientation distribution with 360 angle bins until a steady state is achieved. Fig. 5.6 shows a force-velocity relation obtained in this way for typical parameter values. The external force acting on the network F_{ext} is given relative to $f_{\mathrm{fil}}^{\max}$ here. However, physical values for the external force and the other parameters in the model will be approximated in Sec. 5.5. For zero force, the network is prepared in its fast growth state with the $+70/0/\text{–}70$ orientation pattern. As force increases, the velocity only slowly decreases, because there are sufficiently many filaments almost perpendicular to the leading edge to carry the load. Yet the critical angle continuously grows because increasing load has to be accommodated. If the force passes a certain threshold at $F_{\mathrm{ext}}/f_{\mathrm{fil}}^{\max} \simeq 34$, the $+70/0/\text{–}70$ network is not able to maintain the high velocity anymore and an abrupt change occurs to the ± 35 network, which due to the single filament force relation Eq. (5.5) can carry this amount of load only at a relatively low velocity with large $\theta_{\max}$. As load is increased further, the critical angle grows and the network gradually reorganizes into the $+70/0/\text{–}70$ pattern. As we have found when plotting the order parameter $\mathcal{O}$ for decreasing growth velocity in Fig. 3.10(a) on page 41, this second transition is less abrupt than the first one, leading to mild decrease in the force-velocity relation. In contrast to the first transition, this one goes into a phase which is especially suited to carry load according to the assumed single filament force relation Eq. (5.5), thus an instability does not occur. On the contrary the decrease in velocity v_{nw} is efficiently diminished during the transition and the force-velocity relation is relatively flat. As velocity decreases even further, the orientation distribution starts to broaden (compare Fig. 3.10(a) again) leading to a decreasing number of filaments at small orientation angles. At this point, the velocity of the network rapidly drops with a concave shape. The force-velocity relation also shows that if we initially prepare the network in the intermediate growth phase and then decrease force, the velocity only slowly recovers to its initial value in the fast growth phase. Thus the transition back to the fast growth phase occurs at a smaller force, resulting in a hysteresis loop. The size of the predicted hysteresis loop changes with parameters, but in general it exists over a large range of model parameters, as will be shown in Sec. 5.3.2. In particular, the standard deviation of the branching angle ($\sigma = 5^\circ$) can be increased to a value around 15° before the hysteresis loop vanishes. The existence of a hysteresis loop is an immediate consequence of the competition between the two different orientation patterns and can be used to explain experimentally observed history-dependencies in growing actin networks under force [82], as will be demonstrated below in Sec. 5.3.3.

5.3.2 Sensitivity of the force-velocity characteristics to parameter variations

In the previous section, the force-velocity relation was given in Fig. 5.6 for the following choice of model parameters: capping rate $k_{\mathrm{c}} = 0.05$ per filament and per unit time, branching rate

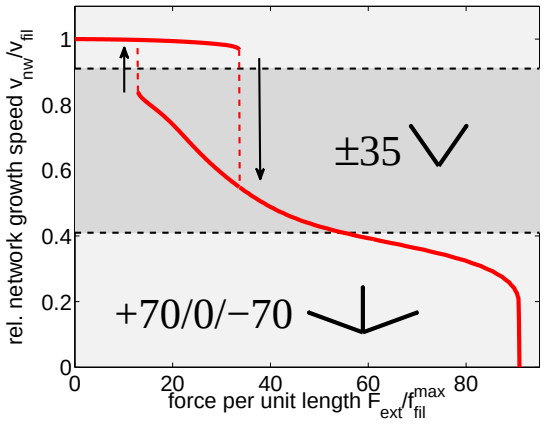

Figure 5.6: Predicted force-velocity relation using the force spring model Eq. (5.5). An actin network is protruding against a changing external force for $k_c = 0.05$ and $k_b = 20$. The external force acting on the network F_{ext} is given relative to f_{fil}^{max}. The most prominent feature is the hysteresis cycle involving the fast and medium growth phases. Abrupt transitions are shown as dashed lines and their directions are indicated by arrows. The full force-velocity curve contains regions with convex, force insensitive and concave regimes. The external force on the network was changed slowly again such that the measured network velocity v_{nw} is always close to its steady state value.

$k_b = 20$ per unit time, standard deviation $\sigma = 5°$ of the Arp2/3 branching angle distribution and the maximum angle $\theta_{f_{fil}^{max}} = 10°$ up to which each filament is able to carry the force f_{fil}^{max}. In the following, we will analyze how sensitive the given force-velocity relation and especially the hysteresis cycle is to variations in these key parameters.

As discussed before already in Ch. 3, a change in the branching rate has no influence on the relative filament number per angle in the network. Therefore this parameter does not alter the relative characteristics of the force-velocity relationship (apart from a rescaling of the total force, as the total number of filaments carrying force does indeed change). In Fig. 5.7, results are shown for different values of k_c and σ. Additionally two different values for the maximum angle $\theta_{f_{fil}^{max}}$ up to which filaments are able to carry the maximum force $f_{fil}^{max} = 1$ were assumed in the calculations. According to these results, the hysteresis cycle at the transition from fast to medium growth phase as well as the relatively flat curve during the transition from medium to slow growth phase is conserved over a wide range of parameters. However, for large values of the standard deviation of the branching angle σ, the capping rate k_c and the angle $\theta_{f_{fil}^{max}}$, the hysteresis cycle vanishes. This behavior can be understood as the large standard deviation as well as a large capping rate diminishes the difference in the filament orientation distribution of the two observed patterns (compare Fig. 3.10(b) and (c) on page 41). Additionally a larger $\theta_{f_{fil}^{max}}$ reduces the difference in load the two different structural phases of the network are able to carry. However, a marked difference in the ability to carry load between the two competing orientation patterns is the essential requirement for the two prominent features of the force-velocity relation, namely the hysteresis cycle and the force-insensitive regime in Fig. 5.6.

An additional feature that can be observed in Fig. 5.7 is that the force-velocity curves for different angular standard deviation σ cross at a similar level of force. However, there exists a simple explanation for this apparently surprising feature: the crossing is always close to the velocity at which the transition from medium to slow growth phase takes place. For $\sigma \geq 5°$ the filament orientation distribution at this velocity is approximately constant in between $-\theta_{max}$ and $+\theta_{max}$, i.e. for all filament angles that contribute in pushing the load. Therefore an approximately equal force can be carried by the networks in this situation. For $\sigma = 2°$, the velocity as a function of force is a flat curve in this domain anyway.

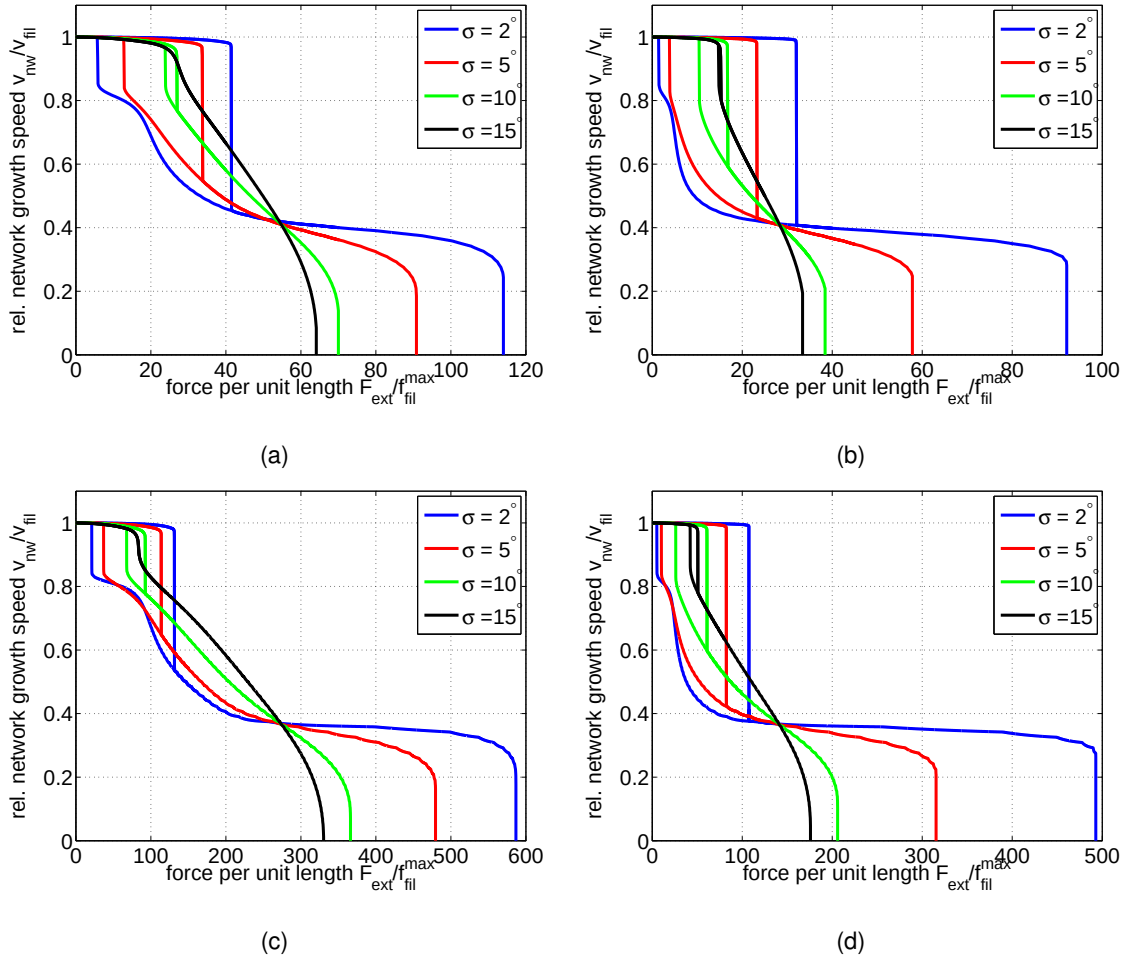

Figure 5.7: Sensitivity of the force-velocity relation to the key model parameters: standard deviation σ of the branching angle, capping rate k_c and maximum angle $\theta_{\mathrm{fil}}^{\mathrm{fmax}}$ up to which each filament is able to carry the force $f_{\mathrm{fil}}^{\max}$. $k_b = 20$ per unit time, (a) $k_c = 0.05$, $\theta_{\mathrm{fil}}^{\mathrm{fmax}} = 10°$; (b) $k_c = 0.05$, $\theta_{\mathrm{fil}}^{\mathrm{fmax}} = 5°$; (c) $k_c = 0.01$, $\theta_{\mathrm{fil}}^{\mathrm{fmax}} = 10°$; (d) $k_c = 0.01$, $\theta_{\mathrm{fil}}^{\mathrm{fmax}} = 5°$;

5.3.3 Experimentally observed memory effects

Now we want to combine the knowledge we have developed in the previous sections to approach the theoretical explanation of memory effects in the force-velocity relation of growing actin networks, that have been observed in experiments before [82], but did not have a convincing microscopic explanation so far. The major results of this experiment have already been discussed in Sec. 1.3 and shown in the corresponding Fig. 1.6 on page 7.

We start by initiating the network in the medium growth phase within the hysteresis cycle in Fig. 5.8. For a constant force of $F_{\mathrm{ext}}/f_{\mathrm{fil}}^{\max} = 30$ the network protrudes with a constant velocity $v_{\mathrm{nw}}/v_{\mathrm{fil}} \simeq 0.6$ in this phase. Next the force is linearly increased (dashed blue line in Fig. 5.8(a)) and so the transition to the slow growth phase is initiated (blue line in Fig. 5.8(b)). At some point, the force has grown large enough and the system will eventually develop the final $+70/0/{-}70$ orientation pattern characteristic for this phase. Now the force is instantaneously reduced to its initial value $F_{\mathrm{ext}}/f_{\mathrm{fil}}^{\max} = 30$. For this rapid change in force we leave the quasistationary regime with important consequences for the new steady state. Instead of going back to the medium growth phase, the system now jumps right into the fast growth phase, because this one is also stable at this force level and in addition is structurally very similar to the existing slow growth

phase orientation pattern. In Fig. 5.8(b), this scenario is also plotted in force-velocity space for illustration.

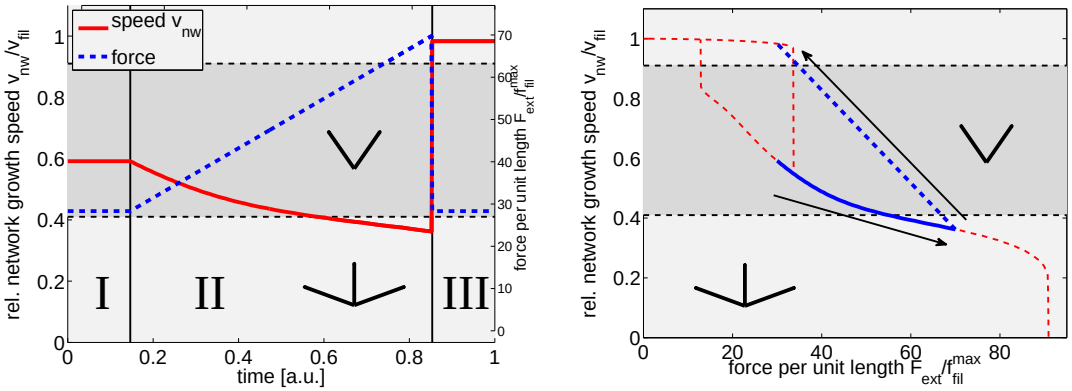

Figure 5.8: Reconstitution of the hysteresis experiment [82] in the force spring model with the same parameters also used in Fig. 5.6. (a) The dashed blue is a prescribed change in external force. The red line is the resulting network velocity. In I the initial velocity as well as the force are constant at steady state in the medium growth phase at ± 35 in which the system is prepared initially. In II the force is linearly increased to prepare the system in the slow growth phase with its corresponding $+70/0/\!\!-\!\!70$ orientation pattern. After a rapid decrease in force to its original value in III the system does not reorganize in the medium growth phase, but rather attains the steady state velocity in the fast growth phase, that is much higher than the initial one. For this instantaneous change in force the quasistationary regime is not active at this point. (b) The same trajectory shown in force-velocity space (blue). The dashed blue line corresponds to the jump in the external force. For comparison, the full force-velocity relation of Fig. 5.6 is also shown in red.

The memory effects in the force-velocity curve demonstrated here are generic and can be obtained for different realizations of the exact force distribution amongst individual filaments, given that the advantage in performance of the two $+70/0/\!\!-\!\!70$ dominated phases compared to the competing ± 35 regime is sufficiently large. This will also be shown in the next section in a model, where single filaments contribute in load sharing like bending rods would. However, for filaments elongating as a Brownian-ratchet [74] this is not the case and the difference in performance of the two competing orientation patterns is too weak to show significant hysteresis effects as shown in Fig. 5.4.

5.3.4 Comparison to bending rods

In order to validate the simplifications made in the force spring model above, here we will obtain the force-velocity relation within an alternative mechanical model. The mechanical stability of every filament will be derived using elementary beam theory.

The tangent orientation angle $\Theta(l)$ of a bent filament at mechanical equilibrium for the setup shown in Fig. 5.9 is governed by the differential equation [60],

$$B\frac{\mathrm{d}^2\Theta}{\mathrm{d}l^2} - F\sin\Theta = 0\,, \tag{5.6}$$

where B is the bending modulus of the filament and $F = -f_{\mathrm{fil}}^{\mathrm{bt}}$ is the point force applied at the upper end of the rod. At the lower end at $l = 0$, the filament orientation angle $\Theta(0)$ is fixed by its foundation in the bulk network and given by its initial direction angle θ. The upper end

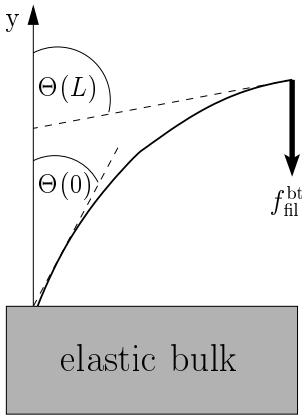

Figure 5.9: Sketch of the setup that is analyzed using beam theory. A filament (beam) is fixed at an angle $\Theta(0) = \theta$ in the dense bulk network. A point force $f_{\mathrm{fil}}^{\mathrm{bt}}$ applies on its tip at backbone length L. The tangent angle of the filament at this free end is given by $\Theta(L)$.

at its backbone length $l = L$ however is free and the external force $f_{\mathrm{fil}}^{\mathrm{bt}}$ applies at this point. Therefore the boundary conditions at both ends are defined as,

$$\Theta(0) = \theta \text{ and } \left.\frac{\mathrm{d}\Theta}{\mathrm{d}l}\right|_{l=L} = 0\,. \tag{5.7}$$

To solve this differential equation, we multiply Eq. (5.6) by the factor $2\frac{\mathrm{d}\Theta}{\mathrm{d}l}$,

$$B\frac{\mathrm{d}}{\mathrm{d}l}\left(\frac{\mathrm{d}\Theta}{\mathrm{d}l}\right)^2 + 2\frac{\mathrm{d}\Theta}{\mathrm{d}l} f_{\mathrm{fil}}^{\mathrm{bt}} \sin\Theta = 0\,, \tag{5.8}$$

and integrate from l to L,

$$B\left[\left(\frac{\mathrm{d}\Theta}{\mathrm{d}l}\right)^2\right]_{\Theta(l)}^{\Theta(L)} - \left[2f_{\mathrm{fil}}^{\mathrm{bt}} \cos\Theta\right]_{\Theta(l)}^{\Theta(L)} = 0\,. \tag{5.9}$$

Using the upper boundary condition at $l = L$, we obtain,

$$B\left(\frac{\mathrm{d}\Theta}{\mathrm{d}l}\right)^2 - 2f_{\mathrm{fil}}^{\mathrm{bt}}\left(\cos\Theta - \cos\Theta_L\right) = 0\,. \tag{5.10}$$

Separation of variables and another integration from 0 to l yields,

$$l = \sqrt{\frac{B}{2f_{\mathrm{fil}}^{\mathrm{bt}}}} \int_{\Theta(0)}^{\Theta(l)} \frac{1}{\sqrt{\cos\Theta' - \cos\Theta(L)}}\,\mathrm{d}\Theta'\,, \tag{5.11}$$

or

$$L = \sqrt{\frac{B}{2f_{\mathrm{fil}}^{\mathrm{bt}}}} \int_{\theta}^{\Theta(L)} \frac{1}{\sqrt{\cos\Theta' - \cos\Theta(L)}}\,\mathrm{d}\Theta'\,, \tag{5.12}$$

where we have inserted the boundary condition at the lower clamped end of the filament and its backbone length L. This equation can be resolved for the force acting on the filament,

$$f_{\mathrm{fil}}^{\mathrm{bt}}(\theta) = \frac{B}{2L^2}\left(\int_{\theta}^{\Theta(L)} \frac{1}{\sqrt{\cos\Theta' - \cos\Theta(L)}}\,\mathrm{d}\Theta'\right)^2\,. \tag{5.13}$$

When comparing the steady state situation in the sketch of Fig. 5.3 to our model equation at this stage, we see that not the filament backbone length L should be the parameter in our model. Rather we have to consider the gap distance $d_{\mathrm{gap}} = y(\Theta(L))$. Although this distance will in general depend on the applied external force, in this simplified model we will neglect this dependence and choose d_{gap} to be constant for arbitrary F_{ext}. To introduce the gap distance in the relation we are using $\mathrm{d}y = \mathrm{d}l \cos\Theta$ in Eq. (5.12), to express the gap distance by,

$$d_{\mathrm{gap}} = y(L) = \sqrt{\frac{B}{2f_{\mathrm{fil}}^{\mathrm{bt}}}} \int_{\theta}^{\Theta(L)} \frac{\cos\Theta'}{\sqrt{\cos\Theta' - \cos\Theta(L)}}\,\mathrm{d}\Theta' \,. \tag{5.14}$$

For our steady state requirement of a constant gap distance d_{gap}, we thus solve Eq. (5.14) for $f_{\mathrm{fil}}^{\mathrm{bt}}$ and obtain the desired orientation dependent force on each filament,

$$f_{\mathrm{fil}}^{\mathrm{bt}}(\theta, \Theta(L)) = \frac{B}{2d_{\mathrm{gap}}^2} \left(\int_{\theta}^{\Theta(L)} \frac{\cos\Theta'}{\sqrt{\cos\Theta' - \cos\Theta(L)}}\,\mathrm{d}\Theta' \right)^2 \,. \tag{5.15}$$

As we are interested on the relative characteristics of the force-velocity relation again, the precise value of the constant $B/(2d_{\mathrm{gap}}^2)$ is not important. Considering Eq. (5.1) again, we can set $\Theta(L) = \theta_{\max}$ in Eq. (5.15),

$$f_{\mathrm{fil}}^{\mathrm{bt}}(\theta) = \left(\int_{\theta}^{\theta_{\max}} \frac{\cos\Theta'}{\sqrt{\cos\Theta' - \cos\theta_{\max}}}\,\mathrm{d}\Theta' \right)^2 \,. \tag{5.16}$$

We thus arrive at a set of coupled equation (i.e. Eq. (3.1), Eq. (5.1), Eq. (5.2) and Eq. (5.15)) that can be iterated numerically to result in the force-velocity relation for this model system (Fig. 5.10). Here it is evident that the prominent characteristics that are necessary to explain the experiments are again present. A hysteresis loop forms around the first orientation transition from fast to intermediate growth phase, while afterwards the force insensitive domain follows. A steady state in the slow growth phase is not observed in this mechanical model and thus it would not be possible to reconstitute the hysteresis experiments using stationary states of the network exclusively. Nevertheless, we have shown that the remarkable features in the force-velocity relation of growing actin networks are not only an artifact of the simplifications in the force spring model used before, but rather robust characteristics of a protrusion model, that is limited by the mechanical stability of the individual working filaments.

5.4 The gearbox of motile cells

Biological systems are the result of an evolutionary optimization scheme. In biology, it can be helpful to think about the consequences of specific observed characteristics for the biological organism. The question, *why* a system evolved the way it did, can lead to a deeper and more illustrative comprehension. However, it is important to note that such considerations try to interpret findings within in an often incomplete picture and have to be appreciated with a necessary portion of skepticism. Nevertheless, at this point we want to dare such an interpretation and ask in which sense the complicated force-velocity relation of growing actin networks that has been shown in Fig. 5.6 could be useful for cell migration.

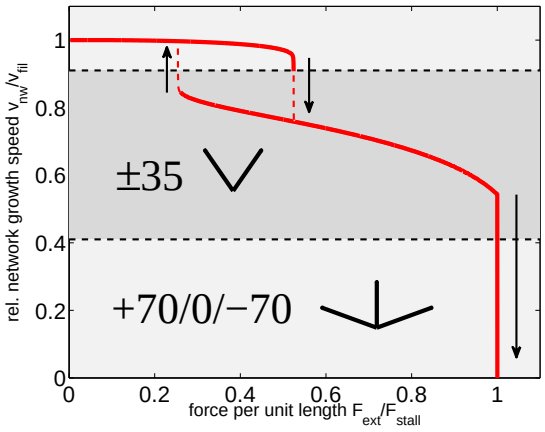

Figure 5.10: Force velocity relation for a model in which filaments at the top of the network behave mechanically like bending rods. The external force is normalized by the stall force F_{stall} . The remarkable features of the force-velocity relation in the much more simplified force spring model (Eq. (5.5)) can be confirmed in this picture. The hysteresis cycle, force insensitive regimes and convex and concave shapes of the curve are robust and observed in this model as well. The network parameters were chosen as $k_{\mathrm{b}} = 20$, $k_{\mathrm{c}} = 0.05$.

To approach this question, we plot the force-velocity dependence of Fig. 5.6 again including the emerging characteristics we have found and described in detail above (Fig. 5.11(a)). In Fig. 5.11(b), the results from the very same calculations are plotted again but this time the power of protrusion $F_{\mathrm{ext}} \cdot v_{\mathrm{nw}}$ rather than the network velocity is plotted over the external force F_{ext}. Now it is apparent that two local maxima exist for the power of protrusion (denoted with 1 and 2). From an engineering point of view, this feature resembles a simplified gearbox of a car. At relatively low forces (i.e. running on a flat road) a driver would use a high gear (2) to drive at relatively high speed. If the car had to climb a hill, the forces acting against the motion of the car were increasing. At some point the driver had to shift down to proceed in a stable motion uphill. Although, the velocity in this lower gear (1) would be much slower than before, the car is now going up the hill and the power of this motion against gravity is still near an optimum locally. Approaching the peak of the mountain the slope of the street would be slowly decreasing. At this point however an experienced driver would not readily switch back up again, as only a minor perturbation or obstacle on the road would jeopardize stable movement in the high gear. In contrast, the driver would stay in the low gear until the external force on the car is a reasonable amount lower than necessary to switch back, and change up subsequently. In this sense, an analogue hysteresis cycle forms in the force-velocity relation of the car.

From this excursion, we can get an idea of what could be the essential benefit of the two different patterns that emerge in the growing actin networks under force. At low forces the network protrudes in the fast growth phase which could be denoted the high gear of the system (2). When the force against movement increases the system self-organizes in a different steady state that is much more suited to carry a large load, however for the price of a reduced growth velocity (1). Once the force is lowered again the high velocity only slowly recovers. The system overshoots the force of the initial transition point and self-organizes back in the fast phase only at much lower forces. This *gearbox of motile cells*, that manifests in the characteristics of the force-velocity relation, yields a good compromise between robustness and efficiency in actin network protrusion.

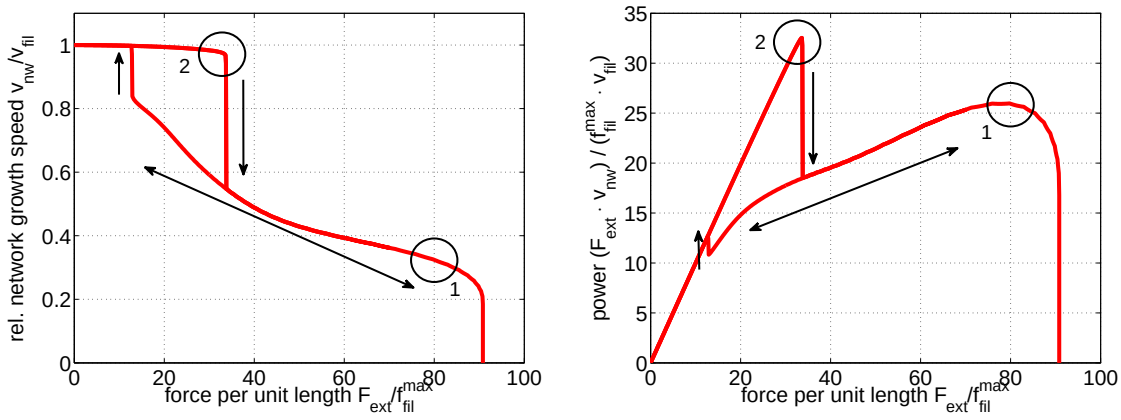

Figure 5.11: Force-velocity relation of the system also treated within the force spring model in Fig. 5.6 ($k_b = 20$, $k_c = 0.05$). Irreversible transitions are indicated by single-headed arrows pointing in the direction of possible changes. (a) The force-velocity relation yields the prominent hysteresis cycle. (b) The same results plotted again as power of protrusion versus external force. The power of protrusion holds two local maxima ((1) and (2)) that can be interpreted as the self-organizing *gearbox of motile cells*.

5.5 Physical values of the model parameters

Our theoretical analysis so far was mostly concerned about the basic features of our network growth model coupled with different versions of a force sensitive filament growth model. For this purpose the general dependence on the model parameters has been analyzed, but so far the exact physical values for these parameters were only of minor interest to us. Here we will calculate these physical quantities to check, if we have been concerned about a realistic parameter range and to get an impression of the time, length and force scales that are involved.

There are three different rates which can be used to scale time: branching rate k_b, capping rate k_c and single filament growth rate v_{fil}/δ_{fil}. Here we choose the last one. The basic length scale of actin growth is $\delta_{fil} = 2.7\,\mathrm{nm}$. A typical filament growth velocity at close to optimal conditions is $1\,\mu m/s$. Then the growth rate 370 δ_{fil} per second. Therefore the branching rate $k_b = 20$ used in many simulations corresponds to $k_b = 7410$ branching events per second in the simulated region of the network. The used capping rate $k_c = 0.05$ corresponds to $k_c = 18.5$ capping events per filament per second.

The results for the force-velocity relation do not depend on the branching rate as mentioned in Ch. 3. However, the branching rate determines the total number of filaments in the network and therefore also the force which it can carry. The external force in the force spring model is given relative to the constant maximal force f_{fil}^{max} that a filament with orientation $\theta \leq \theta_{f_{fil}^{max}} = 10°$ is able to carry in its compression mode dominated regime. For the single filament buckling force, by which f_{fil}^{max} could be approximated, a range from $0.5 - 50\,\mathrm{pN}$ has been reported [18]. Additionally it has been approximated that a maximum force between $2\,\mathrm{nN}/\mu m^2$ [91] and $10\,\mathrm{nN}/\mu m^2$ [1] can be expected from the polymerization of a lamellipodium actin network. So we assume a value of $5\,\mathrm{nN}/\mu\mathrm{m}^2$ in the middle of this range.

In our rate equation approach we typically have 150 filaments within the branching zone close to the leading edge at intermediate network velocity. For migrating cells, a typical value for the number of filaments per leading edge length close to the membrane is $90 \pm 10\ \mu\mathrm{m}^{-1}$ [54]. Dividing by a typical lamellipodium thickness of $0.1\,\mu\mathrm{m}$, we obtain a filament area density of $900\ \mu\mathrm{m}^{-2}$. Comparing with the 150 filaments in our model, we conclude that our model

corresponds to an protrusion area of $0.17\,\mu\mathrm{m}^2$. The stall force of $91\,f_{\mathrm{fil}}^{\mathrm{max}}$ for the network from simulation then corresponds to a value of $5\,\mathrm{nN}/\mu\mathrm{m}^2$ for $f_{\mathrm{fil}}^{\mathrm{max}}$ around $9\,\mathrm{pN}$, which lies well inside the reported range [18].

5.6 Discussion and outlook

In this section we have developed a generic theory of actin polymer network growth against an external force. The modeling framework consisted of two separate entities, which couple the structure of the growing networks to the impact of an external load on the growth dynamics. Subsequently, two limiting cases for the protrusion against an obstacle were formulated and analyzed. On the one hand, efficient network growth was assumed to be limited by the thermodynamics of actin polymerization. This Brownian ratchet model yielded a convex force-velocity curve over the full range of external forces for which stable stationary states have been observed. On the other hand, a simple model for actin filament growth that is limited by the mechanical stability of the individual filaments has been formulated. In this force spring model rich characteristics in the force-velocity relation are observed due to the competition between the two different orientation patterns. This leads to unusual force-velocity relations including also history-dependent behavior. These results follow from the fact that the two patterns have different efficiency in generating protrusion under the constraint of carrying a certain level of load. The $+70/0/\text{–}70$ pattern exists in two variants, one which protrudes very fast at low force and one which is able to carry a high level of force, albeit to the expense of network growth velocity. The ± 35 pattern dominates at intermediate load, because its orientations at intermediate angles provide a good compromise between achieving load and velocity at the same time. In a slightly more complex and realistic model based on bending of individual filaments approximated using beam theory the principle results of the force spring model could be confirmed either. Therefore the key findings of this chapter appear robust in different mechanical models, which limit network growth by the stability of individual filaments.

With the proposed model, different puzzling experimental observations find a simple explanation. For the force-velocity relation, regions of load independent network protrusion [112] and rapid concave growth velocity decay near the stall force have been measured [82, 91]. These observations might correspond to the high force part of the force-velocity curve of Fig. 5.6. One experiment reported a sharp drop in velocity at very small loading force [91]. This observation might correspond to the abrupt transition in the low force part of the force-velocity curve of. Other experiments reported a convex dependence of network growth velocity with force [67, 69], which might correspond to the intermediate force part of the force-velocity curve, when initially prepared in the medium growth phase. Importantly, the predicted competition between the two different orientation patterns provides a generic mechanism to explain an experimentally observed hysteresis loop [82] as demonstrated in a reconstituted in-silico experiment Fig. 5.8.

Because our model explains the rich phenomenology of force-velocity relations by generic mechanisms, we expect that our results are valid for many different situations of interest. Our theoretical framework is able to include growth of the lamellipodium of migrating cells as well as propulsion of pathogens and inert particles by growing actin networks. For each of these situations, it might be appropriate to extend the model in the future by more specific aspects relevant to these different systems and also to reflect new experimental findings. As the modeling framework consists of two separate entities for work performance and network growth, it can be adjusted and extended in each of these parts individually. For example the geometry of the specific obstacle could be incorporated in the network growth model as has been elaborated in Ch. 4. Additionally, it can also be expected that the precise importance and function

of all proteins that are involved in actin network protrusion is not yet fully discovered. For instance the potential role of formin as an end-tracking motor that efficiently incorporates actin filament subunits at the barbed ends of filaments has been discussed controversial in theory [20, 22] and experiment [56]. This actin subunit incorporation could even be combined with ATP consumption fueling the necessary energy for protrusion [93]. At this point it is therefore neither possible nor appreciated to develop a too detailed microscopic theoretical description for the dynamics of working filaments, as some of the key players may not even be known yet. In our generic approach we approximated the situation at a more abstract level. This yields the resulting characteristics in force-velocity space in general, if the ability to carry force is to a reasonable degree more pronounced in the fast and slow growth phases compared to the medium growth phase. This was the case for the mechanically limited filament growth. On the contrary, the protrusion efficiency obtained by assuming a Brownian-ratchet mechanism did not sufficiently differentiate between the two different filament patterns. The protrusion force for proximal network growth velocities above and below each of the two transitions is weakly but monotonically increasing for decreasing network velocity. Therefore, the hysteresis cycles do not emerge and the model can not explain the experimentally observed anomalies [82, 91].

As an alternative to our zero-order branching model for the evolving actin network structure in Sec. 3.3 we have already discussed a first-order branching model, called *autocatalytic model*. As a remarkable consequence of this first-order branching reaction, the precise model formulation for the impact of an external force on the network is irrelevant to a great extend, for the resulting force-velocity relation. As discussed before a unique steady state network velocity v_{nw} is stable in this model independent of the actual force that is applied on the network. An increase in force on a growing network temporarily decreases the network velocity and the outgrowth rate. Therefore the filament number in the network increases *autocatalytically*, until the denser network is able to accommodate the higher external load and the protrusion velocity reestablishes at its initial steady state value again. In this way only the density of filaments in the network is increasing with force, but the network velocity stays constant [16]. This behavior is only physically meaningful to a certain extend because at some filament density (or force) one or the other mechanism will limit the nucleation of new filaments for ever increasing forces. For steric interaction between the individual filaments as the limiting factor, computer simulations of this model revealed non-trivial force-velocity relations [98]. Although these results resemble the force insensitive and concave characteristics of some of the experimentally measured curves, hysteresis effects and convex regimes are not observed.

In order to test our predictions in more detail, different lines of experimental and theoretical approaches seem promising. First, the full hysteresis cycle could be measured experimentally, for example in an AFM-setup. In such a setup, one could also study the effect of slow and fast changes to network velocity and mechanical load. Additionally changes in the structural patterns could be measured by analyzing EM images of the networks treated in the AFM setup. Second, the full actin network dynamics could be modeled in the simulation tool *CYTOSIM* [78]. In this computational tool, the full filament and network mechanics as well as the diffusion of the quantized single proteins in the cytoplasm are considered. Therefore, one could test our zero-order branching approximation and check under which circumstances it is appropriate to consider single filament stability as the limiting factor for network growth under an external force. The insight gained in this way would not only strongly increase our understanding of a fundamental biological process, it also would allow us to develop new protocols to control the growth of actin networks outside the cell, thus opening up exciting new perspectives for applications of this fascinating biomaterial.

Chapter 6

Summary of the modeling part

Within the first part of this thesis, we have been concerned with finding suitable ways to incorporate the structure and growth of actin cytoskeleton networks in a mathematical framework on different levels of detail and complexity. We started with a rather generic random fiber model that reflects the stochastic rules of actin network organization in an abstract way, independent of the detailed molecular mechanisms that are active in the relevant system. It has been possible at that stage to extract from heuristic arguments a reasonable approximation for the percolation threshold in the random fiber model.

Then a more specific theory for actin network growth in the lamellipodia of motile cells has been introduced. This model was motivated by published molecular knowledge from biological experiments. Within this framework, it was possible to identify possible mechanisms that yield the self-organization of specific orientational filament distributions as have been observed in EM micrographs of biological actin networks. Additionally, the model predicts competition of and transitions between two different network patterns. The important parameter that could be adjusted by a hypothetical experimental observer to initiate such transitions turned out to be the network growth velocity.

As the molecular basis of lamellipodia dendritic network growth appears relatively conserved over a wide range of different species at least on our level of detail, we transferred the molecular mechanism to another model for actin network growth in the tail behind small propelled particles. A significant difference compared to the networks that protrude the front of motile cells is the geometry of these small obstacles. Therefore, we adjusted the model geometry to the new environment. Within a suitable reference frame, which is determined by the local skewness of the obstacle surface, we obtained very similar network patterns as before that determine structure and growth of the network.

For the geometry of the lamellipodium in motile cells, we subsequently extended the model to reflect the impact of an external force on network protrusion. According to a simple model in which single filament polymerization is limited by their mechanical stability, we obtained rich characteristics in the force-velocity relation of these networks. These results provide a simple possible explanation for different puzzling experimentally observed anomalies, that have been reported before.

Part II

Quantitative data analysis

Testing model predictions with quantitative experiments

In the first part of this thesis, we dealt with modeling the structure and dynamics of actin cytoskeleton networks on different length scales. In general, a valuable model should be able to make specific predictions that can be tested experimentally for validation. In the concluding sections of the previous chapters, we already discussed our model results in the context of previously published experimental observations like for example the force-velocity relation of growing actin networks. Regarding microscopy images of complex cytoskeleton network structures, however it is often not trivial to find suitable observables that bridge theoretical and experimental results.

In this second part, we will therefore approach different possible methods to quantify microscopic images of actin networks from different experimental setups. In general, we will aim at image analysis protocols extracting information that is *quantitative*, *precise*, *unbiased* and *statistical relevant*. Therefore we will elaborate on different *automated* digital image processing algorithms, that are able to extract quantitative observables from a large number of images under well defined conditions. The potential subjective influence of a human observer is diminished to a minimum in this procedure.

In Ch. 7, we specifically test our model predictions regarding the orientation patterns in growing lamellipodium actin networks (cf. Ch. 3). For this purpose, we evaluate experimental data from moving fish keratocyte cells and extract actin filament orientation distributions from EM images as a suitable observable. In Ch. 8 we introduce a new generic parameter, called *image coherency*, that could be used to automatically quantify and parameterize network structures of different biological polymers in the future. Especially in the high-throughput analysis of automated cell-based screens, this parameter could be a useful addition. We also benchmark these methods with variants of the random fiber model.

All of the biological data that is used in the following two sections has been collected by our experimental collaborators. The starting point for our analysis in each project was the raw data taken during the biological experiments. In particular, the EM images and keratocyte cell experiments in Ch. 7 were conducted by **Edit Urban** and coworkers in the group of **John Victor Small** at the *Institute of Molecular Biotechnology* in Vienna. The experiments with adherent JC-53 cells in Ch. 8 were carried out by **Nikolas Herold** and **Maik Lehmann** in the group of **Hans-Georg Kräusslich** from the *Department of Infectious Diseases, Virology* of the *University Hospital of Heidelberg* using the *Bioquant high-throughput microscopy facility*.

Chapter 7

Orientation analysis of lamellipodium actin networks

In Ch. 3 we analyzed a model for the structure of growing actin networks in the lamellipodium of motile cells. We found that two competing orientation patterns dominate the network structure and that transitions between these patterns are triggered by changes in the network growth velocity v_{nw}. From this model it was possible to deduce a phase diagram (cf. Fig. 3.11 on page 42) indicating the stable pattern with respect to this parameter. For fast and slow network growth speed, relative to the single filament polymerization velocity v_{fil}, a dominant $+70/0/-70$ degree distribution was predicted to be stable, while at intermediate velocities, a complementary pattern at ± 35 degrees dominated the network. In this chapter, we will introduce an experimental procedure and automated data analysis that could be used in the future to test our predictions. As a proof-of-principle, we will show the full analysis on a single representative experiment, indicating reasonable agreement with our theoretical predictions.

7.1 Experimental strategy

In order to test the orientation transitions that were theoretically predicted in Ch. 3, our experimental collaborators **Edit Urban** and coworkers in the group of **John Victor Small** at the *Institute of Molecular Biotechnology* in Vienna performed experiments on motile fish keratocyte cells. The principle experimental strategy for their approach has been introduced before in [54] by **Stefan Köstler** and coworkers in the same group.

As discussed earlier, in our model the *external parameter* network growth velocity v_{nw} can not be easily manipulated from the outside by an experimental observer. Additionally, it is not sufficient to compare two cells crawling with different absolute velocities. Considering Ch. 3, the important parameter that triggers network orientation in the model is the protrusion speed v_{nw} measured relative to the filaments' tangential polymerization velocity v_{fil}. As v_{fil} itself depends on many intrinsic characteristics of the cell, like the available actin monomer concentration at the leading edge, it is a very individual property. Hence, it is not unlikely that two cells, migrating at different speed, are still in the same actin network organization phase.

To approach this problem it is important to understand that the velocity of individual cells crawling on a culture dish quite naturally varies due to random changes in the external and internal conditions at the position of each cell. Using the correlation of two different microscopy setups allows to exploit these stochastic variations and extract the structure of the actin network for different cell velocity and therefore protrusion speed of the leading edge network.

First, different moving fish keratocyte cells are observed in a live-microscope in real time. Once one cell stochastically slows down significantly, all cells are fixed in their present dynamical state. Subsequently, the lamellipodium network of the cells is analyzed in high resolution EM tomography. This means the available data consists of volumetric stacks of two dimensional slices through the lamellipodium parallel to the surface and at a position close to the leading edge of the cell. Although it is not possible to measure directly the relative velocity $v_{\mathrm{nw}}/v_{\mathrm{fil}}$ of a cell in its final state, we know from the live-cell images which cell was slowed down just before fixation. Therefore it is possible that this cell actively switched its velocity at this point. Now we can compare the network orientation distribution in this cell to another cell which was moving unperturbed at relatively high velocity.

7.2 Orientation analysis

To evaluate the orientation distribution of actin filament networks on EM images of the lamellipodium of motile keratocyte cells, we will rely on two different data analysis strategies. First, we will introduce a gradient based orientation measure. As this procedure evaluates the gray value gradients in each pixel of the image and extracts the desired orientation information from this calculus, it is applicable to a wide range of different images. Even if the resolution of the image is far lower than the length scale of the actin network constituents, this analysis can yield accurate results. This will also be demonstrated in Ch. 8, where we will use this gray value gradient based method to parameterize actin networks from fluorescence microscopy images. In our second approach, we will extract an abstract two dimensional actin network representation, consisting of nodes connected by linear line segments. This algorithm was customized for the specific type of EM data that was available to us. Therefore, in order to yield accurate and correct results, this method requires a rather high image quality as a necessary prerequisite. However, after this algorithm has extracted an actin network, the quality of the results can be judged directly by visual inspection. A similar accuracy as observed in these extracted networks can thus be expected from the subsequent orientation analysis.

7.2.1 Gradient based orientation analysis

In order to evaluate the local orientation in a small region of an arbitrary gray value image, the structure tensor is a valuable and established method [49]. An *ideal local orientation* is a small region or *neighborhood* of an image, on which the gray values only change in a single direction (cf. Fig. 7.1).

The structure tensor

A strategy to extract a unit vector $\hat{n}$ defining the local orientation in a small region of the image is to assume, that it deviates least from the gradient direction of the image gray values, $\nabla g(\vec{x})$. For this purpose, a promising procedure is to maximize,

$$\left(\hat{n}\cdot\nabla g(\vec{x})\right)^2 = |\nabla g(\vec{x})|^2\cos^2\left(\measuredangle\left(\nabla g(\vec{x}),\hat{n}\right)\right)\,. \tag{7.1}$$

In the finite region of the *local* orientation, this amounts to an extremum principle,

$$\int_{-\infty}^{+\infty} w(\vec{x}-\vec{x}')\left(\hat{n}\cdot\nabla g(\vec{x}')\right)^2\,\mathrm{d}^2x' \to \max\,, \tag{7.2}$$

where $w(\vec{x}-\vec{x}')$ is a window function, defining the neighborhood around pixel $\vec{x}=(x,y)$. To formulate these mathematical considerations, the discrete gray values of the image were considered as a scalar field $g(\vec{x})$, continuous in position and magnitude. Later, we will express the necessary mathematical operators by 2D filter masks that are suitable to transfer our derived expressions to the quantized gray value images. The optimization problem can be solved by rewriting equation (7.2) as

$$\hat{n}^T \mathbf{J} \hat{n} \rightarrow \max, \tag{7.3}$$

where the structure tensor **J** is defined as,

$$J_{pq}(\vec{x}) = \int_{-\infty}^{+\infty} w(\vec{x}-\vec{x}') \left(\frac{\partial g(\vec{x}')}{\partial p} \frac{\partial g(\vec{x}')}{\partial q} \right) \mathrm{d}^2 x' . \tag{7.4}$$

This is a symmetric, positive semidefinit matrix and therefore there exist two orthogonal eigenvectors with non-negative eigenvalues. Hence, a suitable coordinate rotation reduces **J** to a diagonal matrix and the optimization problem reads,

$$\begin{bmatrix} \hat{n}'_x & \hat{n}'_y \end{bmatrix} \begin{bmatrix} J_{x'x'} & 0 \\ 0 & J_{y'y'} \end{bmatrix} \begin{bmatrix} \hat{n}'_x \\ \hat{n}'_y \end{bmatrix} \rightarrow \max . \tag{7.5}$$

If both eigenvalues are equal, i.e. $J_{x'x'} = J_{y'y'}$, there is no dominant orientation observed in this neighborhood. Therefore, without loss of generality, we can assume $J_{x'x'} > J_{y'y'}$ and hence $\hat{n}' = \begin{bmatrix} 1 & 0 \end{bmatrix}$ maximizes Eq. (7.5) with maximum value $J_{x'x'}$.
This means that in the coordinate system in which the structure tensor **J** is diagonal, i.e. the coordinate system spanned by the two orthogonal eigenvectors of the matrix **J**, $\hat{n}$ and therefore the local orientation is given parallel to the eigenvector with the largest eigenvalue.

The orientation angle

To solve the above eigenvalue problem and calculate the orientation vector on a 2D image, we have to find the coordinate transformation which diagonalizes the structure tensor, $\mathbf{J}' = \mathbf{U}^T \mathbf{J} \mathbf{U}$, i.e.

$$\begin{bmatrix} J_{x'x'} & 0 \\ 0 & J_{y'y'} \end{bmatrix} = \begin{bmatrix} \cos\phi & -\sin\phi \\ \sin\phi & \cos\phi \end{bmatrix} \begin{bmatrix} J_{xx} & J_{xy} \\ J_{xy} & J_{yy} \end{bmatrix} \begin{bmatrix} \cos\phi & \sin\phi \\ -\sin\phi & \cos\phi \end{bmatrix} . \tag{7.6}$$

If we solve for the orientation angle ϕ, we obtain

$$\tan 2\phi = \frac{2J_{xy}}{J_{yy} - J_{xx}} . \tag{7.7}$$

Due to this result the eigenvalue problem in 2D is trivial as the orientation angle is simply given by a combination of the three independent components of the structure tensor **J** (Eq. (7.4)).

Properties of the eigenvalues

The eigenvalues of the structure tensor, $J_{x'x'}$ and $J_{y'y'}$, are the squared gradients in direction of the corresponding eigenvector averaged in a region with respect to the window function. This can be verified as follows: The structure tensor is symmetric with an orthogonal set of eigenvectors. If we assume the two eigenvectors to be given by the unit vectors $\hat{\vec{\lambda}}_1 = (\cos\phi, -\sin\phi)$

and $\hat{\vec{\lambda}}_2 = (\sin\phi, \cos\phi)$ with arbitrary ϕ. The averaged squared gradients in these directions are given by $\hat{\vec{\lambda}}_i^T \mathbf{J} \hat{\vec{\lambda}}_i$. This follows directly from equations (7.2) and (7.3) with the definition of the directional derivative, $\hat{e} \cdot \nabla g(\vec{x})$ in direction of an arbitrary unit vector $\hat{e}$. Further we can calculate,

$$\hat{\vec{\lambda}}_1^T \mathbf{J} \hat{\vec{\lambda}}_1 = \begin{bmatrix} \cos\phi & -\sin\phi \end{bmatrix} \begin{bmatrix} J_{xx} & J_{xy} \\ J_{xy} & J_{yy} \end{bmatrix} \begin{bmatrix} \cos\phi \\ -\sin\phi \end{bmatrix} \tag{7.8}$$

$$= J_{xx}\cos^2\phi + J_{yy}\sin^2\phi - J_{xy}\sin 2\phi\,, \tag{7.9}$$

where we have used the trigonometric identity $2\sin\phi\cos\phi = \sin 2\phi$ to arrive at the last expression. This is exactly the result obtained from Eq. (7.6), if we solve for the eigenvalue $J_{x'x'}$. A similar calculation with the second eigenvector leads to the result for $J_{y'y'}$ from equation (7.6). Hence, Fig. 7.1 illustrates the situation. Using the structure tensor calculus in a small neighborhood of an image, it is possible to find a rotated coordinate frame spanned by the two eigenvectors $\hat{\vec{\lambda}}_1$ and $\hat{\vec{\lambda}}_2$ that indicate the dominant orientation of the gray value gradient in the region. The magnitude of the averaged squared gradients in these directions are given by the corresponding eigenvalues $J_{x'x'}$ and $J_{y'y'}$ of **J**.

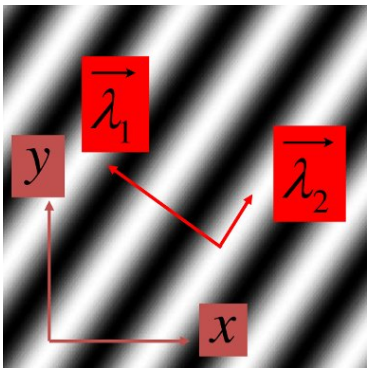

Figure 7.1: Diagonalization of the structure tensor calculates the *principle axis of orientation* within a small region of an image. The eigenvector to the largest eigenvalue $\vec{\lambda}_1$ points in a direction parallel to the dominant orientation, while the second eigenvector is perpendicular to the first. The magnitude of the corresponding eigenvalue is indicated by the length of the eigenvectors in the figure. In this idealized sample image region, the eigenvalue to the eigenvector $\vec{\lambda}_2$ would actually vanish, as the gradient in this direction is zero.

The coherency measure

The two eigenvalues $J_{x'x'}$ and $J_{y'y'}$ of **J** indicate the dominant averaged squared gradient in a small region of the image. Thus, we can distinguish three separate possibilities, assuming $J_{x'x'} \geq J_{y'y'}$. The trivial case $J_{x'x'} = J_{y'y'} = 0$ indicates a constant gray value in the neighborhood. For $J_{x'x'} > 0 \wedge J_{y'y'} = 0$, the region is called a *simple neighborhood* or ideal local orientation in which the gray values only change in one direction (cf. Fig. 7.1 as an example for a simple neighborhood). The remaining case $J_{x'x'} > 0 \wedge J_{y'y'} > 0$ will be observed most often in our microscopic images which are rich in structure and in addition subject to noise and artifacts. Here, the gray values change in all directions and in the special case of $J_{x'x'} = J_{y'y'}$, we observe an isotropic gradient. To evaluate the results for the dominant orientation that is extracted from the image region using the structure tensor in such non-trivial cases, we need an

additional measure that differentiates between strong and weak local orientations. The *image coherency* measure is defined as,

$$c_{\mathrm{c}} := \left(\frac{J_{x'x'} - J_{y'y'}}{J_{x'x'} + J_{y'y'}} \right)^2 = \frac{(J_{yy} - J_{xx})^2 + 4J_{xy}^2}{(J_{xx} + J_{yy})^2} \,. \tag{7.10}$$

This parameter differentiates two extreme cases: an area of constant gray values ($J_{x'x'} = J_{y'y'} = 0$) and an homogeneously random gray value structure ($J_{x'x'} = J_{y'y'} \neq 0$). Additionally, it serves as a measure for the difference of the dominant (averaged squared) gradient compared to the gradient orthogonal to its direction. Furthermore, it can be calculated directly from the structure tensor components, Eq. (7.4), without the need to solve the eigenvalue problem. In general, the coherency varies continuously between 0, in regions without any dominant orientation, and 1, at perfectly oriented structures in a simple neighborhood. In order to overcome numerical instabilities when evaluating Eq. (7.10) at the singularity $J_{x'x'} + J_{y'y'} = 0$, we choose c_c to be zero for a small or vanishing denominator.

Implementation and filter matrices

To implement our considerations so far in an automated algorithm analyzing the images, we need to quantize the relevant operators in Eq. (7.4). Using operator notation, the structure tensor can be formulated as a convolution with a filter $\mathcal{G}$ which has the shape of the window function, while partial derivatives are approximated by discrete derivative operators $\mathcal{D}_x$ and $\mathcal{D}_y$, for which we chose the optimized Sobel filters [49],

$$J_{pq} \simeq \mathcal{G} \left(\mathcal{D}_p \cdot \mathcal{D}_q \right) \,. \tag{7.11}$$

Here, pixelwise multiplication is denoted by "$\cdot$" in order to distinguish it from the successive application of convolution filters.

The optimized Sobel filter matrices are given by,

$$\mathcal{D}_x = \mathcal{D}_y^T = \begin{bmatrix} +3 & +10 & +3 \\ 0 & 0 & 0 \\ -3 & -10 & -3 \end{bmatrix} \,, \tag{7.12}$$

while for the window function we used a rotationally symmetric Gaussian of size $h_{\mathcal{G}}$ with standard deviation $\sigma_{\mathcal{G}}$. For good working conditions, the size and spread of the window function should be larger than the fine structure of filaments in order to average out small-scale variations within the fibers. However, finding the right size of the window function remains a trade off between averaging out noise and small artifacts for increasing its size, but sacrificing information about smaller structures. In this setup we were using $h_{\mathcal{G}} = 30$ and $\sigma_{\mathcal{G}} = 10$ pixel in the quantitative analysis of the actin EM images. One pixel in the EM images has a quadratic spacing of 7.46 Å $= 0.746$ nm, while the typical diameter of a single actin filament is 7 nm or around 9 pixel.

Representative feature images from random fiber networks

As an example Fig. 7.2 shows the exemplary extraction of a feature image from two different variants of the random fiber model as introduced in Ch. 2. In these stochastic realizations of the network model, the orientation distribution was not chosen uniformly randomly, but rather from

a linear combination of Gaussian distributions. In these images the exact absolute orientation of the fibers relative to the lateral boundary of the network is color coded as indicated by the colorbar.

The lower two images in Fig. 7.2 show the results of the structure tensor analysis from these networks in a feature image representation. The color in each pixel indicates its local orientation, while the saturation is given by the coherency measure c_c and the intensity by the trace of the structure tensor, $\mathrm{Tr}\,\mathbf{J} = J_{xx} + J_{yy} = J_{x'x'} + J_{y'y'}$. This is a variant of the *HSV-colorspace* with a constraint hue domain. Colored pixels in the image indicate regions of clear orientation, while black pixels mark the uniform background without any dominant orientation. With regard to visual inspection the feature images appear to capture the original fiber orientation of their individual sample images reasonably well. In the later Sec. 7.3, we will quantify this impression by calculating fiber orientation distributions from such sample random fiber networks and compare them to the initial orientation distribution according to which the model representant was created stochastically.

7.2.2 2D filament network extraction

As an independent alternative to the gradient based orientation analysis introduced in the previous section, here we elaborate on a two dimensional network extraction algorithm suitable for EM tomography slices of lamellipodium actin networks. Parts of this algorithm were motivated by similar considerations concerned with network extraction for astrocyte cell clusters [10] and intermediate filament networks [65].

Filament segmentation

As a preparation for network extraction, the actin network visible on the EM image is segmented. This is a crucial step in the analysis as the final accuracy of this segmentation will significantly influence the quality of the results from later processing steps for network extraction. For this reason it is not possible to apply this approach to low quality image data, as then it is very hard or often even impossible to reliably segment the network constituents in an automated procedure.

To approach a good segmentation, i.e. a black and white version of the actin network in the image, we first binarize the image using Otsu's method [79]. This primary segmentation however is imperfect due to artifacts outside the lamellipodium and between filaments. Therefore we need to specify the bulk region occupied by the actin network in the image. As the EM images are taken in close proximity to the leading edge, not the whole image region is filled by the network. For this purpose, we evaluate the coherency measure c_c already introduced in Eq. (7.10) on the images that have been noise reduced by median and Wiener filters before. The coherency is able to distinguish network structures from a uniform or noisy background (cf. Sec. 7.2.1). A binarized version of the coherency feature image yields an estimate for the boundaries of the actin network in the two dimensional slice of the volumetric image stack. As an additional measure that is able to detect smaller holes in the actin mesh, where no filaments are present, we are using the normalized square root of the trace of the structure tensor **J** (Eq. (7.4)). The tensor itself has already been calculated before to obtain the coherency. After applying a maximum filter and subsequent binarization, we get the relevant network region in the image, in which filaments are actually present. Pixelwise multiplication of the three binarized images, i.e. the one obtained from Otsu's method, the binarized coherency and the binarized trace of the structure tensor yields a result for the segmented network. As a last step, we analyze this image for small artifacts, i.e. separated clusters of pixels with a total area

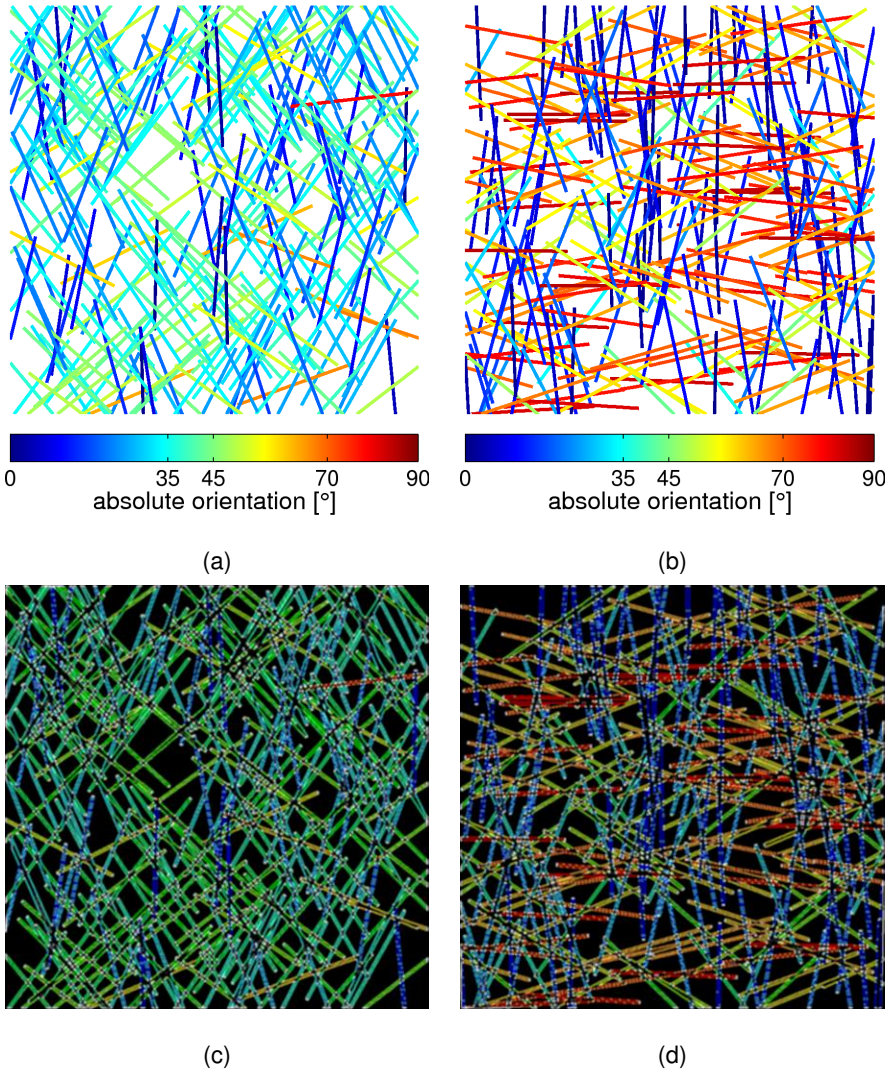

Figure 7.2: Orientation analysis of two realizations of random fiber networks using the structure tensor calculus. (a) and (b) Two examples of random fiber networks according to a $\pm 35^\circ$ (a) and a $+70/0/-70$ (b) degree distribution. The orientation of the individual filaments is color labeled. (c) and (d) Feature images of the orientation, that was extracted by the structure tensor analysis of black and white versions of (a) and (b). The shown colorbar is correct for all images. For these examples the size of the Gaussian filter $\mathcal{G}$ was reduced to $h_\mathcal{G} = 6$ and $\sigma_\mathcal{G} = 2$ to obtain relatively sharp feature representations of the individual fibers.

smaller than a given size, which are then deleted. This completes the segmentation process. An exemplary original image is shown in Fig. 7.3(a), together with its segmented version in (b).

Network extraction

The segmented black and white actin network image as shown in Fig. 7.3(b) is the starting point for the network extraction algorithm, that will be discussed in detail in the following. The final goal of this method is to describe the complex 2D actin network structures by an abstract linearized network consisting of nodes at certain positions and a connectivity matrix indicating which pairs of nodes are directly linked by a straight line segment. In this way we efficiently reduce the experimental data to the information relevant for us, which is the filament orientation

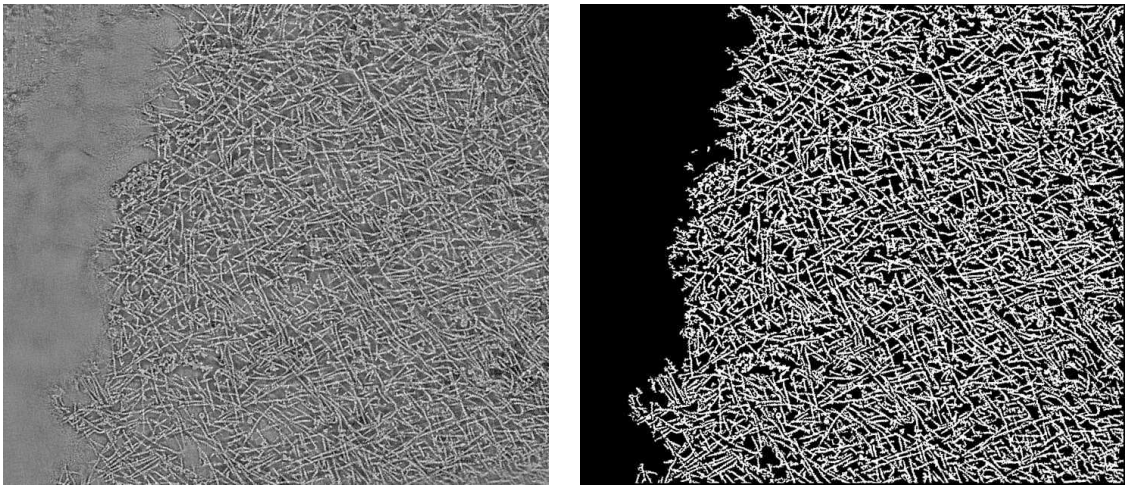

(a) (b)

Figure 7.3: Segmentation of the actin network from an exemplary slice of an EM tomograph of a motile keratocyte lamellipodium. (a) Grayscale representation of one slice of the volumetric data reconstructed from EM tomography. (b) Final black and white network image after binarization, removal of the background and smaller artifacts.

distribution. Actin filament segments in the image are represented as linear (i.e. straight) links between nodes (i.e. crosslinks) in the network. Although the auxiliary crosslinks that are found by the algorithm might often only be artifacts due to the two dimensional projections of the three dimensional network, we are interested in the orientation of the filament segments and this inaccuracy does not influence our results significantly. Later we will evaluate the orientation distribution of the observed filament segments, connecting the nodes in the extracted abstract fiber network.

The algorithm for network extraction can be subdivided in the four sequential steps, *skeletonization*, *classification of nodes*, *graph creation* and *network correction and simplification*. To get an illustrative impression how this procedure applies to an EM image, we will reduce the complete sample image to a smaller exemplary region here and show the impact of the individual steps. Fig. 7.4 indicates this smaller cutout from the sample image.

Skeletonization We start the network extraction from the black and white version of the filament network, that is cut from the binarized full image as shown in Fig. 7.5(a). First, *Matlab*'s thinning or skeletonization method is applied. In this step the width of all segmented objects is iteratively reduced to a final thickness of one pixel. However, thinning is performed in such a way that it does not alter the connectivity of the binary image. In other words two arbitrary white pixels that belonged to the same interconnected cluster of pixels before the operation, will still be connected afterwards. Moreover, the number of connected clusters minus the number of holes in these clusters, that can not be reached from the image boundaries, remains constant. This characteristic is also known as the Euler number, a measure of the topology of the segmented image. The final skeletonization result is displayed in Fig. 7.5(b).

Classification of nodes At this point in the algorithm, we have a skeletonized version of the black and white EM image. The width of all objects is exactly one pixel and therefore, it is possible to classify *endpoints* of objects as nodes. Endpoints are defined as white pixels, with

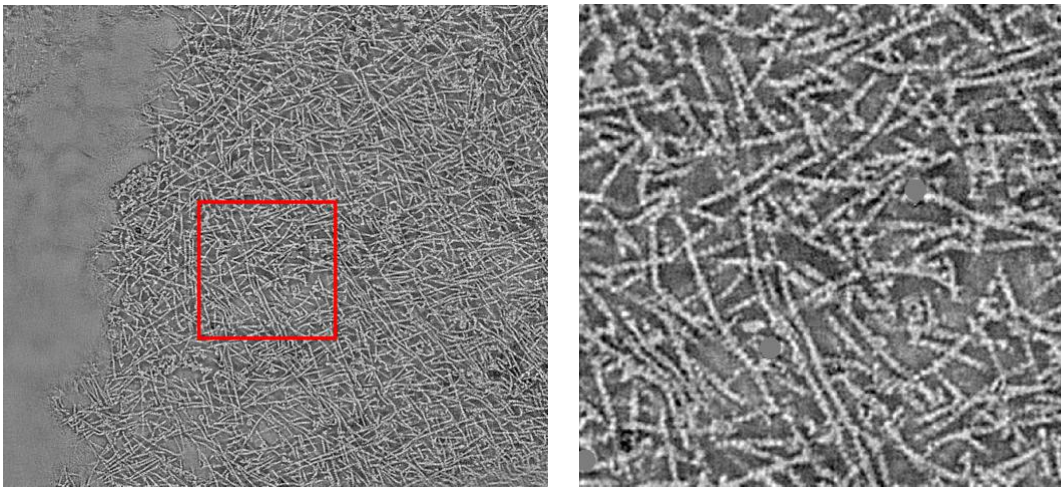

(a) (b)

Figure 7.4: To keep the presentation of the network extraction algorithm illustrative, we will restrict the procedure to a smaller sample section of the full 2D sample image. (a) Full EM slice, with the boundary of the smaller sample region indicated in red. (b) Magnified sample region from (a).

exactly one other white pixel in their direct neighborhood defined by eight surrounding pixels. In Fig. 7.5(c) such endpoints are shown in red. As we disregard single isolated white pixels, every endpoint is connected to at least one other endpoint by a closed path of white pixels. However, it is also possible that a single endpoint is connected to more than one other endpoint, if the white path starting at its position splits up at some position at least once. Hence, we can define a second class of nodes at the position of these split-ups. Such higher order nodes or *crosslinks* are defined as white pixels with at least three other white pixels in their direct neighborhood. Higher order nodes are shown in green in Fig. 7.5(c).

Graph creation Next, it is possible to create a graph or network by tracing connected paths sequentially starting at all nodes which were marked in the previous step. The result of this procedure is essentially an adjacency matrix. This quadratic matrix holds as many columns and lines as nodes were found in the image and is initially set to zero in all its elements. Now, if a connection is established between two nodes with indices i and j, the i, j-th element of the matrix is set to one. As links between nodes are undirected in our graph, the corresponding j, i-th element is either filled as well or only the upper or lower triangle of the symmetric matrix is considered. In this way, we have extracted nodes at certain positions in the image and the additional information, if pairs of nodes are linked. In other words, we already have extracted a primary network from the segmented image. A plot of this rudimentary network is shown in Fig. 7.5(d) and (e). To benchmark the accuracy of the extracted abstract linearized network compared to the actin filament network, the skeletonized binary image and the sample section of the gray value EM image are shown in the background of the plot respectively.

Network correction and simplification The preliminary network holds a rather large number of unnecessary nodes, that do not alter its architecture significantly. Additionally, imperfections in the segmentation process lead to artificial disconnections in filaments. Therefore, we implemented an additional correction and simplification routine for the extracted network.

Due to the specifics of the skeletonization algorithm we are using, multiple higher order

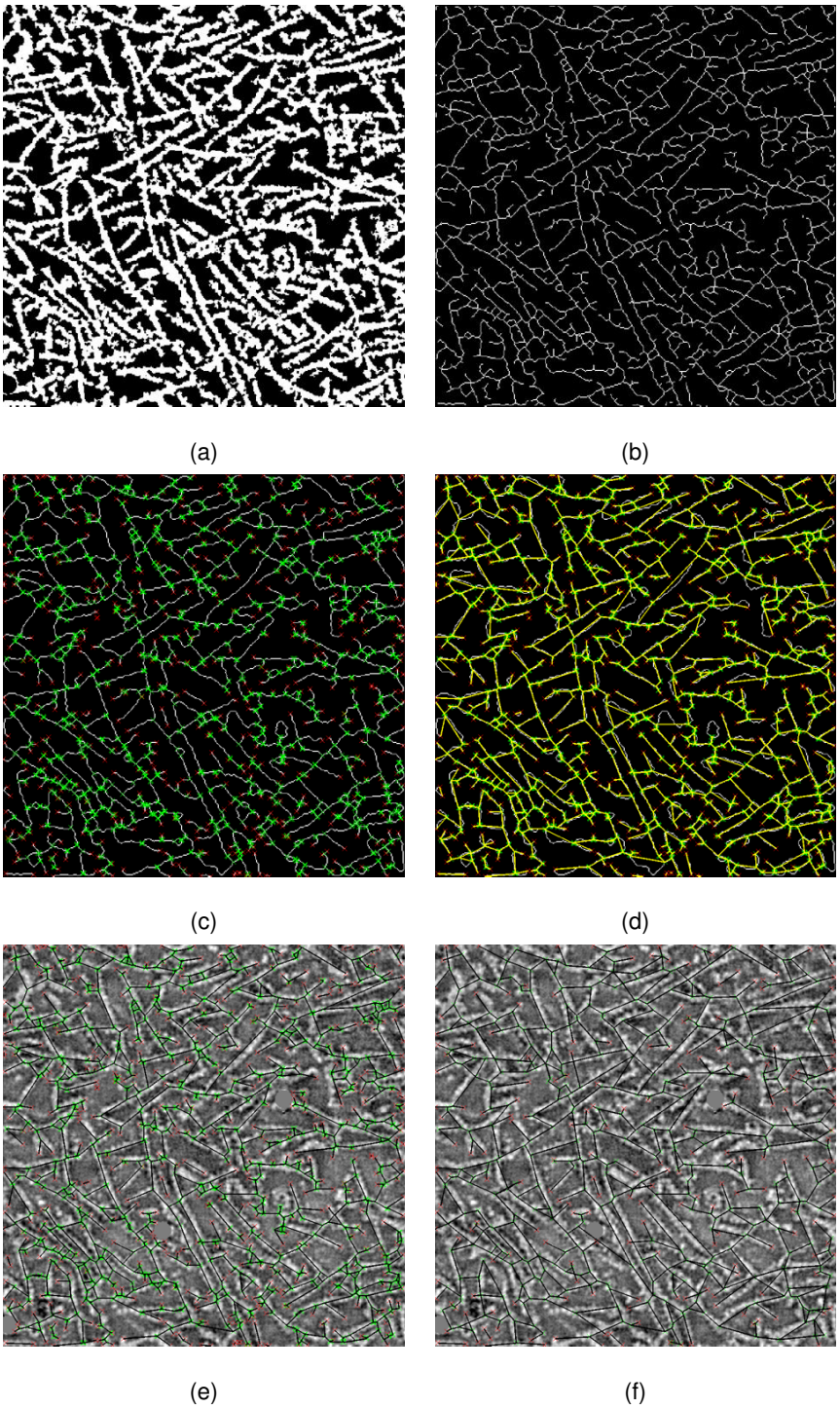

Figure 7.5: Sequential steps of the network extraction procedure. (a) Sample region of the binarized 2D EM image as indicated in Fig. 7.4. (b) Segmented region after skeletonization. The connectivity of segmented objects is not altered in this operation. (c) Nodes are located and classified according to the number of white pixels in their direct neighborhood. (d) An adjacency matrix is constructed, that incorporates which nodes are directly connected by a continuous path of white pixels. An abstract network according to straight links between connected nodes is drawn in yellow. (e) The same graph as in (d) is plotted on top of the original sample section of the gray value EM image for comparison. (f) The extracted network is simplified and corrected to some extend. Unnecessary nodes, short dead ends and small loops are removed, while potential gaps in line segments are bridged.

nodes are often located in their direct neighborhood. We merge these nodes, which efficiently reduces the total number of nodes and therefore the dimension of the adjacency matrix. Newly merged nodes are positioned at the centerpoint of all nodes, that have been considered in merging. They accumulate all connections to outside nodes that were not merged but are connected to any of the merged nodes.

From Fig. 7.5(d) it is also evident that the extracted network incorporates many rather short dead ends. Either these line segments do not correspond to filaments in the gray value image at all or represent filaments that were disconnected due to artifacts in the original image or due to an imperfect segmentation. Therefore, we tried to correct the dead ends in the following way. First, short dead ends are detected in the network as line segments that are shorter than a given threshold, while connecting at least one endpoint with an arbitrary node. Subsequently, the algorithm extrapolates these segments at their endpoint and connects them to other dead ends which are oriented similarly and located close to the extrapolated path. In this way small gaps in filaments due to segmentation failures are bridged. If a connection to another line segment is not possible, the dead end is classified as an artifact and deleted from the network.

An additional artifact of the skeletonization is the appearance of very small loops in the network. Therefore, we are tracing the network for such rather small loops, using a depth first search algorithm. Once a loop is detected, its total circumference is evaluated as the sum of involved line segments. If the circumference is smaller than a predefined value, all nodes in the loop are merged to a single node located in the center of the loop and connected to all outside nodes that were connected to any of the merged nodes.

As a last step, second order nodes, only connected to exactly two other nodes in the network, are analyzed for their importance. Such second order nodes might appear as a result of one of the previous simplification steps discussed above. If the change in orientation of the two connections at the position of such a node is smaller than a predefined threshold, the node is removed and the two connected nodes are linked directly.

For our example region, the final network after correction and simplification is drawn in Fig. 7.5(f). The subsequent Fig. 7.6, shows the abstract fiber network extracted from the full sample slice of the EM data.

Filament tracing

On the one hand, the previous network extraction algorithm yields accurate results for the 2D actin networks that can readily be used to extract the filament orientation distribution from the cells. On the other hand however, there are still also line segments incorporated in the network that do not seem to belong to a specific actin filament when comparing the network results to the original images. In general a network of interconnected nodes does not incorporate information about individual filaments. An actin filament features exactly one starting point and one end point and possible crosslinks or branch points in between those two. To identify filaments with these properties in the network, we implemented an additional 2D filament extraction algorithm. This algorithm traces possible filaments on the extracted 2D networks and calculates a model based score function for possible matches. Subsequently, the score determines if a possible path through the network can be defined as a filament. As we are analyzing 2D slices of a 3D volumetric dataset sequentially, we can not expect to accurately classify real filaments in the network. Actin filaments might leave an analyzed slice in z-direction and disappear, and our 2D analysis is unable to cope with that. However, we expect that it is an interesting approach, which helps deleting dispensable line segments. Also, it could be extended to a three dimensional analysis in the future for a more reliable filament extraction.

The filament tracing routine starts with the extracted network, consisting of a number of

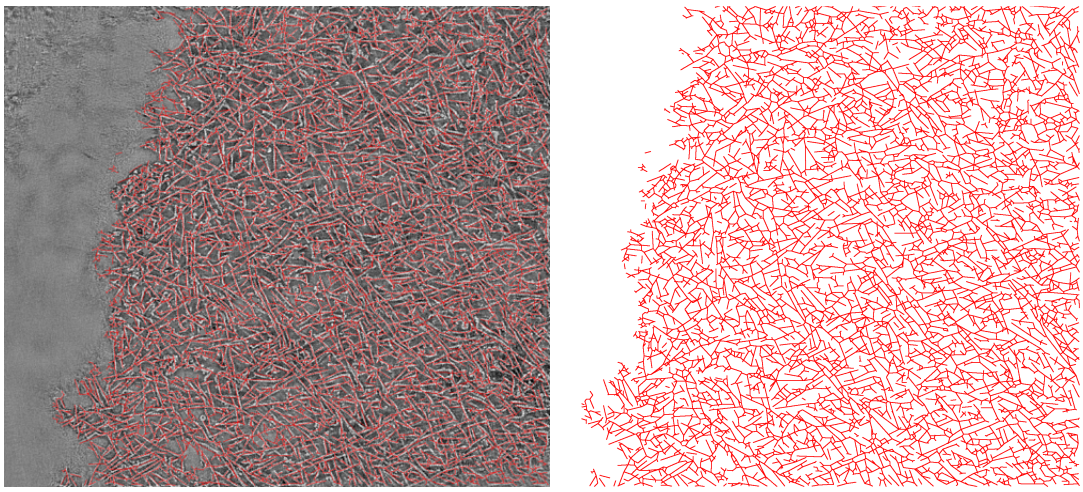

(a) (b)

Figure 7.6: Extracted abstract fiber network as the result of the network extraction algorithm described in the text. (a) For better judgment of the quality of the resulting network, the original gray value EM image is shown in the background. (b) Plot of the extracted network exclusively. Here the subtle structural details of the network are visible.

nodes, their positions and adjacency matrix, like the one shown in Fig. 7.6. Starting at a random endpoint possible filaments are traced up to a maximum depth in the network. If a loop is found in the possible trace, or the accumulated change in orientation over many adjacent line segments exceeds a threshold, the potential filament trace is disregarded in the following. Afterwards a score function is evaluated for all possible filament traces, according to model based properties of actin filaments. In this score, the *filament length* and the *ratio of backbone length and end-to-end distance* and the *magnitude of local changes in segment orientation* are considered and weighted. Subsequently the filament with the highest score is assumed to be most probable and the involved fiber segments are labeled accordingly and deleted from the list of possible filament segments available for later tracing. Fig. 7.7 shows the results of this approach. All filaments are color labeled according to the mean orientation of their segments relative to the leading edge. The left hand side also shows the original gray value sample EM image as a background for comparison, while on the right hand side the assumed leading edge orientation is drawn as a black dashed line. This leading edge orientation was adjusted manually once for all slices in this tomograph stack.

Filament extraction works reasonably well, but not perfect. There are discrepancies to what a human observer would classify as a filament. Additionally, some line segments were deleted in the procedure, which appear relevant to describe the actin network. This is the consequence of the 2D treatment of the volumetric data and our iterative tracing procedure. As a substitute, it could also be possible to implement a Metropolis-like Monte Carlo procedure in the future, globally maximizing a similar score function for all possible filaments in the network simultaneously. Monte Carlo steps could subsequently include the random deletion and reinsertion of line segments in the network and changes in the affiliation of segments to filaments. However, as we are not interested in the details of individual filaments at this point, but rather in the orientation distribution of the whole network. We will see in the following that the results from the network extraction and filament tracing routine do not differ to a great extend. Therefore, we will always consider the results from both approaches, when analyzing the orientation distribution.

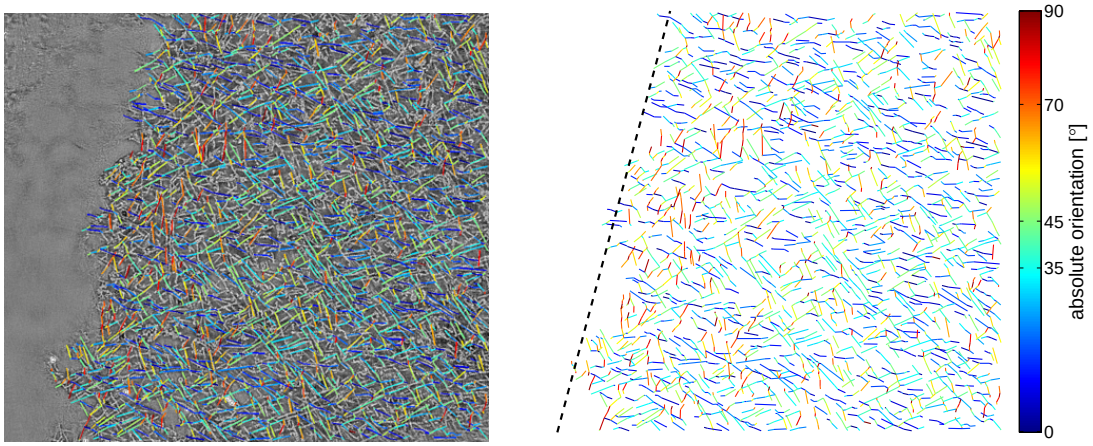

(a) (b)

Figure 7.7: Results from filament tracing. Traced filaments are labeled by their mean absolute orientation relative to a line perpendicular to the leading edge. (a) The original gray value EM image is plotted as the background for comparison. (b) The assumed leading edge to calculate the filament orientation is indicated by the dashed black line.

7.3 Artificial benchmark images

To benchmark the reliability of our two different image processing routines for extracting filament orientation patterns, we rely on a variant of the previously introduced random fiber model. As discussed in Ch. 2 before, the model parameters of the random fiber model are the fiber length l_{fib} and number N_{fib}. Here we will adjust the model in such a way that we can also manipulate the orientation distribution of the fibers. The elementary model incorporated uniformly randomly distributed fibers. Reconsidering the model predictions for the structural organization of lamellipodium actin networks in Ch. 3, we expect two orientation patterns to be especially relevant. Therefore at this point we are switching from uniformly randomly distributed filaments in the random fiber network to distributions with peaks at either $\pm 35^{\circ}$ or $+70/0/\text{–}70$ degrees with respect to some specified line of reference. We are incorporating these fiber distributions as a weighted sum over two or three Gaussian distributions, each with constant standard deviation $\sigma = 15^{\circ}$. In the case of $\pm 35^{\circ}$ networks the weight of both peaks is chosen equal, while for the second $+70/0/\text{–}70$ pattern, the weight of the peak at 0° is chosen twice as high as the constant weight at $\pm 70^{\circ}$.

Fig. 7.8(a) and (b) show two representants of a random fiber model under these conditions. The elementary parameters were chosen as $l_{\mathrm{fib}} = 0.3$ and $N_{\mathrm{fib}} = 300$. Reflecting our different scope in this chapter compared to Ch. 2, here the color of the fibers in the network does not label different clusters, but rather the absolute filament orientations as indicated by the colorbar. The line of reference for measuring these orientations is given in vertical direction parallel to the lateral boundaries of the network. As can be roughly estimated by eye in this orientation labeled representations, the network in (a) was randomly created to simulate a ± 35 pattern, while the complementary $+70/0/-70$ distribution is visible in (b). In (c) and (d) the traced filament networks for the two sample networks above are drawn. The network extraction procedure was applied to a binarized version of the random fiber networks in (a) and (b). Subsequently filaments were traced within the extracted networks as discussed in the main text. Afterwards the resulting filaments were plotted according to their color labeled absolute orientation. Extracted orientation distributions from the exemplary networks according to our two

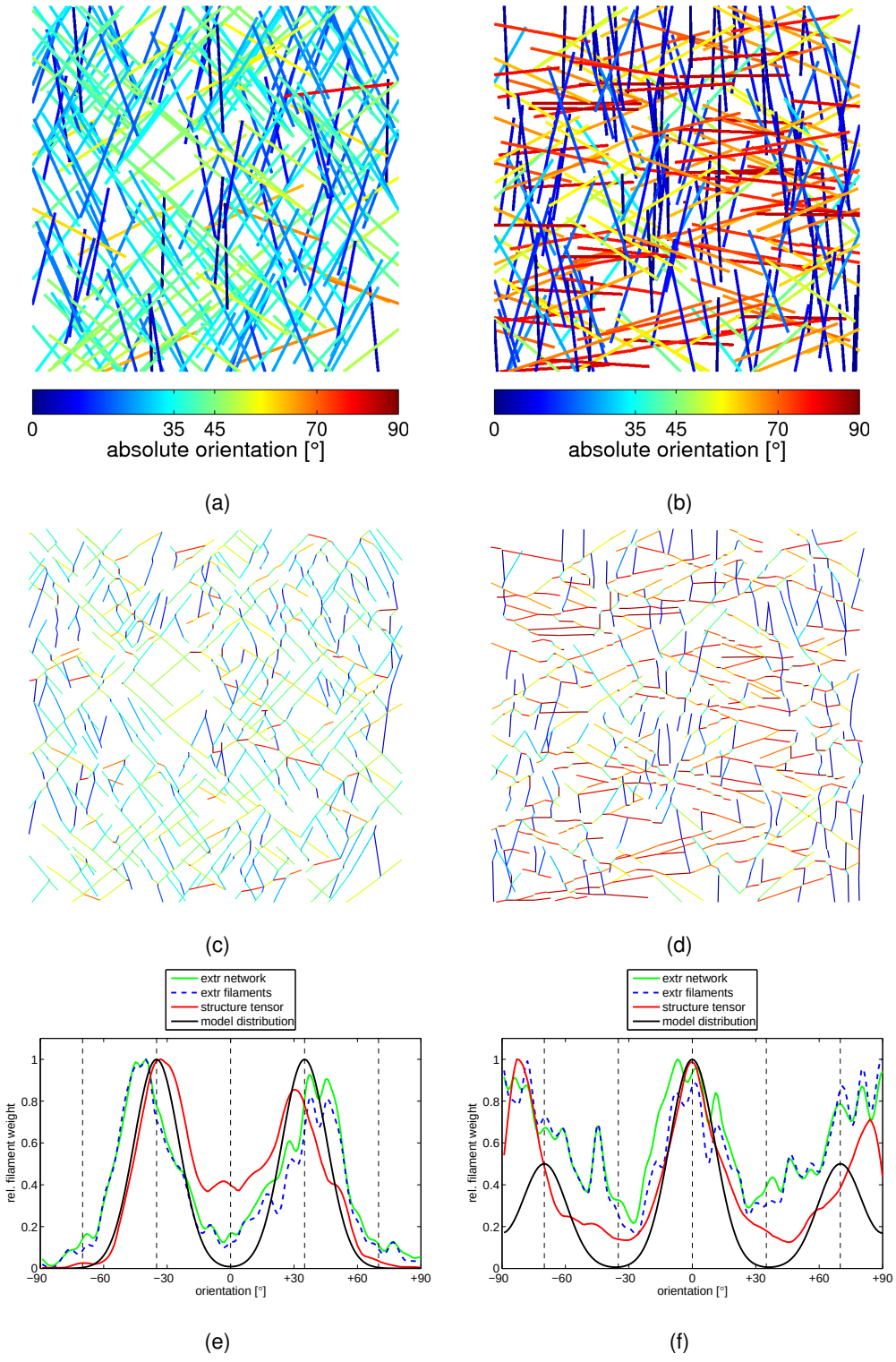

Figure 7.8: Test of the orientation analysis with artificial random fiber networks. (a) and (b) Two realizations of the random fiber networks for $l_{\mathrm{fib}} = 0.3$ and $N_{\mathrm{fib}} = 300$. The orientation distributions are either $\pm 35^{\circ}$ (a) or $+70/0/-70$ degrees (b) as shown in (e) and (f) respectively. (c) and (d) Traced filament networks for the two sample networks above. (e) and (f) Extracted orientation distributions from the networks according to our two independent approaches, using the structure tensor analysis and the network extraction/filament tracing routine. The original distribution used for fiber creation is shown as a benchmark.

independent approaches are shown in (e) and (f). Using the structure tensor analysis and the network extraction routine with or without additional filament tracing, the evaluated orientation distributions are shown. When comparing results from network extraction to filament tracing no major differences can be observed. To obtain the distribution from these two routines, the orientation of each line is considered as a small Gaussian with standard deviation $\sigma = 3^\circ$ weighted with the segment length. In case of the structure tensor the evaluated orientation at each pixel is considered and weighted by the coherency measure c_c at this point. The full distribution is subsequently folded with a Gaussian filter of size 12° and $\sigma = 4^\circ$ to average out fluctuations. All applied methods are able to recover the original fiber orientation distribution of the random networks to a similar, reasonably high degree. The major difficulty arises at the large angles of the $+70/0/-70$ pattern. This is due to the limited separation of the ± 70 peaks. As the orientation of filaments is only defined in an angle domain modulo 180°, the difference between these peaks is only 20°. Apparently, the resolution of the applied analysis is not sufficiently high to resolve those two separated Gaussians.

7.4 Representative actin network analysis

To test our model predictions from Ch. 3, we next analyzed experiments on motile fish keratocyte cells performed by our collaborators in Vienna. The experimental procedure was already discussed in Sec. 7.1. First a live-microscopy movie of crawling fish keratocyte cells on a substrate is taken. After one of the mobile cells slowed down, all cells are fixed. Two snapshots in time from this live-microscopy clip are shown in Fig. 7.9. The absolute velocities of the two indicated cells on the images is not relevant for our considerations. However, it is important to note that cell 1 moves steadily and with approximately constant velocity over the whole recording time, while cell 2 is slowed down due to some perturbation and moves only with relatively slow speed at time of fixation compared to its initial state.

After the cells were fixed, EM tomography images of cell 1 and cell 2 were taken. The position of the EM images lies at a laterally central position of the lamellipodium close to the leading edge of the individual cells. After tomography reconstruction, all slices of the volumetric stack were preprocessed, before the actual filament network analysis started. Here, the contrast of all images was increased and bright prominent marker dots that are necessary for the reconstruction of the tomograph are removed from the images. Example slices of these preprocessed stacks are shown in Fig. 7.10(a) and (b) for cell 1 and 2 respectively. Subsequently the two independent automated orientation analysis routines, i.e. gradient based structure tensor calculus and network extraction, were applied to the images. In case of the structure tensor routine, the preprocessed images were filtered with a median filter to reduce noise before analysis. Results from the filament extraction with color labeled orientation relative to a line perpendicular to the leading edge are shown in Fig. 7.10(c) and (d). Here, also the assumed leading edge orientation is indicated as a separate black dashed line. This leading edge orientation was fitted manually to the stack by visual inspection and assumed constant for the whole stack. The final results for the orientation distribution of the filaments in the lamellipodium networks are shown in (e) and (f) for cell 1 and cell 2. To obtain these distributions, we averaged over twenty adjacent slices in the middle of each stack, where the lamellipodium appeared to be best visible without artifacts from the upper or lower boundaries. The tomograph voxels are cubic and so the spacing in z-direction is equal to the lateral dimensions, $0.746\,\mathrm{nm}$. Therefore, in total we are averaging over around $14.92\,\mathrm{nm}$ in z. Considering typical actin filament diameters around $7\,\mathrm{nm}$ this means that we take into account filaments from at least two independent layers of actin and so the results are not only locally representative but rather for a reasonable fraction of the bulk

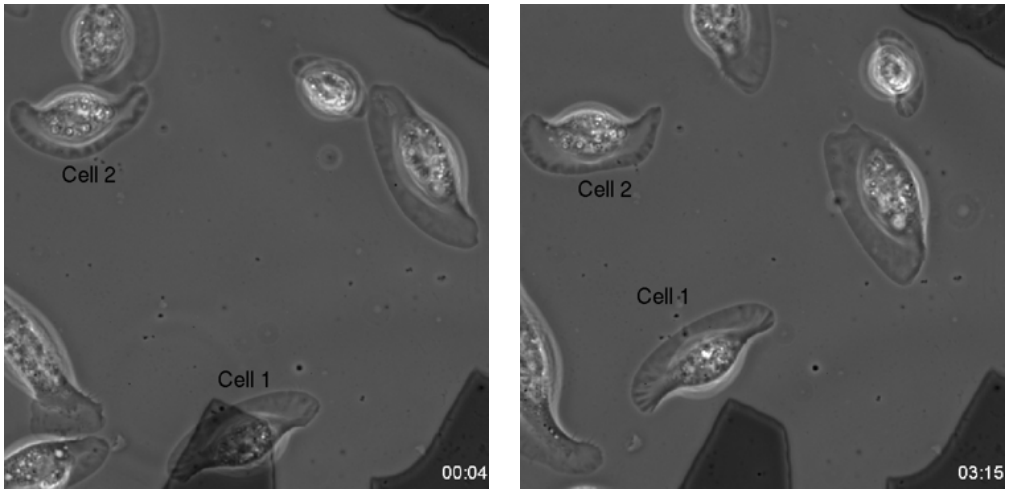

(a) (b)

Figure 7.9: Two snapshots of a live-microscopy video of motile keratocyte cells at the beginning of the recorded movie (a) and just before the fixation of the cells (b). The time code of the individual images is displayed on the respective lower right corner in units of minutes and seconds. The two keratocyte cells that will be analyzed in EM and image processing later are indicated on these images. Cell 1 moves steadily over the substrate at a relatively high velocity. Compared to its initial velocity cell 2 slows down significantly to very slow velocities just before fixation. We will neglect the other cells that are visible on these images in the exemplary analysis.

network. This analysis shows, that we obtain that the actin network protruding in the steadily moving cell 1 features a prominent $\pm 35^\circ$ orientation pattern. Regarding our model this could represent a network protruding in the medium growth phase, which we had classified before as a rather robust state in which cells could move without strong changes in their velocity even for minor external perturbations (cf. Sec. 5.3.1 and the force-velocity relation Fig. 5.6 on page 74). Contrarily, cell 2, which was slowed down before fixation, yields a qualitatively different distribution. First, this orientation pattern spreads to broader angles more parallel to the front and second, a single peak is observed within an angle domain close to perpendicular to the leading edge. Although peaks at ± 70 can not be detected, as would be expected from our model within the slow growth phase, this might be attributed to the close proximity of these populations in orientation space modulo 180° as it was observed for the analysis of artificially created random fiber networks before (cf. Fig. 7.8).

7.5 Summary and outlook

In this chapter we have introduced a possible experimental protocol that could be used in the future to test model predictions resulting from the first part of this thesis. Although it is in principle not trivial to manipulate the protrusion speed of the lamellipodium directly, here we have described a cell motility assay which exploits random changes in the keratocyte motion. Such stochastic events might alter the velocity of the moving cell sufficiently to trigger orientation transitions in the lamellipodium actin networks as predicted by the model. Velocity variations of the cell could be observed in real time with live-microscopy. At the time when one cell in the observed population slows down significantly the whole sample can be fixed using chemical drugs. Afterwards it is possible to compare the actin network at the front of rapidly moving cells to their perturbed counterpart in high resolution EM tomography.

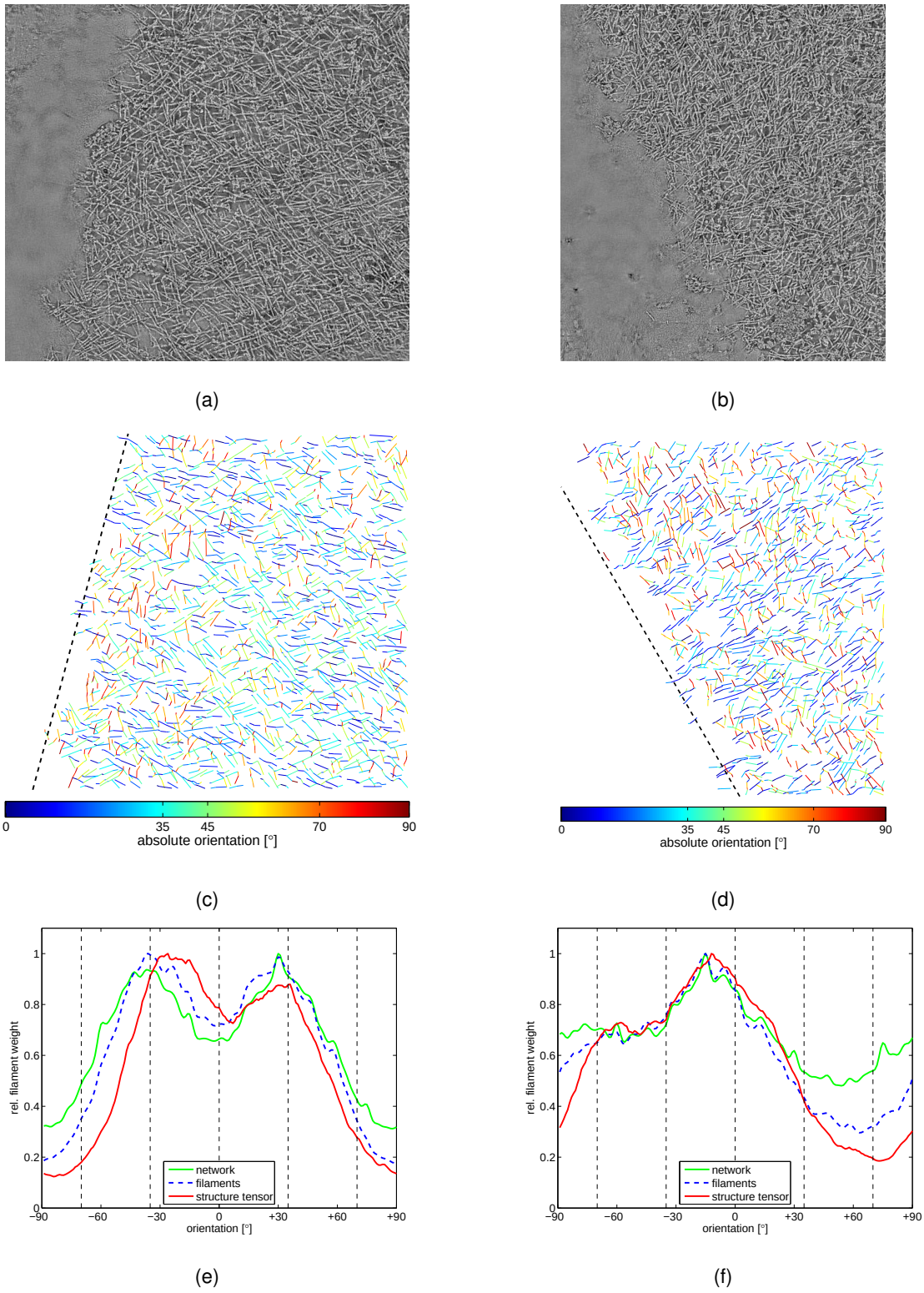

Figure 7.10: Exemplary slices of the EM tomograph and subsequent analysis results. The left hand side corresponds to cell 1 (fast) and the right hand side to cell 2 (slow) as indicated in Fig. 7.9. (a) and (b) Exemplary slices of the original data stack after preprocessing. (c) and (d) Extracted 2D filaments from these images plotted in color coded orientation. (e) and (f) Orientation distributions of the two independent analysis methods averaged over twenty slices of the complete stack (i.e. $20 \times 0.746\,\mathrm{nm} = 14.92\,\mathrm{nm}$). Results from the structure tensor calculus are red and network extraction/filament tracing are green/dashed blue.

For this purpose we have developed two independent data analysis methods for the orientation analysis of the lamellipodium EM images. Both procedures work mostly automated with only minor or no manual adjustments necessary. In the future this would allow to analyze large datasets yielding results of statistical relevance. A possible bias from a human observer is diminished in these objective routines. In detail, we were using an established gradient based structure tensor analysis as a first approach. This method does not incorporate any a priori knowledge that could bias the resulting orientation distributions. As an independent analysis, we have implemented a network extraction algorithm which generates abstract graph representations of the underlying actin networks. The quality of the resulting artificial networks can be tested directly by visual comparison to the original gray value EM images. From this analysis we also extracted another variant by model based tracing of filaments in the extracted networks. Although this measure could in general be biased by the underlying model assumptions for actin filaments, it yields very similar orientation results when compared to the raw extracted networks.

We tested our analysis on artificially created random fiber networks for the two different orientation patterns that were predicted by the model. All approaches were able to reliably distinguish the two patterns and extract a reasonable estimate for the underlying original distribution. However, the two peaks at $\pm 70^\circ$ in the model orientation distribution were not resolved well in image processing. In a proof of principle experiment, testing our protocol we measured and analyzed the actin networks in the lamellipodia of two different cells. One was moving steadily while the other slowed down just before fixation. All three measures from the two independent analysis methods yielded similar results on these two sample cells. The resulting orientation distributions were averaged over 20 subsequent slices of the volumetric EM data. For the fast cell, a dominant distribution with peaks around $\pm 35^\circ$ was measured, which could be attributed to a cell moving in the medium growth phase as defined in Ch. 3. The second perturbed cell featured a broad distribution with a dominant peak at small negative orientation angles. Secondary peaks at $\pm 70^\circ$ which would be expected in the model could not be observed. However, this could be attributed to the limited resolution of the analysis as confirmed with artificial random fiber networks. Hence, the slowly moving cell would hint to motility in the slow growth phase of our model. Still, we were able to evaluate only two sample cells to this point and future experiments have to show, if the obtained results can be confirmed by larger cell populations as well. So far these results are not reliable enough to verify our model predictions unambiguously. Additionally, one could imagine alternative models that also predict changes in the filament orientation for slowed down motile cells. Therefore it would be beneficial if it was possible to also demonstrate the existence of the fast growth phase in living cells. However, it is not clear to this point if our experimental protocol could also yield conditions to trigger this motile state in a keratocyte cell.

Our representative orientation analysis results fit very well to previously published experimental data, where changes in the filament orientation of mouse melanoma cells have been correlated to the speed of lamellipodium protrusion [54]. In this study it was also observed that the orientation distribution broadens for slower velocities of the leading edge. The dominant $\pm 35^\circ$ pattern, that has been observed in the steadily moving cell, has also been reported previously in [66, 108].

In the following chapter, we will not address single filaments as resolved in EM, but rather approach experimental microscopy images of actin networks on a very different length scale. It will turn out that the structure tensor analysis and especially the image coherency that has been introduced in Eq. (7.10) of this chapter, will yield a reliable quantitative measure to characterize actin structures in adherent cells.

Chapter 8

Probing actin bundle networks in fluorescence microscopy

In the previous Ch. 7, we were elaborating on the orientation distribution of filamentous actin networks visible on high resolution EM images. As the experimental amount of work for sample preparation and image acquisition is relatively high when using this imaging technique, commonly only a rather limited number of specimen can be analyzed. Now we are switching from this high content, low throughput approach to an automated high throughput optical microscopy procedure and thus we have to adjust our data analysis techniques accordingly.

Because of the limited optical resolution of standard optical microscopes, like the ones used here, it is not possible to resolve the fine structure of the filamentous actin network in the cell. Therefore this chapter is not concerned about testing any of the specific model prediction made in the first part of this thesis. Rather, our analysis at this point focuses on prominent actin structures like stress fibers and the cortex at the cell boundaries, which are visible as a typical spatial distribution of edges in the overall system. Such screening-like high throughput optical microscopy data has become a common measurement in recent systems biology experiments. Due to stochastic effects, it is quite challenging to quantify specific structural changes in these networks. The key issue is to find a suitable parameter which is sensitive to the relevant changes in the network, while different networks realized for the same set of rules should be ideally indistinguishable. These considerations motivated us to consider *image coherency* as a possible quantitative measure for alterations in the actin cytoskeleton.

We successfully benchmarked our analysis by calculating coherency for both, a variant of the random fiber model for the actin cytoskeleton and for cells whose actin architecture had been disturbed pharmacologically by latrunculin B or cytochalasin D. As a biologically relevant application of our newly introduced automated workflow, we tested the influence of HIV-1 infection on actin coherency.

8.1 Experimental strategy and workflow

On a cellular level, different cell-based screens have been developed to classify morphological phenotypes [25, 81]. For instance, this method has already been applied successfully to drug profiling [83], quantifying viral infection [68] and determining drug effects on cell adhesion [80]. To analyze a large amount of images in an automated fashion, appropriate methods have to be developed to quantify morphological changes in the actin cytoskeleton. Here we combined automated fluorescence microscopy and image processing with biophysical modeling to arrive

at a validated workflow which allows us to quantify structural changes in the actin cytoskeleton of adherent cells.

All experimental sample preparation and image acquisition was done by our collaborating colleagues **Nikolas Herold** and **Maik Lehmann** in the group of **Hans-Georg Kräusslich** from the *Department of Infectious Diseases, Virology* of the *University Hospital of Heidelberg*. For this study, we used an Olympus inverted autofocus multicolor epi-fluorescence microscope. Acquisition of three-color z-stacks at 100 positions for each well of a Lab-Tek 8-chambered cover glass was carried out sequentially without any interruption to ensure a maximum of comparability. The positions were defined as a 10×10 matrix with an arbitrary row and column spacing, whereas the center point of the matrix was determined manually to be in the middle of the chamber. Volumetric stacks were acquired to compensate for failure of autofocus and to be able to analyze the whole cell actin morphology. Using these methods, we performed a screening-like image acquisition resulting in 48000 raw images for a single experimental setup to be computationally processed and analyzed.

For this purpose, first the mean local contrast of all associated actin stained images was approximated for each z-stack. The cell area lying within the stack was estimated by applying *Otsu*'s method [79] for segmentation to one representative image of the stack. After subsequent hole filling of the cell area, the relative local contrast, i.e. the mean relative difference of a center pixel to all of its eight neighbors, was calculated for a large number of random positions within the boundaries of the cells. Afterwards, the mean of the contrasts from all of these positions was taken as an estimate for the mean local contrast of the image. For each z-stack, the image with the highest mean local contrast was chosen for the following evaluation, assuming that it carries the most important structural features of the cytoskeleton. As the stacks were taken at random positions within the sample, not every image contained a sufficient amount of information to be evaluated. To rule out empty or nearly empty image-stacks, the coherency (cf. Sec. 8.2) was calculated, and only those pictures exceeding a constant threshold for the total area of non-vanishing coherency pixel underwent further analysis. Feature analysis was performed, consisting of the calculation of the *relative actin density per cell area*, the *relative coherency per cell area*, the *mean coherency per image*, and the statistical evaluation of these parameters. Eventually, we evaluated an estimator for the parameter mean and its corresponding standard deviation from all images for each sample.

8.2 Coherency as a quantitative measure for structures

A fluorescence image of a biological system is a two dimensional quantized representation of the density of a specific marker molecule. Care has to be taken when extracting a relevant and operative measure from these images. Here we suggest that *image coherency* as defined already in Sec. 7.2.1 is an adequate quantitative parameter for the problem at hand. In contrast to pattern recognition approaches like neural networks or vector-support machines based on motion-invariant image features like the Haralick texture features or Zernike moments [9, 19, 39], which are well-suited for classification of distinct subcellular phenotypes, the coherency measure appears to be particularly suited to characterize gradual changes in fibrous textures like the actin cytoskeleton. By its definition, coherency extracts the relative strength of the edges of structures compared to their surroundings [49]. Thus, the parameter is a measure for the quality and amount of clear structures in an image. It has been used before in the biological context to detect features of moving filaments in actin-myosin motility assays [92], but not yet as a measure for the organization of the actin cytoskeleton.

Image coherency has been defined in Eq. (7.10) on page 93. As mentioned previously this

image feature is able to differentiate an area of constant gray values ($J_{x'x'} = J_{y'y'} = 0$) and an isotropic noise ($J_{x'x'} = J_{y'y'} \neq 0$) from clear network structures, like oriented edges ($J_{x'x'} > 0 \wedge J_{y'y'} \simeq 0$). Indeed c_{c} varies continuously between 0 and 1, extracting a normalized parameter for the observed structures at each pixel in the image. Hence, it is able to distinguish large-scale cytoskeleton constituents, like stress fibers or the cortex, from smaller actin speckles or the diffuse background in the cytosol and measures the amount and quality of structures in the cells on our images, accordingly. Again, to overcome the singularity in the coherency definition at $J_{x'x'} + J_{y'y'} \simeq 0$, c_{c} is set to zero in this case.

As the coherency is readily defined by the structure tensor in Eq. (7.4), the only free parameters in the calculations are determined by the shape and size of the window function, given by $\mathcal{G}$. Again we are using a rotationally symmetric Gaussian smoothing operator of size $h_{\mathcal{G}}$ with standard deviation $\sigma_{\mathcal{G}}$. Fig. 8.1 compares an original actin stain of a latrunculin B treated cell (a) with its coherency mapping as a function of the size of the window function (b)–(d). Apart from prominent cortical actin structures, small speckles are visible within the cell body, as a result of the treatment with the actin drug in the original image. The impact of such smaller structures is averaged out more and more in the feature images with increasing size of the window function. The large-scale structures, however, remain clearly visible and maintain a high coherency. Based on visual inspection of such images, we chose an intermediate size for the window function ($h_{\mathcal{G}} = 15$ and $\sigma_{\mathcal{G}} = 5$ pixel) to evaluate actin networks in this chapter.

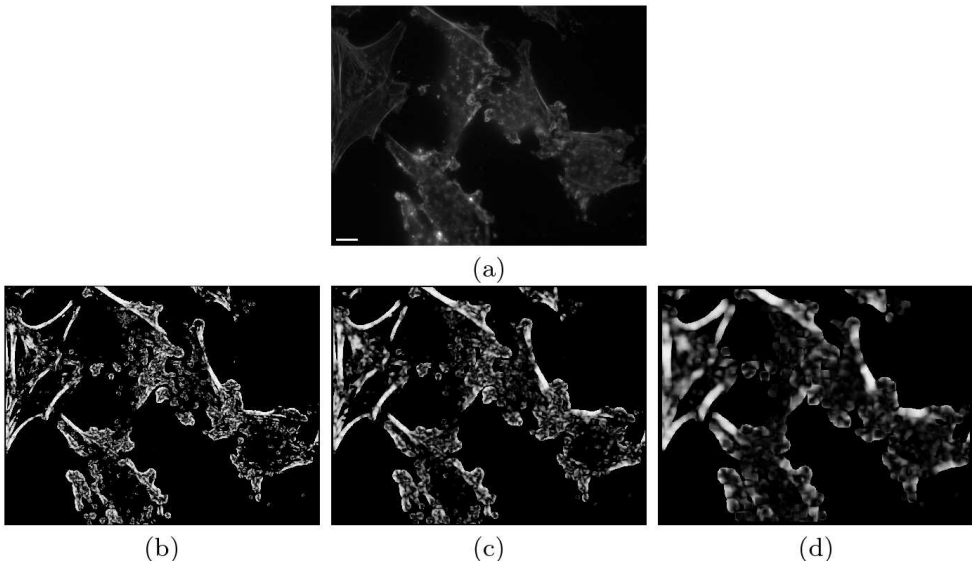

Figure 8.1: Impact of size and shape of the window function on the coherency image. (a) JC-53 cells treated with latrunculin B and stained for F-actin. In these cells, large-scale cortical structures are present, as well as small speckles due to the drug treatment. (Scale bar shows $10\ \mu m$.) (b), (c) and (d) Coherency images with $h_{\mathcal{G}} = 9$, $\sigma_{\mathcal{G}} = 3$ (b), $h_{\mathcal{G}} = 15$, $\sigma_{\mathcal{G}} = 5$ (c) and $h_{\mathcal{G}} = 30$, $\sigma_{\mathcal{G}} = 10$ (d). The size and spread are given in pixel. With increasing size of the window function, small structures are averaged out and lose weight in the coherency image.

Since we are using an automated image acquisition without any preselection for our experiments (cf. section 8.1), the cell area as well as the number of cells in each image varies. In order to statistically evaluate and compare the results of several pictures with each other some normalization procedure for the extracted parameters had to be introduced. On the one hand, we measured the total coherency of an image relative to the total cell area within the image and, on the other hand, the mean coherency. The *coherency per cell area* accounts for the amount or density of structures within the cells, while the *mean coherency per image* is a measure for

the quality of the structures, independent of the frequency of their occurrence.

We segmented the cell area by applying *Otsu*'s method [79] and a subsequent hole filling procedure to obtain a binary image. Concerning the experiments with adherent cells on HIV-1 coated substrates (section 8.5), we used the actin stain for this routine, as it did not change in a way that altered the segmentation. However, for cells which were treated with actin drugs (section 8.4), we used an independent microtubule stain for the area estimation to rule out strong correlations between changes in the actin coherency/density and the cell area (cf. Fig. 8.2). For all cytoskeleton model images processed in the context of Sec. 8.3, the area was chosen to be constant.

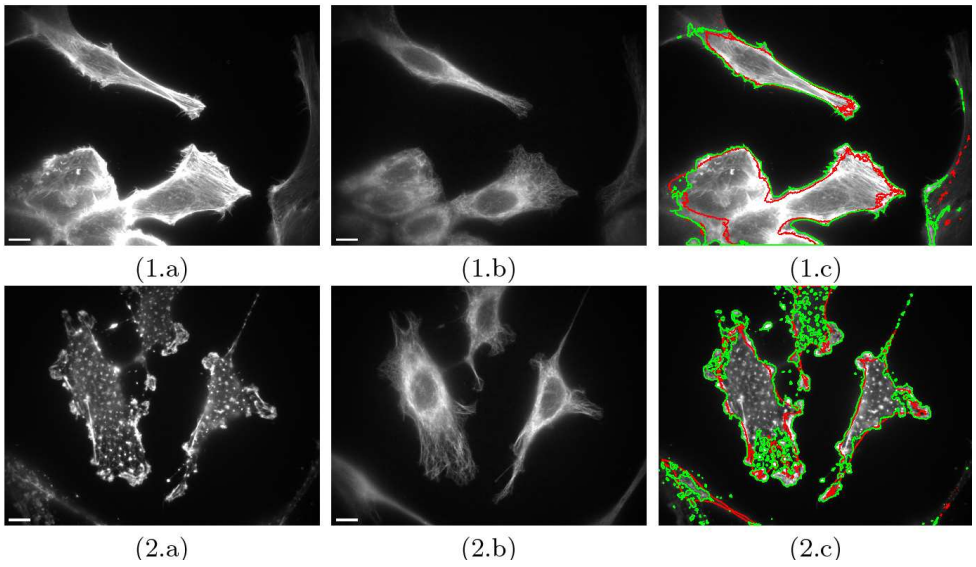

Figure 8.2: Effect of treatment with $1\ \mu M$ latrunculin B on cell area segmentation. (1) Control cells; (2) inhibited cells; (a) actin stain; (b) microtubule stain; (c) segmented cell area for normalizing the extracted coherency and actin density according to *Otsu*'s method using the actin (green) or microtubule (red) stain. The original actin stain is shown as well. For the control cells, the area segmentation according to both stains yields similar results, while for the cells treated with latrunculin B, the size of the cell area is systematically under-estimated. To rule out correlations of the actin coherency and density with the segmented cell area, the segmentation was done according to an independent microtubule stain for the actin toxin experiments (Sec. 8.4). Scale bars always represent $10\ \mu m$ in the images.

8.3 Simulated benchmark images

To test our newly introduced image analysis workflow, we return once more to another variant of the random fiber model as introduced in Ch. 2. To reflect the relatively low optical resolution of the high throughput microscopy facility at this point, we adjusted the model accordingly again. For our purpose, each fiber in the network represents a bundle or thick fiber consisting of many individual actin filaments. Hence, we introduced two additional parameters in the model, namely the bundle strength s_{fib} and width w_{fib}, which parameterize the density and spatial extension of the bundle. The elementary parameters fiber number N_{fib} and length l_{fib} however, also enter the model as described before. We chose the position and orientation of each fiber uniformly randomly again, while its length, number, width and strength were either held constant or chosen from Gaussian random distributions, which are characterized by their mean and their standard deviation. Our simulated networks do not claim to reflect the detailed organization of

single cells, but rather represent the average degree of network formation over an ensemble of many cells. Therefore, the simulated samples presented below (cf. figures 8.3–8.6) do not resemble the images of single cells, although the corresponding feature extraction does.

Thus, it is possible to mimic different situations for structural changes in cells: the number of fibers, their length, strength and width were increased individually to simulate the variable degree of structure formation. For a constant total fiber length in the images (which corresponds roughly to a stationary overall gray value density), the number of fibers was reduced. This mimics the depolymerization of actin bundles and the occurrence of small speckles induced by actin drugs.

We created five realizations of a single network as a function of one or two model parameters. As we initially only analyzed a single image as a representative for each realization, we first had to avoid strong stochastic variations in the networks. Therefore, all parameters, which were not changed explicitly, as well as the initial random positions and orientations of the fibers were kept constant throughout the different realizations. However, later we demonstrate the benefit of an automated technique, when dealing with large variations in the parameters over many realizations. In this case, the model parameters are not defined explicitly but rather the mean and the standard deviation of the corresponding Gaussian distributions. Subsequently, we applied our automated approach to a large number of images for each ensemble of networks.

For an increasing number of fibers in the artificial networks (Fig. 8.3(a)–(e)), the relative fiber density per area (blue), as well as the coherency per area (green), were increasing as expected (Fig. 8.3(f)). The mean coherency of the images (red) however decreased with an increasing fiber number. As this parameter measures the average quality of structures independent of their amount, it is in general possible that an image with only one fiber with perfectly oriented edges might have a higher mean coherency than an image with several fibers. In these examples, the quality was actually decreasing, because the crossing points between different fibers did not feature clear structural details. As their number increased, the mean coherency decreased. Similar results were obtained for constant fiber number with an increasing length of each fiber (not shown).

For the simulated images, both coherency measures were not sensitive to an increase in fiber strength (i.e. mean gray value of the fibers). This is due to the fact that the coherency does not measure the absolute gradient at the fiber edges, but rather compares the difference of the dominant squared gradient to its orthogonal counterpart, i.e. the two eigenvalues of the structure tensor. As we put perfect rods without any background noise in our benchmark images, there was basically just one non-vanishing gradient at the boundaries of the fibers, while the magnitude of the gradient orthogonal to the fiber edges was negligible. Therefore, the fiber strength itself was not detected by the coherency (not shown). However, the situation dramatically changed when we introduced additional Gaussian white noise to the same images, reflecting conditions of biological experiments (cf. Fig. 8.4(a)–(e)). In this case, the smaller eigenvalue of the structure tensor help a finite value, and the absolute strength of the fibers indeed caused a difference in coherency. Now, both coherency measures were able to detect the difference in fiber strength much better than the relative fiber density (Fig. 8.4(f)).

In the previous examples, structural changes were not only detected by the coherency but also by the fiber density per area. Therefore, in the following, the density of fibers was kept constant by increasing the fiber number, while reducing their length accordingly (Fig. 8.5(a)–(e)). This procedure simulates the disruption of stress fibers and occurrence of small speckles due to depolymerizing actin toxins. Here, both coherency measures were sensitive to the changes, but the relative actin density differed only slightly (Fig. 8.5(f)). Thus, in this case, extraction of coherency was required to yield meaningful results.

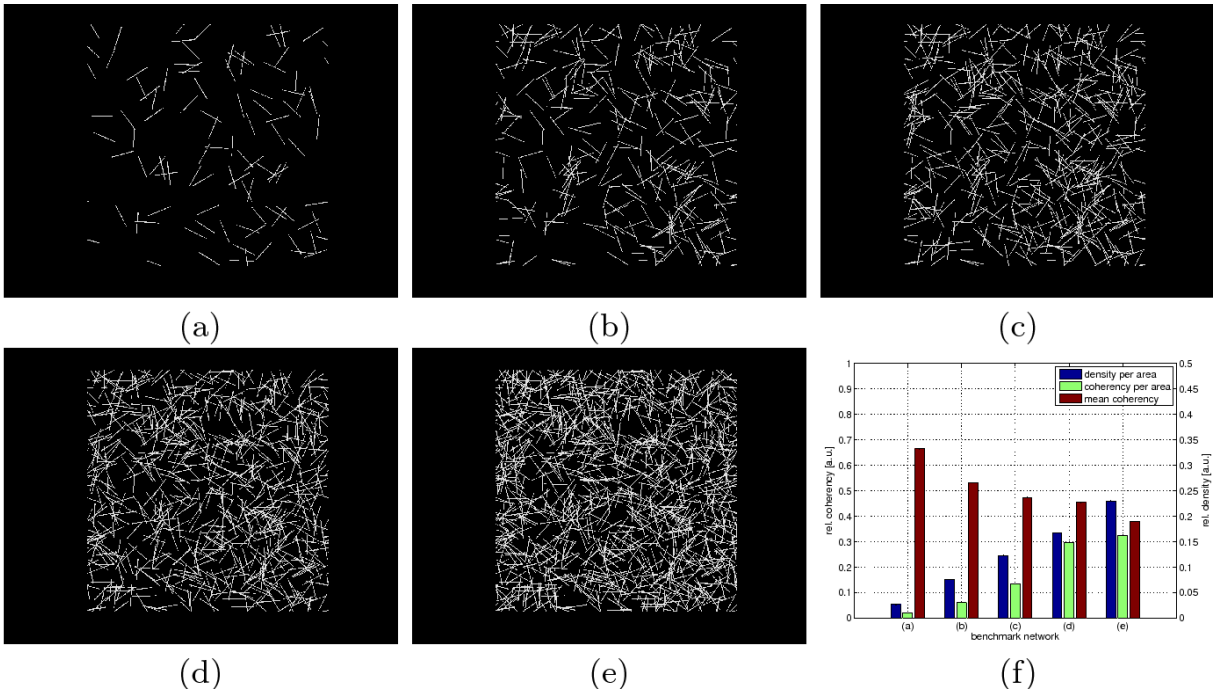

Figure 8.3: Random fiber networks with increasing total number of fibers. (a) $N_{\mathrm{fib}} = 100$, (b) $N_{\mathrm{fib}} = 300$, (c) $N_{\mathrm{fib}} = 500$, (d) $N_{\mathrm{fib}} = 700$, (e) $N_{\mathrm{fib}} = 1000$. (f) Plot of the extracted parameters, namely the averaged gray value density, the coherency per area, and the mean coherency of each image.

The benefit of computer-aided automatic image feature extraction clearly is the correct statistical evaluation of a large number of images, omitting the observer bias. Figures 8.6(a)–(e), feature randomly chosen representatives of network ensembles, with respect to changing Gaussian distributions for the fiber number, strength, and width. Additionally, background noise was incorporated. These networks are highly variant, and it is now much harder to detect significant changes in the example images by eye. The statistical evaluation of the coherency of a hundred images for each network type however was able to clearly detect the changes in the network structures (cf. Fig. 8.7). As we averaged the parameters over several images for each network ensemble, an estimator for the standard deviation of the mean can be given accordingly, as well as a box plot of the measured observable distribution. These networks were created with a roughly constant gray value density, and the density parameter was not able to detect a clear tendency in the changes. In contrast, both coherency measures revealed a clear tendency in the network differences from (a) to (e). These theoretical results encouraged us to apply our newly developed procedure to experimental data.

8.4 Cells treated with actin toxins

We next applied the automated image processing setup to JC-53 cells treated with the actin toxins cytochalasin D and latrunculin B. JC-53 cells adhere to surfaces suitable for two-dimensional tissue culture. As they are flat, they occupy a large area on the cover glass which is virtually in one plane. Staining of actin with fluorescent phalloidin conjugates exhibits actin structures such as focal adhesions, stress fibers, filopodia and the actin cortex, which can be easily monitored by epi-fluorescence microscopy. Cytochalasin D leads to the depolymerization of F-actin, whereas latrunculin B inhibits actin polymerization by sequestering globular actin, resulting in

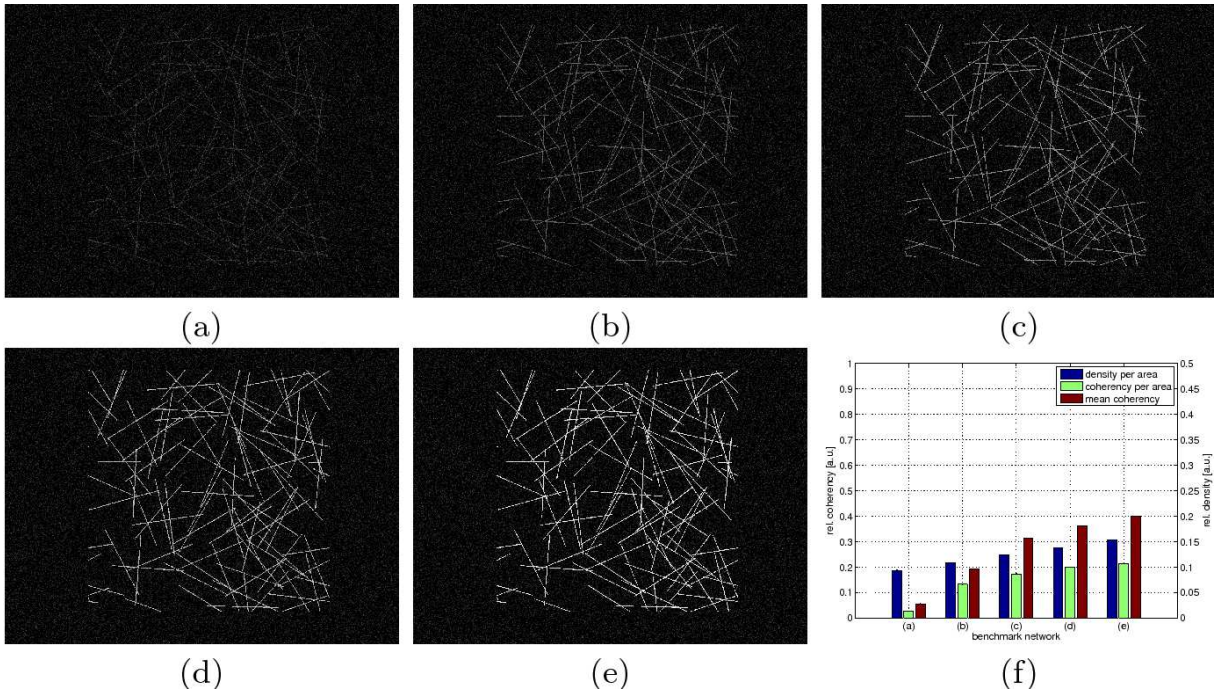

Figure 8.4: Random fiber networks with increasing fiber strength. (a) $s_{\mathrm{fib}} = 0.2$, (b) $s_{\mathrm{fib}} = 0.4$, (c) $s_{\mathrm{fib}} = 0.6$, (d) $s_{\mathrm{fib}} = 0.8$, (e) $s_{\mathrm{fib}} = 1$. The fiber strength s_{fib} is defined as the intensity of the fiber gray values in the image in the range from zero to one. Gaussian white noise was added to the images. (f) Plot of the extracted image features.

the disruption of F-actin over time. We analyzed 96–100 images per assay in this experiment. Figures 8.8(a)–(h) show an example for each experimental condition and figure 8.9 displays the coherency results. Cells were either treated with increasing concentrations of one of the two actin toxins (cf. Fig. 8.8(c)–(e) and (f)–(h)), or with solvent only in two control populations (cf. Fig. 8.8(a) and (b)).

Cytochalasin D treated cells exhibited a substantial decrease in either of the two coherency measures ((c), (d) and (e)) compared to the controls ((a) and (b)), but no concentration-dependent differences. Measuring the actin density, in contrast, was unable to clearly differentiate the samples treated at the two lower concentrations of the toxin from the controls. For the lowest concentration of cytochalasin D, the relative actin density per cell area (c) was even larger than observed for the control populations. For latrunculin B ((f)–(h)), both parameters showed a clear decrease in coherency at higher toxin concentrations, whereas no difference was observed at the lower toxin concentration. No structural differences were observed by visual inspection of cells treated with this toxin concentration, either. In all cases, a detailed analysis showed that the actin structures at the cell borders played a minor role for the coherency measure, which was dominated by the actin structures in the cell body due to its larger extension (data not shown).

We performed two-sided statistical tests of the null hypothesis which states that the means of two different assays in Fig. 8.9 are equal, with a significance level of 5% [40]. The corresponding p-values are given in Tab. 8.1. Under these circumstances, we accepted the hypothesis for the means of the two controls ((a),(b)) in all three parameters. When we tested the hypothesis pairwise for actin toxin treated samples and the two controls, we could not reject the hypothesis for ((a),(d)) and ((b),(d)) in the density as well as ((a),(f)) in both coherency measures, and ((b),(f)) in the coherency per cell area, respectively. We conclude from this analysis, that actin

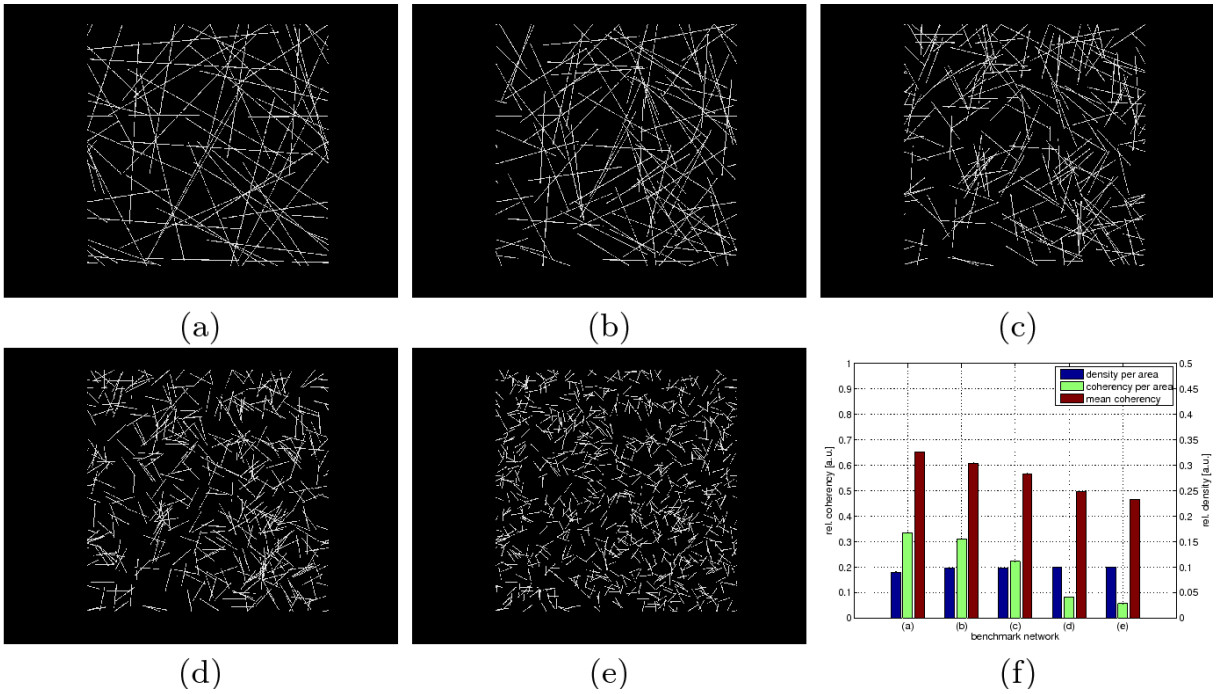

Figure 8.5: Random fiber networks with constant density. As the fiber length is reduced their number is increased accordingly: (a) $N_{\mathrm{fib}} = 50$, $l_{\mathrm{fib}} = 0.8$, (b) $N_{\mathrm{fib}} = 100$, $l_{\mathrm{fib}} = 0.4$, (c) $N_{\mathrm{fib}} = 200$, $l_{\mathrm{fib}} = 0.2$, (d) $N_{\mathrm{fib}} = 400$, $l_{\mathrm{fib}} = 0.1$, (e)$N_{\mathrm{fib}} = 800$, $l_{\mathrm{fib}} = 0.05$; This way, large-scale structures evolve, which can not be detected in the gray value density, but rather with either of the two relative coherency measures (f).

density shows strong non-specific variations in the experiments and is therefore not a reliable measure for the structural changes of the actin cytoskeleton. However, coherency is able to detect and quantify morphological differences induced by the actin toxins.

8.5 Cells treated with HIV-1

Due to its importance for the spatial coordination of the host cell, the cytoskeleton is also one of the major targets for changes induced by cellular pathogens [51, 77]. Despite the large medical relevance of this interaction, the exact underlying mechanisms are in many cases still unknown. We have already discussed an actin based propulsion mechanism theoretically in Ch. 4, which can be exploited by Listeria or Vaccinia virus amongst other pathogens. Here, we will focus on HIV-1 as a medically highly relevant pathogen whose specific effect on the actin cytoskeleton is not yet well understood [109]. However, since its discovery as causative agent of AIDS in 1983 [31], extensive efforts have been made to study HIV-1.

Viruses rely on cellular metabolism for their replication and can be used also as probes to study the host system (cf. Fig. 8.10). Thus, viruses are also important tools to better understand the biology of the cell. In the case of HIV-1, binding to the cell via its envelope glycoprotein has been reported to induce actin remodeling [4], calcium signaling [70] and chemotaxis [4]. The life cycle of HIV-1 is known to relate to various additional aspects of the cytoskeleton. This includes virus surfing along actin rich cell protrusions to reach the cell body [62], crossing the cell cortex after fusion [55], transport towards the nucleus [24] and spreading of the newly synthesized virions to new target cells in the proximity [26, 52]. Indeed, it has been shown earlier that an intact actin cytoskeleton is necessary for successful HIV-1 infection [13], but

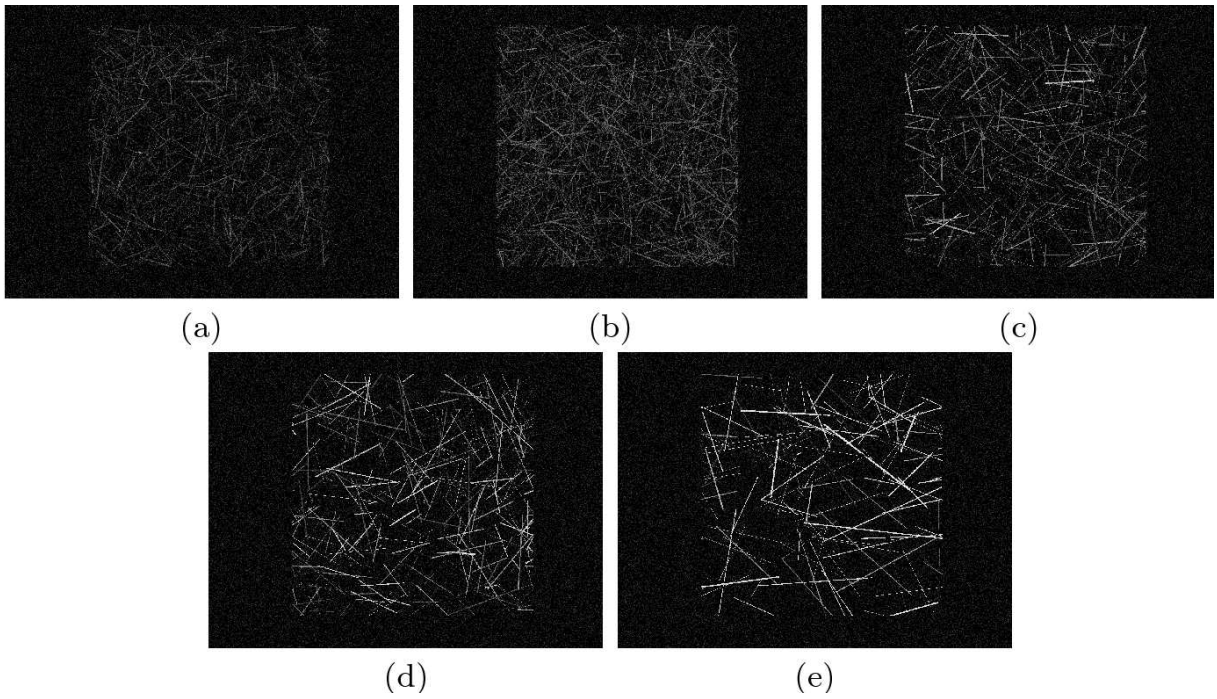

Figure 8.6: Example images from different random fiber network ensembles. The Gaussian parameter distributions of the fiber number, strength, and length have been chosen such that the mean gray value density remains roughly constant, but the quality and amount of the inherent structures increases: (a) $\langle N_{\mathrm{fib}} \rangle = 2250$, $\langle l_{\mathrm{fib}} \rangle = 0.1$, $\langle s_{\mathrm{fib}} \rangle = 0.2$, (b) $\langle N_{\mathrm{fib}} \rangle = 1500$, $\langle l_{\mathrm{fib}} \rangle = 0.12$, $\langle s_{\mathrm{fib}} \rangle = 0.25$, (c) $\langle N_{\mathrm{fib}} \rangle = 750$, $\langle l_{\mathrm{fib}} \rangle = 0.15$, $\langle s_{\mathrm{fib}} \rangle = 0.4$, (d) $\langle N_{\mathrm{fib}} \rangle = 375$, $\langle l_{\mathrm{fib}} \rangle = 0.2$, $\langle s_{\mathrm{fib}} \rangle = 0.6$, (e) $\langle N_{\mathrm{fib}} \rangle = 150$, $\langle l_{\mathrm{fib}} \rangle = 0.3$, $\langle s_{\mathrm{fib}} \rangle = 1$; The standard deviation of the Gaussian distributions is always chosen relative to the corresponding mean at $0.5 \cdot \langle X_{\mathrm{fib}} \rangle$.

the details of this phenomenon are still unknown. The rapidly increasing availability of high throughput microscopy setups now opens up the perspective that such an issue can be clarified within an automated approach. However, such an approach requires the development of new techniques for cell culture and data processing, including quantitative measures which are able to characterize alterations in the host cytoskeleton in a high throughput manner.

Therefore, we finally checked if HIV-1 binding to and entry into the cell, which is mediated by the viral envelope glycoprotein, detectably alters the actin cytoskeleton. To yield a maximum of virus-cell interactions in the focal plane at the bottom of the cell, JC-53 cells were seeded on 8-chambered Lab-Teks which were precoated with HIV-1 (cf. Fig. 8.11). To test whether possible effects are specific for HIV-1 and not simply due to the steric properties of the viral spheres, HIV-1 particles bearing or lacking the envelope glycoprotein were used.

Two independent experiments were performed, and the mean values of both coherency parameters as well as actin density were compared pairwise (cf. Fig. 8.12(a) and (b)). Apart from the usual variations, no reliable difference in any of the three parameters was found over both experiments. We additionally performed similar statistical tests as before. They did not reveal a clear tendency for an HIV-1-specific effect on the structure of the actin cytoskeleton, concerning all three parameters for two independent experiments. Thus, interaction of HIV-1 and the actin cytoskeleton might simply not result in detectable remodeling of the actin architecture. Yet another interpretation, fitting our experimental results, would be that remodeling rather occurs on the single particle level (e.g. only directly at the position of virus entry), and may only become evident at higher resolution [34]. In these cases, our established microscopy workflow and image feature analysis would not be sensitive enough to deal with such subtle

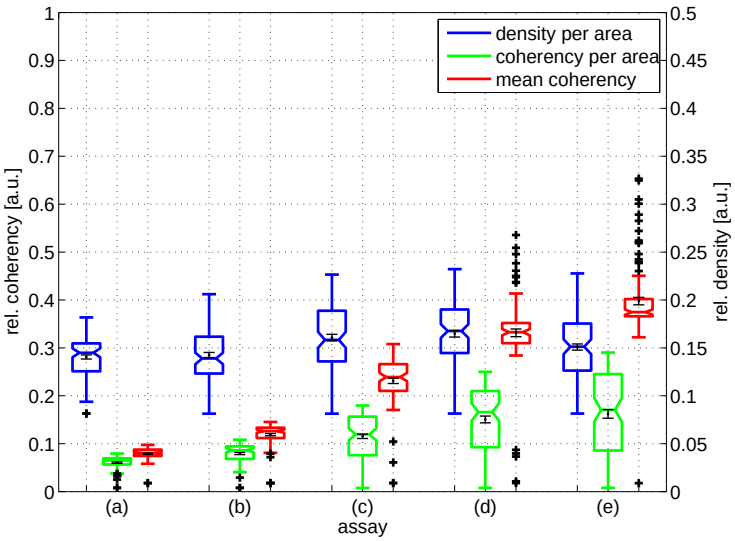

Figure 8.7: Box plots of the density per area (blue), coherency per area (green) and mean coherency (red), extracted from the network ensembles in figures 8.6(a)–(e). For each parameter the box plots indicate the estimated mean and its corresponding standard deviation (black dot with error bars), the median (horizontal line dividing the box), the lower and upper quartile, i.e. $25th$ and $75th$ percentile (lower and upper boundary of the box), the farthest measurement still within the 1.5 interquartile range (whiskers), outliers (+) and the symmetric 90% confidence intervals of the median (notches). Although the randomly chosen images in figures 8.6(a)–(e) cannot be distinguished well by eye, due to the strong variations in the parameters of the different ensembles, the statistical evaluation of the coherency from a large number of these images is able to average out non-specific variations, and is therefore sensitive to the changes in the network parameters.

rearrangements of the actin structures.

8.6 Summary and conclusions

We have shown that image coherency, i.e. the quality and amount of clear structures in an image, is a suitable measure to detect global alterations in the organization of actin cytoskeleton networks. We could verify this theoretically, by processing artificially created samples from a variant of the random fiber model (cf. Ch. 2) with exactly defined properties, and experimentally, by measuring the impact of actin-disrupting drugs on coherency. We thereby established an automated workflow, combining automated fluorescence microscopy with a screening-like approach, subsequent computational image analysis and biophysical modeling. Due to our high throughput approach, statistical significance was very high. We are therefore able to reliably detect even very small effects on actin coherency. Furthermore, an automated image acquisition and analysis again minimizes artifacts due to an potential observer bias.

In the future, this procedure could be implemented for a wide range of biological applications dealing with structures accessible to automated microscopy. Here, we have shown that infecting susceptible cells with HIV-1 had no effect on the coherency of the actin cytoskeleton on the length scale of our resolution and detection limits, independent of virus amount and time. We cannot conclude that HIV-1 has no effect on the spatial organization of actin in its early life cycle, but our results suggest that these effects - if any - are rather subtle. Either HIV-1 induced effects do not affect actin coherency, or a potential impact on the coherency may only become evident at a higher resolution and thus needs super-resolution light or electron microscopy. Thus, even almost three decades after identification of HIV-1, exploring its interactions with the cytoskeleton remains a challenge.

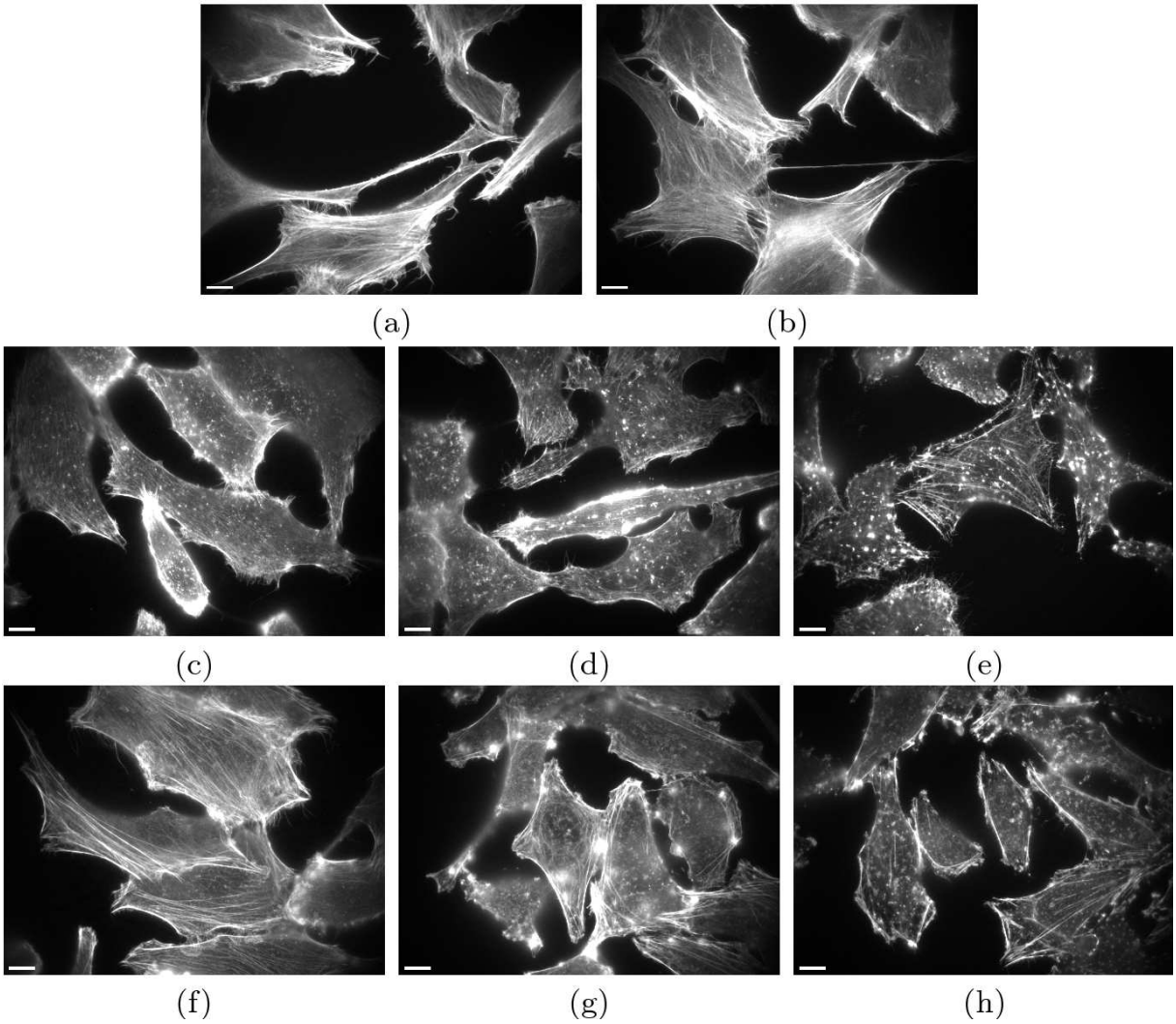

Figure 8.8: Randomly chosen images for the different cell assays: (a) control 1, (b) control 2, (c) cytochalasin D $0.5\ \mu M$, (d) cytochalasin D $1\ \mu M$, (e) cytochalasin D $2\ \mu M$, (f) latrunculin B $0.25\ \mu M$, (g) latrunculin B $0.5\ \mu M$, (h) latrunculin B $1\mu M$; each scale bar represents $10\ \mu m$.

Our study also shows that high throughput microscopy not only requires automated image processing and statistical data analysis, but also can benefit from biophysical modeling. For the lamellipodium, such an approach has already been adopted by different groups [27, 50, 66] as was already discussed in the previous chapters of this thesis. Here, we introduce a similar approach for the actin cytoskeleton of stationary adherent cells, i.e. actin networks appearing on a much larger length scale. Without using the random fiber model, it would be difficult to appropriately benchmark and gauge the coherency measure. The underlying reason is that, although the actual structure of the cytoskeleton is determined by molecular rules guiding the assembly and disassembly of individual filaments in response to extra- and intracellular signals, these rules determine the local structural features but not the exact details of the global cellular realizations. As demonstrated here, one therefore has to use stochastic modeling to assess the relevance of quantitative measures for spatial processes, like the structure of the actin cytoskeleton. Until now also other approaches of model-based analysis of microscopy data have been published, like in [100] for cellular microtubule distributions. We thus expect that in the future, this will become an important tool to study cellular structure on a systems level.

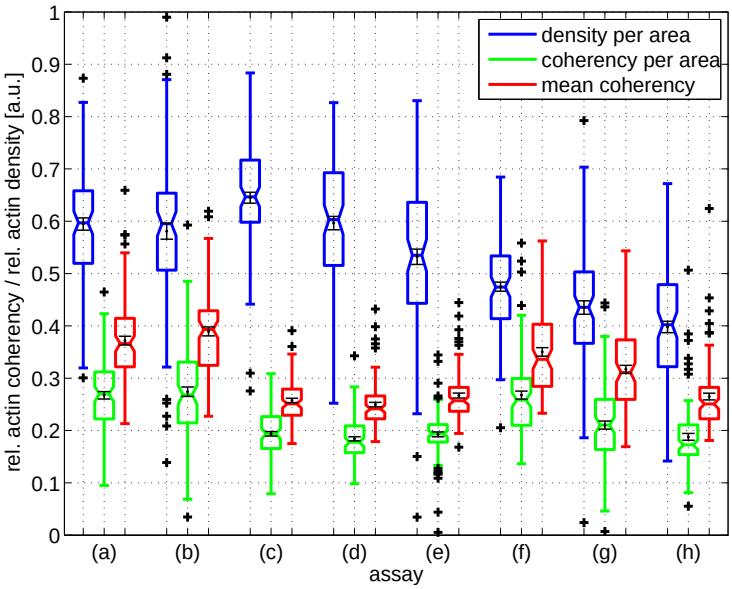

Figure 8.9: Box plots including the estimated mean and its standard deviation for the actin coherency and density of the cell ensembles shown in Fig. 8.8. Control cells 1 and 2 ((a) and (b)) are individually compared to cells treated with two concentrations of cytochalasin D ((c) $0.5\ \mu M$, (d) $1\ \mu M$ and (e) $2\ \mu M$) and latrunculin B ((f) $0.25\ \mu M$, (g) $0.5\ \mu M$ and (h) $1\ \mu M$). The box plot setup is similar to Fig. 8.7.

	(b)	(c)	(d)	(e)	(f)	(g)	(h)
density per area (a)	0.236	0.0008	0.456	0.0005	$\leq 10^{-4}$	$\leq 10^{-4}$	$\leq 10^{-4}$
density per area (b)		0.0003	0.214	0.01	$\leq 10^{-4}$	$\leq 10^{-4}$	$\leq 10^{-4}$
coherency per area (a)	0.276	$\leq 10^{-4}$	$\leq 10^{-4}$	$\leq 10^{-4}$	0.486	$\leq 10^{-4}$	$\leq 10^{-4}$
coherency per area (b)		$\leq 10^{-4}$	$\leq 10^{-4}$	$\leq 10^{-4}$	0.292	$\leq 10^{-4}$	$\leq 10^{-4}$
mean coherency (a)	0.07	$\leq 10^{-4}$	$\leq 10^{-4}$	$\leq 10^{-4}$	0.33	$\leq 10^{-4}$	$\leq 10^{-4}$
mean coherency (b)		$\leq 10^{-4}$	$\leq 10^{-4}$	$\leq 10^{-4}$	0.0005	$\leq 10^{-4}$	$\leq 10^{-4}$

Table 8.1: p-values of the two sided statistical tests with the null hypothesis which states that the means of two different assays are equal. For the underlined p-values the hypothesis was accepted with a significance level of 5%.

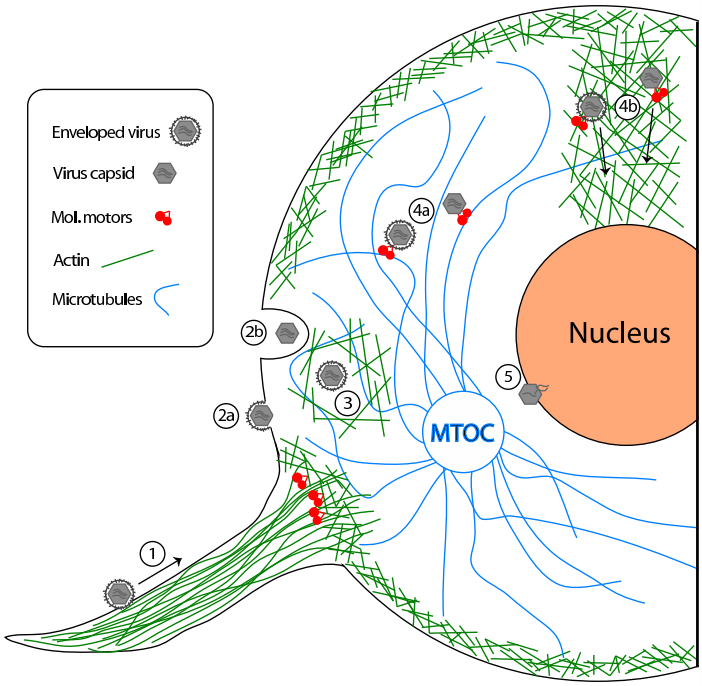

Figure 8.10: Sketch of a generic viral pathway in the cell. Viruses are structurally too simple to replicate on their own. As cellular parasites they hijack various elements of the host cell's machinery. Therefore viruses can also be studied as probes of the cellular host system. A generic replication cycle includes virus entry into the cell (1 and 2), diffusion and active transport to the nuclear region for replication (3, 4 and 5) and viral release and spread to other cells in the proximity. The details of the viral pathway vary for different viruses and cell types. Several steps in the pathway could also include potential interactions with the actin cytoskeleton.

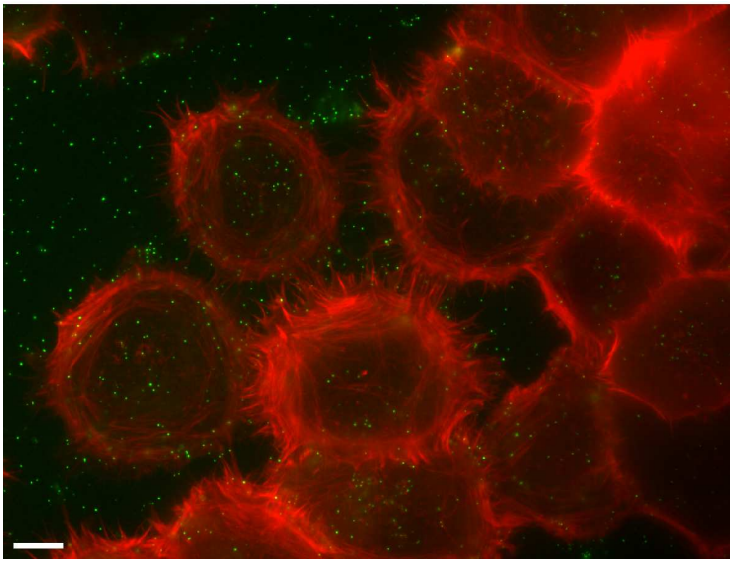

Figure 8.11: Example for JC-53 cells on Lab-Teks which were precoated with HIV-1. Due to the experimental procedure, the plane of prominent actin structures (red) coincides with most HIV-1 particles (green). The scale is $10\ \mu m$.

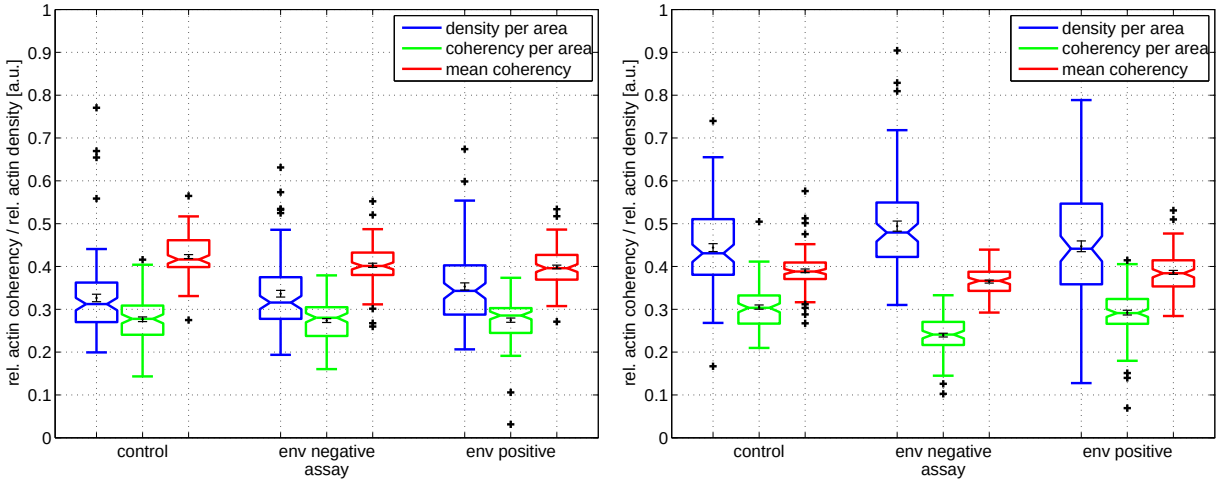

Figure 8.12: Two experiments for the comparison of structures in cells on HIV-1 coated substrates compared to their control. (a) Cells were seeded for 120 minutes on a HIV-1 precoated substrate. (b) Same as (a) with seeding time of 70 minutes.

Chapter 9

Summary of the data analysis part

The second part of this thesis dealt with the problem of extracting meaningful measures from microscopy images of actin networks on different length scales. In our two different approaches, we used mostly automatic digital image processing to obtain reliable and unbiased results.

In Ch. 7, we introduced an experimental framework to specifically test our model predictions for the growth velocity dependent transitions between two different orientation patterns in lamellipodium actin networks (cf. Ch. 3). Correlating light microscopy of living motile keratocyte cells with subsequent high resolution EM tomography, we were able to extract actin network orientation distributions from the images according to two independent analysis techniques. On the one hand, we were measuring a gradient based orientation parameter in local domains of the 2D EM images and on the other hand, we extracted a quantized abstract fiber network which was subsequently statistically analyzed for its orientation. Within a single proof-of-principle experiment our workflow was successfully tested, yielding promising results very similar to our theoretical predictions. However, future experiments have to confirm this trend, as the amount of data so far was not sufficient to draw any final conclusions.

In Ch. 8, we tried to define a specific strategy for comparing ensembles of high-throughput measurements of actin networks on a cell based level. In recent years cellular high-throughput screens have become an important tool in systems biology. Therefore new approaches are required to deal with the increasing amount of abstract data. We introduced a new parameter called *image coherency* to the biological context, which was derived from the gradient based orientation analysis already used before in Ch. 7. For an adjusted variant of the random fiber network, which incorporated parameters also relevant in cellular actin bundle networks on a global scale, we were able to benchmark and gauge our image feature analysis successfully. Actin bundle networks in adherent cells, which were perturbed by increasing concentrations of actin toxins were also reliably differentiated from their wild type analogues. As one exemplary application of our developed experimental and data analysis workflow, we tested HIV-1 treated cells for significant differences in the actin cytoskeleton compared to an untreated control population. However, on the resolution of our light microscopy no measurable differences in the actin networks could be confirmed. This means, that such effects could be rather subtle and in the future it will be worthwhile to switch to higher resolution microscopy measurements and analyze those with our single filament tracking procedure.

Bibliography

[1] ABRAHAM, V. C., KRISHNAMURTHI, V., TAYLOR, D. L., AND LANNI, F. The actin-based nanomachine at the leading edge of migrating cells. *Biophysical Journal 77*, 3 (1999), 1721–1732.

[2] ALBERTS, B., JOHNSON, A., LEWIS, J., RAFF, M., ROBERTS, K., AND WALTER, P. *Molecular Biology of the Cell, Fourth Edition*. Garland, 2002.

[3] AUINGER, S., AND SMALL, J. V. Correlated light and electron microscopy of the cytoskeleton. *Methods in Cell Biology 88* (2008), 257–272.

[4] BALABANIAN, K., HARRIAGUE, J., DECRION, C., LAGANE, B., SHORTE, S., BALEUX, F., VIRELIZIER, J. L., ARENZANA-SEISDEDOS, F., AND CHAKRABARTI, L. A. CXCR4-Tropic HIV-1 Envelope Glycoprotein Functions as a Viral Chemokine in Unstimulated Primary CD4+ T Lymphocytes 1. *The Journal of Immunology 173*, 12 (2004), 7150–7160.

[5] BAUMEISTER, W. Electron tomography: towards visualizing the molecular organization of the cytoplasm. *Current Opinion in Structural Biology 12*, 5 (2002), 679–684.

[6] BEIL, M., LÜCK, S., FLEISCHER, F., PORTET, S., ARENDT, W., AND SCHMIDT, V. Simulating the formation of keratin filament networks by a piecewise-deterministic Markov process. *Journal of Theoretical Biology 256*, 4 (2009), 518–532.

[7] BELTZNER, C. C., AND POLLARD, T. D. Pathway of actin filament branch formation by Arp2/3 complex. *Journal of Biological Chemistry 283*, 11 (2008), 7135–7144.

[8] BETZIG, E., PATTERSON, G. H., SOUGRAT, R., LINDWASSER, O. W., OLENYCH, S., BONIFACINO, J. S., DAVIDSON, M. W., LIPPINCOTT-SCHWARTZ, J., AND HESS, H. F. Imaging Intracellular Fluorescent Proteins at Nanometer Resolution. *Science 313*, 5793 (2006), 1642–1645.

[9] BOLAND, M. V., AND MURPHY, R. F. A neural network classifier capable of recognizing the patterns of all major subcellular structures in fluorescence microscope images of HeLa cells. *Bioinformatics 17*, 12 (2001), 1213–1223.

[10] BRAUMANN, U. D., FRANKE, H., HENGSTLER, J., KUSKA, J. P., AND WEBER, M. Graph-Based Quantification of Astrocytes. *Bildverarbeitung für die Medizin 2006: Algorithmen Systeme Anwendungen* (2006), 379–383.

[11] BROADBENT, S. R., AND HAMMERSLEY, J. M. Percolation processes I. Crystals and mazes. *Mathematical Proceedings of the Cambridge Philosophical Society 53*, 3 (1957), 629–641.

[12] BRUNNER, C. A., EHRLICHER, A., KOHLSTRUNK, B., KNEBEL, D., KÄS, J. A., AND GOEGLER, M. Cell migration through small gaps. *European Biophysics Journal 35*, 8 (2006), 713–719.

[13] BUKRINSKAYA, A., BRICHACEK, B., MANN, A., AND STEVENSON, M. Establishment of a Functional Human Immunodeficiency Virus Type 1 (HIV-1) Reverse Transcription Complex Involves the Cytoskeleton. *Journal of Experimental Medicine 188*, 11 (1998), 2113–2125.

[14] CAMERON, L. A., FOOTER, M. J., VAN OUDENAARDEN, A., AND THERIOT, J. A. Motility of ActA protein-coated microspheres driven by actin polymerization. *Proceedings of the National Academy of Sciences of the United States of America 96*, 9 (1999), 4908–4913.

[15] CARLSSON, A. E. Growth of branched actin networks against obstacles. *Biophysical Journal 81*, 4 (2001), 1907–1923.

[16] CARLSSON, A. E. Growth velocities of branched actin networks. *Biophysical Journal 84*, 5 (2003), 2907–2918.

[17] CARLSSON, A. E. Dendritic actin filament nucleation causes traveling waves and patches. *Physical Review Letters 104*, 22 (Jun 2010), 228102.

[18] CHAUDHURI, O., PAREKH, S. H., AND FLETCHER, D. A. Reversible stress softening of actin networks. *Nature 445*, 7125 (2007), 295–298.

[19] CONRAD, C., ERFLE, H., WARNAT, P., DAIGLE, N., LÖRCH, T., ELLENBERG, J., PEPPERKOK, R., AND EILS, R. Automatic identification of subcellular phenotypes on human cell arrays. *Genome Research 14*, 6 (2004), 1130–1136.

[20] DICKINSON, R. B. Models for actin polymerization motors. *Journal of Mathematical Biology 58*, 1 (2009), 81–103.

[21] DICKINSON, R. B., CARO, L., AND PURICH, D. L. Force generation by cytoskeletal filament end-tracking proteins. *Biophysical Journal 87*, 4 (2004), 2838–2854.

[22] DICKINSON, R. B., AND PURICH, D. L. Clamped-filament elongation model for actin-based motors. *Biophysical Journal 82*, 2 (2002), 605–617.

[23] DOGTEROM, M., AND YURKE, B. Measurement of the force-velocity relation for growing microtubules. *Science 278*, 5339 (1997), 856–860.

[24] DÖHNER, K., NAGEL, C. H., AND SODEIK, B. Viral stop-and-go along microtubules: taking a ride with dynein and kinesins. *Trends in Microbiology 13*, 7 (2005), 320–327.

[25] ECHEVERRI, C. J., AND PERRIMON, N. High-throughput RNAi screening in cultured cells: a user's guide. *Nature Review Genetics 7*, 5 (2006), 373.

[26] FACKLER, O. T., AND KRÄUSSLICH, H. G. Interactions of human retroviruses with the host cell cytoskeleton. *Current Opinion in Microbiology 9*, 4 (2006), 409–415.

[27] FLEISCHER, F., ANANTHAKRISHNAN, R., ECKEL, S., SCHMIDT, H., KÄS, J., SVITKINA, T., SCHMIDT, V., AND BEIL, M. Actin network architecture and elasticity in lamellipodia of melanoma cells. *New Journal of Physics 9*, 11 (2007), 420.

[28] FLETCHER, D. A., AND MULLINS, R. D. Cell mechanics and the cytoskeleton. *Nature 463*, 7280 (2010), 485–492.

[29] FRISCHKNECHT, F., MOREAU, V., ROTTGER, S., GONFLONI, S., RECKMANN, I., SUPERTI-FURGA, G., AND WAY, M. Actin-based motility of vaccinia virus mimics receptor tyrosine kinase signalling. *Nature 401*, 6756 (1999), 926–928.

[30] FRISCHKNECHT, F., AND WAY, M. Surfing pathogens and the lessons learned for actin polymerization. *Trends in Cell Biology 11*, 1 (2001), 30–38.

[31] GALLO, R. C., SARIN, P. S., GELMANN, E. P., ROBERT-GUROFF, M., RICHARDSON, E., KALYANARAMAN, V. S., MANN, D., SIDHU, G. D., STAHL, R. E., ZOLLA-PAZNER, S., ET AL. Isolation of human T-cell leukemia virus in acquired immune deficiency syndrome (AIDS). *Science 220*, 4599 (1983), 865–867.

[32] GIARDINI, P. A., FLETCHER, D. A., AND THERIOT, J. A. Compression forces generated by actin comet tails on lipid vesicles. *Proceedings of the National Academy of Sciences of the United States of America 100*, 11 (2003), 6493–6498.

[33] GILLESPIE, D. T. Exact stochastic simulation of coupled chemical reactions. *The Journal of Physical Chemistry 81*, 25 (1977), 2340–2361.

[34] GLADNIKOFF, M., SHIMONI, E., GOV, N. S., AND ROUSSO, I. Retroviral Assembly and Budding Occur through an Actin-Driven Mechanism. *Biophysical Journal 97*, 9 (2009), 2419–2428.

[35] GOLDBERG, M. B. Actin-based motility of intracellular microbial pathogens. *Microbiology and Molecular Biology Reviews 65*, 4 (2001), 595–626.

[36] GOUIN, E., GANTELET, H., EGILE, C., LASA, I., OHAYON, H., VILLIERS, V., GOUNON, P., SANSONETTI, P. J., AND COSSART, P. A comparative study of the actin-based motilities of the pathogenic bacteria Listeria monocytogenes, Shigella flexneri and Rickettsia conorii. *Journal of Cell Science 112*, 11 (1999), 1697–1708.

[37] GOUIN, E., WELCH, M. D., AND COSSART, P. Actin-based motility of intracellular pathogens. *Current Opinion in Microbiology 8*, 1 (2005), 35–45.

[38] GREULICH, P., AND SANTEN, L. Active transport and cluster formation on 2d networks. *The European Physical Journal E: Soft Matter and Biological Physics 32* (2010), 191–208.

[39] HAMILTON, N. A., PANTELIC, R. S., HANSON, K., AND TEASDALE, R. D. Fast automated cell phenotype image classification. *BMC bioinformatics 8*, 1 (2007), 110–117.

[40] HARTUNG, J., ELPELT, B., AND KLÖSENER, K. H. *Statistik, Lehr-und Handbuch der angewandten Statistik, 14*. Oldenbourg Wissenschaftsverlag GmbH, 2005.

[41] HEAD, D. A., LEVINE, A. J., AND MACKINTOSH, F. C. Deformation of cross-linked semiflexible polymer networks. *Physical Review Letters 91*, 10 (2003), 108102.

[42] HEAD, D. A., LEVINE, A. J., AND MACKINTOSH, F. C. Distinct regimes of elastic response and deformation modes of cross-linked cytoskeletal and semiflexible polymer networks. *Physical Review E 68*, 6 (2003), 61907.

[43] HELL, S. W. Far-field optical nanoscopy. *Science 316*, 5828 (2007), 1153–1158.

[44] HEUSSINGER, C., AND FREY, E. Stiff Polymers, Foams, and Fiber Networks. *Physical Review Letters 96*, 1 (2006), 17802.

[45] HEUSSINGER, C., AND FREY, E. Role of architecture in the elastic response of semiflexible polymer and fiber networks. *Physical Review E 75*, 1 (2007), 11917.

[46] HOSHEN, J., AND KOPELMAN, R. Percolation and cluster distribution. I. Cluster multiple labeling technique and critical concentration algorithm. *Physical Review B 14*, 8 (1976), 3438–3445.

[47] HOWARD, J. *Mechanics of motor proteins and the cytoskeleton*. Sinauer Associates, Sunderland, Massachusetts, 2001.

[48] HUBER, F., KÄS, J., AND STUHRMANN, B. Growing actin networks form lamellipodium and lamellum by self-assembly. *Biophysical Journal 95*, 12 (2008), 5508–5523.

[49] JÄHNE, B. *Digital Image Processing*. Springer, 1997.

[50] JI, L., LIM, J., AND DANUSER, G. Fluctuations of intracellular forces during cell protrusion. *Nature Cell Biology 10*, 12 (2008), 1393–1400.

[51] JIMÉNEZ-BARANDA, S., GÓMEZ-MOUTÓN, C., ROJAS, A., MARTÍNEZ-PRATS, L., MIRA, E., LACALLE, R. A., VALENCIA, A., DIMITROV, D. S., VIOLA, A., DELGADO, R., ET AL. Filamin-A regulates actin-dependent clustering of HIV receptors. *Nature Cell Biology 9*, 7 (2007), 838–846.

[52] JOLLY, C., AND SATTENTAU, Q. J. Retroviral Spread by Induction of Virological Synapses. *Traffic 5*, 9 (2004), 643–650.

[53] KESTEN, H. The critical probability of bond percolation on the square lattice equals 1/2. *Communications in Mathematical Physics 74*, 1 (1980), 41–59.

[54] KOESTLER, S. A., AUINGER, S., VINZENZ, M., ROTTNER, K., AND SMALL, J. V. Differentially oriented populations of actin filaments generated in lamellipodia collaborate in pushing and pausing at the cell front. *Nature Cell Biology 10*, 3 (2008), 306–313.

[55] KOMANO, J., MIYAUCHI, K., MATSUDA, Z., AND YAMAMOTO, N. Inhibiting the Arp2/3 Complex Limits Infection of Both Intracellular Mature Vaccinia Virus and Primate Lentiviruses. *Molecular Biology of the Cell 15*, 12 (2004), 5197–5207.

[56] KOVAR, D. R., AND POLLARD, T. D. Insertional assembly of actin filament barbed ends in association with formins produces piconewton forces. *Proceedings of the National Academy of Sciences of the United States of America 101*, 41 (2004), 14725.

[57] KRUSE, K., JOANNY, J. F., JÜLICHER, F., PROST, J., AND SEKIMOTO, K. Asters, vortices, and rotating spirals in active gels of polar filaments. *Physical Review Letters 92*, 7 (2004), 78101.

[58] KRUSE, K., JOANNY, J. F., JÜLICHER, F., PROST, J., AND SEKIMOTO, K. Generic theory of active polar gels: a paradigm for cytoskeletal dynamics. *The European Physical Journal E: Soft Matter and Biological Physics 16*, 1 (2005), 5–16.

[59] LAMBRECHTS, A., GEVAERT, K., COSSART, P., VANDEKERCKHOVE, J., AND VAN TROYS, M. Listeria comet tails: the actin-based motility machinery at work. *Trends in Cell Biology 18*, 5 (2008), 220–227.

[60] LANDAU, L. D., AND LIFSHITZ, E. M. *Theory of Elasticity, Course of Theoretical Physics vol 7*. 1995.

[61] LEE, K. C., AND LIU, A. J. Force-Velocity Relation for Actin-Polymerization-Driven Motility from Brownian Dynamics Simulations. *Biophysical Journal 97*, 5 (2009), 1295–1304.

[62] LEHMANN, M. J., SHERER, N. M., MARKS, C. B., PYPAERT, M., AND MOTHES, W. Actin- and myosin-driven movement of viruses along filopodia precedes their entry into cells. *The Journal of Cell Biology 170*, 2 (2005), 317.

[63] LI, J., AND ZHANG, S.-L. Finite-size scaling in stick percolation. *Physical Review E 80*, 4 (Oct 2009), 040104.

[64] LICHTENSTEIN, N., GEIGER, B., AND KAM, Z. Quantitative Analysis of Cytoskeletal Organization by Digital Fluorescent Microscopy. *Cytometry Part A 54*, 1 (2003), 8–18.

[65] LÜCK, S., SAILER, M., SCHMIDT, V., AND WALTHER, P. Three-dimensional analysis of intermediate filament networks using SEM tomography. *Journal of Microscopy 239*, 1 (2010), 1–16.

[66] MALY, I. V., AND BORISY, G. G. Self-organization of a propulsive actin network as an evolutionary process. *Proceedings of the National Academy of Sciences of the United States of America 98*, 20 (2001), 11324–11329.

[67] MARCY, Y., PROST, J., CARLIER, M. F., AND SYKES, C. Forces generated during actin-based propulsion: a direct measurement by micromanipulation. *Proceedings of the National Academy of Sciences of the United States of America 101*, 16 (2004), 5992–5997.

[68] MATULA, P., KUMAR, A., WÖRZ, I., ERFLE, H., BARTENSCHLAGER, R., EILS, R., AND ROHR, K. Single-cell-based image analysis of high-throughput cell array screens for quantification of viral infection. *Cytometry Part A 75A*, 4 (2009), 309–318.

[69] MCGRATH, J. L., EUNGDAMRONG, N. J., FISHER, C. I., PENG, F., MAHADEVAN, L., MITCHISON, T. J., AND KUO, S. C. The force-velocity relationship for the actin-based motility of Listeria monocytogenes. *Current Biology 13*, 4 (2003), 329–332.

[70] MELAR, M., OTT, D. E., AND HOPE, T. J. Physiological Levels of Virion-Associated Human Immunodeficiency Virus Type 1 Envelope Induce Coreceptor-Dependent Calcium Flux. *Journal of Virology 81*, 4 (2007), 1773–1785.

[71] MOGILNER, A. On the edge: modeling protrusion. *Current Opinion in Cell Biology 18*, 1 (2006), 32–39.

[72] MOGILNER, A. Mathematics of cell motility: have we got its number? *Journal of Mathematical Biology 58*, 1 (2009), 105–134.

[73] MOGILNER, A., AND EDELSTEIN-KESHET, L. Regulation of actin dynamics in rapidly moving cells: a quantitative analysis. *Biophysical Journal 83*, 3 (2002), 1237–1258.

[74] MOGILNER, A., AND OSTER, G. Cell motility driven by actin polymerization. *Biophysical Journal 71*, 6 (1996), 3030–3045.

[75] MOGILNER, A., AND OSTER, G. Force generation by actin polymerization II: the elastic ratchet and tethered filaments. *Biophysical Journal 84*, 3 (2003), 1591–1605.

[76] MULLINS, R. D., HEUSER, J. A., AND POLLARD, T. D. The interaction of Arp2/3 complex with actin: nucleation, high affinity pointed end capping, and formation of branching networks of filaments. *Proceedings of the National Academy of Sciences of the United States of America 95*, 11 (1998), 6181–6186.

[77] NAGHAVI, M. H., AND GOFF, S. P. Retroviral proteins that interact with the host cell cytoskeleton. *Current Opinion in Immunology 19*, 4 (2007), 402–407.

[78] NEDELEC, F., AND FOETHKE, D. Collective Langevin dynamics of flexible cytoskeletal fibers. *New Journal of Physics 9* (2007), 427–451.

[79] OTSU, N. A threshold selection method from gray-level histogram. *IEEE Transactions on Systems, Man, and Cybernetics 9* (1979), 62–66.

[80] PARAN, Y., ILAN, M., KASHMAN, Y., GOLDSTEIN, S., LIRON, Y., GEIGER, B., AND KAM, Z. High-throughput screening of cellular features using high-resolution light-microscopy; Application for profiling drug effects on cell adhesion. *Journal of Structural Biology 158*, 2 (2007), 233–243.

[81] PARAN, Y., LAVELIN, I., NAFFAR-ABU-AMARA, S., WINOGRAD-KATZ, S., LIRON, Y., GEIGER, B., AND KAM, Z. Development and application of automatic high-resolution light microscopy for cell-based screens. *Methods in Enzymology 414* (2006), 228–47.

[82] PAREKH, S. H., CHAUDHURI, O., THERIOT, J. A., AND FLETCHER, D. A. Loading history determines the velocity of actin-network growth. *Nature Cell Biology 7*, 12 (2005), 1219–1223.

[83] PERLMAN, Z. E., SLACK, M. D., FENG, Y., MITCHISON, T. J., WU, L. F., AND ALTSCHULER, S. J. Multidimensional Drug Profiling By Automated Microscopy. *Science 306*, 5699 (2004), 1194–1198.

[84] PESKIN, C. S., ODELL, G. M., AND OSTER, G. F. Cellular motions and thermal fluctuations: the Brownian ratchet. *Biophysical Journal 65*, 1 (1993), 316–324.

[85] PHILLIPS, R., KONDEV, J., THERIOT, J., ORME, N., AND GARCIA, H. *Physical Biology of the Cell*. Garland Science, 2009.

[86] PIKE, G. E., AND SEAGER, C. H. Percolation and conductivity: A computer study I. *Physical Review B 10*, 4 (1974), 1421–1434.

[87] POLLARD, T. D. Regulation of Actin Filament Assembly by Arp2/3 Complex and Formins. *Annual Reviews in Biophysics and Biomolecular Structure 36* (2007), 451–477.

[88] POLLARD, T. D., BLANCHOIN, L., AND MULLINS, R. D. Molecular mechanism controlling actin filament dynamics in nonmuscle cells. *Annual Reviews in Biophysics and Biomolecular Structure 29*, 1 (2000), 545–576.

[89] POLLARD, T. D., AND BORISY, G. G. Cellular motility driven by assembly and disassembly of actin filaments. *Cell 112*, 4 (2003), 453–465.

[90] POLLARD, T. D., EARNSHAW, W. C., AND JOHNSON, G. T. *Cell Biology*. Saunders Philadelphia, 2002.

[91] PRASS, M., JACOBSON, K., MOGILNER, A., AND RADMACHER, M. Direct measurement of the lamellipodial protrusive force in a migrating cell. *Journal of Cell Biology 174*, 6 (2006), 767–772.

[92] RAISCH, F., SCHARR, H., KIRCHGESSNER, N., JÄHNE, B., FINK, R. H. A., AND UTTENWEILER, D. Velocity and Feature Estimation of Actin Filaments using Active Contours in Noisy Fluorescence Image Sequences. In *Proc. of Conference on Visualization, Imaging, and Image Processing* (2002).

[93] ROMERO, S., LE CLAINCHE, C., DIDRY, D., EGILE, C., PANTALONI, D., AND CARLIER, M. F. Formin is a processive motor that requires profilin to accelerate actin assembly and associated ATP hydrolysis. *Cell 119*, 3 (2004), 419–429.

[94] RUSSO, L. On the critical percolation probabilities. *Zeitschrift für Wahrscheinlichkeitstheorie und verwandte Gebiete 56*, 2 (1981), 229–237.

[95] RUST, M. J., BATES, M., AND ZHUANG, X. Sub-diffraction-limit imaging by stochastic optical reconstruction microscopy (STORM). *Nature Methods 3*, 10 (2006), 793–796.

[96] SCHAUB, S., MEISTER, J. J., AND VERKHOVSKY, A. B. Analysis of actin filament network organization in lamellipodia by comparing experimental and simulated images. *Journal of Cell Science 120*, 8 (2007), 1491–1500.

[97] SCHAUS, T. E., TAYLOR, E. W., AND BORISY, G. G. Self-organization of actin filament orientation in the dendritic-nucleation/array-treadmilling model. *Proceedings of the National Academy of Sciences of the United States of America 104*, 17 (2007), 7086–7091.

[98] SCHREIBER, C. H., STEWART, M., AND DUKE, T. Simulation of cell motility that reproduces the force–velocity relationship. *Proceedings of the National Academy of Sciences of the United States of America 107*, 20 (2010), 9141–9146.

[99] SEAGER, C. H., AND PIKE, G. E. Percolation and conductivity: A computer study II. *Physical Review B 10*, 4 (1974), 1435–1446.

[100] SHARIFF, A., MURPHY, R. F., AND ROHDE, G. K. A generative model of microtubule distributions, and indirect estimation of its parameters from fluorescence microscopy images. *Cytometry Part A 77*, 5 (2010), 457–466.

[101] STAUFFER, D., AND AHARONY, A. *Perkolationstheorie: Eine Einführung*. VCH, 1995.

[102] STROGATZ, S. H. *Nonlinear Dynamics And Chaos: With Applications To Physics, Biology, Chemistry, And Engineering*, 1 ed. Studies in Nonlinearity. Perseus Books Group, January 1994.

[103] SVITKINA, T. M., AND BORISY, G. G. Arp2/3 Complex and Actin Depolymerizing Factor/Cofilin in Dendritic Organization and Treadmilling of Actin Filament Array in Lamellipodia. *The Journal of Cell Biology 145*, 5 (1999), 1009–1026.

[104] SVITKINA, T. M., VERKHOVSKY, A. B., MCQUADE, K. M., AND BORISY, G. G. Analysis of the actin–myosin II system in fish epidermal keratocytes: mechanism of cell body translocation. *The Journal of Cell Biology 139*, 2 (1997), 397–415.

[105] SYKES, M. F., AND ESSAM, J. W. Some exact critical percolation probabilities for bond and site problems in two dimensions. *Physical Review Letters 10*, 1 (1963), 3–4.

[106] UPADHYAYA, A., CHABOT, J. R., ANDREEVA, A., SAMADANI, A., AND VAN OUDENAARDEN, A. Probing polymerization forces by using actin-propelled lipid vesicles. *Proceedings of the National Academy of Sciences of the United States of America 100*, 8 (2003), 4521–4526.

[107] URBAN, E., JACOB, S., NEMETHOVA, M., RESCH, G. P., AND SMALL, J. V. Electron tomography reveals unbranched networks of actin filaments in lamellipodia. *Nature Cell Biology 12*, 5 (2010), 429–435.

[108] VERKHOVSKY, A. B., CHAGA, O. Y., SCHAUB, S., SVITKINA, T. M., MEISTER, J. J., AND BORISY, G. G. Orientational Order of the Lamellipodial Actin Network as Demonstrated in Living Motile Cells. *Molecular Biology of the Cell 14*, 11 (2003), 4667–4675.

[109] WAINBERG, M. A., AND JEANG, K. T. 25 years of HIV-1 research: progress and perspectives. *BMC Medicine 6*, 1 (2008), 31.

[110] WEICHSEL, J., HEROLD, N., LEHMANN, M. J., KRÄUSSLICH, H. G., AND SCHWARZ, U. S. A quantitative measure for alterations in the actin cytoskeleton investigated with automated high-throughput microscopy. *Cytometry Part A 77*, 1 (2010), 52–63.

[111] WEICHSEL, J., AND SCHWARZ, U. S. Two competing orientation patterns explain experimentally observed anomalies in growing actin networks. *Proceedings of the National Academy of Sciences of the United States of America 107*, 14 (2010), 6304–6309.

[112] WIESNER, S., HELFER, E., DIDRY, D., DUCOURET, G., LAFUMA, F., CARLIER, M. F., AND PANTALONI, D. A biomimetic motility assay provides insight into the mechanism of actin-based motility. *Journal of Cell Biology 160*, 3 (2003), 387–398.

[113] WILHELM, J., AND FREY, E. Elasticity of Stiff Polymer Networks. *Physical Review Letters 91*, 10 (2003), 108103.

Acknowledgments/Danksagungen

Eine großer Dank gilt **Ulrich Schwarz** für die Aufnahme in seine Arbeitsgruppe, seine große Unterstützung, guten Ideen und die Zusammenarbeit in den letzten drei Jahren.

Special thanks to our experimental collaborators **Edit Urban** and **Vic Small** for their work so far on the keratocyte experiments and the kind invitation to Vienna.

Ein großer Dank auch an unsere Kollaborationspartner im *Viroquant* Projekt, besonders an **Nikolas Herold**, **Maik Lehmann** und **Hans-Georg Kräusslich**.

Krzysztof Baczynski, **Max Hoffmann**, **Katja Seitz** und **Jérôme Soiné** danke ich für das Korrekturlesen dieser Arbeit und für hilfreiche Tipps.

Vielen Dank auch an die gesamte Arbeitsgruppe Schwarz, bestehend aus **Philipp Albert**, **Krzysztof Baczynski**, **Johanna Baschek**, **Achim Besser**, **Yin Cai**, **Qiang Chang**, **Denis Danilov**, **Carina Edwards**, **Jörg Eisele**, **Thorsten Erdmann**, **Max Hoffmann**, **Christoph Koke**, **Christian Korn**, **Fridtjof Kowald**, **Benedikt Sabass**, **Jakob Schluttig**, **Jérôme Soiné**, **Thomas Striebel**, **Philip Guthardt Torres** und **Johanna von Treuenfels** für die angenehme gemeinsame Zeit und die interessanten Diskussionen.

Heinz Horner danke ich für die Begutachtung der Arbeit.

Melinda Feucht und dem **Bioquant IT Team** danke ich für ihre technische Unterstützung.

Meiner Familie, **Traudl** und **Manfred Weichsel**, **Florian Weichsel** und **Katja Seitz** danke ich für ihre Unterstützung.

Katja Seitz danke ich außerdem für ihr Verständnis und unsere schöne gemeinsame Zeit.